Forschungsbericht 2023-11

Optimization of Thermoplastic Automated Fiber Placement via Model Predictive Control

Lars Brandt

Deutsches Zentrum für Luft- und Raumfahrt
Institut für Bauweisen und Strukturtechnologie
Augsburg

DLR Deutsches Zentrum für Luft- und Raumfahrt

Forschungsbericht 2023-11

Optimization of Thermoplastic Automated Fiber Placement via Model Predictive Control

Lars Brandt

Deutsches Zentrum für Luft- und Raumfahrt
Institut für Bauweisen und
Strukturtechnologie
Augsburg

207 Seiten
77 Bilder
22 Tabellen
201 Literaturstellen

Deutsches Zentrum
DLR für Luft- und Raumfahrt

Herausgeber:

Deutsches Zentrum
für Luft- und Raumfahrt e. V.
Wissenschaftliche Information
Linder Höhe
D-51147 Köln

ISSN 1434-8454
ISRN DLR-FB-2023-11
Erscheinungsjahr 2024
DOI: 10.57676/x39j-tv61

Flugzeugstrukturen, kohlenstofffaserverstärkte Kunststoffe, Thermoplaste, Automated Fiber Placement, FEM, Simulation, Modellordnungsreduktion, Regelungsentwurf, modellprädiktive Regelung

Lars BRANDT
DLR, Institut für Bauweisen und Strukturtechnologie, Augsburg

Optimierung des thermoplastischen Automated Fiber Placements mittels modellprädikativer Regelung
Universität Augsburg

Für die Transformation zum klimaneutralen Fliegen, muss sich die Luftfahrtindustrie drastisch ändern. Beispielsweise müssen fossile Brennstoffe ersetzt und die Effizienz der Flugzeuge durch konsequenten Leichtbau verbessert werden. Kohlenstofffaserverstärkte Kunststoffe (CFK) bieten ein erhebliches Potenzial zur Gewichtsreduzierung, müssen aber großflächiger eingesetzt werden. Thermoplastische CFK bieten hierbei auf Grund ihrer Eigenschaften ein großes Potential, allerdings sind Herstellungsverfahren wie das thermoplastische, in-situ Automated Fiber Placement (T-AFP) nicht ausreichend industrialisiert. T-AFP ist hochautomatisierbar und somit kosteneffizient, steht aber vor Herausforderungen wie der komplexen Prozessentwicklung, geringerer mechanischer Kennwerte und unvermeidbarer Laminatdefekte.

Die vorliegende Arbeit zeigt, wie über die Entwicklung einer Prozessmodellierung und eines modellprädikativen Reglers (MPC) der Einrichtungsprozess, optimiert Prozesstoleranzen verringert und Defekte vermieden werden können. Eine innovative dreidimensionale Multiphysik-Simulation kombiniert mechanische, optische und thermische Modelle. Anhand der validierten Simulation wurden verschiedene Ansätze zur Modellordnungsreduktion evaluiert. Dabei entstanden zwei leistungsfähige Modelle die anschließend in ein MPC Design implementiert wurden. Über den vorausschauenden Regler konnten Defekte und Steuerungsaufwand im Prozess erheblich reduziert und damit die Stabilität und Bauteilqualität gesteigert werden.

Aircraft Structures, Carbon Fiber Reinforced Plastics, Thermoplastic Composites, Automated Fiber Placement, FEM, Simulation, Model Order Reduction, Control Design, Model Predictive Control

(Published in English)

Lars BRANDT
German Aerospace Center (DLR), Institute of Structures and Design, Location

Optimization of Thermoplastic Automated Fiber Placement via Model Predictive Control

Augsburg University

To decarbonize air travel, commercial aviation must undergo a major transformation, including replacing fossil fuels and improving aircraft efficiency through lightweight structural design. Carbon fiber reinforced plastics (CFRPs) offer significant weight reduction potential in aerospace, but require a broader adaptation. Thermoplastics offer a promising solution for large-scale use, but their manufacturing processes, such as Thermoplastic Automated Fiber Placement (T-AFP) with in-situ consolidation, are still evolving. T-AFP can be highly automated and is thus cost efficient, but faces challenges such as complex setup, lower mechanical properties and inherent defects.

This thesis addresses these issues by developing a simulation to streamline the setup process and a Model Predictive Controller (MPC) to manage process requirements and disturbances. A novel three-dimensional multiphysics simulation is introduced that integrates mechanical, optical, and thermal models and is validated through extensive testing. Various model order reduction approaches are evaluated to design an MPC, resulting in two high-performance controllers that significantly reduce errors and control effort. This approach enhances process stability and part quality, promoting the wider adoption of T-AFP in the aerospace industry.

Optimization of Thermoplastic Automated Fiber Placement via Model Predictive Control

Dissertation
presented for the academic degree
Dr.-Ing.

submitted at the
Faculty of Applied Computer Science
Augsburg University

by
Lars Brandt

Augsburg, 2024

First Reviewer:	Prof. Dr.-Ing. habil. Christoph Ament Chair of Control Theory, Augsburg University
Second Reviewer:	Prof. Dr.-Ing. Michael Kupke Center for Lightweight Production Technology, DLR
Date of Defense:	19 August 2024

Acknowledgments

Writing a doctoral thesis is a long journey, unthinkable without substantial help and support, both professional and personal. This chapter is dedicated to the people who helped me the most with this work:
First and foremost, I would like to express my deepest gratitude to Prof. Dr.-Ing. Christoph Ament and Prof. Dr.-Ing. Michael Kupke for their supervision, critical input and helpful guidance.

I would also like to thank Dr.-Ing. Frederic Fischer for the continuous effort and faith he has put in me, by critically questioning and proof reading this thesis. Dominik Deden M.Sc. has kept my schedule free for years by taking over daily research tasks. This, his professional opinion and support during most of the chapters made this work possible in the first place. A special thanks I want dedicate to Dr.-Ing. Michael Vistein and Dr.-Ing. Alfons Schuster for their profound expertise in robotics and vision systems.

Thanks should also go to all my colleagues at the Center for Lightweight Production Technology for the professional and supportive environment. In this regard, I would like to express my sincere gratitude to our technicians, especially Dietfried Henning, who supported me whenever technical problems arose or assistance was needed in a series of experiments.

Throughout this thesis, students have supported the work done here and I would like to express my gratitude for their work. Special mention should be made of Jonas Harig M. Sc. and Johannes Wüstner, as their work contributed significantly to this thesis.

Most importantly, none of this would have been possible without my family and friends. In particular, I would like to thank my beloved Marie. Thank you for tolerating me for the last four years, that you endured the endless discussions about current obstacles and challenges, and for encouraging me every time I was in low spirits and getting me back on track.

Abstract

A major transformation of commercial aviation is necessary to decarbonize air travel, in the coming years. Besides the replacement of conventional fossil fuels, aircraft efficiency will need to be improved, for example by structural lightweight design that saves energy throughout the service time of an aircraft.
Carbon fiber reinforced plastics offer the greatest potential for weight savings in aerospace, but need to be integrated into a wider range of aircraft segments. Thermoplastics with their distinct advantages, provide an appealing solution for large-scale deployment, but manufacturing processes are not yet mature. Thermoplastic Automated Fiber Placement (T-AFP) with in-situ consolidation is a cost-effective, highly automated manufacturing process. However, its major challenges are the laborious setup and comparatively low mechanical properties.

These challenges are tackled simultaneously within this thesis by developing a simulation to support the setup that is subsequently used to develop a Model Predictive Controller. It can set tangible requirements for the process and compensate for common disturbances.
A novel, three-dimensional, multiphysics simulation is designed with interrelated mechanical, optical and thermal models. Silicone rubber deformation is evaluated by mechanical and pressure sensitive sensor tests. The laser is evaluated by irradiance measurement and beam divergence by camera edge detection. To validate the thermal simulation, extensive thermocouple measurements were performed using CF/LMPAEK as a reference material. The trials proved that process temperature prediction with significant higher accuracy than previous models is achieved and detailed process details can be verified.

Utilizing the simulation, a Model Predictive Control (MPC) is designed. First, three model reduction techniques were evaluated, resulting in two reduced, high performance models: a two-dimensional finite element and a lumped element simulation. Both were implemented in the MPC and benchmarked using layup experiments.
The novel control system reduces the integral squared error by one order of magnitude, while cutting the control effort approximately in half. For the first time it is possible to compensate for planned disturbances, such as ply and layup speed changes, by predicting their effects on the process temperature. The approach presented improves significantly process stability and part quality, supporting its adoption in the aerospace industry.

Contents

1. Introduction

In the face of climate change, the aerospace industry needs to reduce its carbon dioxide emissions, while maintaining its business model. The International Air Transport Association (IATA), the world's largest airline governing body, has made a self commitment to achieve net zero carbon emissions for all its airlines by 2050. In Europe, where the Green Deal aims to reduce CO_2 emissions of around 50 % by 2030 (based on 1990 emissions), this is even more time-sensitive.[1, 132]
The ambitious target to decarbonize air travel cannot be added to the ongoing efforts of aircraft manufactures to improve fuel efficiency, increase flight range, optimize payload and reduce operating costs. Whereas these efforts are usually faced with incremental improvements to the aircraft programmes, a rather radical, innovative approach is needed to develop new zero-emission aircrafts.

There are a number of possible approaches to reduce aircraft emissions: firstly, the substitution of fossil kerosene with Sustainable Aviation Fuels (SAF), produced from feedstock, or the use of liquid hydrogen. Secondly, improving the efficiency of the propulsion systems. In addition, aerodynamics can be improved in order to reduce the aircraft's drag or to increase the uplift provided by the wings and fuselage. Finally, the reduction of structural weight is particularly desirable, as it enables energy savings throughout of an aircraft's service life.
One promising approach to structural weight reduction is the increased use of carbon fiber reinforced plastics (CFRPs), which have the potential to achieve mass savings of around 20-25 %. Modern aircraft designs such as the Boeing 787, Airbus 350XWB and the Airbus 220 (formerly CSeries) use between 50-53 % CFRP by weight and are considered to be the most efficient aircrafts ever built.
However, the widely used single-aisle aircrafts, which account for about 80 % of the market, do not take advantage of the opportunities offered by the use of CFRPs.[10, 130] Besides the economic efficiency, barriers to adoption include the time consuming laminate lay-up and subsequent consolidation. The latter usually requires an autoclave for the currently applied thermoset, prepreg CFRPs. This limits not only the number of units that can be produced at a time, but also the part size.

In this environment thermoplastic composites offer distinct advantages, that could solve some of the challenges posed by the use of CFRP in high volume production. Examples of

these advantages include unlimited shelf life, good thermal and chemical resistance, and potential recyclability and repairability.
The ability of thermoplastic CFRPs to be re-melted offers the opportunity of using welding and overtaping techniques, that reduce the need for fasteners and thereby offering downstream savings. In addition, thermoplastics are fully cured, so consolidation takes minutes, rather than the hours required for cross-linking of thermosets. In-situ consolidation offers further benefits, potentially eliminating the need for downstream consolidation steps, such as vacuum bagging. Combined with Automated Fiber Placement (AFP), it provides a fully automated, lean manufacturing process.
However, thermoplastic AFP (T-AFP) with direct consolidation is still under research because the produced laminates exhibit reduced mechanical properties compared to, for example hot press consolidated parts. One of the main reasons for this is that process parameters and environmental influences are highly interrelated, making it difficult to assess their respective effects.
The application of sensors is non trivial as visibility is limited, lost sensors have a direct impact on the consolidation and the process is highly transient. As a result, most current research relies on incremental improvements, which are often dependent on the layup machine and material. Furthermore the process is highly sensitive to temperature variations, which is particularly problematic as sensors for a closed-loop control can only observe the nip point in front of the consolidation roller. Additionally high performance laminates incorporate changes in thickness and fiber orientation that lead to changes in heat absorption and thus defects.

In order to overcome these systematic drawbacks a holistic approach is proposed in this thesis. Using a three-dimensional, multi-physics finite element simulation (FEM), a detailed understanding of the effects of the different physics and components such as the heat source, material etc. is generated. This model is then used to formulate requirements for optimal layup parameters, rather than defining individual parameters.
Building on this, temperature control, which has received little research attention, will be improved. The innovative Model Predictive Control (MPC) compensates for inevitable but predictable disturbances and ensures constant process temperatures, while maximizing the layup velocity.
This approach increases process stability and material quality, thereby reducing the knockdown factor between in-situ T-AFP and other consolidation processes. Besides this, efficiency is improved by optimizing lay-up speed. This will enable the introduction of CFRPs into the high volume aerospace market to ensure future, carbon-neutral commercial aviation.
Once this method of modeling a non-linear, not observable, multiphysics process is established, it can be easily generalized and adapted to other processes. For example to ultrasonic or resistance welding or press consolidation. All these technologies combine several physical effects in a confined, closed space.

This work starts with the theoretical background used to implement the proposed approach. As T-AFP is highly dependent on the the material quality, an introduction to aerospace relevant, high performance CFRPs is given, before the physical effects that occur during the process are described. Practical implementations are then given, including an overview of the current performance of T-AFP and examples of aircraft components produced using the process.
The state of the art in T-AFP process simulation is outlined in the subsequent chapter, using the different process components to provide a structured overview. The theoretical background concludes with common control strategies for transient heat transfer processes, including concepts that have been implemented in T-AFP so far.
With this comprehensive overview the demand for a modern, three-dimensional and multi-physics simulation is demonstrated in chapter 3. In addition, it is analyzed that current research lacks the evaluation and implementation of new control strategies, particularly for the latest generation of infrared laser-assisted T-AFP.
This is followed by a detailed description of the design of the FEM simulation, starting with the mechanical and optical simulation and ending with the thermal simulation. The tuning and validation of each model is described in the corresponding subchapters.
The development of the Model Predictive Control is presented in chapter 5. It includes the introduction and extension of the existing setup, the model order reduction including a second modeling approach, the design of the actual MPC and its validation. The work concludes with final remarks on the progress made and an outlook on future activities required to further improve the T-AFP process.

2. Theoretical Background and State of the Art

This chapter aims to describe all required and used theory around T-AFP. For this purpose the three subchapters shall outline the process itself as well as the approaches to simulate it. Afterwards a short summary of the applicable control theory is given and controllers designed for the process in the past are described.

2.1. In-situ Automated Fiber Placement

2.1.1. Introduction

The following sections are intended to give a comprehensive overview over the manifold aspects of thermoplastic AFP and how they affect the efficiency and quality of the process. First a short introduction to the raw materials and the state of the art regarding pre-impregnated tapes is given. Subsequently the AFP process and the physics involved are described including their corresponding, adapted models. After the theoretical considerations a summary on the applied research done in this field in the past is given. This comprises the development of suitable heat sources, layup machines, determination of material parameters and an outline of the components and products manufactured with thermoplastic AFP. At the end of the section a critical review summarizes the research and identifies research opportunities.

2.1.2. Advanced Thermoplastic Composites

For readability the description of raw materials is limited on high performance thermoplastic matrices and fibers, that are commonly used in structural components in aerospace.

Carbon Fibers

Carbon fibers are commonly used as reinforcements in advanced composites. The use of carbon fibers is commonly given preference where material performance is rated higher than costs, for example in the aerospace and energy production industries. They offer the highest specific strength and modulus compared to all other reinforcement fibers known (e.g. Glass, Aramid), while having a low density that yields a great lightweight potential. Due to their brittleness they exhibit a low strain to failure of about 1-2% and a low impact resistance. A linear stress-strain behavior can be observed. Additionally, carbon fibers show excellent fatigue resistance. Their low coefficient of thermal expansion is often beneficial for applications but poses problems during production and in material combinations that are used in thermal gradients. The fibers are electrical conductive, leading to galvanic corrosion if in contact with anodic materials such as aluminum. The exact properties of carbon fiber can be adjusted depending on their production. A common classification for carbon fibers are high strength (HS), intermediate modulus (IM), high modulus (HM) and ultra high modulus fibers (UHM).[20, 24]

Precursors for the manufacturing of carbon fibers are Polyacrylonitrile (PAN) and petroleum-based pitch. Pitch based carbon fibers were introduced as a more economical production technology, however their properties are inferior to the fibers produced with PAN, that offer the best combination of properties.
For the manufacturing of PAN based fibers these are stretched and stabilized first, in order to orientate and oxidize the precursor. Afterwards it is carbonized in an inert nitrogen atmosphere at approximately 1500 °C. To yield high modulus or ultra high modulus fibers an additional graphitization step is applied under argon atmosphere and a temperature up to 2800 °C. Ultra high modulus fibers are sometimes also referred to as graphite fibers.
After fabrication the fibers are wound onto bobbins with common tow sizes of 1, 3, 6, 12 and 24k fibers. To improve the adhesion to polymeric matrices or handling in subsequent steps their surface is often treated and a sizing is applied.[20, 24, 42, 118]

Common fibers and their properties, used for aerospace grade carbon fiber reinforced plastics, can be found in table 2.1.

Matrices

The mechanical properties of polymeric composites are dominated by the fiber used. Nevertheless the matrix covers vital functions in the compound. It holds the fibers in correct position and protects them from abrasion, chemicals and moisture. Besides this,

Table 2.1.: **Properties of common aerospace grade fibers for TAFP**

		Standard elastic modulus		
Properties	Units	AS4	HTS45	T700S
Tensile Strength	MPa	4,447	4,500	4,900
Tensile Modulus	GPa	231	245	230
Elongation at Failure	%	1.7	1.8	2.1
Density	g/cm^3	1.79	1.76	2.10
Filament Diameter	µm	7.1	7.0	7.0
Carbon Content	%	94	95	93
Electrical Resistivity	$10^{-3}\Omega$ cm	1.7	1.6	1.6
Thermal Expansion (CTE)	ppm/°C	-0.6	-0.1	-0.3
Thermal Conductivity	W/mK	6.8	10.2	9.6
Specific Heat	J/gK	1.13	0.71	0.75
		[72]	[176]	[180]

transverse forces are absorbed and transferred in to the fibers. Heat resistance of a composite part depends on the matrix selection. Two types of matrices exist: thermosets and thermoplastics.

Thermosets are usually processed with a resin plus a corresponding curing agent. They are amorphous with cross links that provide strength, stiffness and temperature stability. Most common thermosets are: polyesters, vinly esters, bismaleimides, polymides, epoxies, melamine, ureas and phenolics. The latter three require high processing pressures which is disadvantageous in combination with fiber reinforcement. On the other hand they offer a low flammability with little smoke and toxic gases. One of the challenges for the utilization of polyester is that it exhibits high shrinkage, with leads to a decrease in mechanical parameters. Most high performance applications do not require thermal stability over 130 °C, in these cases epoxies are commonly used. A wide range of formulations are offered by industry to simplify processing and optimize properties. Once cured, thermosets can not be softened or melted again and are not suitable for in-situ consolidation or other one step processes and are therefore not discussed further in this work. [20], [44, p. 82]

Relevant thermoplastics are the semi-crystalline polyetheretherketone (PEEK), polyphenylen sulfide (PPS), polypropylene (PP) and amorphous polyetherimide (PEI). PEEK, PPS and PEI can be considered as high performance plastics with increased mechanical properties,

but also higher costs and glass transition temperatures T_g compared to e.g. PP. At T_g the material turns from rigid to semi-flexible with the polymer structure still in tact but loosened cross links. Thermal stability of thermoplastics derive from phenylene rings that increase the T_g. High aromatic thermoplastics are flame retarding due to the protective layer build by charring.
The molecular structure of thermoplastics influence the material performance. Amorphous thermoplastics are randomly entangled molecular chains (refer to figure 2.1 left). In the chains strong covalent bonds apply to keep them together. Whereas between the chains weaker secondary bonds occur and make chain movement possible. As a result amorphous thermoplastics exhibit good elongation, toughness and impact resistance.
In semi-crystalline thermoplastics polymer chains are tightly folded with amorphous regions connecting these areas (refer to figure 2.1 right). Crystallinity increases the density of the matrix resulting in a better chemical resistance as well as strength, stiffness, creep and temperature resistance. However chain mobility and fracture toughness is reduced.[20], [44, p. 82] The aforementioned thermoplastic matrices and their key properties can be found in table 2.2.

Figure 2.1.: **Illustration of thermoplastic molecule structures (redrawn from [158])**

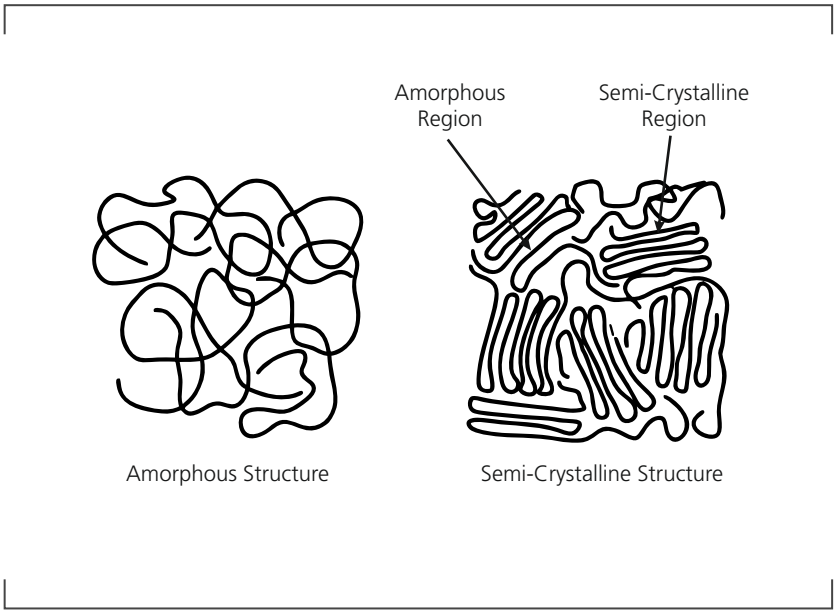

Compared to thermoset resins thermoplastics offer a distinct set of advantages: Increased mechanical properties in the area of impact and abrasion resistance. Enhanced environmental resistance against chemicals, moisture and corrosion. The raw material has unlimited shelf life and while production no toxic reactions occur or solvents evaporate.

Table 2.2.: **General properties of common aerospace grade matrices for TAFP [25, 55, 166, 180, 181]**

Properties	Units	PEEK	LMPAEK	PPS	PEI
T_g	°C	144	147	85	217
T_m	°C	340	305	285	None
Crystallinity	%	33	20-25	32	None
Density	g/cm^3	1.30	1.30	1.36	1.27
Modulus	GPa	3.79	3.50	3.91	2.96
Strength	MPa	103	90	80	104
Elongation	%	11	15	3	60

Additionally thermoplastics show better potential regarding recyclability due to their fusibility.
Regarding the processability thermoplastics offer reduced tooling costs since they might not need furnace compatibility. Large structures can be build up in sequence, with rapid cycle times. Afterwards joining methods like ultrasonic and resistance welding can be applied or the parts can be co-consolidated.[7, 17, 184]

CFRP Tape Material

For thermoplastic AFP pre-impregnated, fiber reinforced tapes (prepregs) are used as raw material. Due to the separation of the time consuming impregnation process from the layup and consolidation, high production rates are feasible. The incoming tape influences the laminate quality of the process directly as the highly transient process can not compensate entirely for inferior impregnation with a high viscosity polymer or heal other defects. In the following paragraph common prepreg technologies and their challenges are briefly explained. Subsequently recommended tape properties are summarized and most common tape prepregs are presented.

In general carbon fibers are aligned in production direction resulting in an uni-directional reinforced tape. Challenging for impregnation are high processing temperatures and viscosities of thermoplastic polymers. Solution degassing builds voids that lead to losses in mechanical properties and high resin contents. The various prepreg production technologies can be distinguished in six main processes: film stacking, fiber co-mingling, solution

processing, melt impregnation and powder impregnation.
In film stacking process two thermoplastic sheets are placed on top and bottom of the fiber rowing, followed by press forming. The process is non-continuous and therefore uneconomic for larger tape quantities. Additionally a high resin content is yielded.
Co-mingled tapes are fiber rowings that are mixed with fine matrix yarn. Impregnation of the fibers is done in the layup. This produces highly drapable tape, the wet out is shifted into the process, however. Co-mingled tape usually produces lower laminate quality [159].
For solution processing the polymer is dissolved in a solvent to lower the viscosity and the fiber tow is impregnated. After the impregnation the solvent has to be removed completely which is difficult. Additionally this method only works for polymers that are soluble. The fiber is passed through a slurry tank containing the polymer and a liquid carrier for slurry processing. In a second step the rowing is formed in a die to tape material. Finding the right mixture for the slury is time and material consuming and excessive resin accumulates on the entrance of the die.
During melt impregnation the fiber is coated in molten polymer. It is either submerged in a molten resin bath or a cross head extruder feeds the molten polymer around the roving into a die. For the resin bath, heated pins increase the impregnation into the tow. Good quality tape is yielded if the fibers are kept under tension for impregnation. For both cases applied pressure of the subsequent die or extruder may harm the reinforcement fibers and has to be adjusted accordingly.
Dry powder impregnation is widely used for the prepeg production of CFRP tapes. In this process the fibers are fed into a impregnation chamber where thermoplastic powder particles are circulated via electrostatic attraction or air flow. After the powder application the rowing is heated and fed through a die. Powder bed impregnation may deliver a good matrix fiber distribution if the powder application is closely controlled, the tows are spread out and the particles are not bigger than the fiber diameter.
Tape prepreg material is either manufactured directly to a desired width (tow pregs) or slitted after manufacturing (slit tapes). The latter may result in a higher width standard deviation whereas tow pregs tend to have a less homogenous matrix/fiber distribution. In general it can be stated that melt impregnation of the tape currently shows the best quality for in-situ T-AFP consolidation, as is forms a relatively homogenous and resin rich surface. [77, 80, 87, 118]

Key properties of thermoplastic tape prepreg for T-AFP are the fiber and matrix content and their distribution. Research indicates that resin rich surfaces are beneficial but may reduce the lap shear strength of the laminate [137]. Additionally the surface should be as smooth as possible to enhance intimate contact.
Voids in the material may be compressed while consolidation but not pressed out on a large scale, thus they will incorporated into a final laminate and have to be minimized.

Table 2.3.: **Thermoplastic prepreg tape quality criterions (adapted from [60, 80, 118])**

Quality criterion	Indicative/Optimal value	Impacts
Fiber areal weight	145 g/m^2	• mechanical properties • heat transfer • resin rich surface
Fiber orientation	minimize waviness	• mechanical properties • surface quality laminate
Resin weight fraction Fiber/resin distribution Surface roughness Surface resin thickness	35% +- 1 homogenous plus resin rich surface < 2.3 µm match carbon fiber diameter	• resin flow • intimate contact • reduces interply voids
Voids	minimize	• mechanical properties
Thickness variation	< 6%	• laminate waviness • heat distribution
Width variation	-0.1 - 0 mm	• gaps and overlaps • mechanical issues machine
Tape edge	rectangle and impregnated	• joint consolidation

Dimensional control in width and thickness directly influence gaps, overlaps and the waviness of the laminate and might reduce problems in manufacturing if under control. Thickness variations may result in fluctuating heat distribution and processing temperatures might run out of tolerances.
In general good fiber wet out is crucial for tape quality and long continuous tape lengths directly increase production efficiency. Table 2.3 gives an overview of desired quality parameters for T-AFP.

Most commonly used prepreg tape in aerospace is carbon fiber reinforced PEEK (CF/PEEK) due to its high operating temperature, large existing database and mechanical performance. Literature shows an extensively use of APC-2/AS4, a trade name of CF/PEEK produced by Solvay S.A., with its less used variations APC-2/IM6 and IM7 [73, 120, 151, 178]. AS4/PEEK is the second PEEK representative used in research. Its manufactured by Toray and Suprem S.A. The latter provided material for this work, that was used as reference. Others combinations that have been under investigation are CF/PPS, CF/PEI, CF/PEKK, CF/PA, CF/PP. The latter two with less relevance for the aerospace industry, however.[192]
In the last years a new polyaryletherketone with low melting temperature was introduced

(LM-PAEK). The lowered processing temperature and crystallinity is intended to improve processability.[6, 153] In this work a LM-PAEK/T700 manufactured by Toray is used for validation.

2.1.3. Physical Processes during In-situ Consolidation

General Process Steps

Thermoplastic automated fiber placement builds up laminates by laying up an individual or a set of uni-directional reinforced prepreg tapes. A layer is build by consecutively laying tapes next to each other. A stack of layers builds up the laminate, where typical tapes widths are between 1/4" and 2" inches (6.35 - 50.8 mm). Depending on the curvature and complexity of the part, smaller widths may be beneficial due to improved steering.

The tape is fed from a material bobbin or an external cabinet to the tape placement machine. Its usually either a gantry machine or in the last years increasingly an industrial, articulated robot with enhanced accuracy. Both are equipped with a special layup device as tool. Depending on the mechanical design, the tapes are redirected over a varying number of pulleys, to be guided under the compaction roller. Corresponding to the rigidity of the roller, the line or area where the tape is clammed first is called nip-point. For adequate tape alignment and to support cutting a tension has to be maintained between material storage and roller. A principle sketch can be found in figure 2.2.
In the area between the last tape guide and the nip point, the tape is heated by the heat source. Commonly the same heat source is used to heat up the tape and laminate simultaneously. Its aimed to heat up both over the melting temperature T_m of the matrix. Underneath the compaction roller intimate contact develops and tape is bonded onto the laminate via polymer self-diffusion. While being in the compaction area, the polymer is cooled down under T_m. For higher layup rates air or water cooled rollers are used. For most tape laying machines and layup velocities the formed laminate is cooling down under T_g at open environment. In order to enhance crystallinity heated molds are used frequently. For adhesion between the first tape layer and the mold, different concepts have been developed, most common are the manual attachment of areal prepeg material, the use of adhesive tape or polyimide foil.

At the end of each track the tape is cut by a knife or cleaver. The free length between cutting unit and compaction roller defines the minimal track length disposable by a layup machine. In the following subsections the individual physical effects occurring in the AFP process are explained in detail.

Figure 2.2.: **In-situ laser assisted AFP principal sketch**

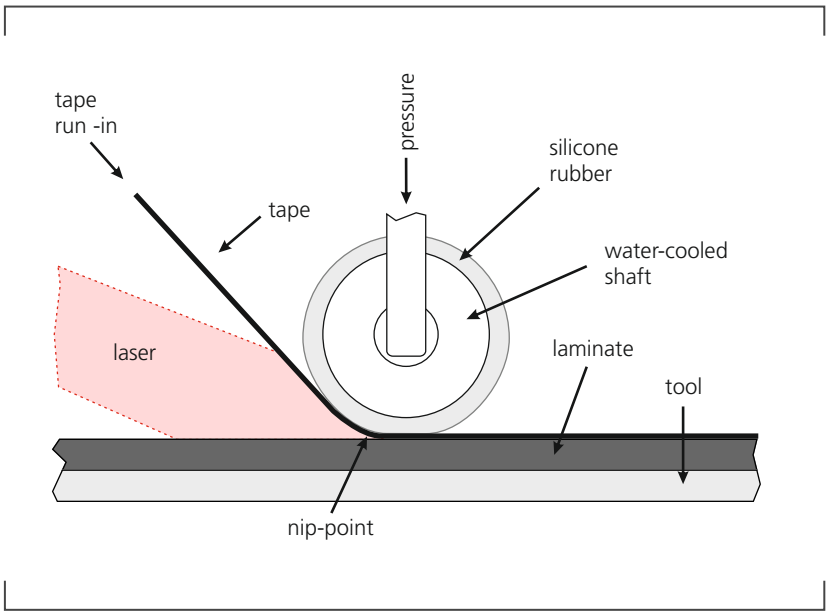

Thermoplastic Melt and Degradation

The process of melting thermoplastic polymers depends on their molecular structure (refer to subsection 2.1.2 for details). Amorphous thermoplastics are gradually softening starting at temperatures around T_g. Whereas semi-crystalline materials get into a rubbery state at T_g due to increasing mobility of polymer chains. They exhibit a sharp melting point at T_m when the crystalline regions dissolve, the lattice structure breaks and the molecules are free to rotate and translate. At this stage the polymer shows relatively low viscosity and is processable.
Heated well over T_m or held at high temperatures in oxidizing atmosphere for longer times, degradation and decomposition of matrix occurs, e.g. PEEK tends to cross link over T_m in oxygen environments which leads to decreasing crystallization.[20]

Degradation and decomposition obviously impact the process quality. Nam and Seferis developed a degradation model using a chemical kinetics function to assume the reaction mechanism. The model was implemented for PEEK in a nitrogen environment. It shows exemplarily how degradation may be evaluated for AFP processes. Two competing mechanisms are described: first is a bezoquinone evolution accompanied by chain scission. The reaction is producing gases or free radicals that act as a catalyst for the second mechanism: generating phenol and benzoquinone gas products.[117]
Sonmez and Hahn adopted the model for PEEK AFP processing. The oxygen transport into

the melt was neglected due to the short time the material is above T_m. The amount of degradation is given as [163]:

$$\alpha_d = \frac{M_0 - M}{M_0 - M_f} \tag{2.1}$$

With M, M_0 and M_f being the current, the initial and the final weight of the polymer. The degradation rate for PEEK with the two described degradation mechanisms w_1 and w_2 is modeled by [163]:

$$\frac{\delta \alpha_d}{\delta t} = k[w_1(1 - \alpha_d) + w_2 \alpha_d (1 - \alpha_d)] \tag{2.2}$$

Where constant k is described as Arrhenius function:

$$k(T) = A\ exp(-\frac{E}{RT}) \tag{2.3}$$

With A as the pre-exponential factor, E the activation energy, R the universal gas constant and T the absolute temperature. The overall weight loss is described as:

$$M_f = 0.64 M_0 \tag{2.4}$$

$$Weight\ Loss(\%) = 36 \alpha_d \tag{2.5}$$

The weight loss can be directly used to assess the degradation of the material. The model has to be adapted to it and the prevalent degradation mechanisms, however this can be done with reasonable effort.

Intimate Contact

Once the thermoplastic CFRP is heated over T_m a close physical contact between tape and laminate has to be established. Polymer self-diffusion can only take place when intimate contact is reached between the interfaces. Depending on the roughness of the CFRP the surface asperities have to be flattened and resin has to fill existing valleys. It is assumed

that the fibers are not contributing to the gap refill. Time required to build intimate contact depends on the initial roughness of the CFRP, applied pressure and viscosity of the polymer. The latter is temperature dependent, a higher temperature results in lower viscosity and thus faster intimate contact. Poor intimate contact on the other hand leads to incomplete bonding and interply voids.[57]

A first mathematically description of intimate contact was given by Dara and Loos (see figure 2.3, a). They used a statistical distribution of rectangles in varying heights and widths to model surface roughness. A viscoelastic behavior of a homogeneous fluid is assumed.[33]

Figure 2.3.: **CFRP surface roughness models a) Dai and Ye, b) Lee and Springer, c) Yang and Pitchumani [33, 95, 190]**

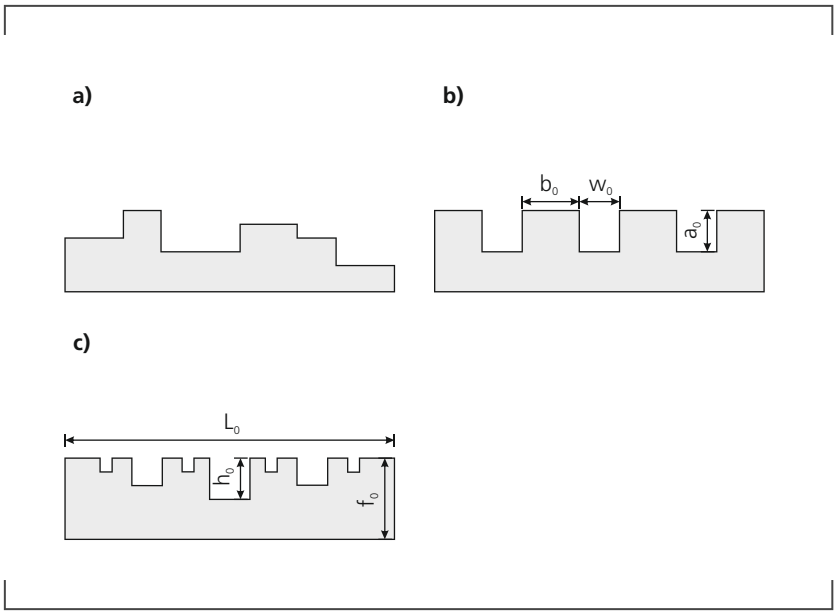

Lee and Springer simplified this model for their processing model of thermoplastic composites. For this purpose rectangles with uniform length, height and constant distances are introduced (see figure 2.3, b). The geometrical parameters are adjusted according to experimental data. Applied pressure and viscosity is considered constant. The flow of asperities into gaps is modeled as laminar. A intimate contact parameter D_{ic} is defined, which becomes one if full contact is reached.[95]
Mantell and Springer upgraded the model by adding a time dependence of pressure and viscosity. For tape laying they considered the roller contact length as small and thus the viscosity as constant.[109] A consideration that does not apply for conformable

rollers.[192]
Pitchumani, Gillespie and Lamontia added pressure and temperature profiles to the mathematical description, that were derived from simulations. Even though the model has been widely used for intimate contact prediction, one of its simplifications is to delete one term of the formula because its insignificance compared to the rest.[134] This does not apply for higher speeds (>125 mm/s) which are quite common today and might increase in the future. Another fundamental problem is that the geometric parameters of the model have to be fitted to experimental data rendering usage of the model impractical.
Guglhör showed that the model of Lee and Springer is not applicable to PA6 resin, due to its low viscosity. The surface tension of the resin was added as parameter to achieve compliance.[62]

Yang and Pitchumani proposed a step back to the beginning of intimate contact modeling, with a more complex description of surface roughness. It resembles the asperities (here AS4/PEEK) more accurate, since asperities are described in varying lengths and sizes (see figure 2.3, c). The model uses a fractal cantor set, a mathematical procedure to transform a flat line to a contour of asperities with decreasing size in each additional generation. Equal scaling factors f are implemented for length and height of the asperities due to a good resemblance of thermoplastic CFRP. The smallest asperities of the last generation are flattened first before the predecessor. Intimate contact for the nth generation of asperities is given as [190]:

$$D_{ic}^{(n)}(t) = \frac{1}{f^n}\left[\frac{5}{4}\left(\frac{h_0}{L_0}\right)^2 \frac{f^{\frac{2nD}{2-D}+n+4}}{(f+1)^2}\int_{t_{n+1}}^{t}\frac{p_{app}}{\mu}\,dt + 1\right]^{1/5}, t_{n+1} \leq t \leq t_n \qquad (2.6)$$

The fractal dimension of the surface is given by D, with $D = 1.32$ for AS4/PEEK. The height of the first generation asperity is h_0 and L_0 is the total length of the Cantor set block. The applied pressure is described by p_{app}, whereas μ defines the viscosity of the resin.
Advantages of this elaborate model is a good fit to the thermoplastic surface and parameters can be easily obtained by profilometry. Weaknesses of the model are that the size, material and line speed of the roller is not considered in this model. Additionally the temperature changes significantly under the compaction roller which neglected in this model.[192]

Following the previous work Levy et al. proofed that Lee and Springer gives a good estimation of intimate contact for AS4/PEEK tapes.[99] Investigations with CF/PA6 showed that intimate contact can be reached within seconds at temperatures slightly above T_m. However, both models of Levy et al. and Yang and Pitchumani overestimate the required time for intimate contact of CF/PA6. This indicates that the models may not be accurate

for low viscosity polymers and sensitive to viscosity in general. The models above used the viscosity of a fiber-resin mix whereas Grouve et al. used a value for neat PPS.[57, 152]
Çelik et al. state that the squeeze flow models assume an even fiber-resin mix and ignore accumulations of fibers and percolation of resin in thickness direction and suggest to extend the models accordingly.[22]

Polymer Chain Self-diffusion

When the polymer is heated above T_g and intimate contact is achieved, polymer chains start to interdiffuse due to random thermal motion. They cross the interface between bonding partners and entangle with polymer chains on the other side. Self-diffusion ascends over time and leads to increased bond strength, until the interface is indistinguishable from the bulk polymer. Figure 2.4 illustrates the process starting from semi-crystalline tape and laminate, to melted bonding partners that are bonded eventually.
Chain mobility of amorphous polymer was described with the so called polymer reptation theory by Gennes and was later extended with the description of strength development by Kim and Wool.[54, 85] The degree of healing D_h for isothermal healing can be described as [19]:

$$D_h = \frac{\sigma}{\sigma_\infty} = \left(\frac{t}{t_R}\right)^{1/4} \tag{2.7}$$

Where σ is the actual bond strength and σ_∞ describes the potential bond strength obtainable, and t defines the elapsed time. The reptation time at a given temperature is defined as t_R. Research with semi-crystalline thermoplastics with at least one welding partner under T_m show that crystallites obstruct, however not prevent, the interdiffusion due to fact that the molecule chains are mainly fixed in crystalline regions.[57]

A nonisothermal fusion bonding model that is more suitable for the AFP process, was introduced by Yang and Pitchumani.[191] The reptation time t_R is replaced by the temperature dependent welding time t_w which is reasonable for low molecular weights and generalizes the formula for a wider range of materials:

$$D_h = \left[\int_0^t \frac{1}{t_w(T)}\, dt\right]^{1/4} \tag{2.8}$$

Figure 2.4.: **Polymer self diffusion (redrawn and extended after [19])**

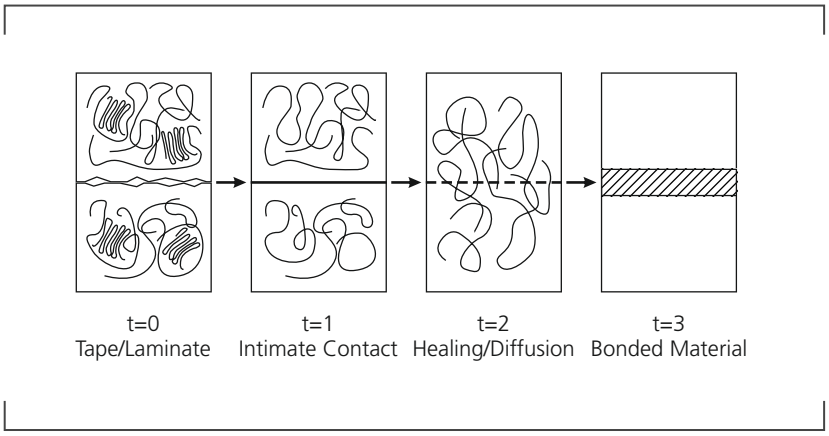

Yang and Pitchumani and Tierney and Gillespie validated the models with experimental data and found good correlation of the results.[177, 191]

Void Dynamics

There are two types of voids: interlaminar and intralaminar voids, based on their location in the laminate either between tapes or in the tape. Interlaminar voids originate from poor intimate contact due to surface roughness, lack of resin or contaminants that may lead to volatiles entrapped during processing between two layers (refer to chapter for intimate contact definition 2.1.3).

Intralaminar voids originate from the unprocessed prepreg tape. Commercially available tapes contain void with a volume percentage of 0.7 to 10 %, APC2 is reported to have a mean void content of 2.7 %.[21, 82, 138, 147, 178, 198] Void contents decreased in the last two decades due to improved impregnating processes. For aerospace applications a void content of < 1 % is required, whereas matrix dominant mechanical properties show a drop off at a void content of approximately 1.2 to 2.7 %.[147] This illustrates that void content is a critical quality measure for T-AFP.

Ranganathan, Advani and Lamontia identified four void transformations, depicted in figure 2.5. Void coalescing describes the merge of voids in the softened matrix (figure 2.5, upper left). Under presssure gradients or mechanical movement void migration in a predefined

Figure 2.5.: **Categorization of void behavior in AFP processing [138]**

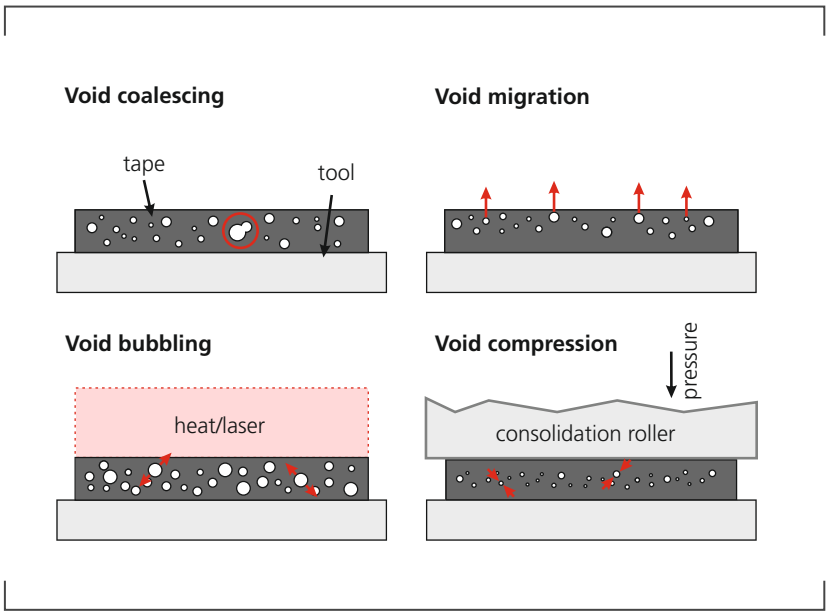

direction is possible (figure 2.5, upper right). At cool down voids shrink because the gas is cooling down and vice versa, the so called void bubbling (figure 2.5, lower left). It occurs if the matrix softens and internal pressure of voids cause their growth. This can be prevented or limited if the voids are compressed under the compaction roller (figure 2.5, lower right). The authors established a macroscopic flow model for the void transport in the resin and a microscopic model to assess void bubbling and compression. Relative movement of the voids in resin was ignored. The material is modeled as compressible fiber-resin-void mixture with temperature dependent viscosity and fixed fiber volume fraction. It predicts the final void fraction and tow thickness. All geometric assumptions were made with a rigid compaction roller, thus modification would be necessary for a process with conformable roller.[138]

Pitchumani et al. used this squeeze flow model and added void growth in unpressurized areas of the system. In their study these areas are specified as static polymer in atmospheric pressure with void and consequently tow thickness growth.[135] The model was validated by Tierney and Gillespie and showed good correlation to experiments.[178]

Simacek et al. developed a model for non-local voids, originating from dry fiber areas in the material. Resin flow from resin rich areas into the void is described. It links the volatile pressure in voids with the compaction pressure and redistribution of resin. The model is adaptable for different layup machine setups.[160]

Parametric studies and experimental work show contributing factors for void volume content. A few aspects may be regarded on the AFP process side: void compression and filling is time dependent thus the time over T_m and under the compaction roller should be maximized. This contradicts the goal to maximize layup velocity. Higher temperatures decrease the resin viscosity and enable resin flow, however a natural limit to this optimization is resin degradation.
Furthermore it has to be considered that to decrease the final void content and prevent deconsolidation the material has to be below T_m after the roller.[82] Simultaneously, unpressurized heating leads to void growth due to thermal expansion of the volatiles in the void. Experimental data proved this effect and showed void growth of up to 3.6 % in CF/PEEK depending on the heated tape length and time.[21]
In-situ consolidated laminates show large void volume contents in the upper layers. Repassing the laminate, meaning the application of heat and consolidation pressure to the laminate without additional tape layup, reduces this effect.[178]
Nevertheless the input material is still a dominant factor for voids in the final laminate. Zhang, Heider and Gillespie discovered that voids do have various forms and the majority are rod-like. The time needed for void reduction is sensitive to even void distribution and their size.[198] Large intraply voids may not be removed due to limited resin flow and high viscosity.[160]
Well adjusted Automated Fiber Placement may hold or decrease the void content in a laminate. Research showed that a reduction of approximately 1 % volume fraction is possible.[82, 147]

Crystallization

During cool down of the laminate, semi-crystalline thermoplastics form crystalline structures. Degree of crystallinity strongly depends on crystallization kinetics, which in turn are influenced by heating and cooling gradients of the thermoplastic resin. Depending on the cooling rate crystallinity may range from low percentages to over 40 % [30, 120]. The relationship between crystallinity and cooling rate for CF/PEEK is given as an example in figure 2.6.
Thermoplastics exhibit double melting behavior while heating and cooling, measurable in differential scanning calorimetry (DSC) studies. These arise from two mechanisms: the spherulitic and epitraxial crystal growth. The spherulitic crystals grow rapidly from a single nucleation point, in CFRP this is mainly circular from fiber to material surface. Its the dominant mechanism whereas epitaxial crystals build in remaining amorphous material and is thus limited.[178]

Figure 2.6.: **Crystallinity in CF/PEEK matrix as function of cooling rate [28]**

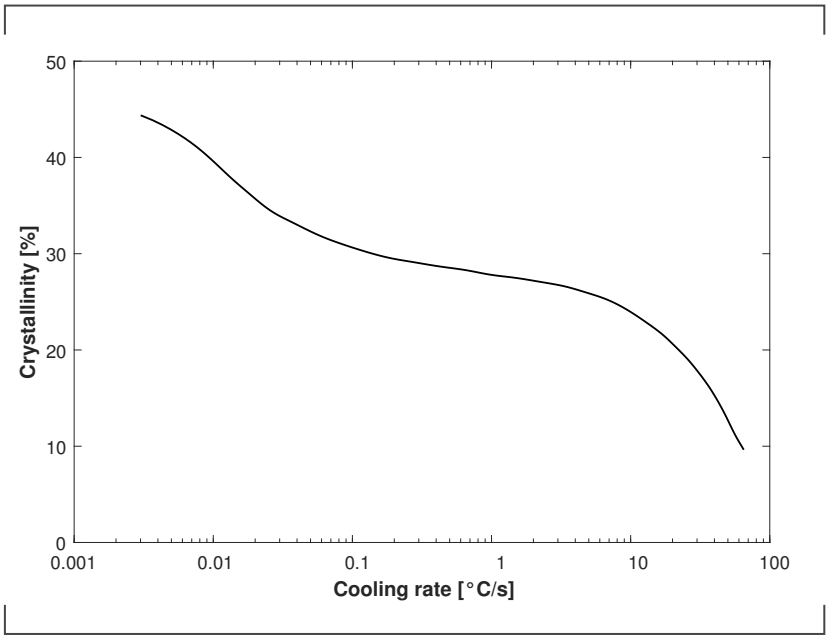

As mentioned in section 2.1.2 crystallinity influences mechanical properties of the final laminate. High crystallinity increases tensile strength, elastic modulus, interphase bond strength while decreasing ductility and fracture toughness [50, 140]. Therefore it is desirable to predict the resulting crystallinity in relationship to the AFP processing parameters.
Most work in this area is based on the crystallization kinetics model of Avrami [15]. The basic isothermal Avrami expression is defined as[185]:

$$X_{VC} = X_{VC\infty}\left(1 - e^{-k(T)*t^n}\right) \tag{2.9}$$

With $k(T)$ being the crystallization rate constant. The Avrami exponent n is depending on growth geometry and the fact if the nucleation is sporadic or instantaneous. The time is defined as t and capital T describes the temperature. X_{VC} is the volume fraction crystallinity and $X_{VC\infty}$ the equilibrium volume fraction crystallinity.
Since the AFP process is highly dynamic and non-isothermal, this formula has to be adjusted. Velisaris and Seferis observed experimental data for PEEK and combined two parallel nucleation and growth processes, based on the Avrami formula.[185] This is in good accordance with crystallization described above. The combination of the two Avrami expressions is given as:

$$\frac{X_{vc}}{X_{vc\infty}} = w_1 \left(1 - e^{-k_1(T)*t^{n1}}\right) + w_2 \left(1 - e^{-k_2(T)*t^{n2}}\right) \tag{2.10}$$

With two different Avramis exponents n_1 and n_2, two crystallization rate constans $k_1(T)$ and $k_2(T)$ and two weight factors $w_1 + w_2 = 1$. Tierney and Gillespie implemented this model for the AFP process in the temperature range between T_g and T_m. Above T_m they calculated the melted resin fraction by integrating the heat rate. Their model showed good agreement with experimental data for heating and cooling rates of 700 °C/s and 150 °C/s, respectively.[178, 192]
An accurate model for the estimation of the degree of crystallization for a complete laminate would need to consider the entire temperature history for each ply in it. That is because the subjacent layers underneath the current placed are still heated well over T_g while cooling rates drop.

Residual Stresses

Residual stresses build during cool down from high processing temperatures to ambient temperature. They may lead to distortion of the final laminate, matrix cracking or interply delamination. Mechanical properties of the CFRP may deteriorate significantly, due to the tensile stresses evoked by the residual stresses. They can represent a large fraction of the overall tensile stress and thus are important to consider in a final component.[164]

Formation of residual stresses occur on three different mechanical levels: on a mirco, macro and global mechanical level. On the micro mechanical level, diverging thermal expansion coefficients (CTEs) of matrix and fiber lead to substantial volumetric shrinkage of the first and almost none of the latter. From these stresses in longitudinal and radial direction of the fiber arise. Volumetric shrinkage of the resin depends on the degree of crystallinity due different densities of amorphous an crystalline domains [74].
On a macro mechanical level the laminates anisotropy has to be considered. Due to their considerable shrinkage in transverse fiber and negligible shrinkage in fiber direction, bonded plies with e.g. orthogonal fiber directions impose a mechanical constraint to each other. They form a behavior similar to a bi-metallic strip and if the laminate is unbalanced and unconstrained it will deform. Figure 2.7 illustrates this effect on a 0°/90°-laminate: on the left side is a top view of the spatial deformation and developing tensile stresses after thermal cycling for the two fiber directions. On the right side the three dimensional laminate with tensile and compressive stresses is shown. The resulting moments are depicted as a lateral view and as the laminate is unconstrained in this example, it is bent.
The different cooling rates and temperature histories in laminate thickness direction can be

described as global mechanical level. Residual stresses are introduced by inhomogeneous solidification of the material where solidified areas impose a constraint on shrinkage for melted areas.[129]

Figure 2.7.: **Residual stresses in a CFRP laminate (based on [129])**

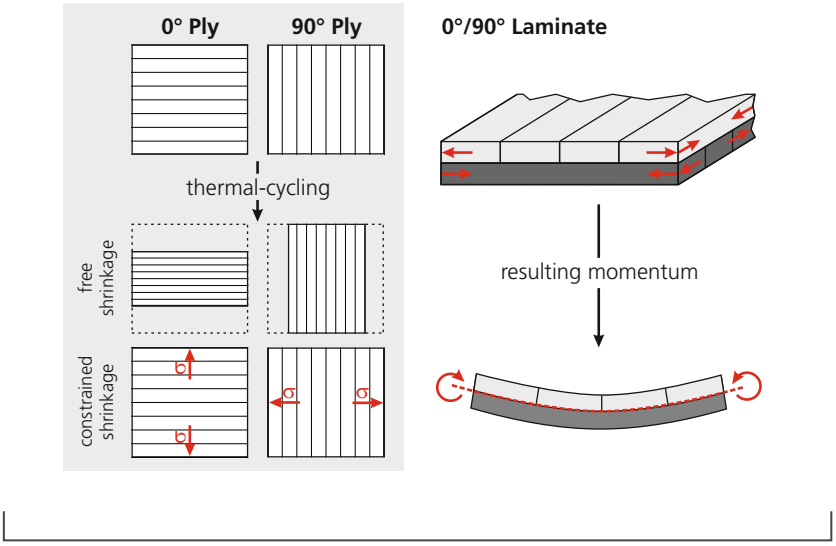

Nejhad, Gillespie and Cope introduced a three dimensional model for induced stresses and deformations in fiber winding. The viscoelastic matrix modulus was defined as a function of the degree of crystallinity and combined with tow properties. The model shows that stresses are introduced in vicinity of the local heat source. The reasons for this are large gradients in heating and cooling rates, that lead to different crystallinity and divergent material properties. A drawback of the model, mentioned by the authors, is that it needs excessive computational time.[97, 119]
Sonmez, Hahn and Akbulut developed a thermo-viscoelastic Finite Element Model (FEM) to predict the stresses in AFP. The quasi static simulation also considers relaxation of residual stresses of previous layers at a repass. Results of the parametric study showed that a localized temperature distribution for the heat source leads to higher residual stresses and unsymmetrical laminates will cause distortion of the final component.[164]
Lemarchand et al. coupled the evolution of thermo-mechanical properties with a marco-scopic plain strain analysis to model in-situ consolidation.[97]

2.1.4. Practical Implementations

Next an overview of the existing work in the field of T-AFP is given. As the heat source is a main driver of quality and productivity for the process, key technologies and research on the topic are presented and their effect on the process is shown. This is complemented by a summary of the historic and current research on T-AFP, including an analysis of the mechanical properties achieved. The chapter is concluded with an overview of existing components manufactured with it, to give an impression of its current relevance as CFRP manufacturing technology.

Heat Sources

Large heat generation is crucial to reach melting temperatures up to 400 °C, required for processing high performance thermoplastic polymer matrices. A variety of heat sources are available to melt thermoplastics: lasers, infrared lamps (IR), hot gas or combustion torches, microwaves, ovens, hot shoes, ultrasonic generators, joule or induction heaters and pulsed lights. Some of the heat sources can only be applied statically (e.g. oven) and are not suitable for a continuous AFP process. The energy density of the heat source is the main bottle neck regarding layup velocity. Previous studies evaluated possible heat sources for AFP, ranking diode lasers, flame and hot gas torch heating (HGT) as the most promising options [49, 155]. In the following heat sources that were utilized for T-AFP are introduced:

Hot gas torches have been adopted from thermoplastic welding, a well known process that was patented by Phillips in 1945 already. With a reasonable investment good interply bonding is obtainable. Nevertheless excessive heat is lost at the outer region of the process area and the system lags which leads to complex control challenges. [143, 194]

Infrared light (IR) transfers heat via radiation, which is almost entirely absorbed by the CFRP tape and thus more efficient than HGTs [78]. Since infrared light is not highly focused, a targeted heat zone is difficult to implement. For this reason the technology is commonly used as preheater [29, 156]. However a few authors showed that IR heaters can be used as main heat source [78, 120, 195]. Nejhad, Cope and Güceri reached reproducible results with IR heating, reducing the residual stresses and reaching good dimensional stability [120]. Disadvantages are that the lack of focus results in heated boundary areas and residual heat in the lamps exacerbate responsive control.

Laser heating has been investigated for thermoplastic AFP early on, first introduced by Beyeler, Phillips and Güçeri in the 1980s [14]. Lasers have higher efficiency compared to

HGTs and IR lamps and offer good controllability due to their rapid heating [82]. Laser beams can be focused on localized points or areas, reducing stresses and damages to the material arising from overheating [3]. Three alternative laser sources have been examined in the past: CO_2-, Nd:YAG- and infrared diode lasers.
CO_2-lasers emit radiation at a wavelength of 10,600 nm that is absorbed by the resin. Thus overheating may directly lead to resin degradation. The beam of a CO_2-laser is a small round spot widened by zinc selenide lenses into narrow heated lines. This results in steep temperature gradients and a high impact of the beam position on the consolidation quality. CO_2-lasers are spacious and can not be mounted on robot-based layup machines.[173]
Nd:YAG solid state lasers provide beams with a wavelength of 1064 nm. In this spectrum the resin is almost transparent for the radiation and only the fibers are heated. Thus charring of the resin on the tape surface is unlikely and heating is homogeneous due to the higher thermal conductivity of the fibers.[192]
With a wavelength of 810-980 nm infrared diode lasers have the same advantages. Additionally they are less costly and more efficient than CO_2- and Nd:YAG lasers. Modern systems reach an efficiency up to 50 % [91]. Diode lasers offer good reliability and low maintenance. The systems have a modular design and fibers can be coupled to yield increased heat fluxes. Using optical equipment the beam shape can be transformed in various shapes, e.g. in a rectangular irradiation area which is preferable for T-AFP. Due to their advantages diode lasers prevail on the market and are widely, commercially available. Diagram 2.8 shows the intensive use of infrared lasers in experimental work and the increase of layup velocity due to increased energy density.[173, 192]
In order to increase adjustability Vertical-Cavity Surface-Emitting Lasers (VCSEL) are currently under investigation. These system combine a multitude of diode lasers to build up a heating grid in which individual diodes are switched off. This is especially advantageous for multi-tow layup machines.[186]

Continous ultrasonic consolidation has be patented by Foster-Miller. In perspective the direct generation of energy in the welding area may have a low energy consumption. Consolidation heat and contact pressure can be applied by the same device. Rizzolo and Walczyk demonstrated its applicability. However, the heat source is not widespread due to a complex, difficult to anticipate heat generation via micro frictions.[143]

Williams and Brown invented a pulsed xenon light as heat source for AFP processes. It shall offer good controllability and reduced safety requirements compared to laser heating. However the system is still under development and a final evaluation is pending.[189]

Figure 2.8.: **Development layup velocity over time and for different heat sources [36, 148, 169]**

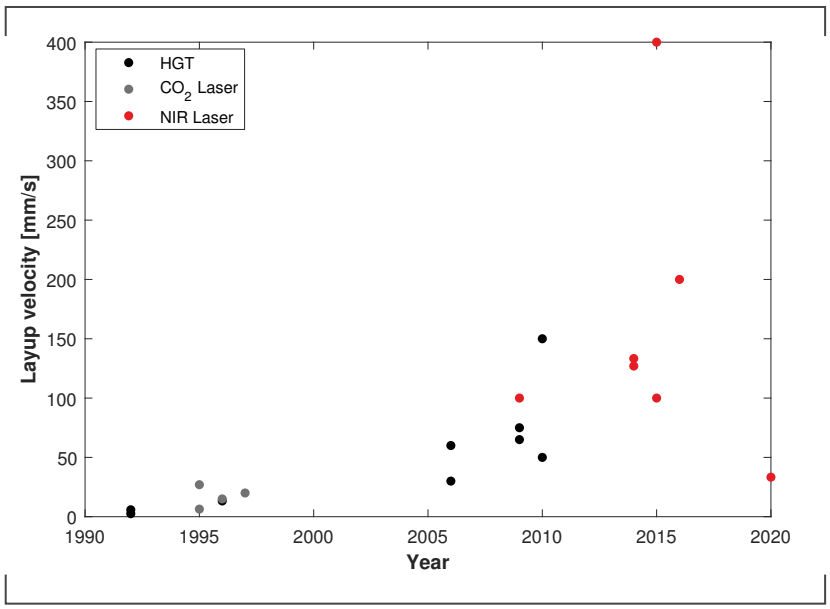

Experimental Work

Development of first AFP systems started with a patent 1974 and early commercial suppliers emerged in the late 1980s. First implementations suffered from technical problems such as insufficient tow tension, reliability, productivity and layup accuracy. Early on the number of tows were increased and Computer Aided Design (CAD) integration was pushed to enhance productivity.This was intensified in the 2000s, with a research focus on reliability and productivity.
The need for large, monolithic parts for spacecrafts increased the interest in in-situ thermoplastic AFP, due size limitation of autoclaves, the risk of thermoset curing and joining of substructures [59]. First attempts were conducted by Beyeler and Guçeri, Grove, Mantell and Springer [13, 58, 109]. Layup speed was limited by the heat sources to 60 - 83 mm/s. Research explored and tried to predict optimal processing conditions for maximal layup rates, inter-ply bonding and low void contents. Most work was done on hot gas heating systems. However, lasers were also used early on by Beyeler and Guçeri, Funck and Neitzel, Pistor, Yardimci and Güçeri [13, 49, 133]. An extensive summary of the historical research can be found in Lukaszewicz, Ward and Potter and is recommended for more details [106].

Recent research, focused on engineering aspects of tape laying machines, identified the need for a modular structure. Current AFP systems are highly integrated, thus updating

single functions or upgrading the machine is not possible.[34, 46, 79] Other aspects have been the development of conformable and flexible rollers, faster feeding and cutting units plus the downsizing and individual tow heating of heat sources. In addition to research, there are a variety of commercial providers for layup machines, for example: Coriolis, Mtorres, Electroimpact, Fives Cincinnati, Ingersoll Machine Tools, Trelleborg, AFPT, Accudyne Systems, Mikrosam, Compositence and Conbility. For further reading on the engineering aspects the work of Zhang et al. is recommended [200].
Component design can be distinguished in constant and variably stiffness. The latter implements load path optimized tape deposition and is still under research. In addition process and path planning is optimized and simulation improved for better accuracy.[17]

Studies showed for the higher industrialized thermoset AFP, that the time share of actual material deposition is below 50 % [17, 34, 146]. The remaining time is consumed by manual inspection, correction and maintenance. This is an optimistic prediction for thermoplastic AFP. Therefore inline quality assurance may have a tremendous effect on economic efficiency of AFP systems and therefore laser light section systems and cameras are currently under investigation. A concise summary is given by Oromiehie et al. [127].

Extensive work has been done to determine material properties for thermoplastic AFP for both hot-gas and laser heated AFP equipment. As elaborated in chapter 2.1.4 infrared laser systems offer a distinct set of advantages. This is especially true for higher layup rates necessary for industrialization. For this reason the summary in this chapter is focused on research with IR laser heating.

Most commonly used material test for thermoplastic AFP is the interlaminar shear strength (ILSS), described in the standard ASTMD2344 and the closely related DIN EN 2563 [31, 38]. This short beam test is sensitive to the resin properties and inter-laminar bond strength, both important to evaluate the process quality. Valid test results can be expected for high performance matrices such as PEEK. For resins with lower stiffness, shear failure mode occurs instead of a interlaminar crack.
In this case wedge or mandrel peel test may be preferable – two quick screening methods to evaluate interply bond strength. The corresponding test specimens are material saving and easy to manufacture. Additionally wedge peel testing correlates well with double cantilever beam testing. However, measurement data shows considerable noise and has to be post-processed statistically. Additionally both methods are not standardized yet.
Single lap shear specimens are also easy to produce and define a shear strength zone by separation of two distinct ply pairs with polyimide foil (refer to [139]).
Less used testing schemes are open hole compression, flexural strength and in-plane shear strength. The former is particularly relevant for bolted or screwed components. Perpendicular tensile testing of uni directional test specimen gives a good indication of

Table 2.4.: **Mechanical properties IR laser assisted T-AFP**

Material	Equipment	Mechanical Property	Measurement method	Unit	max. Value AFP	Reference Value[1]	Reference
AS4/PEEK	ADC	ILSS	ASTMD2344	MPa	78.9	85 %	[137]
	AFPT	ILSS	ASTMD2344	MPa	∼ 98.0	103 %	[169]
	Coriolis	ILSS	ASTMD5868	MPa	40.0	67 %	[36]
	Mikrosam	ILSS	ASTMD2344	MPa	48.2	-	[150]
	MTorres	ILSS	EN2563	MPa	71.0	65 %	[148]
		IPSS	EN6031	MPa	155.0	86 %	
		Flexural strength	EN2562 Type B	MPa	1505.0	81 %	
IM7/PEEK	AFPT	Wedge peel strength	Wedge peel	N/mm	3.9	134 %	[30]
		ILSS	EN2563	MPa	78.0	70 %	
		Flexural strength	EN2562	MPa	1207.0	70 %	
		OHC	ASTMD6484-09	MPa	248.0	78 %	
T700/PAEK	AFPT	ILSS	Single Lap Shear	MPa	33.6	-	[139]
		ILSS	ISO14130	MPa	52.3	72 %	[16]
		Perpendicular tensile	EN2597	MPa	37.4	44 %	
CF/PPS[2]	Coriolis	ILSS	ASTMD2344	MPa	49.2	∼ 75 %	[26]
	MTorres	ILSS	ASTMD3846	MPa	62.3	-	[201]
	AFPT	Mandrel peel strength	Mandrel peel	kJ/m^2	2.2	210 %	[57]
AS7/PPS	AFPT	ILSS	ISO14130	MPa	72.7	-	[23]
		Perpendicular tensile	EN2597	MPa	36.0	-	
CF/PA6[2]	AFPT	Wedge peel strength	Wedge peel	N/mm	4.3	215 %	[171]

[1] Autoclave/Hot-Press, [2] Fiber unspecified, ∼ derived from chart

resin properties. However, the method is material intensive and at least ten valid specimen are required (refer to DIN EN 2597).[30, 39, 171] Additionally, a prebending for the unidirectional test specimen is difficult to avoid and lower the measurement values.

Table 2.4 shows a strong focus of recent research on PEEK and PPS matrices. The maximum reached values are not comparable for a number of reasons: Firstly, tape quality is alternating between suppliers and in time. Secondly, the results are highly dependent on the equipment they are manufactured on. Third, different measurement methods and standards are used and finally the optimization of layup parameters are crucial.
Therefore the comparison of these values to a given reference specimen is more reasonable. Considering the reference values, a significant knock-down factor of 14-35 % can be observed for almost all composites. An exception are the results of Stokes-Griffin and Compston with a slighty better interlaminar shear strength than their reference [169].

Zhao et al. indicates that the main influence for ILSS might be the void content in the laminate, instead of crystallinity. This could explain the better performance of autoclave and hot-press examples, as they can reduce voids efficiently.[201]
All AFP samples tested with wedge and mandrel peeling showed better results compared to their benchmarks, with values that are double for PPS and PA6 resins. However the results of this non-standardized processes remain qualitative.

Components

Apart from mechanical characterization advanced thermoplastic composites have been used in structural parts early on. A first flying component was used by the US military in the F22, where the landing gear and weapon bay door are made of thermoplastic CFRPs.[125] Later on, the wing leading edges of the Airbus A340 and A380 were manufactured using an autoclave cured thermoplastic skin and electrical resistance welded rips. For the A350 and Boeing 787 thermoplastic clips are thermoformed [40]. Additionally the Gulfstream G640s rudder and elevators are produced with thermoplastic composites.[112, 128] For all these components the skin parts are consolidated either by autoclave or hot-press.
Industrialized T-AFP and Automated Fiber Winding (AFW) products can be found in the oil and gas industry where the mechanical and chemical resistance are beneficial for pipes, pressure vessels, antenna shields etc.[52]
The main obstacles for implementation in the industry is not the mechanical feasibility but the process affordability, the material quality and costs combined with acceptable porosity levels for the aerospace sector.[144]

In order to prove the capabilities of the technology, numerous demonstrators were manufactured, of which a few are listed here: Automated Dynamics (now Trelleborg) built a 3-dimensional stiffened helicopter tail boom using HGT AFP to process CF/PEEK [96]. Henne et al. manufactured a rocket booster motor casing with 2.5 m in length and a 1.3 m diameter. They used laser assisted AFP and CF/PPS.[71] Engelhardt et al. showed a CF/PEEK cylindrical shell for a sounding rocket, produced by laser assisted T-AFP. The part proved its airworthiness and realized a weight reduction of above 40 % compared to Aluminum.[43] The same process and material was used in the work of Oliveri et al. to manufacture a variable stiffness, stringer integrated, composite wingbox. The part was dimensioned to fit a single isle aircraft.[125]
For commercial aviation thermoplastics offer an innovation push due to their distinct advantages (refer to chapter 2.1.2). To reduce the above stated barriers for market acceptance, European research focused its strategy on the development of better materials and improved processes. In the last decade the projects TAPAS 1 and 2, CleanSky 1 and 2, CORAC and INSCAPE showed a consistent scale up of demonstrators. Stelia built a

generic airplane fuselage demonstrator including welded stringers, frames and lightening strike protection manufactured with laser assisted T-AFP.
The Netherlands Aerospace Center developed a two step process with ultrasonic AFP and subsequent autoclave curing. With this process a 4 m fuselage panel and flat 12 m horizontal stabilizer torsion box was build in TAPAS 1. In the successor project a 3 dimensional torsion box, including stiffeners, was built. Ingen et al. developed a fuselage demonstrator with welded frames, using an orthogrid as stabilization [75]. Additionally a 6 m long and 28 mm thick CF/PEEK engine pylon upper spar was produced.
FIDAMC a Spanish research center showed that one step consolidation with laser assisted T-AFP for fuselages with less than 1 % porosity is possible. Several fuselages were build with the largest beeing approximately 4 x 1 m in width and length. Additionally a CF/PEEK cockpit frame was presented.[53, 144] The up scaling is has reached its final phase with project STUNNING and MFFD where a 8 m singe aisle fuselage was built. Omairey et al. detail the development of the lower shell whereas the upper shell is still under development.

Within the research to this thesis a 2.2 m LH_2 tank made out of CF/LMPAEK with flashlamp heated AFP was built. Further an upper shell fuselage skin with 1.5 m in length and a diameter of 4 m was manufactured and equipped with stringers and frames via ultrasonic and resistance welding as predecessor for a 8 m fuselage upper shell. Which was built subsequently. A dual curvature bulkhead segment was manufactured implementing tape steering. All demonstrators are shown in figure 2.9.

2.1.5. Conclusion

In summary it can be recognized that required material properties for sufficient in-situ consolidation are well understood. Nevertheless tape with even resin distribution and low defects per roll is still scarce. Additionally material prices are still considerably higher than thermoset tapes but are expected to fall due to economy of scale.

For the highly transient AFP process a thorough understanding of the involved physics help to assess the interactions and improve these. To do so mathematical descriptions for melting, intimate contact, polymer self diffusion, void dynamics, crystallization and residual stresses are available and described in the previous sections. All models depend on material characteristics and need to be adjusted to them.
Intimate contact description started with a rather complex, statistical approach to describe the surface roughness. Major simplifications were made and in consequence the time to build intimate contact was overestimated. With the usage of Cantor sets in the model of Yang and Pitchumani good correlation is achieved. This shows that the right granularity of a model is crucial. All models ignore possible larger dry spots in the tape and assume an

Figure 2.9.: **Demonstrators manfactured during this thesis**

(a) **Liquid hydrogen tank (1.3x2.3 m)**

(b) **Test panel fuselage (5.0x1.0 m)**

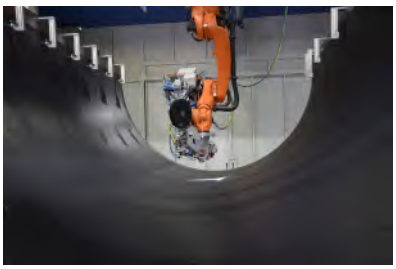

(c) **Singe aisle fuselage (4.0x8.0 m)**

(d) **Dual curvature bulkhead segment (1.0x1.2 m)**

even fiber resin mix.
The effect of polymer self diffusion has been formulated for a wider range of materials and can be combined with an intimate contact model to describe the degree of bonding in total.
Several approaches have been developed to explain the void dynamics. Mainly the focus is on void compression, bubbling and a resin squeeze flow. A non-local void movement modeling has been proposed but a combination of the models has not yet been implemented. Most work is done for rigid rollers and additional work will be needed for conformable rollers.
Models for crystallinity are available and of relevance due to its impact on the mechanical properties of the final laminate. The adjustment of crystallinity models can be easily done via DSC measurements. A few models, based on the crystallization model of Tobin have not been described in this work as it was proven incorrect [15].

The parametric and experimental studies discussed in this chapter, show correlations between layup parameters and quality metrics. Additionally they give guidance how to define them in order to ensure good laminate quality. Main implications for the AFP layup are:

- Higher consolidation pressure ensures enhanced intimate contact. With limits regarding fiber breakage and rubber wear down for consolidation rollers.

- To prevent deconsolidation the laminate should be beneath melting temperature after the consolidation roller.

- Processing temperatures should be maximized to decrease viscosity with degradation as natural limit.

- Void compression and filling is time dependent, which is contradictory to high layup speeds

- Crystallinity of semi-crystalline resins correlates with the cool down gradient, a sharp drop will result in lower crystallinity, which is again incompatible with higher layup rates unless heated molds are used. Repassing might mitigate this problem to a certain degree.

- Resulting tensile stresses may influence the material properties. They can be reduced by heated toolings and possibly by repassing.

Over the decades several heat sources have been evaluated for thermoplastic AFP. A high energy density is needed to accelerate layup velocity with good controllability to stay in

temperature tolerances. With introduction of IR lasers other heat sources lost relevance, especially with nowadays targeted layup velocities above 125 mm/s. Research focuses on systems that may divide heating zones of tape and laminate or provide pre- and main heating with one device.

Studies on in-situ AFP show a broad range of subjects including research on layup parameters, process simulation and improvement of engineering aspects. Mechanical characterizations of thermoplastic AFP manufactured laminates have an emphasis on CF/PEEK and CF/PPS. An expansion to a variety of materials seems beneficial.
The standardized ILSS testing is commonly used, as it provides conclusive information on resin properties and interply bonding. Literature research has shown that knock-down factors for laser assisted T-AFP vary between 14-35 % compared to autoclave or hot-press benchmark specimen.

Advanced thermoplastic composites produced by AFP have not been adopted by industry yet, despite the advantages. Demonstrators proofed that mechanical properties are sufficient. However, robustness of the process must be improved while material costs have to decline. At the same time tape quality has to be enhanced. European research focused its strategy in this field to consistently scale up components and overcome these obsticals.

2.2. Simulation of Thermoplastic Automated Fiber Placement

2.2.1. Introduction

Since thermoplastic AFP is a single stage process without quality enhancing subsequent steps, the quality of a manufactured part is mainly dependent on the process parameters used. As stated before the temperature gradient in the cooling phase influences crystallinity, residual stresses and the degree of bonding. If temperatures reach higher levels thermal degradation deteriorate the laminates characteristics. Although the physical description for the individual effects are introduced in chapter 2.1.3, the temperature profiles resulting from the inputs during the process are missing. A profound knowledge of the thermal effects in the process supports parameter identification and informs about interrelations between them. Consequently substantial research was conducted in this field. This chapter will show the current state of the art regarding T-AFP heat transfer simulations.

2.2.2. Frame of Simulation

The presented simulations can be distinguished into their frame of simulation: either Eulerian fixed or Lagrangian. Models that use an Eulerian frame commonly use a fixed coordinate system, on the compaction roller. This results in a stationary system, with mass flows passing through its borders. There are steady state as well as transient models. Usage of a Lagrangian frame automatically results in transient boundary conditions, that are passing over tape and laminate and describe either a complete laminate or subsections of it.

Dependent upon simplifications made, heat transfer in T-AFP is modeled as a one, two or three dimensional problem in literature. One dimensional solutions focus on the through thickness heat transfer in the laminate. Due to the higher heat transport of the moving material compared to the heat flow in fiber direction, the latter is neglected. Tierney and Gillespie developed a steady state simulation, while numerous models use transient heat fluxes.[29, 32, 56, 82, 86, 102, 178, 187]
Two dimensional Lagrangian models, using a finite difference method, were developed by Tafreshi et al. and Tumkor et al. [175, 183]. Mantell and Springer showed a simple two dimensional model for fiber winding and tape placement using a cylindrical coordinate system [109].
However, a vast majority of models use a two dimensional Eulerian approach. This is justified by the an-isotropic heat conduction of CFRP. The transverse heat diffusivity, perpendicular to the fiber, and the heat loss through the edges is assumed low. Hence heat flow in tape width is considered negligible for two dimensional models. As a side effect this results in the assumption that the heat flux of the heat source is regarded as homogeneous across the width of the material as well. Several solutions have been presented with transient heat transfer equations [122, 135, 149, 151]. Whereas most approaches do implement a steady state model [3, 9, 13, 58, 61, 65, 84, 101, 114, 121, 163, 167, 174].

A couple of three dimensional simulations, do exist. Schledjewski and Latrille introduced a three dimensional transient model as part of a planed process simulation tool, for thermoplastic filament winding with infrared heating.[156] Toso, Ermanni and Poulikakos modeled the same process with hot gas torch heating, aiming to describe the three dimensional heat transfer between HGT and composite material [182]. Gruber et al. simulated the thermoplastic AFP process with HGT heating [60]. Jeyakodi and Shroff developed a thermomechanical, transient analysis to model a thermoplastic AFP process with laser heating [81]. Nejhad, Cope and Güceri introduced an Eulerian three dimensional finite element approach that describes a HGT filament winding process [120].
Chinesta et al. used the same Eulerian approach but used a proper generalized decomposition method to describe a three dimensional, laser heated T-AFP process via order

reduction.[27]
If one examines the simulations in consideration, it can be seen that finite element and finite difference methods were used in the majority of solutions [192].

2.2.3. Simulation Elements

In order to understand with which assumptions and simplifications the individual simulations work and how they do compare, a detailed assessment is required. Therefore the models for all main physical components, needed for T-AFP simulation, are discussed: heat source, optical laser model, material, consolidation roller and tooling. Subsequently the validation methods of the simulations are examined, to conclude the assessment.

Heat Source

Many thermal models have been developed for fiber winding or placement with hot gas torch heating. It was often described as homogeneous heat flux [32, 65, 82, 84, 122, 135, 174, 175, 178]. Only a few modeled heat transportation of hot gas in detail, and used finite element methods to do so [60, 182].

Laser heating has been described in various models as uniform heat flux[9, 13, 27, 35, 101, 111, 114, 120, 152, 163, 187]. Agarwal et al. introduced a quotient to distribute the heat flux to the tape or laminate surface, respectively [3]. Sarrazin and Springer included the newly placed tape instantaneously and modeled a constant irradiation [151].
Kölzer used a intensity distribution depending on the distance between optic and tape material. Also a shadow cast has been implemented that is inevitable for AFP. where the heat source has to be above the layup tooling.[89]
For more accurate results regarding laser irradiation, modeling has to be performed via an optical model, these are discussed in the next paragraph.

Optical Model for the LAFP Process

To specify the heat flux and it's distribution generated by the laser, it is essential to model its ray propagation as well as the absorption and reflection of the tape, laminate and roller respectively. However, previous thermal models considered the laser heating typically as

homogeneous heat flux and shadowing in front of the consolidation roller was neglected [163].

Grove used a simple, two dimensional geometric approach to consider reflections on the tape (see illustration 2.10, a). The concept was supplemented by other authors with angle dependent reflection coefficients and shadowing [3, 47, 58, 170].
For improved accuracy two dimensional ray tracing methods were introduced, to consider a large amount of rays and compute the heat distribution of their specular reflection [56, 86]. A temperature dependence of the absorption coefficient was discovered and integrated [87]. Stokes-Griffin and Compston examined the radiation absorption of CFRP and found that the crystalline part of PEEK polymer absorbes the laser. However, since the polymer is only a thin film on the carbon fiber, this effect has a neglectable influence on the overall absorption. A half cylinder surface was introduced to resemble the fiber surface irradiated by the laser and was fed into a three dimensional ray tracing model (see illustration 2.10, b). It reproduces the specular and scattering properties of the CFRP. The result were used in a optical-thermal model that showed a good accordance to measurements.[167, 168]
A second approach to simulate the scattering was implemented by using a bidirectional reflection function, integrating a Gauss distribution for the scattering. The simulation showed that the scattering transverse to the fiber direction is relatively small compared to the scattering in fiber direction for CF/PEEK.[141, 197]
Zaami, Baran and Akkerman used a three dimensional ray tracing model to calculate the laser distribution. The laser radiation itself was modeled as ideal Gaussian distribution.[196]

Figure 2.10.: **Optical models for laser irradiation (redrawn [58, 167])**

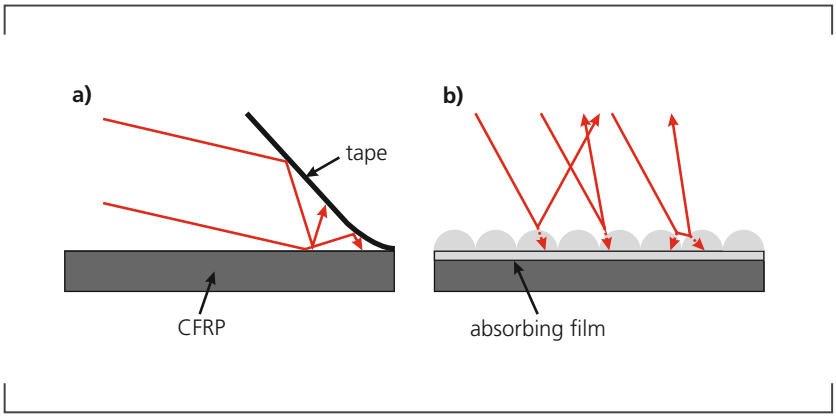

Despite the fact that most research acknowledges that a detailed optical model is beneficial for the accuracy of the over all process model, most thermal models use a two dimensional model.

Material Model

All simulations considered in this work assumed a macroscopic, homogeneous material, although the fiber and matrix system are in fact heterogeneous. One dimensional models consider the thermal dissipation in laminate through-thickness direction and therefore model one heat conductivity only. Two and three dimensional models take the unisotropic material conductivity into account and use different values longitudinal and transverse to the fiber. An exception is Levy et al. because the thermal diffusion in fiber direction is neglected due to the high layup rates and the relatively slow heat conduction [101]. Convection between material and environment is modeled in all simulations. Some also factor heat radiation in.[56, 114]

Key material properties for the description of heat transfer in laser assisted AFP are: thermal conductivity λ, the specific heat capacity c_p and the density of the material ρ. All the above are temperature dependent, but are simplified as constant in many approaches [9, 29, 56, 65, 82, 86, 114, 122, 174, 178, 187].
Mantell and Springer use a piecewise description of the material properties depending on the temperature being below T_g, between T_g and T_m, or melted. Linear material properties are used by Beyeler and Guçeri and many authors followed this solution [3, 13, 111, 120, 151]. More accurate approach to use non-linear, measured values, which was conducted by several authors [58, 81, 84, 88, 102, 135, 152, 163, 167, 175, 183].

Semi-crystalline polymer acts as heat source or sink during solidification or melting. In order to account for it, several authors introduced a linear variation for the specific heat capacity between T_g and T_m [13, 58, 120]. The calculation of Mantell and Springer was mentioned in the last paragraph implementing crystallization in the material properties [109]. Another approach is to use a dedicated heat generation term, in the energy balance formula [13, 61, 122, 151, 163]. Despite the fact that a few models to consider this effect, its comparatively small to the heat introduced by the heat source and therefore commonly neglected, e.g. [56, 135, 187].

Most simulations model the laminate as one body, accumulating inter- and intraply heat conductivities in through-thickness direction. Barasinski et al. introduced an interply thermal contact resistance to replicate a suboptimal intimate contact and bonding [9]. This was adapted by several other authors [27, 88, 152]. Levy et al. found a formula to couple thermal resistance and intimate contact [100].

Beside the direct representation of the material in heat transfer modeling, several downstream models were established and integrated into the simulations to predict intimate contact, bonding quality and mechanical properties of the laminate. Mantell and Springer

followed Lee and Springer by replicating the irregular surface of the material as series of rectangles, to introduce a variable D_{ic} to evaluate the intimate contact in their simulation.[109] For more details refer to chapter 2.1.3. Sonmez and Hahn adopted the same model but allowed temperature and pressure changes during the bonding process [162]. Nicodeau et al. specified the probability that a polymer chain is diffusing between plies, to model the self-diffusion.[122]
A void compression model is used by Pitchumani et al. with compressible squeeze-flow to specify the compression of air and partial recovery after consolidation [135]. [178] divided the phenomenon in a compressible squeeze-flow on a macroscopic and void compression on a microscopic level [178]. Gruber et al. used a model that depicts void filling, flow, compression and escape [60]. Details on void models are also given in section 2.1.3.
Several crystallinity models were proposed, with the goal to predict the degree of crystallinity of the laminate in the simulation [109, 151, 163].
Thermal degradation occurs if the material is overheated, a couple of authors added this effect to their model to discharge parameters that might be optimal for the heat transfer but mischievous for the material [27, 122, 163].
Chinesta et al. integrated a stress analysis for the laminate caused by pressure and heat introduction, during the manufacturing [27].

Consolidation Roller

The influence of the compaction roller on the heat transfer is highly dependent on the exact fiber placement process setup that is modeled. In winding processes the tape is usually wrapped a quarter around the compaction roller, with the possibility to heat the nip point directly. AFP allows for more complex components but the heat source has to be above the mold resulting in unavoidable shading. The roller may act as a heat sink for the tape and laminate and thus influences the cooling curve or support the heating process.
Nevertheless several authors did not consider the compaction roller at all [32, 102, 120, 122, 135]. Weiler et al. state that the AFP process at large could be regarded as quasi-insulated and therefore neither the consolidation roller nor the tooling needs to be modeled [187]. The review of consolidation rollers can be divided into rigid and conformable rollers:

Rigid steel rollers are commonly integrated using Newtons law of heating, with a heat transfer coefficient between roller laminate. However, the heat transfer coefficient values vary strongly from 40 to 1500 W/m^{2}K.[13, 27, 56, 58, 65, 82, 84, 151, 163, 183]
Pitchumani et al. added the contact length between tape and roller [135]. Most authors use rollers with ambient temperature, but a few use heated rollers with 80 °C [32], 96 °C [82], 200 °C [114] and even up to 262 °C [182]. Obviously this results in a very different

process compared to the one discussed in this work.
In contrast to the aforementioned simulations Modi et al. integrated the rigid roller in their FEM model, using a hollow steel roller with a thermal conductivity of 44,5 W/mK and used a constant outer temperature of 200 °C as boundary condition [114]. Maurer and Mitschang modeled the steel roller as flat trapeze in their FEM with a constant temperature applied to it [111].

Conformable roller assists the layup of more complex shaped parts and alternating numbers of layers. The usage of conformable rollers is only described for tape laying not for winding processes and is a relatively new approach that arised in the 2010s. All mentioned authors use some form of a high temperature silicone, combined by with a steel or aluminum axis.
Levy et al. integrated it in their FEM heat transfer simulation. However, due to the laser fixation perpendicular to the laminate a nip point heating was not achieved [101]. Stokes-Griffin and Compston modeled a deformed silicone segment in their FEM simulation. As boundary conditions the inner part of the roller was perfectly insulated with a temperature of 50 °C and perfect contact between CFRP prepreg and roller was assumed. The process described by the authors is quite similar to the process discussed in this work.[167]
Schaefer et al. used a similar machine, the deformable roller was integrated as boundary condition with a heat transfer coefficient of 500 W/m^{2}K (thermal contact resistance of 2.0 m^{2}K/kW) and a specified contact length [152]. The same concept is used by Kok, even though a different roller (almost complete silicone foam) is used with a heat transfer coefficient of 200 W/m^{2}K [86].
Baho et al. added a roller deformation model for the determination of the contact length rendering a measurement unnecessary [8]. Kollmannsberger et al. used the rough shape of the deformed roller and integrated it in the FEM simulation. As boundary condition the roller had a constant inner temperature, because it was water cooled. Additionally a lower incoming temperature was assumed and a heat transfer coefficient of 500 W/m^{2}K was implemented.[88]

Tooling

Depending on the target structure that is produced, AFP is performed on flat molds, mandrels or complex shaped geometries. These are usually made out of steel or aluminum and represent a large thermal mass in the process. In a few cases ceramics with low heat conduction are used to reduce the necessary heat input [174].
Nevertheless molds are not always represented in heat transfer simulations [9, 32, 61, 122, 187]. Two distinct assumptions allow for this approach. First, if the process is exclusively studied after the first layers are already laid down, due the significant insulation evoked

by these plies. Second, the heat input via the heat source and the mass transport are regarded as dominant and the process is quasi isolated.

Levy et al. combined the convective and conductive heat losses to the surrounding air and the tooling in one term [101].
A different approach is to assume perfect contact between the tooling and laminate, resulting in a constant tool temperature on the bottom of the laminate. This was shown for an aluminum tool at 20 °C and a mandrel at 100 °C and 280 °C. [114, 135, 167]
A more realistic implementation introduces a heat transfer coefficient between mold and laminate [13, 27, 56, 58, 82, 84, 86, 109, 152, 177]. However, the heat coefficient show a wide span from 500 to 1408 W/m^{2}K at a tooling temperature of 20 °C [13, 56, 58, 84, 86, 152]. Additionally, a coefficient of 400 W/m^{2}K was proposed by Khan, Mitschang and Schledjewski, for a mold temperature of 280 °C [82].

Tafreshi et al. and Kollmannsberger et al. included the mold into their finite difference models. Both work with a tooling temperature of approximately 25 °C. Tafreshi et al. is implying a perfect contact between laminate and aluminum mandrel, whereas Kollmannsberger et al. use a heat transfer coefficient of 1650 W/m^{2}K. They use temperature dependent material properties for the aluminum and consider the bottom of the tool as isolated.[88, 175]
In several finite element models the tooling is meshed and included in the simulation [8, 60, 65, 81, 102, 111, 151, 163, 174, 182, 183]. Maurer and Mitschang used an aluminum with isolated bottom [111]. Sarrazin and Springer compared the influence of a ceramic and aluminum tooling [151]. Steel molds were considered by several simulations [65, 163, 182, 183]. All authors used the specific density, heat capacity and thermal conductivities matching their individual molds, which renders a comparison impossible.
A few papers model a heat transfer on the bottom of the mold with a coefficient from 5 to 21 W/m^{2}K [65, 182, 183]. Jeyakodi and Shroff introduced a tool return time to compensate for the fact that the Eulerian approach ignores that a tooling area is heated on reoccurring layups [81].

Validation

The degree of validation of heat transfer simulations vary extensively, with a few that lacking it completely [13, 27, 32, 58, 81, 102]. Others vary input parameters, monitor the behavior of the simulation and evaluate its conclusiveness [61, 65, 111, 135].
Tumkor et al. compared the simulation with published experimental results [183]. An approach that has its weaknesses because measurement data highly depends on the machine setup. To check plausibility, several authors compared their numerical models

with simple analytical calculations [120, 151, 163, 187]. This is a feasible way to give an estimate if results are in the correct range.

For a detailed analysis of exact temperatures and gradients experimental data is crucial. Measurements were done via pyrometer, infrared cameras and thermocouples. Toso, Ermanni and Poulikakos used a pyrometer showing a maximum error of approximately 10 %. Pyrometers measure only a relatively small area and emissivity of the material has to be known, while being temperature dependent at the same time. The measurements in the paper show significant deviations.[182]
Sampling of a larger area is feasable using an infrared camera. Nevertheless specular reflectivity of CFRP at long wave infrared wavelength is problematic and emissivity has to be adjusted carefully if quantitative values should be measured [178]. Grouve indicates the dimensionless value with 0.9 [56]. Kok compared the values to thermocouples and determined a value of 1.055 for his prepreg. In the work no quantification is given but temperatures are shown to be within the expected areas.[86].

Thermocouples need no specification of the emissivity. The temperature is measured by an electrical potential that builds between two different metals due to a temperature difference between the measurement point and a reference. They are deployed in the material and therefore lost after the measurement. Correct placement of the thermocouples is crucial in order to have good contact to the substrate and measure correct values. Additionally its arguable that measured temperatures before the nip-point represent the laminate temperature only with a high uncertainty, due to their different reflectance compared to CFRP. Nevertheless thermocouples are one of the most reliable sensors and were chosen for most validations [3, 8, 9, 60, 84, 88, 101, 122, 152, 167, 174, 175]. Unfortunately some of work is neither specifying the sampling rate nor the thickness of the sensors [9, 60, 82, 101, 122, 174], which is problematic because both parameters influence responsivity of the sensors. In order to mitigate the reflection issue, two authors decided to use the thermocouples only after an additional layer is placed on top, which also guarantees sufficient thermal contact between sensor and CFRP [82, 122].

Agarwal et al. used 12.7 µm thin foil thermocouples with a sample rate of 50 Hz. Trials showed that the simulation was underestimating the energy consumption with 6 W to reach a temperature of 200 °C instead 30 W that were actually needed.[3]
Kim, Kim and Lee used slightly larger K-type thermocouples with a 76 µm diameter. A reasonable agreement between simulation and experiments was found, with a strong deviation in the nip-point, however [84]. Tafreshi et al. used K-type thermocouples as well with a sample rate of 100 Hz. Thermocouples were fixed with polyimide adhesive tape. The maximum temperature was found to be correct, but neither the heating zone nor the cool down phase was in good accordance to the measurements.[175]
Stokes-Griffin and Compston combined a infrared camera with thermocouples. Fine wire

thermocouples with 25 µm and a sample rate of 100 Hz were used. They were soldered on to the laminate with prepregs shavings, to reach the same emissivity as the rest of the material. The camera was callibrated with these thermocouples at 100 °C. Simulation results showed a 7,% higher peak temperature, which was accounted to losses in the optical fiber and laser.[167]
Schaefer et al. build up on this results with K-type thermocouples (60 µm and 100 Hz) that were also fixed with shavings. The infrared camera was used with an emissivity of 0.95 measured at 95 °C. While laying down tape directly on to a thermocouple, a large standard deviation of 36 °C was observed whereas it lowered to 2.8 °C in the next layer. Thermal imaging found that the simulation underestimates the substrate temperature before the nip-point.[152]
Kollmannsberger et al. neither mention how the thermocouples are welded onto the laminate nor the emissivity used for the infrared camera. Results show a steeper heating curve for the simulation and that thermal resistances have a significant influence. The same combination of sensors was used by Baho et al. (80 µm, 300 Hz) in order to measure the temperature in the visible nip-point area and mitigate aforementioned inaccuracies. Thermocouples results were only used one layer below the current laid tape. Measurements showed good agreement of the simulation with less than 6 °C difference but deviations were seen in heat-up and cool down phases.[8]

Modi et al. avoided the challenging measurement in the process and studied the raw tape and the resulting laminate, conducting interlaminar shear strength, flexure and double cantilever beam tests. A direct comparison and validation of the simulation is not possible with this approach [114].

2.2.4. Conclusion

A fair amount of simulations done in the past model a tape winding process instead of tape placement or are not using a laser heat source. Even though the basic heat transfer effects are the same, machine design which depends on the process and heat source chosen has a strong influence on the simulation needed. Complexity and accuracy of the proposed simulations tend to increase and decrease over the time. Additionally material characteristics and parameters for thermal dissipation vary in a wide range which makes a comparison difficult.

The assumptions made in one and two dimensional simulations that high mass flows, negligible edge cooling and low heat transfer in tape width render a three dimensional simulation unnecessary, should be contested. As a side effect these simulations regard the heat source homogeneous which is an additional simplification that might accumulate to

significant temperature differences on tape edges.
Steady-state simulations neglect a possible heating of the overall system, therefore a transient analysis is preferred to account for the layup of longer tracks. In order to reach relatively short computational times, the simulation should focus on the nip-point area and thus implement an Eulerian approach.
Only two authors used 3D ray tracing to model the shadowing of tape placement. Both rendered the results down to a two dimensional thermal model. A more consistent optical-thermal model without manual simplification is preferable. That allows for the usage of realistic, measured irradiation data, easy adaption of machine design changes and varying laser angles.

The material properties are temperature dependent and should be modeled in this way. The vast majority of simulations use material parameters found in the 1980s and often APC2-PEEK is used, as it is an available, high quality material. A broader selection of materials should be characterized and simulated. As their importance have been shown in recent publications, thermal resistances resulting from incomplete consolidation should be considered.

The compaction roller is of particular interest in this work, since it is water cooled and has a silicon rubber exterior layer. Some researchers do consider the roller as heat sink but it was not modeled in its entirety. This is necessary to observe the heating process of the roller over time and to model longer layups. The deformation of the roller was simulated by a few authors. Integration in a simulation would allow for parametric studies that show the influence of varying pressures on the thermal analysis.
In numerous finite element simulations the tooling is meshed and the heat flow is calculated. This helps to investigate the influence of the mold on the first few layers. Additionally a tool return time was implemented to account for a returning layup machine, that would otherwise be ignored in an Eulerian frame simulation. It would be worthwhile to visualize the influence of the tooling material and other confounding factors like reinforcements.

The literature review shows that many simulations are not validated via measurements. Pyrometers and thermal imaging do strongly depend upon correctly determined emissivity parameters. Its influenced by the materials temperature, reflectivity and angle to the camera which vary in a wide range in T-AFP. Hence the majority of validations have been conducted with thermocouples.
Previous studies showed that the measurement especially of the current tape placed is challenging. This has several reasons: the reflectivity of the thermocouple, its thermal inertia, the sampling rate, the wiring that is interfering with consolidation and the precise

fixation of the sensor. As a result measurement do have a high standard deviation. These challenging factors should be mitigated in order to obtain a precise validation.

2.3. T-AFP Process Control

2.3.1. Introduction

As described in the previous chapter, process simulations enable a fundamental understanding of thermal gradients, inherent physical processes and the effect of selected process parameters. Once the process parameters are chosen, control systems are essential to keep the values in the defined tolerance limits in case of disturbances. Main parameters that have to be controlled are layup velocity, irradiation and compaction pressure.
Typically the first is controlled by the robot and compaction force is readily controllable with standard pneumatic components. Additionally previous work showed that the influence of the compaction pressure is less significant as long as it is held constant and it is applied over a specific threshold (6 bars) [139]. Main focus is therefore on the irradiation control either directly or by increasing the distance or angle of the heat source to the tape and laminate.
This chapter will introduce basic control elements, for heat sources that are applicable for T-AFP. Subsequently the state of the art on control systems for the process is discussed. It will show that impact of thermal gradient is of such importance to the part quality, that direct integration of process models in the control systems has been approached early on. Finally a thorough examination of the existing control designs for T-AFP is given and short comings are identified in their application in modern layup machines.

2.3.2. Process Control of Transient Heat Processes

Three controls types have been identified in this work, that are currently used in AFP machines and are of interest to improve controllability of the process: the classic PID control, Linear Quadratic Regulator and Model Predictive Control. All three are briefly described in this chapter.

PID Controller

The PID controller is one of widest spread controllers, due to its ability to compensate most industrial processes. It is suggested that only 5-10 % of these processes cannot be controlled by PI or PID controls. In 1995, 95 % of all controllers in process control have been of PID type. They are recommended for processes with low to medium order, small time delays and benign dynamics. Parameter setting has to be done via tuning rules e.g. Ziegler-Nichols or iterative feedback.[123]
PID combines three basis control components: a proportional, integrator and differential component. For the proportional controller P the input is linked with a proportional coefficient K_P to the control variable u(t), given as [107]:

$$u(t) = K_P e(t) \tag{2.11}$$

Where *e(t)* is the time dependent control error. A higher K_P leads to faster error reduction. However, a single proportional controller cannot reduce the error to zero. The output of the integrator I is the time integral of the control deviation *e(t)*:

$$u(t) = K_I \int_0^t e(\tau) d\tau \tag{2.12}$$

$$T_I = \frac{K_P}{K_I} \tag{2.13}$$

With the integration coefficient K_I. The component enables the error reduction to zero. The integration time T_I is introduced, which determines how fast the integral term responds to the accumulated error. The differential component can not be used as stand alone controller. Its output is proportional to the time differential of the input variable:

$$u(t) = K_D \frac{de(t)}{dt} \tag{2.14}$$

$$T_D = \frac{K_D}{K_P} \tag{2.15}$$

K_D is the differential coefficient, T_D is called the derivative time. It gives the control the ability to react on changes before the control value gets so large that it becomes relevant. The parallel combination of all three components gives the PID control law:

$$u(t) = K_P \left(e(t) + \frac{1}{T_I} \int_0^t e(\tau) d\tau + T_D \frac{de(t)}{dt} \right) \tag{2.16}$$

Figure 2.11.: **Structure of a PID controller as block diagram [107]**

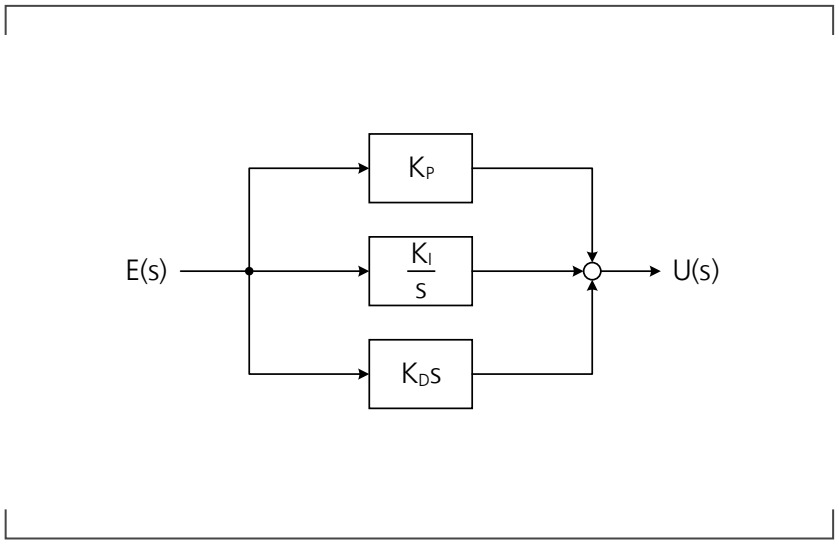

The layout of a PID controller is illustrated in figure 2.11. It shows the transformation of the error into a control signal. In order to illustrate the behavior of a PID control its transfer function K_{PID} is given by:

$$K_{PID} = K_P \left(1 + \frac{1}{T_I s} + T_d s \right) \tag{2.17}$$

The step response of the PID is depicted in figure 2.12 and gives visual overview of the control portions of the three different components: the constant part of the proportional control, the linear part of the integrator and derivative part on the y axis.

Linear Quadratic Regulator

Whereas PID coefficients are optimized by trial and error or specific tuning rules to optimize e.g. overshoots or settling time, in the optimal control concept a mathematical optimization is performed to design the control system. Therefore a performance index

Figure 2.12.: **Step response of a PID controller [107]**

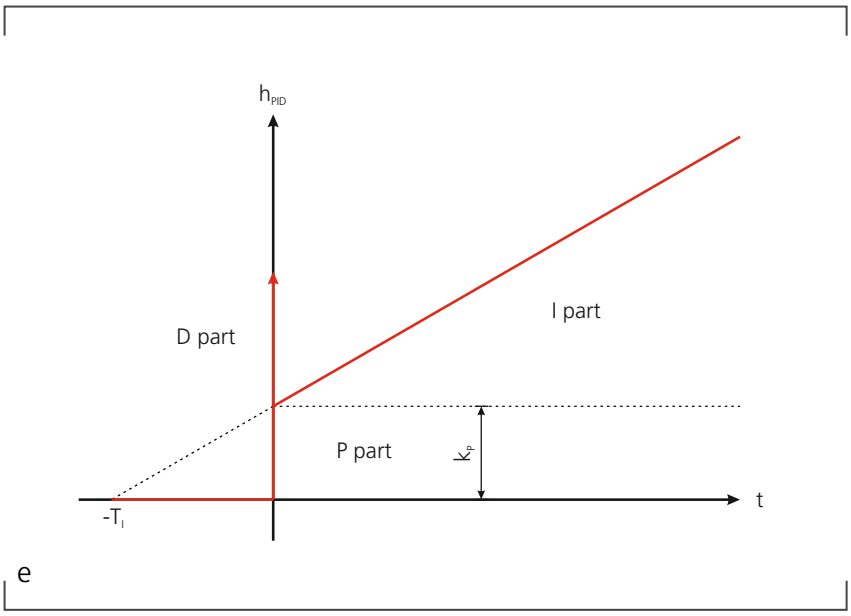

is introduced as function of the state and control variables. It indicates the degree of compliance between reference signal and control vector and is minimized via algorithms to find an optimal control regime.
The specific definition of the performance index is dependent on the process that should be controlled and determines the nature of the control system. Thus its definition is important and difficult at the same time. Due to the adjustment over a performance index, behavior of optimal control systems is often regarded as intransparent. However, one advantage is its applicability to multiple control values.
Optimal control design is commonly used with linear plant systems and based on quadratic performance indices, which leads to linear quadratic problem. It is solved by using the Hamilton-Jacobi-Bellmann equation.[4, 5, 83, 108, 124] The linear plant system can be described as:

$$\begin{aligned} \dot{x}(t) &= Ax(t) + Bu(t) \\ y(t) &= Cx(t) \end{aligned} \tag{2.18}$$

With the current state vector $x(t)$, the control vector $u(t)$ and controlled variable $y(t)$. A describes the system matrix, B is the input and C the output matrix. The linear controller law is given by:

$$u(t) = -Kx(t) \tag{2.19}$$

For a controller with infinite optimization horizon a constant regulator gain matrix K is obtained. The cost function J, for stable systems, is defined as [4]:

$$J = \frac{1}{2} \int_0^\infty \left[x^T(t) Q x(t) + u^T(t) R u(t) \right] dt \tag{2.20}$$

The first term models the influence of control error with the state vector $x(t)$ and the second term evaluates control effort with control vector $u(t)$. Q and R are positive, definite, hermitian weighting matrices. They facilitate adjustment of the influence of the two terms. A higher Q compared to R will lead to a faster adjustment but larger control values. The opposite will reduce the control effort.
In case a specific state has to be adjusted prompt the individual matrix element q_i is increased. This applies equally to an individual control variable whose adjustment is costly and the individual weight r_i should be raised.

The Linear Quadratic Regulator (LQR) is a specific type of optimal control, where A, B, Q and R are all constant. The following description is based on the book of Lunze, which is recommended for further details [108].
LQR is designed as closed loop control that regulates the error $e(t)$. It is assumed that all state variables are measurable and available. The weighting matrices are either determined by trial and error or an iterative processes. The regulator gain matrix K is defined by:

$$K = (R + B^T P B)^{-1} B^T P A \tag{2.21}$$

Where P is the transformation matrix between the states. The solution of P can be found by solving the steady state Riccati equation, which is given by:

$$P = Q + A^T P A - A^T P B (R + B^T P B)^{-1} B^T P A \tag{2.22}$$

In case state variables are not measurable, a linear quadratic estimator (LQE), also known as Kalman estimator, may be applied. The combination of LQR and LQE leads to the linear quadratic gaussian controller approach. These concepts will not be discussed in detail here, the interested reader may refer to Anderson [5].

Model Predictive Control

Linear model predictive controls (MPC) have been developed since the 1970s. Initially many applications were found in chemical industry, however the concept expanded fast in other areas e.g. the food and aerospace sector. In the last two decades research focused on non-linear MPCs to increase prediction quality of models, for processes with large set point changes and time delayed sensors. For a comprehensive summary of MPC evolution and applications the work of Qin and Badgwell is recommended [136].
The idea of MPCs is to compute the process inputs over a given time interval, called the prediction horizon, to optimize the future plant behavior. Prediction of the plant is derived from a process model, that can be described in any mathematical form. Similar to the LQR a cost function is used to formulate process input and output constraints, directly into the control problem. Boundary conditions and their violation are acknowledged and prevented. Main advantages of MPC control is this definition of constraints, which allows to safely drive a system near to the boundaries of its constraints, as well as the transparent definition of performance criteria. [12, 51, 136, 199] A detailed introduction can be found the monograph of Zhang, Xue and Gao [199].

For a linear MPC the model is commonly described in time-discrete, state space form:

$$\begin{aligned} x(k) &= A_D x(k-1) + B_D u(k-1) \\ y(k) &= C x(k) \end{aligned} \tag{2.23}$$

Where A_D is the system matrix containing the coefficient of state variables, B_D is the input and C the output matrix. $x(k)$ is the state and $u(k-1)$ the input vector.
Figure 2.13 illustrates the basic concept of model predictive control. For a given time k, a cost function is minimized and optimal values are calculated for all manipulated variables within the control horizon N_C ($u(k)$, ..., $u(k+N_C)$). Only the first value $u(k)$ is applied on the system, all other values are recalculated at every sample time. An example cost function is given as [12]:

$$J(k) = \underbrace{\alpha \sum_{i=k}^{k+N_H} (r(i) - y(i))^2}_{\text{error to ref. trajectory}} + \underbrace{\beta \sum_{i=k}^{k+N_c} (u(i) - u(i-1))^2}_{\text{actuator effort}} \tag{2.24}$$

$r(i)$ denotes the reference trajectory which could be derived from the set point value w, for example by applying a filter to smooth out step changes (as depicted in red and dark blue

lines in figure 2.13). N_h and N_C are the prediction and control horizon respectively. y is the controlled and u the manipulated variable. α and β are weights that can be adjusted to the process e.g. to minimize the control effort or punish overshooting. The cost function can readily be extended to more manipulated and controlled variables.
To minimize the function, different optimization strategies can be used most commonly applied for fast response plants is the unconstrained least square errors optimization [12, 41].

Figure 2.13.: **Basic principle model predictive control [12]**

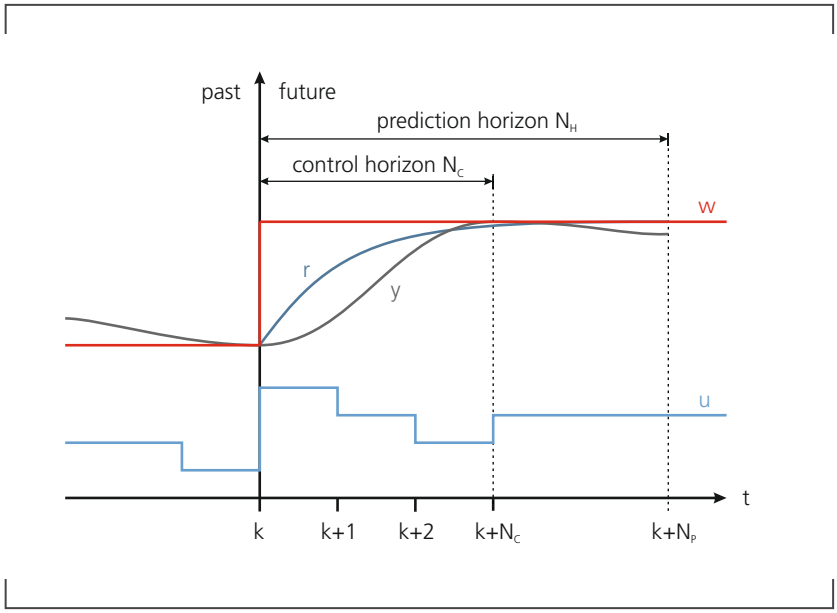

2.3.3. Thermal Control Strategies for AFP Processes

Some work can be found that specifically focuses on the field of T-AFP process control. However, only a few authors designed controllers for laser heating. The majority of systems are developed for conduction, namely foot and rigid roller, heating. In the following an overview of control systems developed by research is given:

Lichtenwalner presented a control based on an artificial neural network. It is trained to represent the inverse model of the process, aiming to surpass conventional controls. First the untrained system acts like a PI controller, in the course of training it converges faster to the set point and reduces temperature deviations.
The system consists of a laser heating, one consolidation roller, an infrared sensor, a feed

rate sensor and a control pc working with a cycle time of 10 Hz. For the neural network a cerebellar model articulation controller (CMAC) was chosen. It is a memory based learning system that can be described as dynamically adjustable look up table. Simple processing elements are interconnected and executed in parallel. Their information exchange is realized with weighted connections. The weight values are adjusted during the training, to build an inverse model of the AFP process. Advantageous is the CMACs speed due to the localized weight adjustment.
It is noteworthy that the neural network models a steady state inverse model of the process, which in result neglects the temperature dynamics.
In the control the neural network is integrated as feed forward controller. Its output is a function of target temperature and actual feedrate. It is added as proportional feedback to the control signal as depicted in figure 2.14.[103]

Figure 2.14.: **Block diagram Control design by Lichtenwalner [103]**

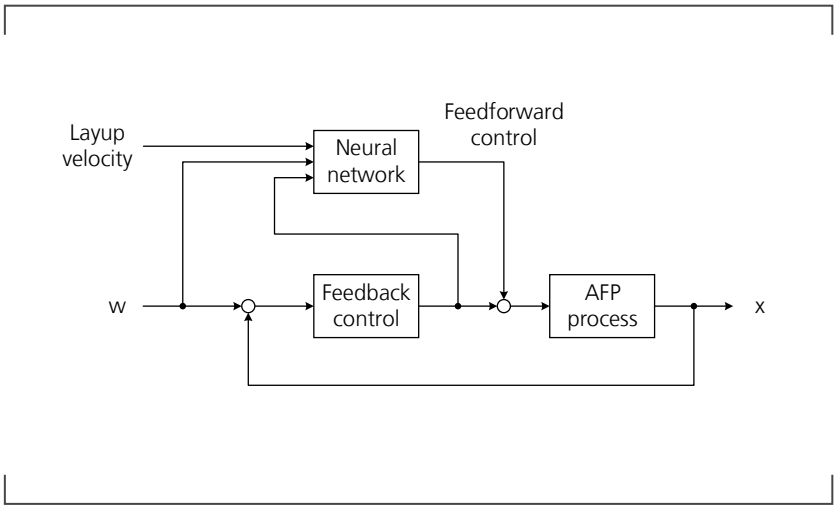

The neural network showed two main advantages: the inverse function of the AFP process was replicated automatically and it was able to model linear as well as non-linear control laws accurately.
Training showed that the temperature was held close to the target after four and six set-points for temperature and feed rate respectively. Compared to a standard PID controller significant improvement regarding temperature deviation and convergence could be reached. Process dynamics and other influences such as the layup geometry were neglected.[103]

The concept of Lichtenwalner was adapted by Heider and Gillespie for a layup system with two height adjustable hot gas torches and two consolidation rollers. Input for the CMAC are the layup velocity and the distances of the two torches to the laminate, which

results in a prediction of the two maximum temperatures under the torches. A numerical optimization changes the distances, until a close match between desired and predicted temperature is found.
Subsequently these values are send to the stepper motors. The CMAC temperature prediction is trained with process online data, acquired by a thermal imaging camera. Figure 2.15 presents the control design, with the numerical optimization left and the online training on the right side.
For validation several layers of CF/PEEK were placed, with a constant velocity of 35 mm/s. Steps to different set points showed that new distances for the torches were calculated accordingly. The paper mainly presents how the torch distances are optimized regarding a new temperature set point. Whereas an active process temperature control is not shown.[67]

Figure 2.15.: **Flow Chart of Control design by Heider and Gillespie (redrawn after [67])**

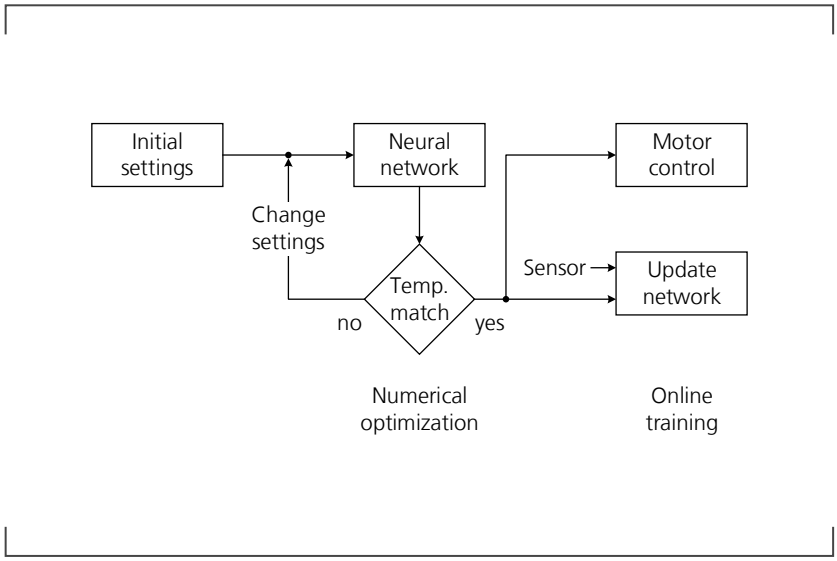

Sun, Mantell and Stelson developed a model predictive controller for a system with air preheater and foot heater as main heat source. Due to the concealed process area, temperature is not measurable and a model was implemented to predict the temperature at ply and laminate interface, and thereby the bond quality. The control design is illustrated in figure 2.16, reference variable w is given as predesigned process temperature and translated into a nominal input power p_n by the inverse process model. A temperature estimator and state feedback controller were designed for a closed loop temperature control.
The model consists of three lumps: the foot heater, the consolidation zone and the area behind the heater. Bond quality and the spatial variation are predicted by the latter two

lumps, respectively. Differential equations are solved via Finite Difference Method (for details on the simulation refer to 2.2). The ambient temperature was set to zero, to get a model in state space form with two inputs and three outputs [174]:

$$\begin{aligned} x(k) &= A_D x(k-1) + Bu(k-1) \\ y(k) &= Cx(k) \end{aligned} \tag{2.25}$$

Where A is a matrix describing the material properties, B the boundary conditions and C the identity matrix. The system output is described by $y(k)$ and $u(k)$ is a vector that consists of both: the air temperature of the preheater and power of the foot heater.
Additionally a empirical model was identified to adjust and validate the theoretical model. For this a system identification with step responses is used to construct a transfer function in the frequency domain of the Bode diagram.
The state feedback and estimator controller was designed using the linear quadratic method of optimal control (compare to chapter 2.3.2). Its cost function J for optimization is given by [174]:

$$J = \sum_{k=1}^{\infty} x(k-1)^T Q x(k-1) + \sum_{k=1}^{\infty} u(k-1)^T R u(k-1) \tag{2.26}$$

Where Q and R are positive, definite, diagonal matrices determined by trial and error. The system input matrix is given by $u(k-1)$ and $x(k-1)$ gives the temperatures in the three lumps at time $k-1$.
The same method was used to design the state estimator replacing A_D and B_D with the transposes A_D^T and C^T. Two experiments were conducted to evaluate the control: one at 115 °C to validate the Kalman estimation and one at 340 °C to show the controller performance. For the first experiment six thermocouples were embedded and the experiments showed a steady state error that was eliminated using a bias estimate technique. The thermocouples measured that the lump temperatures were predicted accurately.
The controller oscillated with a tolerance of 5 °C around the set point temperature. Whats of more importance is that it took 20 seconds to reach it, which is only acceptable at very low layup velocities and for inertial systems. Moreover the system was compared to an on/off control which is a rather low bar to surpass.[174]

With a first publication in 2002, Heider, Piovoso and Gillespie combined the concepts of MPC and neural networks, for the hot gas system described earlier in this section. An online optimization algorithm was created to calculate the optimal process set points, for a open-loop process controller based on quality requirements.

Figure 2.16.: **Block diagram Control design Sun, Mantell and Stelson [174]**

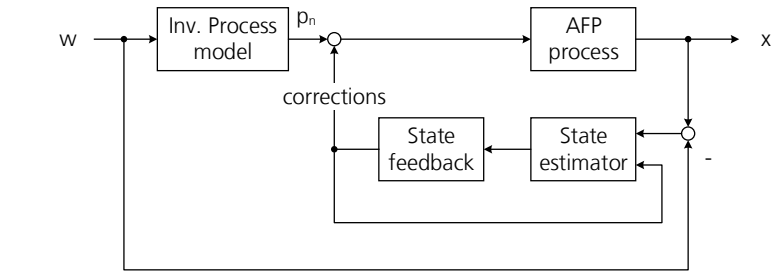

Due to the lack of material quality sensors, a process model was used to predict optimal process parameters. From the model void content and degree of bonding are derived for the laminate. Additionally it predicts the outputs e.g. temperatures and pressures as functions of process parameters. Computation of these models are complex and therefore usually slow, which is unproblematic in offline but poses a problem for online control. Thus the authors used a neural network to reproduce the first principle process model of Tierney and Gillespie [178]. The overall objective of the work was to maximize throughput, with a definable minimal acceptable quality threshold. Figure 2.17 presents the interaction of the components.[68, 69]
A supervised learning cascading feed forward neural network was used. In this case it has one input and output layer, with multiple hidden layers in between. Weighted connections between units of the network render uncorrelated connections less important. The output is calculated by transforming the inputs by an activation function. The network is trained with data generated by the process model and a nonlinear optimizer. The aim is to find a optimum set of layup velocity and torch distances for the process.
First it was determined by a cost function including the void content and healing, where a constant term for velocity was added as soon as the quality was reached. Later Heider, Piovoso and Gillespie changed the optimization to a normalized, stepped quality function. If quality is not reached the input values are first changed slightly, if no viable set points are found for desired quality the speed is decreased.[68, 69]

The basic approach was validated experimentally with two laminates, one using a constant speed and one with optimized parameters. The constant velocity was calculated to the

Figure 2.17.: **Bock diagram Control design Heider, Piovoso and Gillespie [68]**

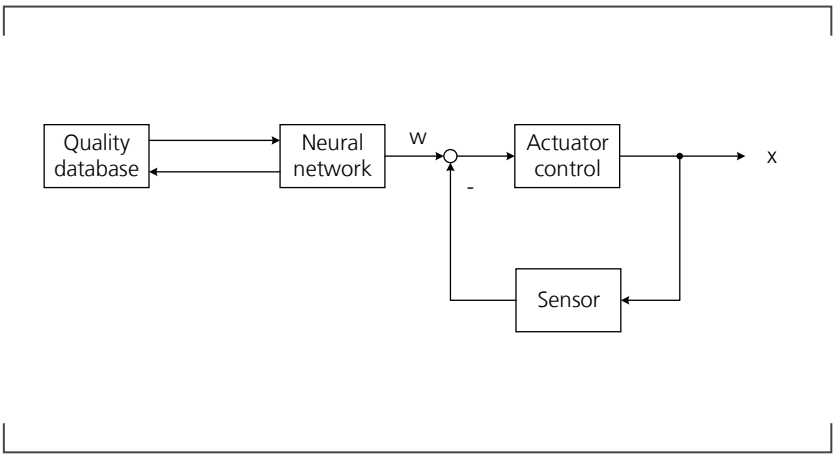

same cycle time and showed undesired quality gradients, whereas the optimized laminate maintained the quality.
The revised system was compared to a static controller on a virtual part and showed increased throughput mainly based on elevated speed levels in higher layers.

In 2004 Lee showed a PD controller, for a system with rigid roller heating. Due to the large difference to the process discussed in this work, it has limited relevance here but is mentioned for the sake of completeness.[94]

Kölzer developed a closed loop temperature control, using a multi point radiometer as sensor and added an additional laser position control. A focus was the design of algorithms to compensate for emissivity and angular deviations in the sensor, in order to reduce measurement errors.
A tape laying system with infrared laser heating and a rigid compaction roller was investigated. The control system was equipped with an additional pyrometer for localized, faster measurements and compared to a version without. In figure 2.18 the closed loop concept is depicted. The work reports that for both, laser power and position controller a PI design was chosen, due to high frequency errors that occurred as soon as an differential component has been introduced.
Validations were done with step responses to a set point change to 380 °C, while layup of CF/PEEK. They showed that the control system is capable to reach a set point temperature within a 5 °C tolerance. The system with additional pyrometer showed faster compensation of deviations. However, the system overshot set temperature significantly.[89]

Hajiloo et al. intended to impede inconsistent heating via advanced controllers and benchmarked different controllers. They developed two controllers: a linear quadratic regulator

Figure 2.18.: **Block diagram Control design Kölzer (simplified after [89])**

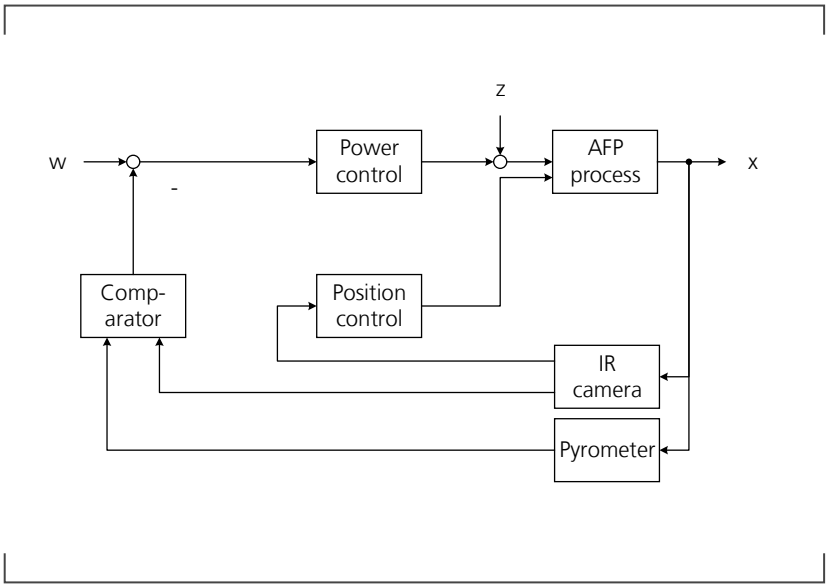

for optimal control and a MPC to consider physical boundaries, such as performance constraints of the heating system.[64]
Both controllers were developed for a footer heating system with preheater, similar to the system of Sun, Mantell and Stelson. Thus, the same thermal model was used and a short description of it can be found earlier in this section.[174]
A description of the basic principle of a linear quadratic regulator can be found in chapter 2.3.2. In this instance an integrator element was added to increase accuracy and eradicate the steady state error.
The designed MPC in this work implements physical constraints for power of heater (0 - 80 W) and temperature of preheater (0 - 900 °C). Compared to the standard MPC the weighing factor for the control error is not implemented (refer to chapter 2.3.2). Figure 2.19 presents the basic principle of the controller. The cost function with constraints is arranged as [64]:

$$J(k) = \sum_{n=1}^{N_p} \left(y(k+n) - y^{ref}(k+n) \right)^2 + \lambda \sum_{n=0}^{N_c-1} \Delta u(k+n), \qquad (2.27)$$
$$y_{min} \leq y(k+n) \leq y_{max}, u_{min} \leq u(k+n) \leq u_{max}$$

Where N_p and N_c are prediction and control horizons, n is the sampling time and λ is the weighing factor for control increments. The cost function is minimized after every

Figure 2.19.: **Block diagram MPC control design Hajiloo et al. [64]**

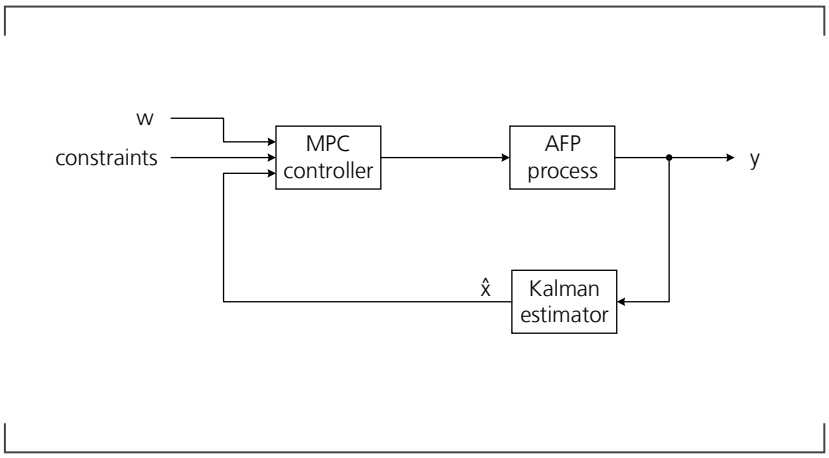

prediction and the state variables $\hat{x}$, inputs of the MPC, are estimated using a Kalman filter.
Both controllers were evaluated using the thermal model by Sun, Mantell and Stelson. The MPC showed better performance regarding its settle time but its steady state error was higher. LQR and MPC controller equally coped well with step disturbances and converged back to steady state values.[64]

Weiler et al. discuss the issue of decreasing melting depth which intensifies with increasing layup speeds. They argue that if the polymer is not melted at least in a thin area near to the surface, insufficient bonding is the result. As a countermeasure it is suggested to not only control laser power, but also the irradiated area. As a solution VCSELs or diode lasers with additional zoom homogenizers are proposed. Two control models for this idea are presented in the paper:
The first concept is a model-based control, based on thermal gradients. The necessary heated length t_L is calculated by a process model, depending on two inputs: a given temperature ratio between surface and backside as well as the layup velocity. By specifying the irradiation length sufficient through heating is ensured. Further sensors for the gradient measurement would not be needed, with the disadvantage that disturbances are not recognized or mitigated. The laser power p is controlled via a standard controller using a sensor feedback loop. The control architecture is depicted in figure 2.20.
Second a closed-loop control of the thermal gradients is suggested, with two possible sensor setups. Both measure the temperature shortly after the bonding process. One approach uses a pyrometer, that measures at the backside of tape. A simplified thermal model would give the correlation to the actual bonding temperature. However, this would only work for process velocities that ensure a tape backside temperature above the ambient temperature. Alternatively a thermography camera is proposed, to measure

Figure 2.20.: **Block diagram Control design Weiler et al. (simplified after [187])**

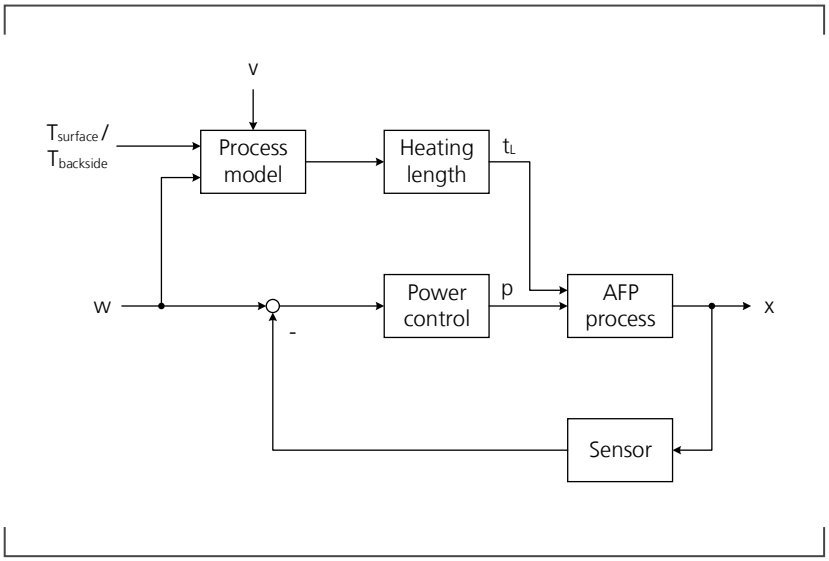

the temperature distribution in the tape. Both concepts were only proposed on a concept level and were not realized yet.

Francesco et al. developed a semi empirical model to correlate laser power and layup speed with the surface temperature for CF/PEEK and dry fiber material. An open-loop, velocity dependent power control was implemented. The authors justify the approach with the argument that closed loop systems would not be stable enough.[47]
The thermal model of Tierney and Gillespie was adapted for laser heating, using several simplifications [178]. For example the thermal properties are defined as constant through thickness of the laminate and not temperature dependent. The model is used to guide the empirical definition of the coefficients and for validation of the developed heat function.
Temperature measurements are conducted using an infrared camera to determine a linear function between temperature in the nip point and laser power. Non linearity was observed due to thermal properties of the materials. However, it was proven that these are statistically insignificant for higher temperatures. The slope and intercept of the linear function were described as functions of the layup speed and fitted using linear regression. The following power function was derived [47]:

$$P(W) = AV^B; A = \frac{T_{NVP} - (m_{c-V}V + c_{c-V})}{A_{m-V}}; B = -B_{m-V} \tag{2.28}$$

Where T_{NVP} is the nip point temperature, m_{c-V} the slope and c_{c-V} the intercept of the linear regression, V the layup velocity, B is a constant exponent and A_{m-V} resembles the machine setup and the material properties. A_{m-V} and B_{m-V} are defined by empirical data. To validate the system measurements with varying velocities were done, by deposition of 1.2 m tracks. Results showed that temperature could be held in a confidence interval of 40 °C. Which is quite poor compared to the controls discussed. Additionally, correlation between the analytical and empirical coefficients is poor, which is explained by the simplifications and unrepresentative material properties sourced by literature.
Monnot, Williams and Francesco adapted the procedure to find a power function for flashlamp heating [115].

Brecher et al. presented a tool to calculate the intensity distribution of a VCSEL heater for parts with narrow radii and proposed an open-loop control based on inverse heat conduction description [18].
The MATLAB based tool calculates the absorbed intensity of the material, taking into account the incidence angles, the geometry in the nip point region and the absorption coefficient. For every laser diode individual incidence angles are calculated.
The heat conduction problem is solved by application of several simplifications: heat transfer between roller and tape as well as substrate and tool are neglected. In addition the divergence angle of the laser diodes is considered constant. Subsequently an optimization based algorithm is used to calculate the scaling of the intensity of the laser diodes. Experiments showed that the inverse model was imprecise. Validation of the open control was not shown in the paper and is pending.[18]

2.3.4. Conclusion

Basic controllers are widely used for heat management in AFP. The relevant controllers PID, LQR and MPC were introduced in this chapter. Subsequently, previous research on the topic was summarized. Whereas several sophisticated controllers were proposed, the state of the art controller in the industry and the layup machine used in this thesis are based on a PID controller.

Little work has been published aimed at T-AFP control compared to the overall traction research gained in this field. Lichtenwalner was the first to introduce a concept for implementation of a feed forward process model [103]. The use of an artificial network showed significant improvement compared to a standard PID. Disadvantageous is that the steady state inverse model ignores temperature dynamics and the control was tested with maximum feed rates below 100 mm/s. The latter helped compensating for slow cycle times of the system.[103]

The concept was later adapted as cascaded controller to control the process on basis of void content and bonding degree. On the inner loop a faster control loop guides the process. However, the HGT-process is only vaguely comparable to laser T-AFP. Other model predictive controls showed either time delays with settling times up to 20s or were only simulated and conceptualized.Weiler et al.
No model predictive control could be found for modern layup machines and with high layup rates (>100 *mm/s*). Additionally aspects that would increase accuracy of the models are missing, like the current laminate structure, tooling properties et cetera.

Recent research on the control of laser T-AFP systems developed a rather basic, open-loop controller to find a relationship between layup velocity and input power [47]. This is not sufficient since no reaction to external disturbances like material and laminate changes, defects or deviations in heat conduction can be triggered. Closed-loop systems showed that they can control the temperature before the nip point to a satisfactory extent with a basic PID setup. More advanced control and tuning strategies like e.g. system identification were not evaluated so far.
Infrared cameras or pyrometers are used as sensors for these controls. Control of the temperature beneath the consolidation roller or of the entirety of the temperature gradient is not possible with these systems.[89]

In general most of the existing control systems would need considerable adjustments to be used for a laser T-AFP with the widespread heating area design of the machine used in this work. Higher feed rates need fast responding systems.
Basic controllers like PID showed good results if sensors are well adapted to material properties and the control parameters have been identified with diligence. Nevertheless they control the process in front of the nip point and not in the process point. In order to control the temperature at the process point a model based control is necessary. With the development of such a system, missing aspects of the process could be added to the control design while using a cascaded design for low cycle times where needed.

3. Objective and Scope

Chapter 2 showed in depth how quality of components manufactured with T-AFP is dependent on precisely selected and stable production parameters. Nowadays, sufficient parameters are found via time and cost extensive experimental studies, which impede the adoption of the process in industry.
Additionally to increase the appeal of T-AFP to economic stakeholders, deposition rates have to be increased while simultaneously mechanical knock-down factors have to be reduced. However, higher layup velocities impact consolidation time and through thickness heating and thus bonding quality. As a result the process becomes more error-prone and material defects may develop or already existing ones can not be healed anymore.
One option to cope with these challenges is to reduce tolerances to a minimal viable quality and ensure compliance with fast and concise control strategies.

However, despite the necessity for high precision controls little research has been published until today. Sophisticated systems such as model based controllers were only applied to vastly differing systems e.g. foot heaters and HGT driven T-AFP. Modern layup machines commonly use basic PIDs for closed loop control and proofed that good conformation to set point temperatures can be achieved before the nip point. This applies for minor disturbances and sufficient prepreg material quality though, to which the control is tuned for specifically. Smarter control systems that handle disturbances intelligently are not yet available for these setups.
The T-AFP process comes with inherent and known disturbances such as: mold temperature deviation, laminate fiber direction and thickness changes and divergence in the machine path or velocity. These disturbances are predictable and can be accounted for in an intelligent control. Ideally such a system should:

- control the temperature in the process area rather than in the nip point
- take known disturbances and parameter changes in the layup path into account
- directly control quality parameters

- be readily adaptable to new setups

In order to realize these aspects the complex interrelationships between parameters, disturbances and their influence on the outputs have to be implemented in the control. This can be achieved by designing a model based controller with a precise model of the process.

As laid out in subsection 2.2.4, numerous process models have been developed. However, the vast majority of them focused either on fiber winding, non-laser heated T-AFP or otherwise incomparable machine layouts. Additionally models proofed to be hardly comparable due to varying material characteristics, complexity and inherent assumptions, which leads to an aggravated evaluation of their accuracy. In order to maximize the benefit of a process model it should implement all key elements of the T-AFP process: the consolidation unit, the heat source and the heat transfer.
A mechanical model is necessary to evaluate the impact of different compaction forces, applied by the roller. For a conformable roller setup, compaction force directly changes the heating and consolidation areas and thereby influence the heating and cooling behavior.
For the heat source relevant process parameters are: laser power and intensity distribution as well as position and angle of the laser. Due to the fact that laser optics have a drop in performance at the edges, the model should cover the tape width to simulate this effect. This is especially true because multiple tapes are deposited simultaneously. However, a fully integrated optical model for all dimensions is not available yet.
Heat transfer simulation links the process parameters with the emerging process temperatures. Hence a multi physics model is preferable to model all predictable disturbances and support the goals above. However, to the best knowledge of the author, such a model does not exist today and has to be set up first.

In conclusion this thesis will adapt existing simulations where possible and append these where necessary. As a three dimensional, multi-physics and transient simulation is planed, a FEM approach is sensible. For the implementation in a control system, complexity of the simulation will be reduced beforehand, to save computational effort.
A controller will be designed that plans for known disturbances, while a fast temperature control core ensures responsiveness to errors. With this approach component quality will increase for high layup rates. Additionally, it will showcase future opportunities to rather specify part quality than process parameters and thus simplify setup.
The newly developed method will be readily adaptable to any transient heating process, where direct sensor measurement is unfeasible and predictive control may offer advantages. Due to the closed software pipe line other physical effects e.g. electronic currents or vibrations can be modeled easily. Adaptation of the control system proposed will be possible with minor modifications.

4. Modeling of the Laser-assisted Automated Fiber Placement

The development of the three dimensional, multiphysics and transient finite element model is described in this chapter. In order to give a structured overview, it is divided into sections that describe the individual physics modeled: solid mechanics, optics and distribution of heat. Since the mechanical model determines the geometry for the latter two, it is detailed first. Following this logic the optics succeed, as they deliver the input for the heat transfer simulation which is described last. Figure 4.1 gives an overview of the three submodels, their interaction and the subsequent inputs and outputs. The mechanical, optical and thermal material properties are denoted as m_{mech}, m_{opt} and m_{th}, respectively. As process inputs the consolidation pressure p_{cons}, laser power P_{laser} and layup velocity v_{layup} are given. The outputs of the individual models are the geometry of the consolidation roller and tape, the spacial irradiation I_{laser} and the process temperature at any given point T. Theoretically a back-loop between the heat transfer and optical model is implementable using the material temperature T_{CFRP} and its resulting optical properties. Due to the computational effort and comparatively low impact on the overall results this was neglected.
Validation of the models is described in their corresponding subsections. However, given that the thermal simulation is the downstream model that is fed from the others, it is evident that its validation gives an overall evaluation of the system and general simulation parameters are optimized using the thermocouple measurement in this chapter.

Figure 4.1.: **System Design Multiphysics Simulation**

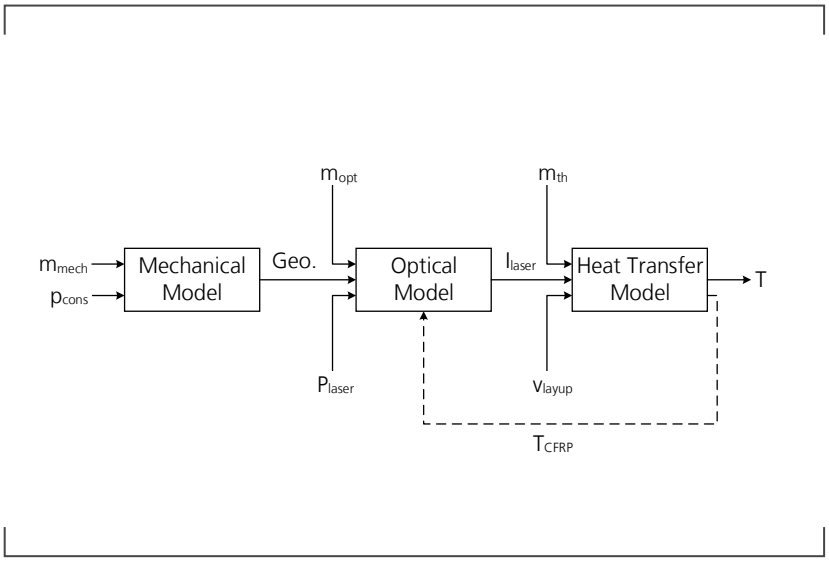

4.1. Mechanical Model of the T-AFP process

4.1.1. Introduction

The mechanical model describes the deformation of the conformable roller and the resulting geometrical conditions in the irradiation area of the T-AFP process. It thus enables the evaluation of changing heating behaviors for different consolidation forces in the overall simulation.
A detailed description of the model is given with an explanation of the compaction roller design and system borders. Next the meshing with its main features to ensure correct results is discussed. For the silicone rubber a hyperelastic model is presented and the physical boundaries applied to the simulation are outlined.
Validation of the model is carried out by measurement of the resulting compaction forces, the pressure distribution and a comparison of static and dynamic compaction forces using pressure sensitive foils and sensors. Subsequently the measurement values are compared to the simulation results to proof its applicability.

4.1.2. Mechanical Model

With a diameter of 70 mm and a width of 60mm, the aluminum shaft forms the core of the compaction roller design. Near surface channels passing through the shaft are implemented to cool the roller via water during the process. A silicone rubber sleeve (Silikonfabrik SF45-RTV2), with a thickness of 5 mm and a shore hardness of 45 Sha, ensures conformability of the roller. It is secured with guides on both sides of the roller against slippage. Silicone and shaft accumulate to a total diameter of 80 mm.

There are two main mechanical effects that should be covered in the mechanical model: one is the formation of the consolidation area between laminate and silicone. The second is the description of the roller geometry at tape feed in, where it supports the tape. On the lateral guides complex silicone buckling is expected. As the roller is considerably wider than both the tape with 38.1 mm and the laser focus with approximately 43 mm, this effect is negligible. In order to avoid unnecessary computational effort and non convergence in these highly constrained areas, the deformation is calculated as a two dimensional problem and extruded subsequently. The simulation is built in COMSOL Multiphysics.

Meshing is achieved by using a triangular, coarse mesh for the shaft to decrease computation time. Similar to the tooling the rubber is meshed utilizing rectangular elements, with significant smaller edge length (maximum 1 mm). Additional boundary layers are added for the contact side between substrate and rubber respectively and element size is further reduced for the immediate contact area.
Progressively down-scaled element sizes in this area enable a precise contact model, prevents possible penetration of interacting elements and enhances the convergence of the model. Additionally the accuracy of the footprint reading improves. The mesh is illustrated in figure 4.2.

Silicone rubber exhibits an isotropic, hyperelastic material behavior, defined by its nonlinear elasticity and incompressibility. For hyperelasticity several mathematical representations exist, e.g. the Neo-Hookean, Odgen, Gent and Mooney-Rivlin model. The latter is based on the Neo-Hookean model and utilizes the elastic strain energy to characterize the mechanical properties. It is used to model the rubber in this simulation.
Three versions of the model are known with two to nine parameters to model the stress strain curve. Depending on its shape for a specific material, a fitting model is selected. As the SF45-RTV2 shows a double curvature shape, the five parameter version is utilized [11, 116, 142]:

Figure 4.2.: **Mesh mechanical model with detail of the contact area**

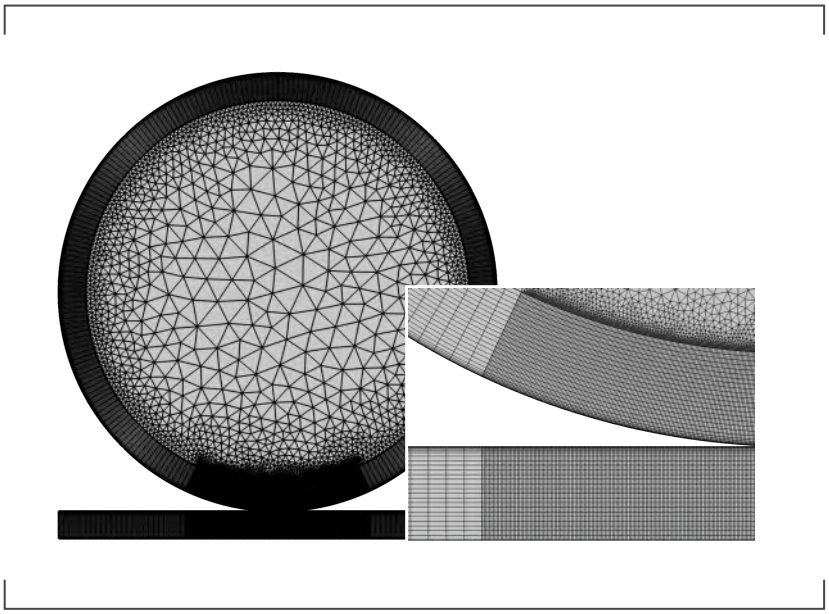

$$W = C_{10}(\bar{I}_1 - 3) + C_{01}(\bar{I}_2 - 3) + C_{20}(\bar{I}_1 - 3)^2 + C_{11}(\bar{I}_1 - 3)(\bar{I}_2 - 3) + C_{02}(\bar{I}_2 - 3)^2 + \frac{1}{D_1}(J - 1)^2 \tag{4.1}$$

Where W is the stress strain potential, $\bar{I}_1$ and $\bar{I}_2$ the invariants of the Cauchy-Green deformation tensor and J the determinant of deformation gradient. $C_{10}, C_{01}, C_{11}, C_{20}, C_{02}$ and D_1 are material specific constants, that were defined by previous work in the institute [188]. If $D_1 = 0$ the material is considered as incompressible and a weak constraint $J = 1$ is added, which deletes the last term of the formula. The values can be found in table 4.1.

Instead of a direct force applied to the shaft, its displacement vertically onto a flat, fixed mold is modeled. This is advantageous because the force propagation through the shaft into the mold can be ignored and pressure is applied directly between the contact partners. A total displacement of 1 mm is imposed with a simulation step size of 0.005 mm. Accuracy of the model is influenced considerably by the step size and has to be set accordingly. The simulation is solved for the contact force between rubber and mold, with a stop condition if 600 N are exceeded.
Contact between roller and mold is described using the fully-coupled Augmented Lagrangian Method. This method is a compromise between the penalty method and a

Table 4.1.: **Material constants Mooney-Rivlin model [188]**

Parameter	Unit	Value
C_{10}	MPa	–0.0340
C_{01}	MPa	0.3610
C_{20}	MPa	0.8316
C_{02}	MPa	0.7987
C_{11}	MPa	–1.6720
D_1	1/MPa	0.0000

non-penetration condition, that uses week constraints and lagrange multipliers (refer to [2]). The contact method was chosen because it enforces non-penetration while the solver configuration is comparably straightforward.
In order to stabilize the simulation two measures were implemented: the first is a spring load with a negligible spring constant $k = 1 \cdot 10^{-7} N/mm^3$, that preloads the compaction roller. The second is a friction in the contact area with a friction coefficient of $\mu = 0.8$.

The final computation is done in a two stage process. In the first stage the simulation is run without tape, to calculate the rubber deformation at a specific force. Thus a false force calculation due to a force flux through the tape is prevented. Afterwards the tape is added as incompressible, fixed part to the simulation that is recalculated with the same shaft displacement. This way the geometry is usable as direct input for the downstream models.

4.1.3. Results and Validation

The mechanical model is validated by analyzing the total compaction pressure and distribution as well as the resulting contact surface. Both values are subsequently compared to the simulation. The multitow layup head (MTLH) provided by AFPT GmbH is equipped with a controlled, pneumatic cylinder that keeps the compaction force constant for a horizontal load case. A range of three to six bar pressure was examined. Beside the absolute force values, it was investigated if the two dimensional simulation approach is representative for the silicone deformation on the machine and if the static model is deviating from a moving, real compaction roller.

Table 4.2.: **Validation compaction force for 3-6 bar pressure**

p [bar]	m [kg]	F_{nom} [N]	F_{sim} [N]	E [%]
3	36.02	353.38	346.01	–2.1
4	44.12	432.85	441.14	1.9
5	52.37	513.79	504.65	–1.8
6	60.32	591.69	597.07	0.9

For the measurement of total pressure a precision scale, DE 150K2D supplied by Kern & Sohn GmbH, with a resolution of two grams was used. It is capable of storing continuous data, which allows to check for peak loads. These have to be eliminated for the subsequent trials because they distort the foil and sensor readings.
For every pressure point a total of three measurement are taken and averaged. The results are indicated in table 4.2, with p as consolidation pressure, m as the measured total weight, F_{nom} as the resulting nominal consolidation force and F_{sim} as the simulation result. The error E is calculated as fraction between F_{sim} and F_{nom}. The results show an expected linear increase for F_{nom}, with a maximum of 591.7 N for the highest adjustable pressure $p = 6\,bars$ on the machine. A close match between simulation data and measurements is evident.

Compaction pressure distribution was measured using Fujifilm Prescale LLLW Ultra Super Low pressure sensitive foil. The two-foil-system has a color forming and a developing layer. Inside the color forming layer, micro-capsules with varying sizes and strengths are integrated. They contain dye that causes a chemical reaction together with the developer and produces a red color. If the resulting imprint is scanned with a color balanced scanning device, the color density can be quantified and translated into pressure values via an evaluation software. However, the measurement tolerance for quantitative trials are relatively high (approximately 10 %), thus results were solely used for determination of imprint dimensions, shape and a qualitative impression. Quantitative values are measured in an additional step, with a different measurement technique.[48]
The measurements were performed with programmed movements of the robot onto a flat surface, where the measurement foil was positioned. Peak loads, resulting from the robot movement, were minimized by decreasing its velocity to 10 mm/s. Following the first trials, for every pressure point three trials were conducted. Example images can be found in figure 4.3.
They show a comparatively homogenous pressure distribution for each pressure point and

Figure 4.3.: **Imprints SF45 silicone on Fujifilm Prescale LLLW**

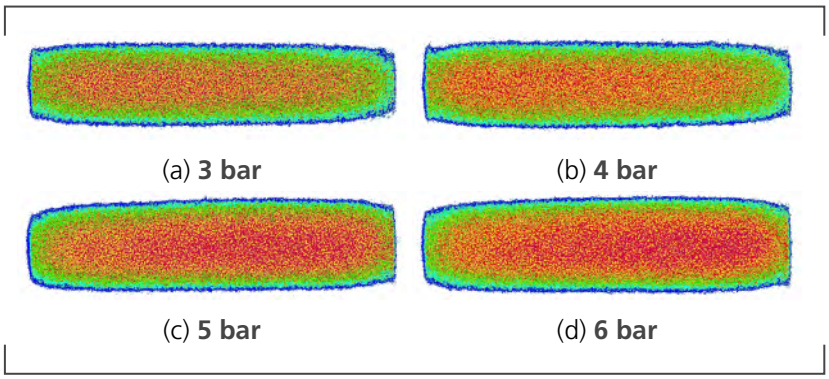

an increasing compaction area for higher values. The compaction roller has a greater width (60 mm) than the consolidated tape width of the three half inch tapes (consolidated approx. 41mm). From this follows that only the middle two thirds of the imprint are relevant.

For all pressure points a rectangular imprint can be assumed, a relative even compaction force is visible with a decline in radial direction. Qualitatively it can be stated that red color indicates high pressure areas, where as green and blue areas indicate low pressure. The rectangular dimensions were measured and are depicted in table 4.3 as roller imprint width l_{wmeas} and length $l_{l}meas$. As expected only minor changes in the roller imprint width are visible. Even though the contact length $l_{l}meas$ is of less relevance, it is a first indicator that a two dimensional simulation approach is sufficient.
For the contact width in layup direction an increase of 2 mm can be seen from three to six bar pressure.

The following procedure was used to validate the simulation on the basis of measurement data: a displacement of the roller shaft of 1 mm was simulated, using a step width of 0.005 mm. For every step the resulting force on a flat surface was calculated. A stop condition was implemented to end the simulation if a maximum force of 600 N is exceeded. Afterwards the closest match between simulated and measured compaction force and the corresponding contact width $l_{w}sim$ was identified. This is repeated for each individual measurement.
Table 4.2 shows the derived compaction forces and the error between simulated force F_{sim} and measurement F_{nom}. It can be seen that a maximum error E of -2.1 % is generated. The volatile change likely originates from the match making between the force values. Contact pressure distribution in the simulation looks like an elliptic section, which compares well to the imprints in figure 4.3.

Table 4.3.: **Validation compaction area dimensions for 3-6 bar pressure**

p [bar]	l_{wmeas} [mm]	l_{lmeas} [mm]	l_{wsim} [mm]	E [%]
3	13.4	60.3	13.1	-2.6
4	14.1	60.7	14.0	-1.1
5	14.9	60.8	14.6	-1.8
6	15.4	60.9	15.3	-0.6

The resulting contact widths l_wsim can be found in table 4.3. A systematic underestimation of the values is identifiable, since all simulated contact widths l_wsim are too small. Nevertheless with a maximum error E of -2.6 % for $p = 3\,bar$ compaction force, all errors are in a sub-millimeter span and correlate with the measurements sufficiently.
As a result it can be stated that the compaction unit is reproduced accurately with the mechanical model proposed. The remaining question is if the compaction roller changes its behavior while layup, therefore transient measurements are needed.

The pressure distribution and a possible consolidation roller footprint change during layup are investigated by means of a thin-film pressure-sensitive sensor (5101 150 PSI), manufactured by Tekscan Inc. It consists of a matrix conductor with a spacer of pressure-sensitive material between the meshes. Each intersection acts as one pressure sensor, that is read out individually and in sequence. This results in a resolution of $2\,mm^2$ per sensor.
In order to increase accuracy of the system, a calibration curve for static and dynamic load cases was implemented using a universal testing machine (Zwick Roell 1484). Static measurements are taken after five seconds of pressure, which is aligned with the calibration curve obtained beforehand. The test was conducted at six bar pressure.

Results for the trials can be seen in figure 4.4. On the top the static load case is depicted and on the bottom the dynamic measurement with 125 mm/s layup velocity and 6 bar compaction force. It can be observed that the static load case has a higher cumulated pressure area in the middle of the foot print, whereas the dynamic measurement shows a more balanced pressure distribution. A look at the local maxima of 10.8 bar (static) versus 9.8 bar (dynamic), shows that the differences are acceptable.
Within the accuracy of the sensor system, both contact widths amount to 15 mm. This aligns well with the pressure sensitive foil trials. A compaction force of 575 N for the static and 555 N for th the dynamic load case is found. Compared to the values measured by the precision scale an error of 3 % (static) and 6 % (dynamic) is obtained.

Figure 4.4.: **Static and dynamic measurement pressure at 6 bar set pressure**

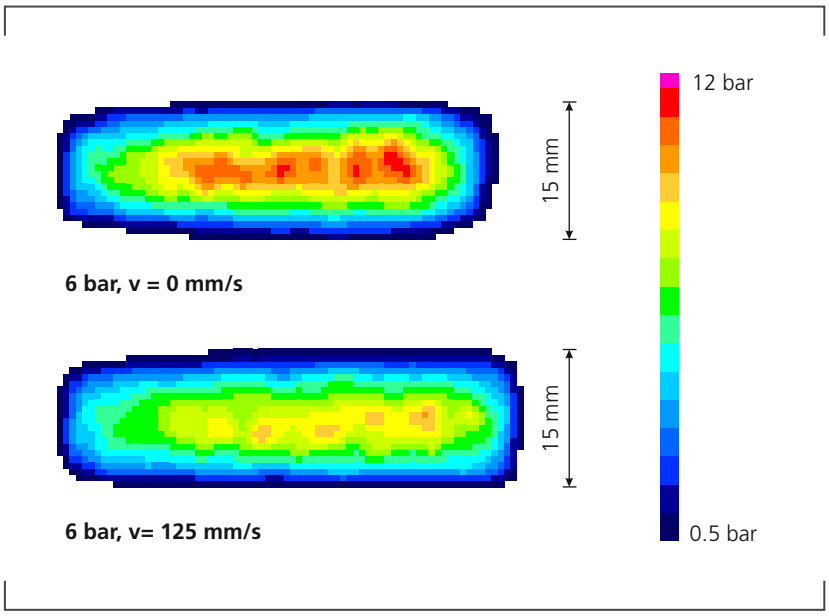

In conclusion the static, two dimensional mechanical model is representative for the dynamic process simulation and will be used further on.

4.2. Optical Model for the T-AFP Process

4.2.1. Introduction

The optical model describes the power distribution, absorption and reflection of the laser irradiation. It helps to determine to which proportions the tape and laminate are heated, where to expect hot spots and how shadows form.
As an introduction to the optics simulation, the diode laser with its light guide is presented and its essential features are laid out. Thereafter the design of the heating domain in the layup machine is described. With these basics, the individual aspects of the model are addressed namely the formulation of the ray source, the implementation of the beam divergence and the optical behavior of the CFRP prepreg.
To validate the model, the simulated intensity distribution is compared to a measurement. Similarly is proceeded with beam divergence, where the model is compared to a camera based experimental setup. To specify the accuracy of the heat source output, the system

efficiency is recorded.
The chapter is concluded with the results of the ray tracing simulation and an analysis of the resulting heat distribution on the laminate and tape. It is noteworthy that the final evaluation and adjustment of the optical model is incorporated in the thermal model, where thermal measurements are conducted.

4.2.2. Optical Process Model

In this work an infrared diode laser source with a wavelength range from 980 nm to 1040 nm is used. The device is a LDM 6000-100 supplied by Laserline GmbH with a maximum rated output power of 6 kW.
In contrast to other laser sources, diode lasers combine many individual bundles of rays. They originate from small semiconductor diodes. These are in turn grouped inline to laser bars. Several laser bars are stacked to get the full power of 6 kW. The rays need to be collimated and shaped in order to be guided into an optical fiber, due to their varying emission angles.[92]
The collimated laser light is guided via the optical fiber OTS-1 to the optic. The optic is a combination of a collimator and two lens arrays that collimate, homogenize, shape and focus the beam. Its profile is a rectangle with an nominal edge length of 43 mm, measured at a intensity drop of 50 %. The focus distance is specified to 200 mm and the optics are water cooled to allow for a continuous process.[93]

Unlike the laser source that can be located off the moving equipment, positioning of the laser optic strongly effects irradiation distribution between tape and laminate. Therefore, its shortly described and a simplified drawing (refer to figure 4.5) illustrates the layout of heating domain of the layup machine.
As for all subsequent considerations the coordinate system, marked red, is centered under the compaction roller in the consolidation zone. Its x-axis points in negative layup movement and the z-axis in normal direction to the laminate.
At an angle of 60° with respect to the x-axis, the tape is fed on to the consolidation roller. The optics angle of attack can be adjusted online with a stepper motor, in a total range of 15°. The default angular position is 30° with respect to the x-axis. The optics are centered in front of the consolidation roller. The pivot joint is located at x_{RP} and y_{RP}. In order to ensure exact values, they where measured via a three dimensional laser tracker and can be found in appendix B.
It is possible to shift the optics back and forth mechanically on a linear slide, during setup to adjust the focus point. The optical center line is below this axis and its position is given by the parameters h_{laser} and h_{laser}.

Figure 4.5.: **Layout laser optic mount**

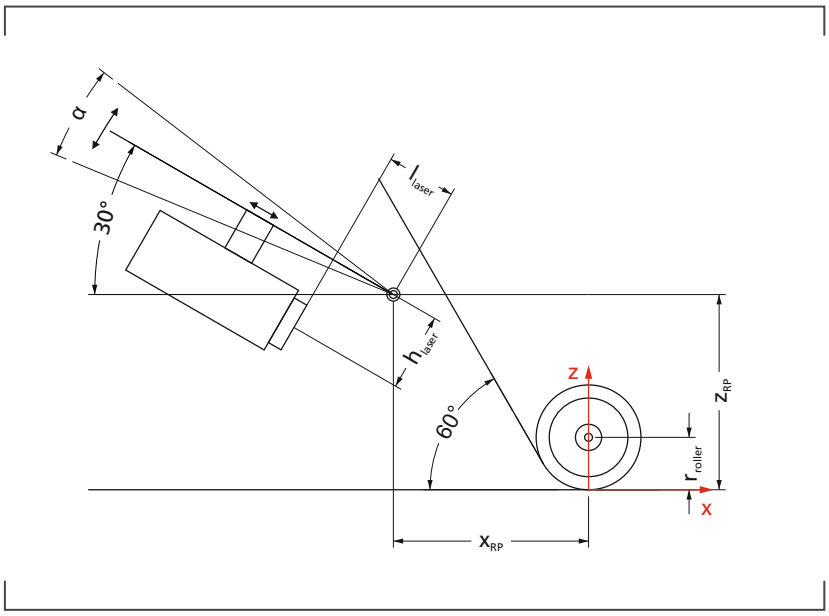

In order to model the irradiation distribution a ray tracing simulation is established, using COMSOL Multiphysics. Its basic principle is that a discrete number of rays are released in a system and their propagation is advanced in small increments. Due to their mitigation in the media or impingement with other domains they may bend, reflect or change their direction.[165]

A square surface, positioned in the default laser optic position (refer to figure 4.5, is implemented as simplified ray source. Its dimensions, 17 x 17 mm, reflect the size of the optics aperture. Evenly distributed rays are emitted normal to this surface. For the validation of the optics model a total of 4 million rays are simulated. This is mainly to obtain high resolution results, needed to compare the optics model to the validation measurements.
The laser intensity is not equally distributed across the optics, but rather builds a top hat profile. Its shape was supplied by the manufacturer and was measured using a CinCAM CMOS 1204 infrared beam profiler, at focus distance. A two dimensional image of the intensity was taken. It shows an almost symmetrical distribution, with intensity dropping at the borders and in the corners.
In order to establish a mathematical description of the intensity distribution for the model, measurement values of cross sections at the x- and y-axes were taken and analyzed with the MATLAB curve fitting toolbox. A Gaussian model with seven terms showed the best

Figure 4.6.: **Top hat profile laser beam intensity distribution spanned over gaussian functions**

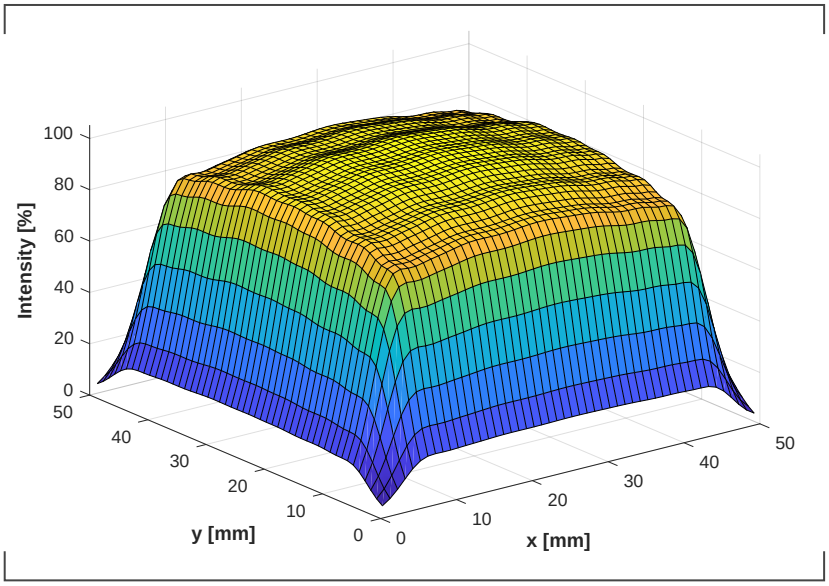

fit, achieving root mean square errors of 0.18 and 0.32. The equation of the Gaussian model is given by:

$$y = \sum_{i=1}^{n=7} a_i e^{-\left(\frac{x-b_i}{c_i}\right)^2} \tag{4.2}$$

The coefficients for the two intensity cross sections are given in table A.1 in appendix A. The measurement data and the resulting fit can be found in diagram A.1 in the same appendix.
In order to be able to include the functions in the model they are centered on the x-axis. Furthermore, the diverged beam intensities at focus distance, were scaled back from 43 mm to the ray source surface size of 17 mm.
The resulting functions are superimposed using the square root of their product to build the top hat profile. The resulting surface is depicted in figure 4.6 and implementation in the ray source is done as weight function multiplied with the total laser power.
It is anticipated that the optics simulation can not model all sources of losses. Therefore a parameter for all sorts of energy losses is introduced, called η_{laser}. It will be tuned using thermal process data in section 4.3.

Beam divergence is replicated by means of an equi-concave lens representation, with a diameter of 25 mm to fit all rays. Its center thickness is specified to 1 mm, which is comparatively small to the image distance and thus can be regarded as thin lens. As the environment of the lens is air its refractive index n_{air} is regarded as 1. Given these assumptions the refractive index of the lens can be approximated using the following formula [131, pg.65]:

$$CMOS \tag{4.3}$$

Where r_1 and r_2 are the lens surface radii and f the focal length of the optics. With r_1 and r_2 being -120.1 mm, a refractive index for lens of 1.3 is determined.
An anti reflective coating for the lens is assumed, which implies that no power is absorbed by the lens. As the optics are water cooled this is obviously an incorrect simplification. However, for readily adjustment of the overall heat source efficiency only one parameter η_{laser} for the complete heating mechanism is introduced (see above).

The optical behavior of the CFRP is modeled as specular reflection. Absorbtion, reflection and transmission coefficient are formulated using the Fresnel equations of electromagnetic waves between two media. A smooth surface and unpolarized radiation is assumed. If combined with Snell's law to describe the reflection angle, the reflectance can be described as [36, 87, 131, pg.580]:

$$r(\theta, n_{CF}) = \frac{1}{2}\left[\left(\frac{n_{CF}^2 \cdot \cos\theta - \sqrt{n_{CF}^2 - \sin^2\theta}}{n_{CF}^2 \cdot \cos\theta + \sqrt{n_{CF}^2 - \sin^2\theta}}\right)^2 + \left(\frac{\cos\theta - \sqrt{n_{CF}^2 - \sin^2\theta}}{\cos\theta + \sqrt{n_{CF}^2 - \sin^2\theta}}\right)^2\right] \tag{4.4}$$

Where r defines the reflection coefficient for each ray, dependent on the refractive index of the CFRP n_{CF} and the angle of incidence θ. For n_{CF} a literature value of 1.96 for CF/PEEK is applied [197].
An impinging ray is divided into an absorbed, reflected and a transmitted fraction. Following the law of energy conversation the coefficients are linked as follows [66, pg.29]:

$$\alpha + r + \tau = 1 \tag{4.5}$$

With α being the absorption, r the reflection and τ the transmission coefficient. Previous work showed that the matrix is nearly transparent for infrared laser beams, whereas carbon

fibers are completely opaque [168, 197]. Thus the transmissivity of the CFRP tape can be considered as zero and the absorption coefficient can be calculated as:

$$\alpha = 1 - r \tag{4.6}$$

In order to compensate for the roughness of the CFRP surface a second reflection mechanism is introduced: the isotropic scattering. A probability factor of 0.75 is used, meaning that in 75 % of all cases the emergent angle does not equal the incident angle, but is instead determined randomly.
Ray termination is implemented with two conditions: either a ray is reflected more 10 times or it hits a boundary box that is defined around the heating zone of the system.

4.2.3. Results and Validation

Intensity Distribution

To compare the intensity distribution in the model with the measurement, an additional, simplified version of the optical model is developed. In this model a surface normal to the ray source is introduced to recreate the measurement setup. The rays are collected at this surface and each element accumulates the number of rays and their inherent intensity. On the left side of figure 4.7 one can find the original measurement and on the right side the simulated image is depicted.
The colors represent the dimensionless intensity where dark red is the highest and dark blue the lowest value. The black line around the simulated image marks the measured profile size, a rectangle with 43.3 mm by 43.4 mm,. Using these images a qualitative evaluation can be done: the overall distribution of intensity compares well, with high intensity in the center that is degrading to the borders. Additionally the lowest intensity in the profile can be seen in the corners on both sides. The measurement shows a smoother intensity drop on the profile edges. From this follows that its overall footprint is a bit larger than the simulated one. Despite these minor differences, the profiles show a close match. The simulated intensity in x-axis direction is 0.60 mm and in y-direction 0.57 mm larger than the measured values and thus well in the needed accuracy.

Figure 4.7.: **Intensity distribution laser**

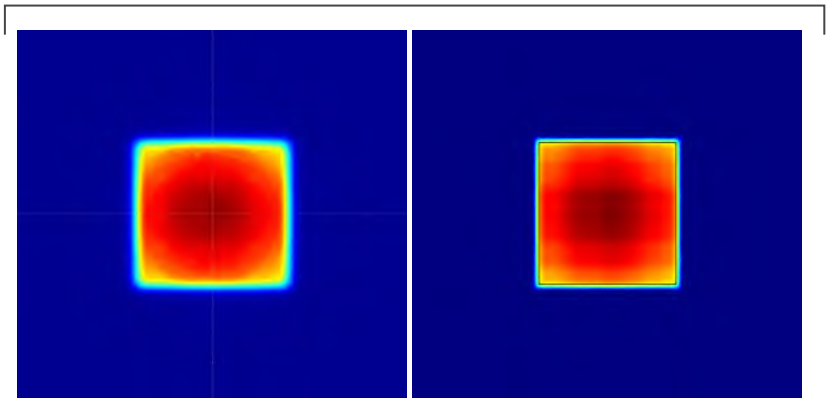

(a) **Measurement** (b) **Simulation**

Laser Beam Divergence

Laser beam divergence is largely accountable for the actual size and intensity distribution of the irradiated area in the heating zone. It was approximated in the model using the refractive index formula for thin lenses. In addition a rather wide working distance tolerance of the optics is with ± 5 mm is specified by the supplier. Due to its high impact on the heating process it is concluded that the divergence has to be verified experimentally.

The experimental setup comprises an camera system (Mako G-125B POE 5054) supplied by Allied Vision with an infrared long-pass filter. The layup machine is mounted to a KUKA KR120 R2700 HA robot that is aligned such that the laser light impinges the test bench perpendicular. All components in the way of the laser beam were removed. The experimental setup is depicted in figure 4.8.
As laser target a calcium silicate plate (K-Therm CS1000), with a comparatively low thermal conductivity of 0.4 W/mK, is used. The low conductivity minimizes heat conduction that would increase the measured beam profile. Additionally, the plate is coated with graphite spray to reduce its reflectivity, which could interfere with the camera measurement.
To assign a size to each camera pixel and simultaneously eliminate the image distortion, a reference frame with an optical pattern is placed on top of the ceramic plate. The pattern displays four cycles with crosshairs in the center. Due to a defined distance between the the cycle center points it is possible to conclude on the irradiation profile size. Reference point distances of 90 mm for close distance measurements and 180 mm for the three largest distances, were used.

Figure 4.8.: **Experimental setup laser beam extension**

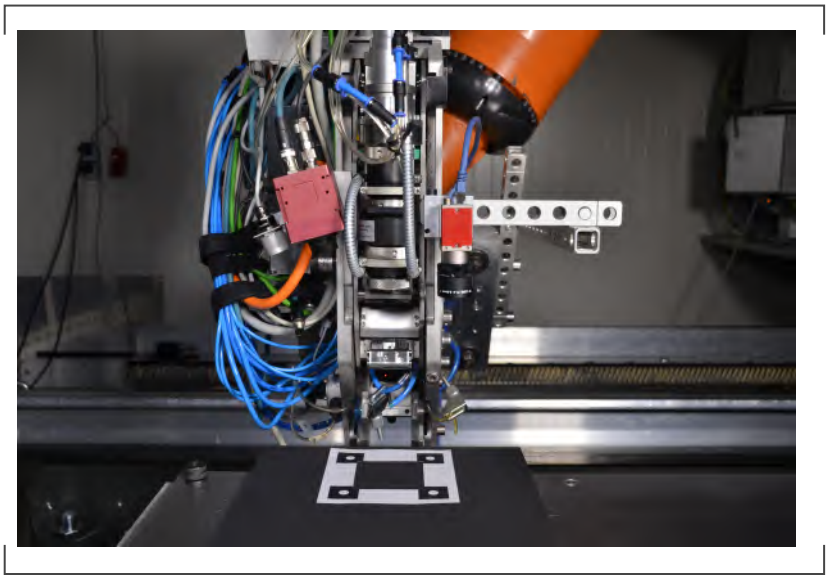

Thus each pixel of the taken images has a resolution of approximately 0.1 mm. Measurement of the beam extension was performed under exclusion of interfering light and with 100 W laser power. The distance between laser aperture and plate was varied from 195 mm to 315 mm in increments of 20 mm. An additional measurement point was set at 190 mm on the grounds that it marks the minimal tolerance limit of the optics.
In order to compare the beam divergence in the optical model with the measured values, a simplified version similar to the model in section 4.2.3 is used: A surface normal to the ray source is introduced and its distance to the lens is changed according to the measured values. The incident beams are accumulated and an algorithm is used to measure the squared beam profile.

For each distance the beam extension is measured in x and y-direction, from a 50 % drop in intensity to the same drop at the opposite side of the top hat profile. The evaluation follows the intensity measurements provided by Laserline GmbH (refer to chapter 4.2.2). The measurement results are depicted in diagram 4.9.
A squared laser beam profile with quadratic expansion is assumed. Thus a linear interpolation is fitted to the measurement data to check the validity of the results. As indicated by the black line in the graph, the data shows good correlation to the quadratic behavior. For a working distance of 190 mm the intensity measurement indicates a beam size of 43.3 mm x 43.4 mm, whereas the linear interpolation gives a size of 43.5 x 43.5 mm. This is a good fit, however it has to be taken into account that is matches the lower tolerance

Figure 4.9.: **Laser beam extension measurement**

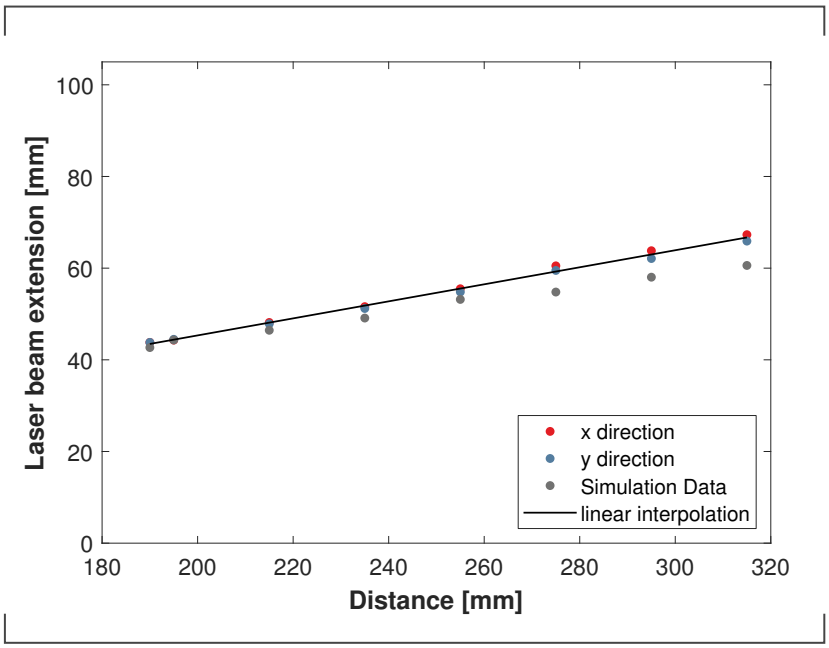

limit.

The simulation results are depicted in grey dots in figure 4.9. It is evident that measured and simulated values show a decent fit for distances up to 255 mm and the error is comparatively large for the last three values. The maximum error is 1.24 mm and the mean deviation is 0.46 mm.
One explanation for the step in the measurement data could be that the intensity measured at large distances was to low and added an additional error or the usage of a larger reference frame for the camera system. This assumption is supported by the fact that the last 3 measurement values show a visible step.
As the optic is used in its focal length of 200 mm this effect is of lower relevance for the model.

System Efficiency

In a diode laser system at the following stages losses occur: power to irradiation conversion in the diode array, transport in the fiber and beam shaping in the optics. The equipment

supplier for the utilized system specifies the efficiency of the diode array to nearly 50 % and for the optical fiber to approximately 93 % [90, 92]. Previous work reported an efficiency of around 90 % for the optics [87].
These losses are compensated by the layup machine with the usage of an calibration curve for the laser control. In order to be able to estimate its accuracy, the power output after the optics has to be measured.

For this task the laser power absorber Cube A supplied by Primes GmbH is applied. The system uses the temperature difference before and after the measurement. With known material parameters for the absorber, namely heat capacity and conductivity, the impinging energy can be calculated. The system has a defined accuracy of ± 3 %.
The measurements where conducted at a distance of 100 mm to the device, to ensure complete coverage of the laser beam. Power levels from 250 to 6000 W with an increment of 250 W where tested. In order to increase measurement accuracy, the applied energy is held roughly at 300 J for each power level. This is done by decreasing the exposure time for increasing power levels.

The results are plotted in figure 4.10. On the x axis P_{ref}, the set power is plotted, ΔP is defined as:

$$\Delta P = \frac{P_{meas} - P_{ref}}{P_{ref}} \tag{4.7}$$

With P_{meas} being the measured power. For the processing of high performance thermoplastics the range of 1750 to 3000 W are of interest, depending on the layup velocity and material.
In this area a mean divergence of 3.1 % can be seen. This is only slightly above measurement tolerances of the absorber, which renders an adaption unnecessary. Nevertheless due to the increased accuracy measured in factory calibration, an indicator is given, that laser power is slightly over compensated.

Raytracing and Intensity Distribution

In figure 4.11 the result of the ray tracing is displayed, for visibility only 100 beams are shown. The color legend refers to the intensity of each ray.
Apparent in this overview is that almost all rays hit the nip point area between tape and laminate. Only a small fraction of the rays hit the roller and adjacent laminate, respectively. Despite the introduced isotropic scattering, most rays do not leave the domain as they

Figure 4.10.: **Measurements divergence set power to is power**

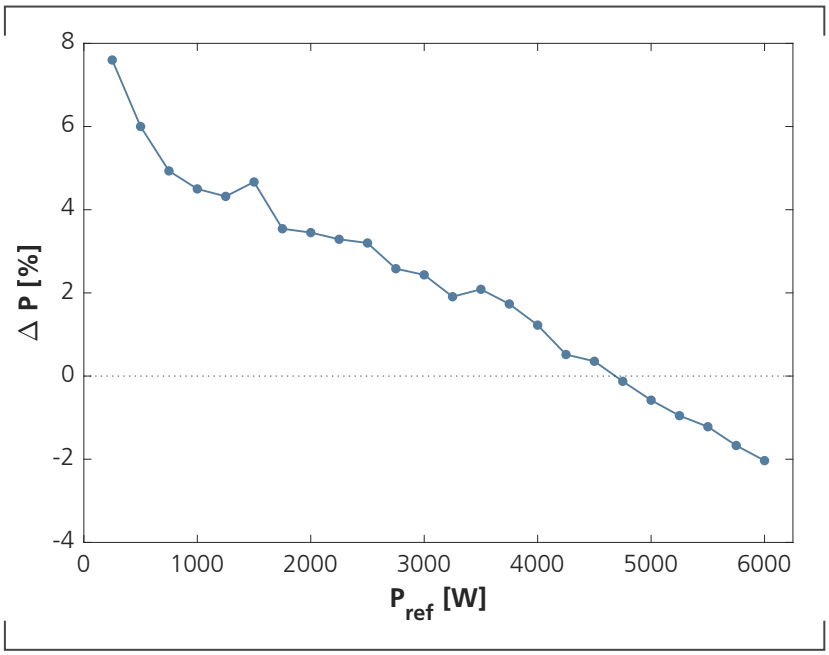

are trapped within the wedge shaped heating zone. For the rays that do leave the domain, a vast amount have been reflected at least twice, which means that they carry a small amount of energy. All the above leads to a comparably slim loss of power to the environment of around 4.7 %.

Heat distributions, calculated with 4 million rays, on the laminate and tape are depicted in figure 4.12. The laminate is shown as top view on the right, with the horizontal as x-axis and vertical as y-axis respectively. For better visibility the incoming tape is shown as side view in line of sight of the laser optics. The horizontal axis is in tape width and the vertical in z-axis. The intensity is normalized using the total power *P* (here 2600 W) and is therefore dimensionless with a maximum of 1.
For the laminate it can be observed that the irradiation widens in direction of the nip point and a shadow of 4.3 mm is casted before the consolidation roller. Higher intensity hits the tape center and weakens towards the laminate edge. A light irradiation on left side of the profile originates from reflected beams on the tape side.
The highest irradiation can be found on the top of the incoming tape. Due to the incident angle change, a relatively steep descent in irradiation can be observed from the center of the tape to the bottom.
The model calculates that 55,5 % of the total power impinges the tape and 36,9 % the laminate.

Figure 4.11.: **Simulation of laser rays for the T-AFP process**

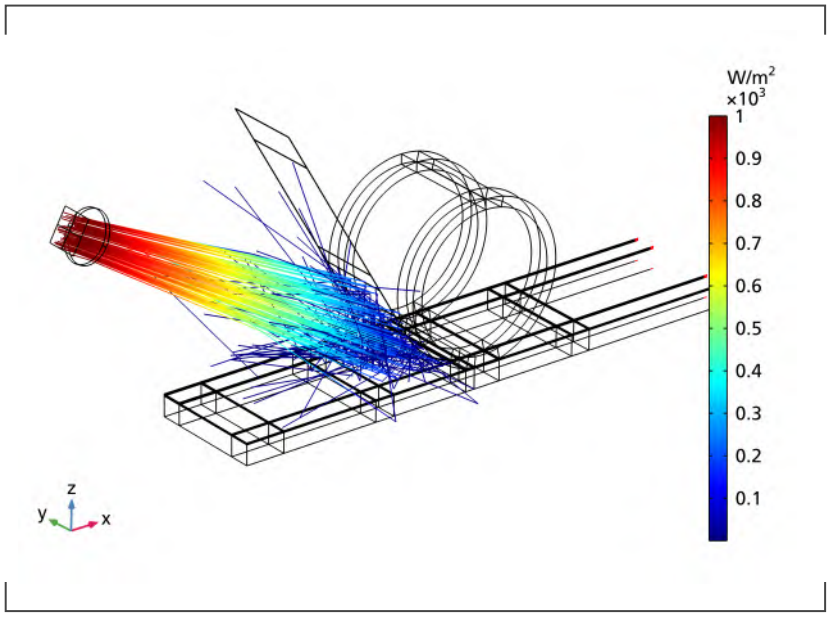

Figure 4.12.: **Intensity distribution tape and laminate**

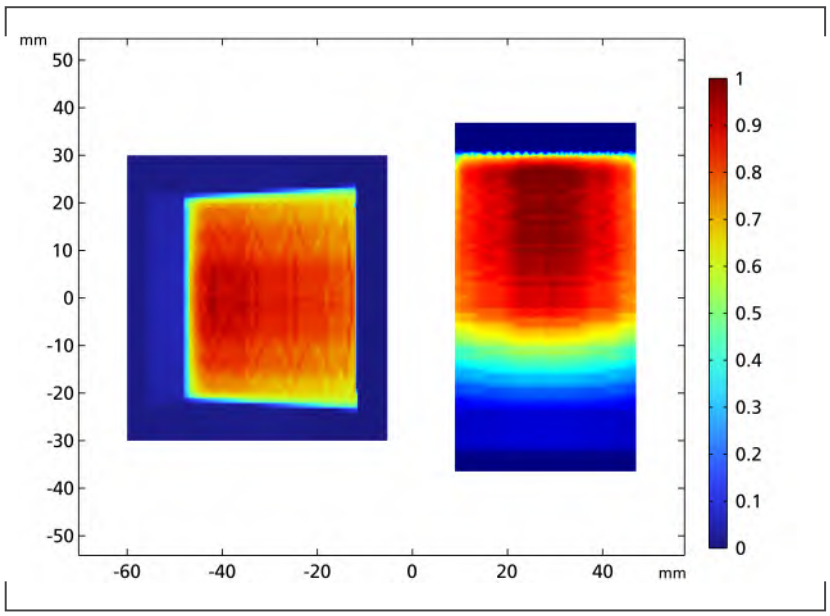

4.3. Thermal Model of the AFP Process

4.3.1. Introduction

Using the mechanical and optical model it is now possible to create a heat flux model to describe the temperature evolution during T-AFP. It describes the resulting heat propagation especially in the processing zone and thus one of the main drivers for good consolidation. The thermal model builds the basis for the model predictive controller and its development is described in this chapter.
First a brief introduction to the mathematical description used in the FEM simulation is given and the system borders are defined. Meshing for this highly loaded system is sensible and described subsequently. Next all relevant thermal material parameters are gathered or measured where necessary to model the anisotropic CFRP behavior and its simulation approach is discussed in detail. Afterwards, the remaining boundaries namely the radiation, convection and conduction between the components are determined.
Because not all boundary conditions are measurable, a parameter variation provides information on how each of them affect the temperature propagation. This is the foundation to define their specific values by means of thermocouple measurements. They are described in the last sub-chapter and the corresponding results are compared to the tuned simulation eventually. In order to conclude the validation, the laser power is varied in the trials and it is shown that the simulation maps the change correctly.

4.3.2. Thermal model

An Eulerian specification is used for the thermal simulation. One major benefit of this approach is the comparatively small system size needed, which allows for greater detail in the processing area. For this, a system border is set around the compaction roller, with a coordinate system centered under the compaction roller and beneath the currently placed tape. It is identical to the systems in the upstream models. An overview of the simulation is given in figure 4.13, it should be noted that the system is truncated on the right side.
Mass flows in and across the system borders for tape, laminate, roller and tooling represent the layup process. Following the first law of thermodynamics the three dimensional system can be described as:

$$\rho c_p \left(\frac{\partial T}{\partial t} + v_x \frac{\partial T}{\partial x} + v_z \frac{\partial T}{\partial z} \right) = \frac{\partial}{\partial x} \left(\Lambda_{xx} \frac{\partial T}{\partial x} \right) + \frac{\partial}{\partial y} \left(\Lambda_{yy} \frac{\partial T}{\partial y} \right) + \frac{\partial}{\partial z} \left(\Lambda_{zz} \frac{\partial T}{\partial z} \right) + \rho r \quad (4.8)$$

The variable ρ describes the density of the material, c_p the specific heat capacity, v the layup velocity and Λ the heat conductivity matrix. Energy generation or absorption by the composite during melting or solidification is determined by r. However, it will not be neglected due to its comparatively small impact here (refer to chapter 2.1.3).
On the left side of the function the energy storage in the material and heat transportation via mass flow is described. It can be discovered that no mass flow exists in tape width. On the right side of the equation heat conduction in the material is determined.

For the heat transfer model a system length of 519 mm in layup direction (negative x-axis) is determined in COMSOL Multiphysics. It allows to simulate the process for layup speeds up to 125 mm/s and still evaluate the temperature gradient from melt to glass transition. For higher layup speeds or longer evaluation times, infinity areas are defined that allow to scale the outputs accordingly.
In tape width the simulation is limited by the compaction roller width and an accumulated height of 183 mm is specified to cover all irradiation configurations and the mold. For thicker laminates the system size increases consequently.
The laminate configuration is chosen to cover the most common layup situation: at least one ply is beneath the current layer and the previous tape is already placed on the y positive side.
The tape has a width of 3x12.7 mm and thickness of 0.18 mm. It is simplified as incompressible, without squeeze flow and flattening. Although both do occur in the process, the effect is assumed to be negligible. For the consolidation roller the deformed silicone sleeve of the mechanical model is used and the shaft will be considered as boundary condition only.
A flexible number of layers and fiber angles can be defined for the laminate, whereas the tooling is specified as monolithic, isotropic aluminum alloy with a thickness of 10 mm.
Infinity areas at both ends of the tape, laminate and tooling with a length of 20 mm, prevent large temperature drops at the simulation borders. A more detailed description regarding the individual simulation aspects is given below:

Mesh

Due to the high deformation of the mechanical model, its geometry is imported an a independent, new mesh has to generated. Therefore a linear element growth rate is used for the mesh elements to reduce the number of degrees of freedom and thereby computational effort. However, it requires a precise design of the meshing to get mesh independent, non oscillating results. In this regard a conforming, matching mesh is applied that mitigates the large aspect ratios e.g. between tape thickness and length.

Figure 4.13.: **Overview thermal model**

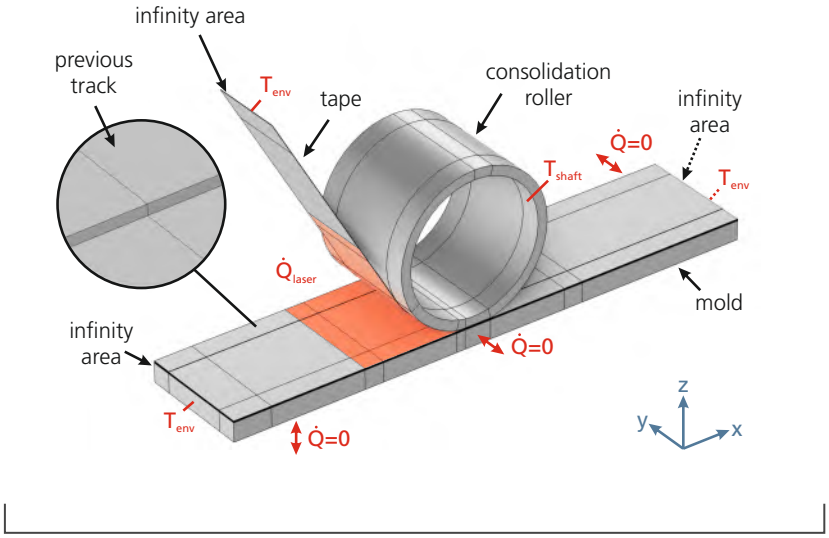

Quadrilateral elements were used for a predominant share of the geometry, with tetrahedral transition zones between different element sizes. In order to avoid high temperature and element size steps respectively, the mesh transitions from small elements in the highly loaded nip point to larger ones on the simulation borders. In the nip point area the smallest elements have an edge length of 0.05 mm, the largest elements in the peripheral zones reach an edge length of 2 mm.
The individual tapes are modeled with three elements in thickness direction, to allow the evaluation of temperature gradients in tape thickness. A cutout of the most critical part of the mesh, the nip point area, can be found in image 4.14.

Materials

For the simulation CF/LM-PAEK TC1225 supplied by Toray Industries is defined as baseline material. It is assumed to be a macroscopic homogenious material, meaning a distinction between fiber and matrix is not done. To account for the anisotropic material characteristics, individual parameters in fiber and matrix direction are determined. The following temperature dependent material properties are required for the thermal simulation: the density, the surface emissivity, the specific heat capacity and the heat conductivity. The required values are determined in the following paragraphs:

Figure 4.14.: **Detail cutout mesh thermal model**

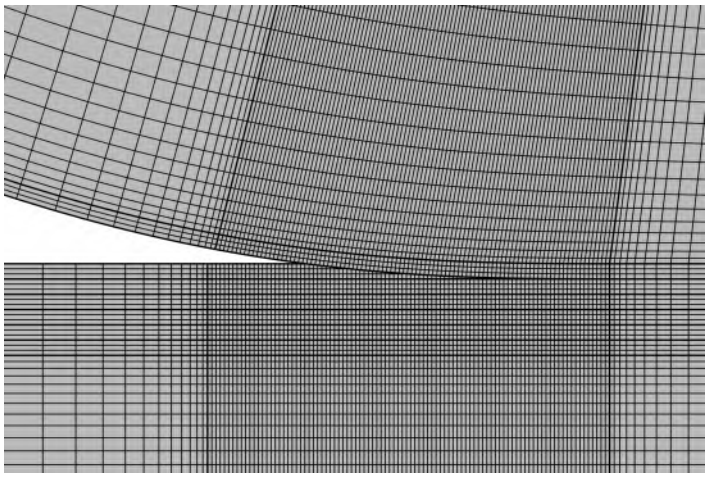

Several methods exist for the measurement of material density at room temperature, e.g. hydrostatic scales or pycnometers. For higher temperatures this is proving more difficult. One feasible procedure is to determine the thermal expansion of the material and to conclude to its density by scaling the room temperature value. Since CFRP exhibits different thermal expansions in fiber and matrix direction, two measurements are necessary. It should be mentioned that this indirect approach adds inaccuracies to the measurement data.
The thermal expansion was measured using a Netzsch DIL 402SU dilatometer. Test specimens were made from a 12 layer, unidirectional laminate, with dimensions of 25x5x2 mm and 5x5x2 mm for in fiber and transverse direction, respectively.
Above 300°C the material softened and the measurement tip sunk in, resulting in negative thermals expansions. Thus the density is held constant above the melting temperature. The result are presented in figure 4.15 (red, solid) accompanied by literature values for CF/PEEK (black, dashed) for classification. A slightly lower density compared to CF/PEEK is visible but generally CF/LMPAEK shows the same, almost constant density over temperature increase.

Specific heat capacity is commonly determined using Differential Scanning Calorimetry (DSC). However, a calibrated machine by means of a sapphire comparison sample is necessary. For this method a small sample and a reference are heated and the emitted and absorbed heat are evaluated. For more details one can refer to standard DIN 51007 [37]. The heat capacity measurements were provided by the material supplier and can be found

Figure 4.15.: **Density CF/LMPAEK and CF/PEEK [28]**

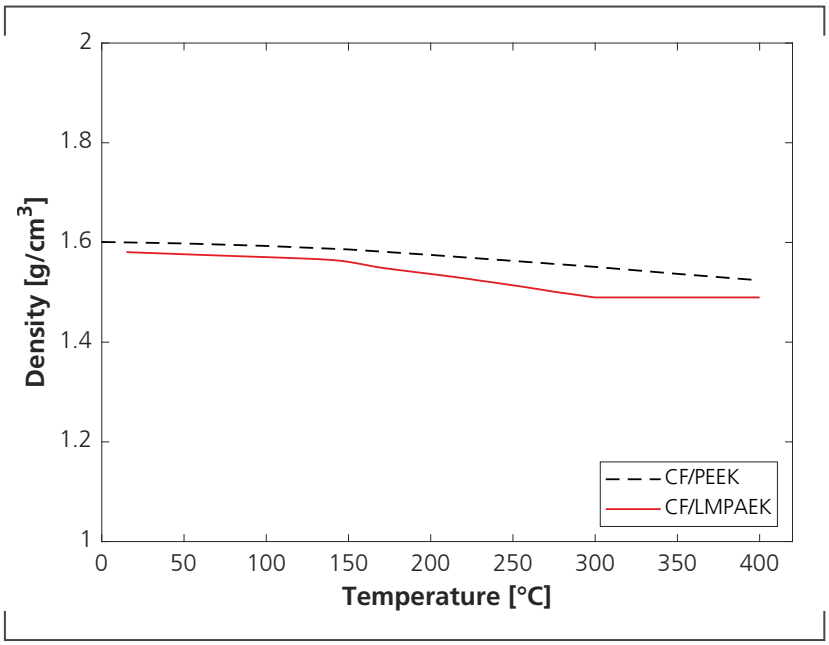

in figure 4.16. Between $230 - 330°C$ melting and solidification distort the measurements, hence the results are linearized between these temperatures. Similar to figure 4.15, literature values for the chemically related CF/PEEK are added to give a categorization. It can be observed that the specific heat capacity of CF/LMPAEK shows close accordance to CF/PEEK and both do exhibit a almost linear increase for higher temperatures.

In order to model the heat conductivity it is important to determine its factors. It is defined as:

$$\dot{q} = -\lambda \Delta T \tag{4.9}$$

Where the temperature difference ΔT is obtained via the FEM simulation and λ is the thermal conductivity and defined as:

$$\lambda = \rho c_p \alpha \tag{4.10}$$

The thermal diffusivity α measures the rate of heat transfer between the hot and cold side of a material. It is measured using the laser flash analysis device LFA 467 supplied by

Figure 4.16.: **Specific Heat Capacity CF/LMPAEK and CF/PEEK [28]**

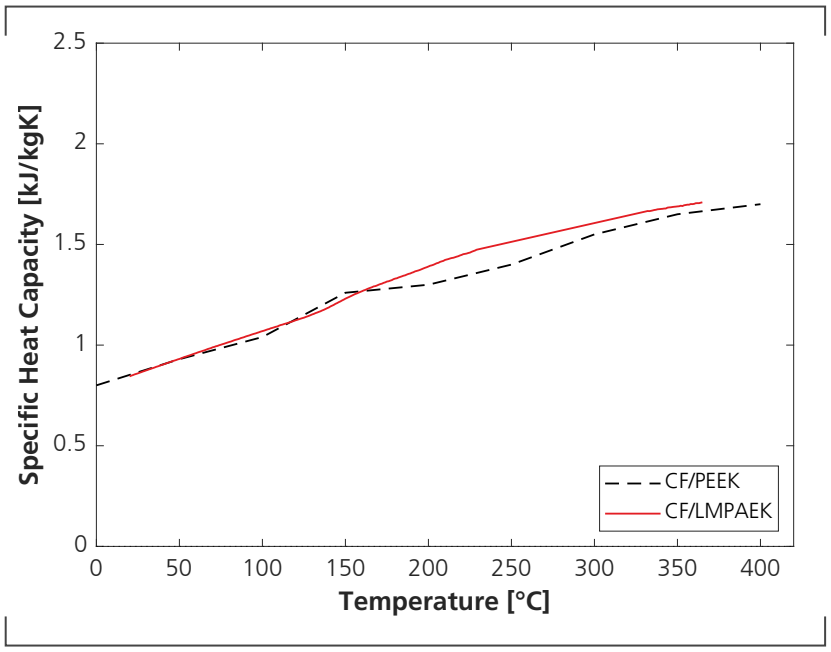

Netzsch GmbH. It heats the sample with a xenon flash lamp on one side and measures the temperature diffusivity with an infrared sensor on the other side.
For each direction, in fiber and perpendicular, seven samples were evaluated whereby three measurements per temperature point were taken. For the measurement in fiber direction a 6 mm thick laminate was consolidated via hot press and round samples, with a diameter of 6 mm and a thickness of 2 mm, were cut out. The matrix diffusivity was measured using square samples with a size of 10x10x2 mm. The values were measured for temperatures between 22°C to 400°C with an increment of 50°C between measurements.
In figure 4.17 the thermal conductivities are summarized. As expected the heat conductance in fiber direction (FD) is nearly one order of magnitude larger than in matrix direction (MD). As seen in the previous measurements only small deviations compared to the PEEK values can be seen for the conductivity matrix direction. However, a large deviation of approximately 2 W/mK is visible for the conductance in fiber direction. This is accounted to the different carbon fiber contents in the measured materials of 61 % versus 66 %, for CF/PEEK and CF/LMPAEK, respectively.
The thermal conductivities are added as a diagonal matrix in the simulation and different fiber orientations are implemented by means of individual, rotatable coordinate systems for each tape.

Figure 4.17.: **Thermal Conductivity CF/LMPAEK and CF/PEEK [28]**

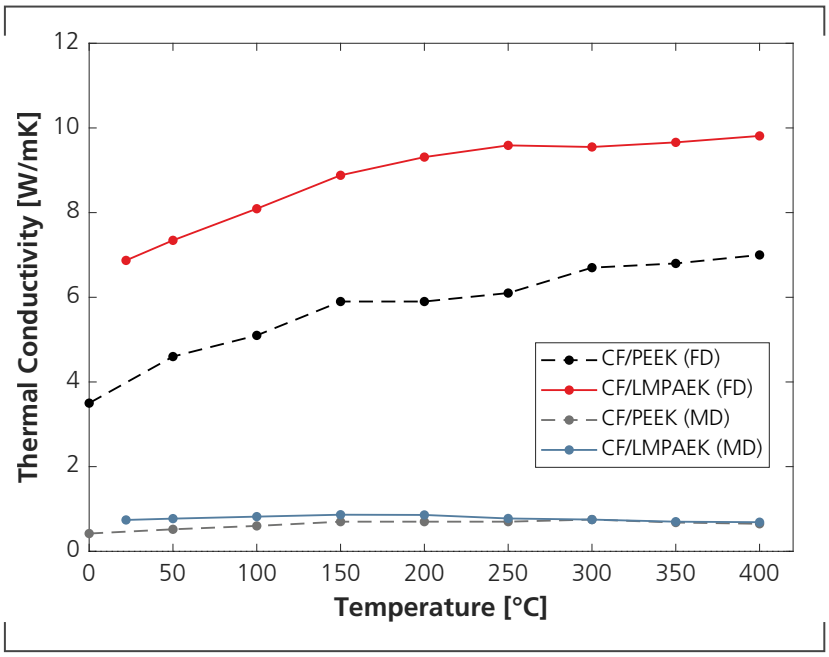

Thermal resistances between individual layers may occur in case of imperfect bonding. Levy et al. showed that the laminate can be regarded as series of contact resistances and capacities. By comparison of the thermal conductance of T-AFP manufactured laminates with ones that are consolidated optimally e.g. via hot press, the specific heat resistance is determinable. The equations is given as [88, 100]:

$$R_{lam} = \frac{n \cdot t_l}{n-1} \left(\frac{1}{\lambda_{AFP}} - \frac{1}{\lambda_{HP}} \right) \tag{4.11}$$

Where n are the number of layers, t_l is the thickness of the tape and λ_{AFP} and λ_{HP} are the measured thermal conductivities. Measurement of the difference in heat conductance is performed with 12 layer, 10x10x2 mm samples for the T-AFP and hot press consolidated laminates, respectively. The identical method used to measure the thermal conductivities of the last paragraph, was applied. The results can be found in figure 4.18.
For temperatures over $300°C$ it is likely that delamination occurred and measurements are inconclusive. Between $22°C$ and $300°C$ an increase of resistance is visible, with the highest value of 8.7E–5 m^2K/W at $250°C$. The values are in range of the literature values for CF/PES, however a constant value can not be identified. Thus the measurements will

Figure 4.18.: **Thermal Resistance CF/LMPAEK**

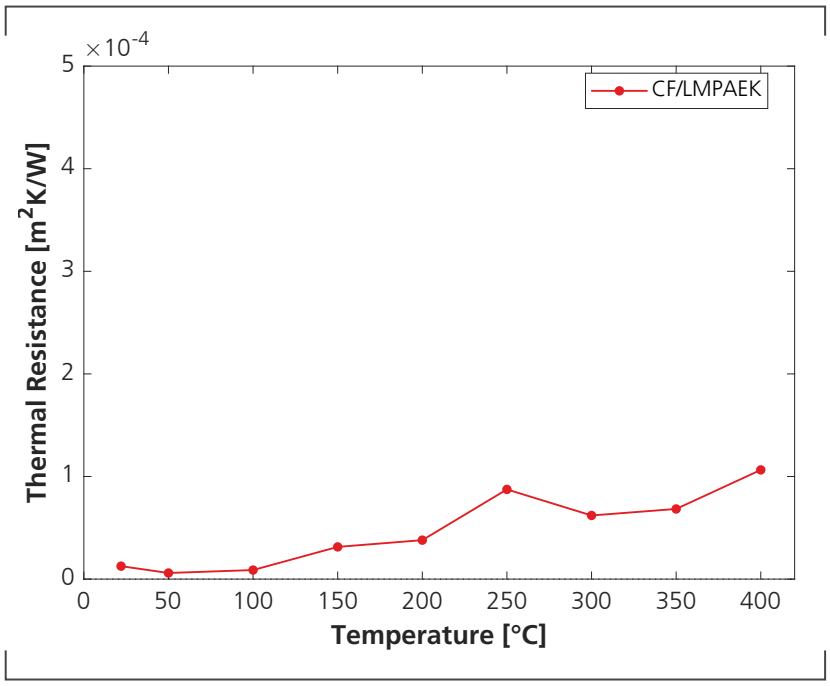

supported by performing a parametric sweep and tuning the value using the thermocouples measurements.

For the mold a standard aluminum alloy is defined (EN AW 5754, AlMg3), the corresponding material properties can be found in literature [105, 161]. Constant material properties are used for the silicone rubber with a density of 1.25 g/cm^3, a heat capacity of 1.255 *KJ/kgK* and thermal conductivity of 0.18 W/mK [173].

Boundaries

In the following chapter the definition of the boundaries are described, all boundaries interfacing the systems limits are depicted in figure 4.13. Irradiation and the resulting heat fluxes on the tape, laminate and roller are calculated by the optical model and are applied as inputs on all surfaces in front of the nip point. The dominant heat transfer mechanism is the layup velocity itself, thus a translational movement in direction of the positive x-axis is applied for the laminate and tooling.
As the tape and roller are both deformed by the compaction force a simple, combined

circular and linear translation is not applicable. For this reason curvilinear coordinate systems are calculated, that define a vector field in the complex shaped areas. Using these vector fields the movement is described in layup direction and as rotation for the compaction roller, respectively.

Between the individual components of the manufacturing process, surface asperities, auxiliary materials and other disturbances may decrease the heat conduction. For these purposes thermal contacts are introduced. In literature complex models are presented to estimate their effect and are commonly based on description methods to classify the height and slope of the asperities (refer to [145, pg.3.1]).
A different, simpler approach was taken for this simulation by application of equivalent thin layers. These can be used to apply properties without the need to model the layer itself. With the definition of either a heat conductivity or a specific thermal resistance for the layer, the approach is both computational lean and versatile.
For the contact between compaction roller and tape, a specific contact resistance is introduced. It is defined as the reciprocal of the thermal conductivity:

$$R = \frac{1}{\lambda} \tag{4.12}$$

The thermal resistances between the individual layers in the laminate have already been introduced in chapter 4.3.2. Between laminate and tooling a layer of woven glass fabric and polyimide is applied, to provide the necessary first ply adhesion. This layer is also modeled as thermal contact and a heat transfer coefficient is specified. Since direct measurement of all three values is either inconvenient or impossible, they are determined by means of parameter variations.

Convection between the tape, laminate and roller and air is added to all surfaces that are in contact with the surrounding air. The convective heat flux is defined as:

$$\dot{q} = h\Delta T \tag{4.13}$$

Here h is the heat transfer coefficient and ΔT the temperature difference between the environment and the material surface. For a natural, extern flow a heat transfer coefficient between 5-20 W/m^2K can be expected [172].
Due to the mixture between laminar and turbulent flow of the air, the definition of a valid heat coefficient is quite complex. One practical solution is to apply connective correlations: the concept is that similar geometrical surfaces were tested empirically and formula for the

determination of h and the Nusselt number Nu are given. Nu determines the ratio between convective and conductive heat flux.
The laminate and horizontal tape are modeled as a heated plate with natural, extern convection and a specific length of L = 0.5 m is applied. The incoming tape is correlated to a tilted plate with an angle of 30° in reference to the vertical axis and a specific length of L = 0.1 m. Both correlations are already incorporated in the FEM software COMSOL as standard boundary options and were utilized consequently.
For the compaction roller a correlation for short cylinders is taken from literature, where the heat flux coefficient is defined as [145, pg.4.20]:

$$h_{rol} = \frac{\lambda_{rol}}{D} \cdot Nu \tag{4.14}$$

The ratio between compaction roller length and diameter Nu is defined as 1.59, which results in a heat transfer coefficient for the roller of $h_{rol} = 3.58\,W/m^2K$.
In order to model the interface between silicone rubber sleeve and the non existing shaft, a convectional therm is introduced as substitution. As the roller is water cooled, a shaft temperature of 22 °C is assumed. The heat transfer coefficient for the shaft $h_{shaft} = 500W/m^2K$ is derived from literature [56].

Radiation is adopted on all surfaces that also implement convectional heat transfer. It is defined by the following equation:

$$\dot{q} = \epsilon\sigma(T_{env}^4 - T^4) \tag{4.15}$$

The variable ϵ describes the surface emissivity of the corresponding material, σ is the Stefan-Boltzmann constant and T and T_{env} are the surface and ambient temperature, respectively. Given that σ is small and the radiation surface area is limited, a minor impact of the radiation is anticipated.
For the surface emissivity of the materials literature values for the CFRP of 0.9 and silicon rubber of 0.98 are specified [113, 179].

Underneath the tooling and on the left and right edges of the simulation a heat flux of zero is defined (depicted in figure 4.13). At both ends of the tape, laminate and tooling a constant temperature is applied. Additionally initial values are given for all components and depending on the tool return time, temperatures for the laminate and tooling can be specified independently. It describes when the layup machine passed a specific spot last. In case for small individual tracks the laminate and tool still might be preheated.

4.3.3. Results and Validation

In order to get accurate results, the designed simulation is used to understand the influence of parameters on the temperature history in the process first. Afterwards, thermocouple measurements are conducted to tune the missing simulation parameters and proof the accuracy of the model.

Parameter Variation

For all parameters the inputs are held constant namely with a laser input power of 2600 W, a layup velocity of 125 mm/s and a five layer, unidirectional laminate. Additionally a compaction pressure of 6 bars and a total of 500k rays are implemented. For this fixed process parameter set former work has shown that full consolidation of the material is reached and thus all physical mechanisms are discoverable [153].
In the following chapter the efficiency of the laser, the laminate interlayer specific resistance, the roller specific resistance, the heat transfer coefficient of the mold and the CFRP thickness are evaluated.
In order to visualize the effects of the parameter changes on the process, all following diagrams show the temperature gradient on the surface of the laminate in $y = 0$ and $z = 0$. This corresponds to a line in layup direction (x-axis) following the exact middle of the deposited tapes. As a reminder, $x = 0$ marks the middle of the consolidation roller, between $-50 \leq x \leq 0mm$ the laminated is heated. At $x = 0$ the heated tape introduces its heat capacity before the cool down starts.

As shown in the optical model results, specular and isotropic reflection produce little scatter of irradiation especially in the geometrical setup of the layup machine. The half moon shape reflection behavior exhibited by CFRP in literature is expected to result in a significant larger energy loss to the surroundings [168, 197]. In order to account for this effect, for inconsistency of the laser diodes rated with about 2 % and unaccounted losses in the system e.g. in the tape guides, the efficiency factor η_{laser} was introduced [92]. It is a dimensionless variable that is multiplied with the laser input power.
The impact of the efficiency factor is tested by modifying it between 1.0 and 0.8 and the results are depicted in figure 4.19, it shows the temperature on the laminate surface. As expected only the heating phase of temperature curve is changed by the efficiency parameter. An increase of the efficiency shows a increase of the temperature to a maximum of $426°C$. The lowest temperature of $352°C$ is yielded with a factor of 0.8.

Figure 4.19.: **Parameter variation efficiency laser**

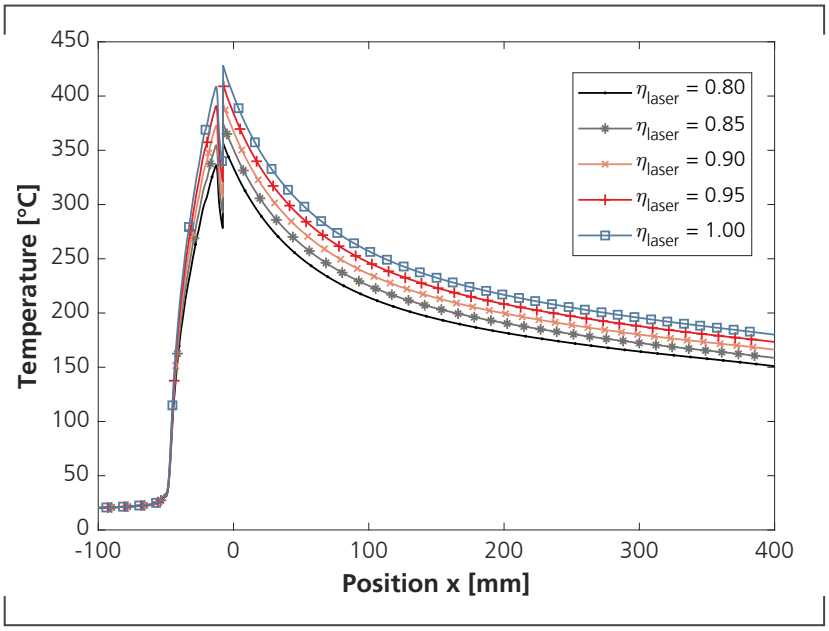

The specific interlaminar resistance was measured indirectly via the comparison of a hot press and AFP laminate and resulted in values between 0.1-0.9E-4 mK/W. The parameter is varied between 0.25 and 2.0E-4 mK/W. To illustrate the impact of the parameter its step size had to be doubled for each step.
Figure 4.20 shows that a higher interlaminar resistance results in a temperature increase in the consolidation area. Moreover the cooling between the consolidation area and x = 125 mm levels off with higher values.

In order to evaluate the influence of the thermal specific resistance between compaction roller and tape, values between 0 and 2E-3 mK/W are investigated. The results are shown in plot 4.21.
As expected the compaction roller contact thermal resistance has a limited influence on the laminate surface temperature curve when it is in contact with the tape. With an increasing resistance, the temperatures of the tape and laminate in the process area rise. Interestingly also the cooling rate is the highest with the highest resistance value. This is explainable with a notable higher tape temperature due to the missing cool down before the nip-point, resulting in a higher temperature delta and heat flow accordingly.

The influence of the tooling on the laminate surface temperature, is made visible by changing the heat transfer coefficient between 0 - 400 W/m^2K. In graph 4.22 the results are presented.

Figure 4.20.: **Parameter variation thermal resistance CF/LMPAEK**

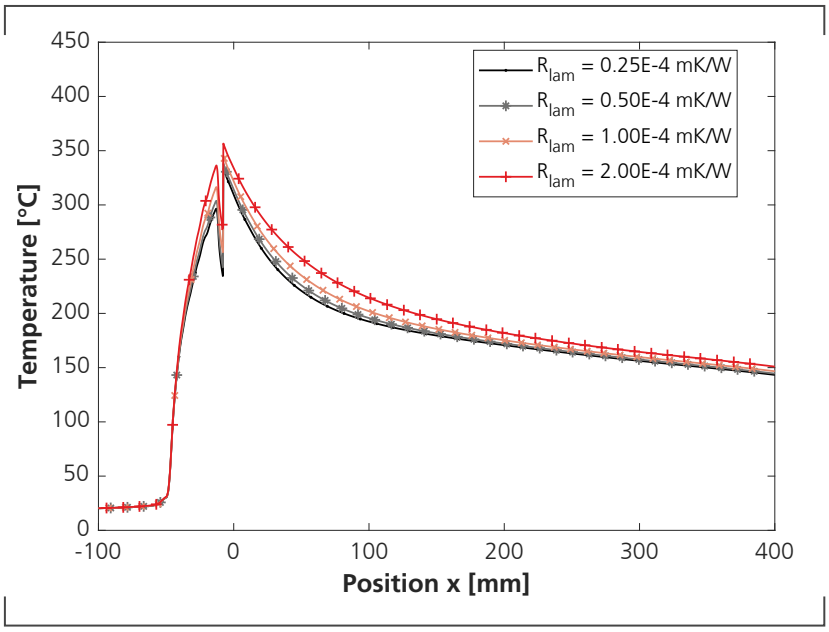

Figure 4.21.: **Parameter variation thermal resistance compaction roller**

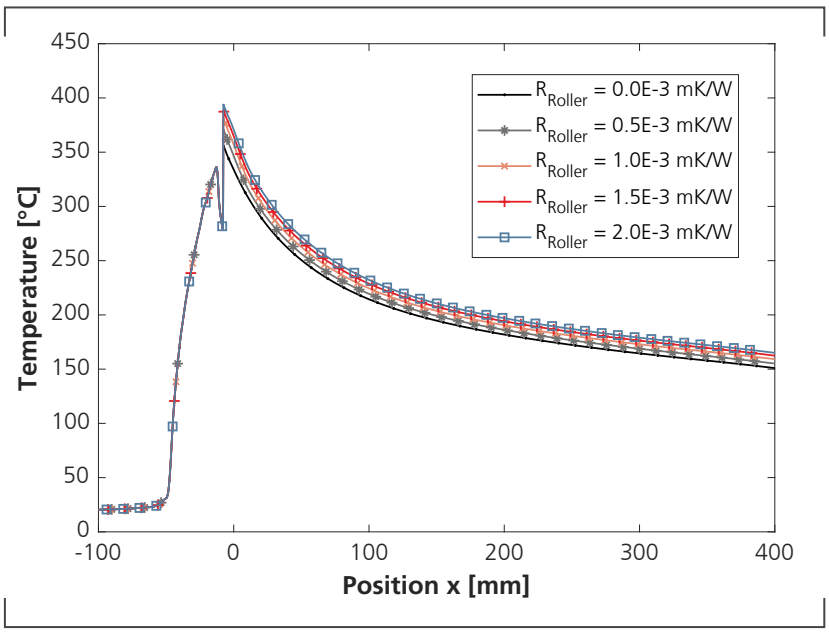

Figure 4.22.: **Parameter variation heat transfer coefficient tooling**

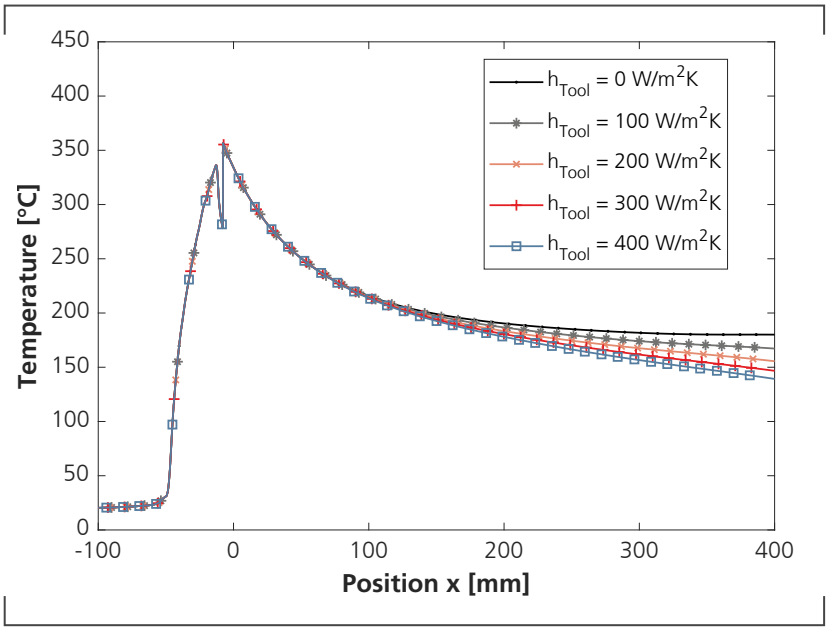

Due to the high input power and comparatively fast layup process, no influence of the mold can be seen for layer five at the heat up and first part of the cool down trajectory. Starting 100 mm after the consolidation roller the temperature profiles start to diverge. This is attributed to the fact that through thickness heat transfer starts to reflect on the highest ply at this point. It is noticeable that higher heat transfer coefficients result in a lower end temperature at position x = 400 mm. However, with increasing values the resulting temperature converges asymptotically.

For the laminate no change of the tape thickness is assumed in the simulation. The degree of tape layer flattening depends on matrix flow and reconfiguration of the fibers. To check the influence of the thickness evolution the ply thickness of the laminate is varied between 0.12 and 0.18 mm, the latter being the thickness of the unprocessed tape. The results are depicted in figure 4.23.
It can be seen that with declining laminate thickness the maximum temperatures rise. However, the biggest effect is visible for the free cooling after the consolidation roller, where the cooling rate flattens for a thinner laminate and linear cooling starts earlier.
Cross-sections of T-AFP laminates were measured using a digital microscope (Keyence VHX 5000), to quantify the flattening. As a result a laminate thickness of 0.177 mm was determined and showed that the flattening of the CF/LMPAEK is negligible, as it was assumed in the simulation design.

Figure 4.23.: **Parameter variation tape thickness laminate**

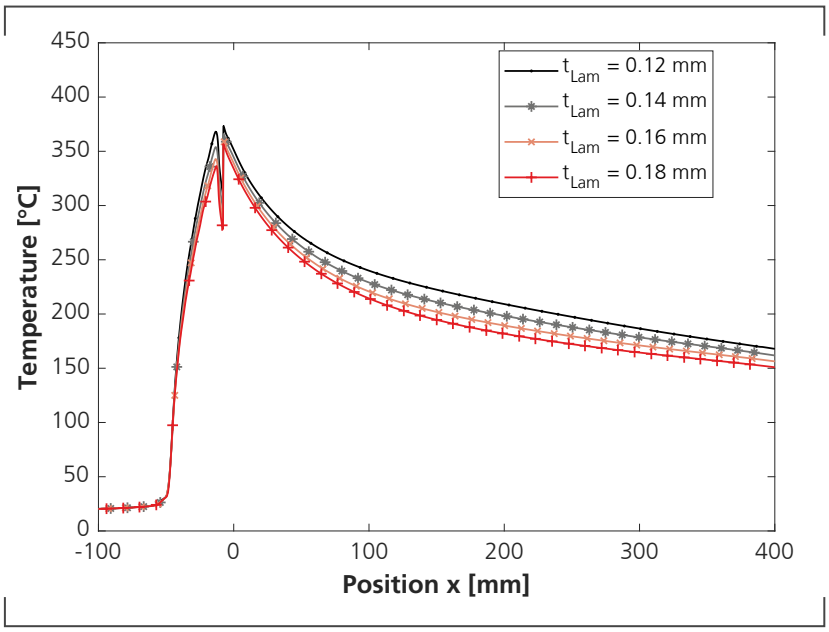

Experimental Validation

It was aimed for a precise, error-resistant evaluation method of the occuring process temperatures. Therefore thermocouples measurements were conducted using type K sensors, as they do not require any further adjustment to the material.
To reduce the introduced disturbances fine wire cables with a diameter of 20 μm were applied and the sensors are welded into LMPAEK neat resin foil. This has certain advantages: on one hand the sensors are isolated and can be fixed readily on to the CFRP, using an ultra sonic welding sonotrode (Branson 200 LPe). On the other hand no foreign materials are incorporated in to the composite, which helps to reduce measuring errors at the tip of the thermocouples and in subsequent layers.
The data is recorded with an external data logger LR8400 supplied by Hioki. It is capable of logging with a frequency of 100 Hz, this guarantees a high sampling rate especially important for higher layup rates to limit measure point distances.
In order to acquire a precise position to every temperature value, encoder signals are fed into the data logger and linked to the measurement data. For this purpose the KUKA technology option fast send driver (FSD) is used. It sends virtual encoder signals when the compaction roller has moved a given distance. Together with a known start position this allows for an exact localization of the measurement values.

Table 4.4.: **Overview thermocouple measurements**

Trial	Position	Measurements
Layer Temperatures	Layer 1 / Track 1,2	15
Layer Temperatures	Layer 1 / Track 3	7
Layer Temperatures	Layer 5 / Track 1,2	15
Layer Temperatures	Layer 5 / Track 3	7
Layer Temperatures	Layer 10 / Track 1,2	15
Layer Temperatures	Layer 10 / Track 3	7
Boundary Effects	Layer 10 / Track 1,2	15
Boundary Effects	Layer 10 / Track 2,3	15

For the process temperature evaluation, tracks with three tapes each are laid resulting in a total width of approximately 41 mm. The aluminum mold used is coated with a glass fabric to distribute the vacuum and a polyimide film on top. The latter provides the required adhesion for the CFRP. Individual measurements are conducted on the first, the fifth and the tenth layer, to investigate the impact of the mold.
For each ply two test specimen are produced: on the first test specimen 7 and 8 thermocouples are welded onto the center of the tape on the right edge and on the middle tape, respectively. For the second test specimen the tape on the left is instrumented using 7 thermocouples as well. An overview of the all experiments is given in table 4.4. The sensors are positioned starting 150 mm after the tape start to omit non-recurring effects. Equally every thermocouple is placed with a distance of 40 mm to the next, to avoid interference between the sensors. Figure 4.24 gives an overview of the thermocouple placement for these two trials, with all positions for the first run in red and the second run in blue.

In order to increase the data resolution in tape width an additional setup was tested: on layer 10 the trials were repeated. However, the thermocouple instrumentation was changed to 8 thermocouples with a distance of 3 mm to the edge of the right tape and 7 on the middle tape, using a distance of 17 mm to the right stripe edge. It can be imaged as a complete shift of the red thermocouple positions in figure 4.24 to the track border. A second run was performed mirrored on the opposite, left track edge.
All measurement above are done with the same parameters as mentioned in the parameter variation: 6 bar compaction force, 2600 W laser power and a layup velocity of 125 mm/s. Due to the fact that crucial parameters such as laser efficiency are tuned with the results, validity for different input parameters have to be checked. To achieve this, input power is varied between 2300, 2450 and 2600 watts and compared to the tuned simulation.

Figure 4.24.: **Experimental setup thermocouple measurements**

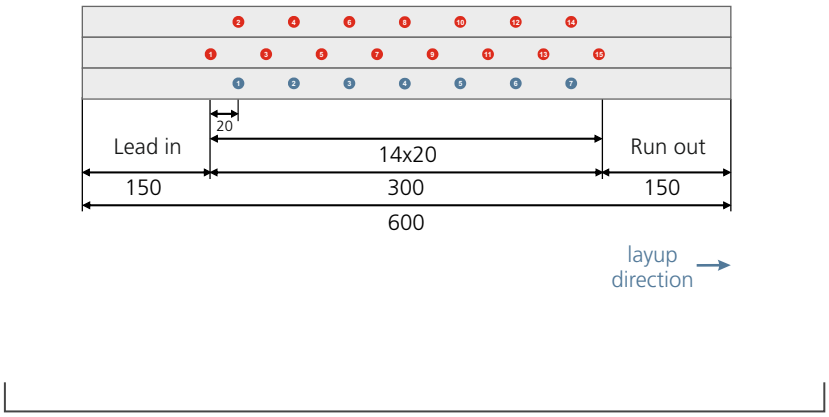

All measurements combined give a total of 120 samples, sufficient enough to compensate for relatively large scatter that is expected for this highly transient process. A sample measurement setup is depicted in image 4.25.

Figure 4.26 shows the measured and simulated temperature curves on the laminate surface. As no significant difference between the measurements on ply 5 and 10 was detectable, all measurements done in the middle of the central tape are pooled.
The solid black line depicts the mean temperature of all samples, whereas the light gray lines mark the highest and lowest temperatures measured at a specific position. The simulation result is highlighted with a dashed, red line. For recollection the melting temperature of LMPAEK is indicated as horizontal, dotted, blue line.

For the measurement data a steep temperature increase between a x value of -50 mm to the consolidation roller is visible. A mean maximum temperature of 342°*C* is reached at the nip point, with a spread of 48 *K* between minimal and maximal temperature measured. Despite this relatively large spread the standard deviation of 15.8 *K* shows that the measurement method is reliable.
Underneath the compaction roller the cooling rate is the highest and cools down the laminate under the melting temperature. Behind the roller the laminate cools down non linear until approximately 250 mm, form this point on linear behavior can be approximated.

Using the parameter variations results of the previous chapter and the measured temperature profile, the simulation was tuned manually. The final parameters can be found in

Figure 4.25.: **Evaluation setup thermocouple measurements**

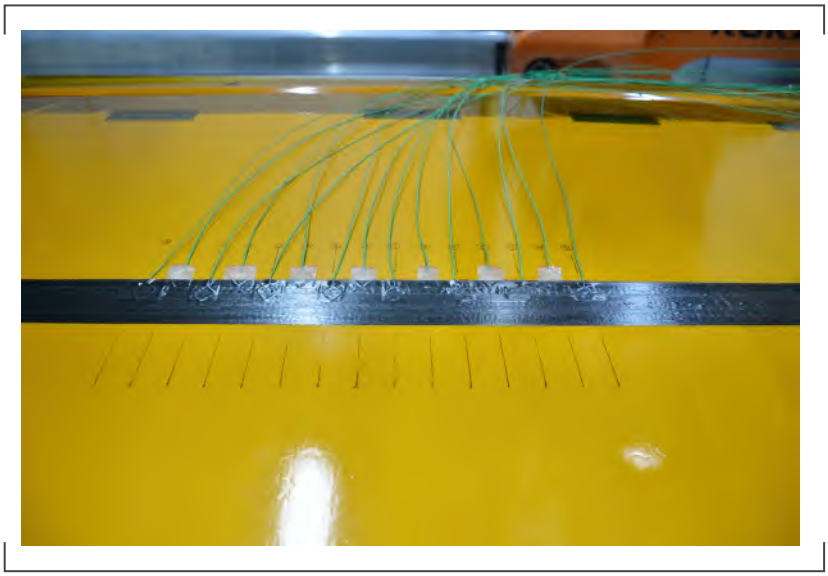

Figure 4.26.: **Results measurement and simulation temperature laminate surface**

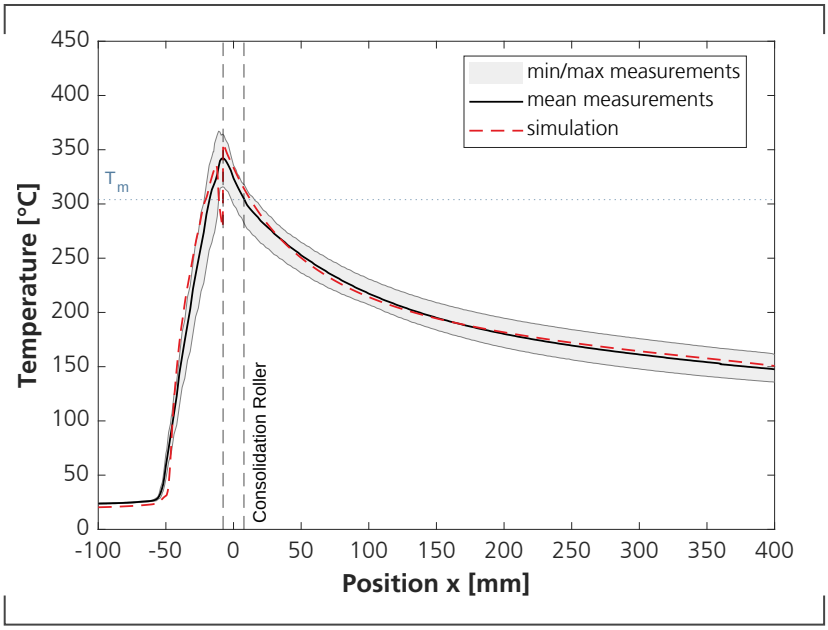

Table 4.5.: **Simulation parameters**

Parameter	Unit	Value
η_{laser}	1	0.8
T_{env}	$°C$	20
R_{lam}	mK/W	2E-4
R_{roller}	mK/W	0.0
h_{tool}	W/m^2K	250

table 4.5.
For the heating phase a good conformance between measurement values and the simulation can be seen. Heating of the laminate begins slightly after the measurement and follows the maximum values. Before the nip point a sharp decline in the simulated temperature profile is visible, where the consolidation roller casts a irradiance shadow. This effect is not measured by the thermocouples. One possible explanation is that the sensors are to inert due to their own heat capacity.
The maximal temperature of the simulation is 14 K (4 %) higher than the measured mean values. However, it is still within the range of the measured standard deviation.
The cooling behavior of the consolidation roller matches the measurements and the cooling curve behind it differs only slighty from the mean measured temperatures.
In general a good agreement between simulated and measured laminate surface temperature curves is ascertainable.

For the temperature development in tape width, seven different positions on the tape were measured. The temperatures for the moment directly beneath the compaction roller (position x = 0 mm) can be found in diagram 4.27. The measurement points are marked as black circles whereas the simulation results are given as red, dashed line. The grey area defines the lowest and highest values measured, based on illustration above.
For a wide area of the tape the temperature is homogenous with values around 330$°C$. The mean standard deviation of 6.7 K is comparatively low. Remarkable is that the measurements on the tape edges show a significant temperature drop. This indicates that the laser alignment was not optimal or a larger focal point would be beneficial.
The comparison between measured and simulated values shows that they are almost identical. An exception can be found at -14 mm on the y-axis, where a difference of approximately 20 K to the mean and 10 K to the lowest value measured is observable. Ultimately there should be little to no difference to the measurement on the opposite side of the tape, therefore a measurement artifact is assumed.

Figure 4.27.: **Results temperature laminate surface in tape width**

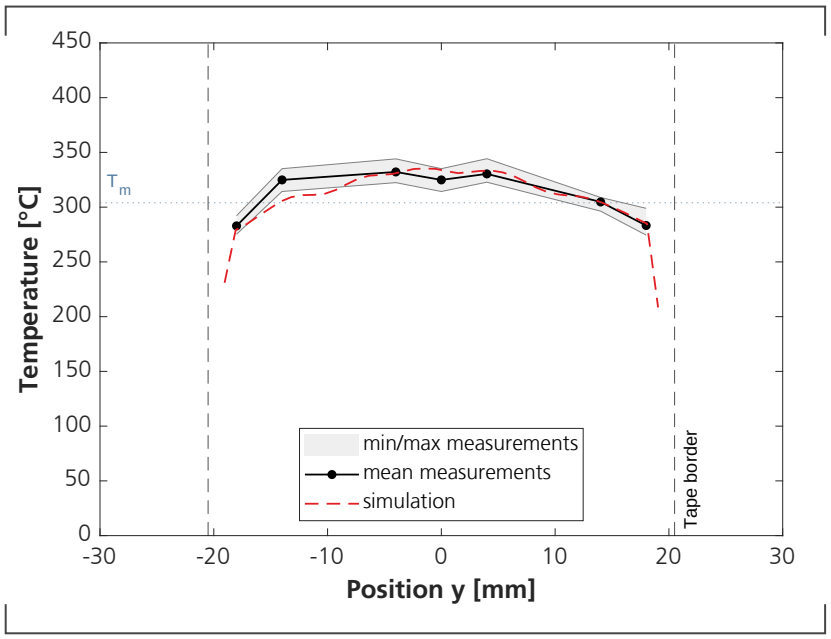

An additional validation was performed by varying the laser input power. This is particularly relevant to check if the selected laser efficiency is applicable for all simulated power levels. Due to the relatively small processing window of the material the variation was performed in 150 W steps. The results are depicted in plot 4.28. For every power level the dashed, lighter curve marks the simulation and the solid, darker curve the measurement. To improve legibility the power levels pairs do have a similar color and the same markers applied.
From the diagram it is evident that the maximum temperature and cooling behavior in the consolidation zone is simulated correctly for changing power levels. A divergence between measurements and simulation is emerging in the free cooling zone of the tooling. However, since the same deviation can also be seen at 2600 W, the power level the simulation was tuned for, this is accounted to a disturbance caused by a deviation in first layer quality, likely an insufficient vacuum or slightly thicker glass fabric.

In general the simulation showed that it can model the T-AFP process correctly and in high detail. With a computational time of approximately 3 hours and 15 minutes per parameter set it is apparent that the model has to be reduced for the model based control.

Figure 4.28.: **Results measurement and simulation power level laser**

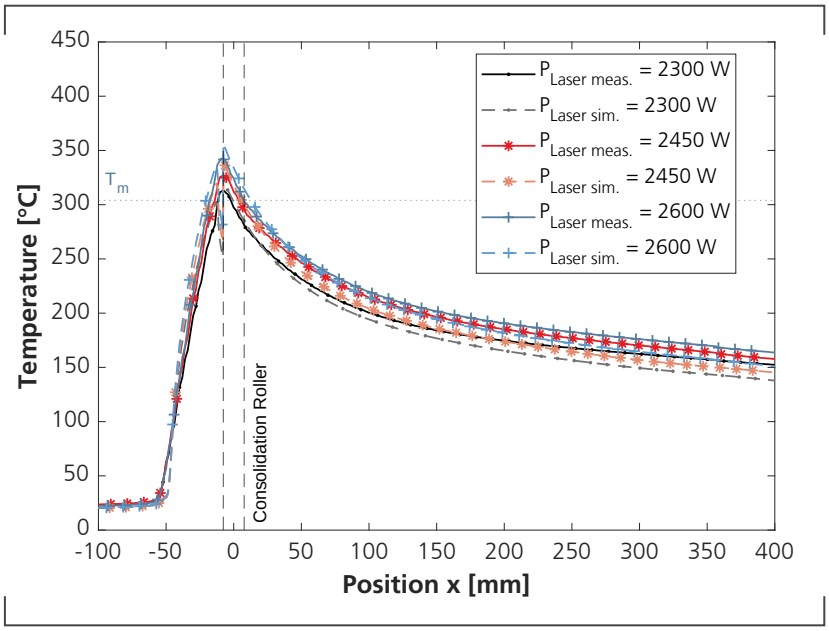

5. Model Predictive Controller

5.1. Introduction

This chapter's aim is the design and validation of a Model Predictive Controller for the process. In order to build the MPC, two main building blocks are required: an efficient, fast computing simulation and a well tuned internal feedback control.
For the former, it is necessary to perform a model order reduction, due to the fact that the three-dimensional FEM simulation takes about 30 minutes for the heat transfer alone. Therefore, three different approaches are tested, namely the mathematical reduction to a state space model, the manual reduction to a lower dimensional FEM simulation and the implementation of a lumped element model.
The chapter starts with the identification and optimization of the current control system, including the hardware components. Then the model order reduction approaches are detailed and the prediction accuracy is determined.
The next step is to design and implement the MPC using the model reductions. Performance is maximized and a cost function plus non-linear constraints are developed to feed the optimizer. The chapter concludes with a benchmark between the two process models, which are compared to each other and to the standard temperature controller. For this purpose, two different layup experiments are carried out, covering all the main planned disturbances that occur in T-AFP: thickness, fiber orientation, laminate temperature and velocity changes.

5.2. Current Control System

5.2.1. Hardware

The current temperature control adjusts the laser power between 0 and 6000 W, at the same time the laser angle of incidence can be adjusted to keep the tape and laminate

temperature in equilibrium. Temperature is measured via an infrared camera with a resolution of 168 x 128 pixel, supplied by Automation Technology GmbH. The system works with an emission coefficient of 1, which yields repeatable yet uncalibrated, higher values, within an accuracy of ± 2 %. They are gathered with a frequency of 60 Hz.
Image processing is done row-wise, ignoring the hottest pixels in order to minimize the effect of local overheating and measurement inaccuracies. For every row a total of 10 values are calculated to one mean temperature, the highest row value is used for the power control.
Laser angle adjustment is performed at significant slower cycles and the laser position is adjusted incrementally in a way that the highest temperature stays in the nip point region.

All signal control functions are realized with a Beckhoff CX2040 industrial personal computer (IPC) using a TwinCAT programmable logic controller (PLC). This multi-core system implements two different task cycles. All functions related to the layup machine are computed using a task with 2 ms execution time. The temperature control system runs at a 30 ms task.

5.2.2. Control System

The temperature control system is designed as a PI controller (for details refer to section 2.3.2). As depicted in schematic 5.1 the temperature control system is composed of three input elements that can be defined via graphical user interface: a constant offset that is given in watts B_{off}, a proportional factor that is multiplied with the current layup velocity k_v and a constant scalar B_v, all contributing to the feed-forward control part of the system. The feedback controller is implemented as integrator that is combined with a dead-time in order to delay its contribution at the start up. The delay is designed to prevent overheating while the tape is transported underneath the compaction roller.
The controller is programmed to maintain the last velocity reading obtained from one of the guide pulleys after the tape cut, to enable a steady laser power output until the end of a track. Inputs for the control are the set temperature w the velocity measured with an encoder at the tape v and the control parameters B_{off}, k_v and the integral action time T_I. The feedback loop for the temperature is measured with the infrared sensor discussed in section 5.2.1.

As the control was delivered as black box, parameters had to be determined first to provide a transparent initial state of the control system. This is accomplished using step responses for the integral part and parameter variations for the proportional factor. The gain factors are described by the following equations:

Figure 5.1.: **State of the art control concept**

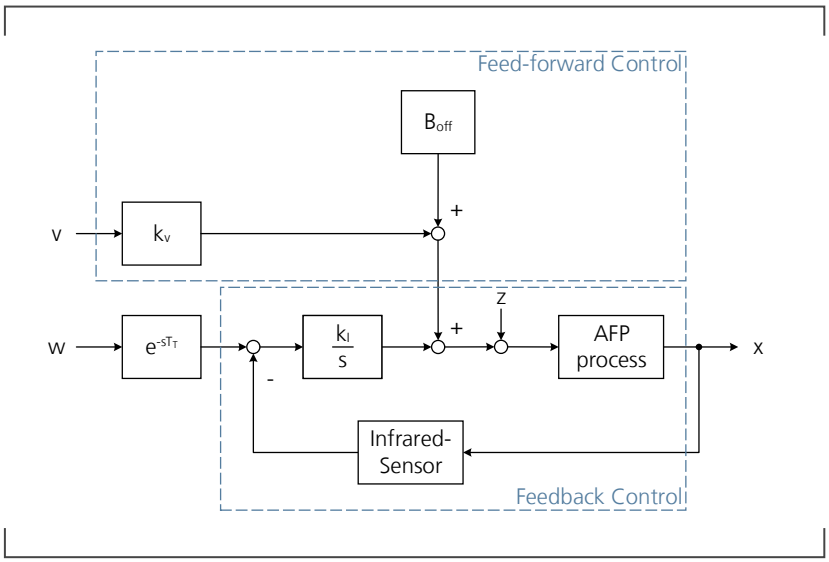

$$k_V = B_V \cdot \frac{6}{100} \tag{5.1}$$

$$k_i = \frac{k_V \cdot v + B_{off}}{1000} \tag{5.2}$$

5.2.3. Analysis and Improvement Temperature Control

The as-is control described in the previous section is analyzed via test runs on a single layer laminate of CF/LM-PAEK. Eight tracks consisting of three tapes are deposited with a track length of 800 mm. The set temperature is adjusted to 500 °C. As a reminder it has to be stated that all temperature values are measured relatively and do not resemble the actual temperature in the process. The temperatures are measured with the existing infrared camera, using the evaluation method described in section 5.2.1. Control parameters were optimized for the material before hand, to acquire an optimum temperature gradient. The dead-time T_T was set to 0.72 s, T_I to 0.05 s, B_V to 1.8 Ws/mm and B_{off} to 1750 W.
All eight measurements are represented in dark grey (see plot 5.2). The shaded area shows the distribution of temperatures and the set temperature is depicted as dashed black line. All blue lines represent the resulting laser power output in watt given by the control system.

Figure 5.2.: **State of the art controller performance**

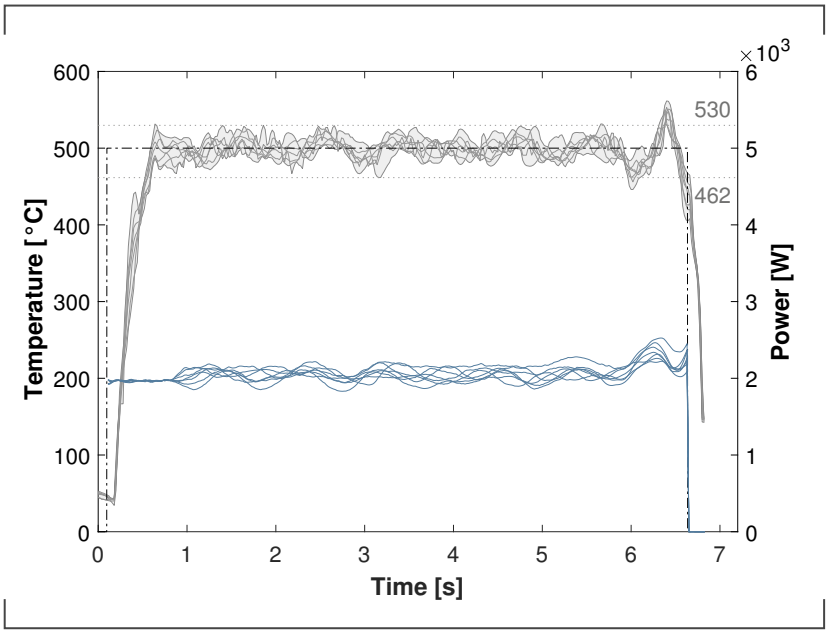

Several observations can be made regarding these results: at layup start the laser power is almost constant due to the dead-time which deactivates the integrator. Small deviations originate from the velocity measurement as the total power output is composed by the constant and velocity dependent control parts in this instance. Within this heating phase the plant shows first an inertia and reaches the set temperature after approximately 0.6 s. As soon as the integrator contributes to the power output, it is adjusted to compensate for the temperature differences observable as a wavy output. It can be analyzed that adjustments do come late and overcompensate. This results in over- and undershootings in the temperature up to approximately $\pm$ 30 K, that occur in almost equal proportions. In the area of undisturbed material deposition (between 1.5 and 5.5 s) temperature value fluctuation between 462 °C and 530 °C was observed.
After the tape is cut, it is not guided closely along the compaction roller anymore and flips onto the laminate. In this area the control shows high deviations from the set temperature. However the quality and correctness of the measurement in this phase is unclear.

Considering these results several improvements are reasonable: in the area of tape run-in the set temperature is modified via a PT1 filter, this allows for a faster response of the variable control elements, without temperature over-shootings. For the remaining initial inertia of the plant the existing dead-time is maintained. However, it is expected to be a lot shorter and thereby decreases the likeness of temperature over-shootings at the layup start additionally.

Figure 5.3.: **Enhanced temperature control concept**

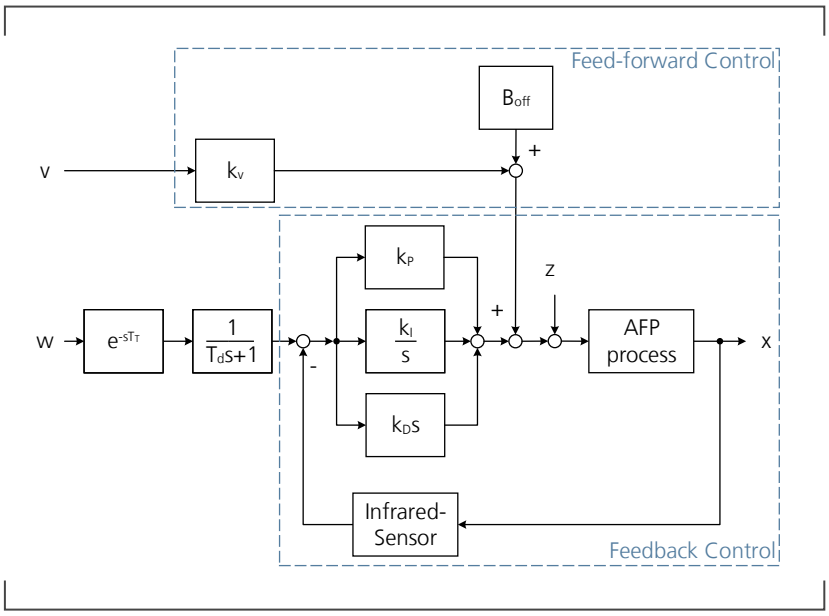

During tape deposition reaction of the as-is control has proven to be too slow, a more responsive behavior is introduced by an additional derivative term. In order to reduce noise, against which the new controller is susceptible, the tape layup velocity is directly retrieved from the robot instead of the tape encoder. The resulting block diagram is presented in figure 5.3.

The parameters of the adjusted control where optimized for trials described at the beginning of this section. Dead-time duration could be reduced to 100 ms, whereas the PT1 time constant T_d was set to 175 ms. For the PID controller best results were found for K_P at 10.0, T_I at 0.3 ms, T_V with 0.1 s and T_d with 0.125 s. All other parameters where held constant.
These settings where used for identical eight measurements on a first ply of CF/LM-PAEK and the results can be seen in figure 5.4. The figure is organized similar to the preceding chart 5.2, where the set temperature is a dashed line, grey are the measured temperatures and blue resemble the power outputs.

In general it can be seen that the control effort has increased with noisier power levels for all measurements. However, since laser power adjustments are relatively inexpensive and responsive control is aimed for, this is considered acceptable. During undisturbed layup in the time from 1.5 to 5.5 s tolerances between 478 °C and 518 °C can be observed. This corresponds to a error reduction of 58 % compared to the as-is control.

Figure 5.4.: **Enhanced PID controller performance**

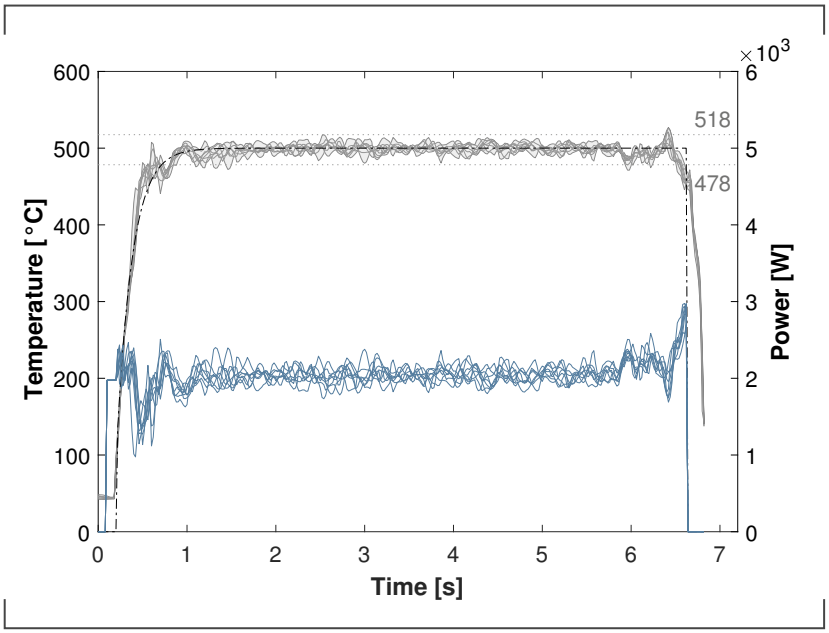

At layup start, the laser power is controlled by the velocity based and constant offset of the control. After the dead-time terminates both the PID controller and PT1 filter for the set temperature boot. This results in a much smaller difference between set and is temperature and avoids over compensation of the PID. As a result the temperature follows the set temperature closely.
Due to the new layup speed values that are provided directly by the robot, an extra procedure for the tape end is not necessary anymore. The faster controller keeps the peak temperature at track end at a maximum of 527 °C, approximately 35 °C under the old value.
Table 5.1 gives a brief comparison between the as-is and enhanced control with maximum reached values, the tolerance range and the integral of squared errors. The latter are commonly calculated as [70]:

$$ISE = \int_{t_0}^{t_s} e(t)^2 dt \tag{5.3}$$

With t_0 as control start point and t_s as settle time after a step response. Due to the difficulties to implement a distinct disturbance step in the T-AFP process the complete control duration was taken into account. It can be seen that the error is reduced by an order of magnitude. However, the set point was changed for the control start which gives

Table 5.1.: **Comparison as-is control versus enhanced PID control**

Control	T_{max} [°C]	Tolerance [K]	Mean ISE [K^2]
as-is control	561.5	±34.0	$3.92 \cdot 10^7$
PID control	526.9	±19.6	$1.08 \cdot 10^6$

the PID controller a minor advantage.
For all following work in this thesis the enhanced PID controller is used and the experiments are benchmarked against this controller.

5.3. Model Reductions

5.3.1. State Space Model

As a first concept the usage of state space models was evaluated. The used COMSOL finite element software offers a direct export of a linear state space model, representing the thermal model, to MATLAB. This large model can be analyzed and reduced using mathematical models e.g. modal truncation or Krylov subspace methods [63, 104]. Which, described simplified, identify non-characterizing states and delete or combine them.
The thus derived model could be directly fed into a MPC afterwards, which may be developed in MATLAB also. Due to the fact that the same interface exists between MATLAB and the control system of the layup machine (Beckhoff TwinCAT) a semi-automatic, closed software loop could implemented. This would render changes to the model and direct adaption in the machine effortless.

Since T-AFP is a highly transient, non-linear process it is ambiguous if a linear model could yield a good estimate of the actual process temperatures. Evaluation of the state space model export was conducted using a simple cuboid to validate the necessary functions. In the work Schijndel the principal procedure to obtain a state space model is described [154]. Using this approach main functions needed for the model were tested in order to evaluate if a sufficient model is obtainable.

The state model size increases with every element that is added. In order to get a manageable model sparse matrices are exported and the rod was reduced to a two dimensional

rectangle. With these adaptions a model could be obtained.
As one major non-linearity the mechanical properties were investigated. It was shown that the temperature dependent materials can neither be linearized by the software nor manually but have to be set constant.
In order to simulate a fast reoccurring layup machine the temperature of laminate and roller should be adjustable. It was found that the state space model needs a initial state of zero and therefore the laminate temperature could not be implemented in the state space model.
As final investigation the layup velocity was introduced to the simplified model. Since this parameter is decisive for the overall temperature its implementation is crucial. However, the linear state space model was not able to map the results correctly.

In conclusion an array of state space models representing different laminate thicknesses, velocities and base temperatures would be needed to map the process temperatures correctly. Due to the cumbersome adjustment of such a design and its close resembles of a mere look up table, it was decided to not pursue this approach further.

5.3.2. 2D Finite Element Model

In order to reduce the computational time of the FEM simulation, a manual dimensional reduction is conducted with the goal to keep the results of the reduced model as close as possible to the originals.
In this two dimensional approach the tape width is disregarded, however to convert the input boundaries obtained by the full simulation, e.g. the laser power, a total tape width of 38.1 mm is assumed.
The geometry is simplified with a circular tape feed-in and an adjacent consolidation area underneath the roller. In tape length direction (x-axis) the system is minimized to cover only critical components: the laminate irradiation length (36 mm), the shadow before the nip point (4.25 mm) and consolidation area (15.4 mm). All lengths are derived from the optical and mechanical model using a irradiation threshold of 10 % and 6 bar compaction pressure (refer to chapter 4). An inlet and outlet area, both extended with an additional infinity area, are applied to compensated oscillations. Their combined length is 20 mm.
The simulation height in y-direction is defined by the irradiation length of the tape (14 mm), the tape nip point shadow (14.7 mm) and the variable laminate height, depending on the number of plies that are simulated. In parallel to the laminate a 10 mm inlet is added. According to the geometrical setup of the machine, a tape feed-in angle of 60° is implemented. Figure 5.5 gives an overview of the simulation geometry, the tape thickness is tripled in the graph in order to increase visibility.

Figure 5.5.: **Layout 2D FEM Simulation**

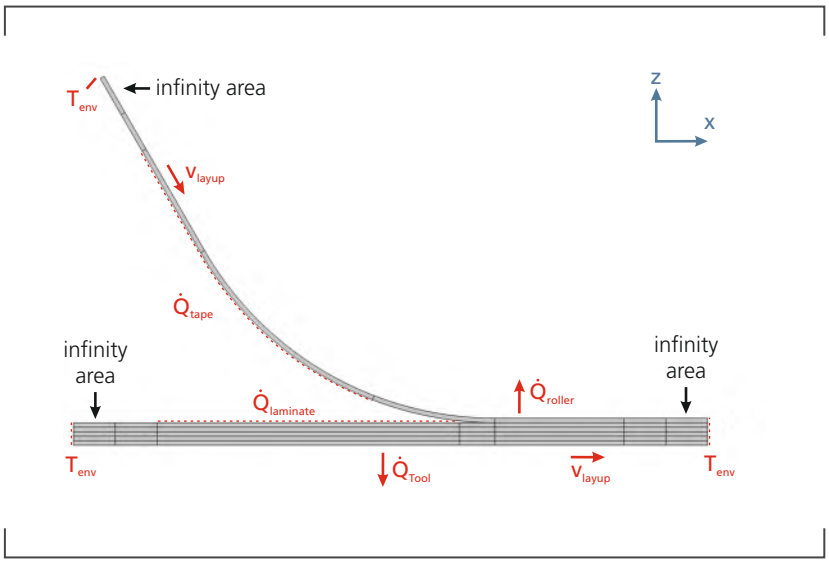

As a result of the reduction several boundaries have to be modified: the consolidation roller is substituted as heat flux with coefficient of 325 W/m^2K. During layup the roller heats up and acts as a thermal mass, this is especially true for lower layup velocities. To account partially for this effect, a roller silicone rubber temperature of 120°C is adopted.
The tooling is reduced to a heat flux with a coefficient of 250 W/m^2K, similar to the first ply implementation in the three dimensional model. Convection and radiation are applied on all open surfaces and modeled using one single heat flux with a coefficient of 15 W/m^2K with an ambient temperature set to 22°C.
The laser power is deployed directly onto the irradiation edges of the simulation, using a constant power. A share of 55 % and 45 % of the power is directed to the tape and the laminate, respectively. This is a slight shift to a more equal distribution in the amount of 5 %, compared to the full simulation. This effect is accounted to the missing heat conduction, originating from the laminate adjacent to the current layup. Due to the larger irradiance of the laser these boundaries are heated up as well in reality. However in the 2D simulation they are considered as part of a 9 % laser power loss, ascertained by evaluating the irradiance on all surfaces around the tape and laminate in the full simulation.
Unchanged adopted are the efficiency of the heat source and the laminate resistance. For integration in the MPC a MATLAB wrapper for the simulation was designed. Using LiveLink the model parameter and geometry can be changed and the solver is triggered.

The reduced model is compared to the full model using 24 different parameter sets: covering layup velocities between 25 and 250 mm/s in 50 mm/s steps and using power levels between 1000 and 5000 W in steps of 800 W. These simulations are repeated for

Figure 5.6.: **Comparison reduced 2D with full simulation for 5 layers**

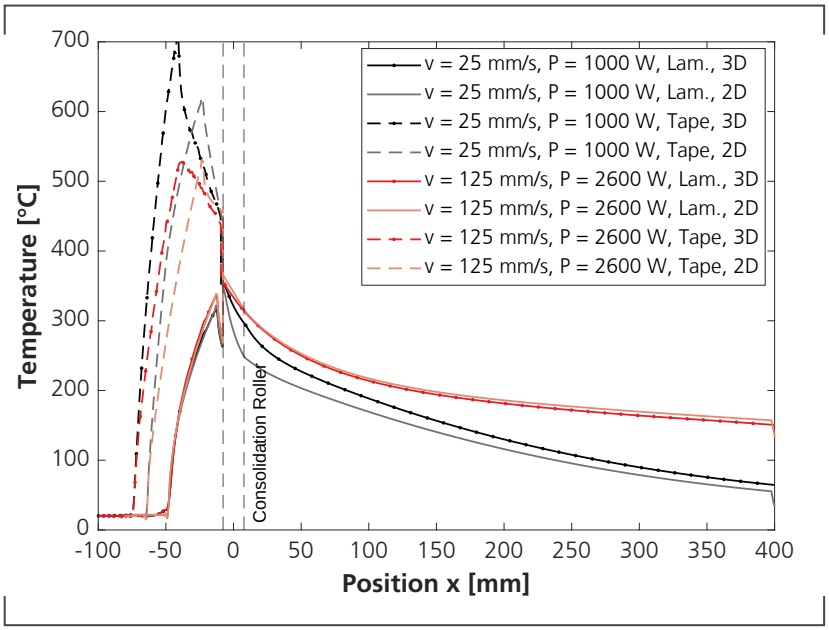

laminates with 1, 2, 3 and 5 layers. Figure 5.6 shows two example sets which show characteristic elements on which all major findings can be explained.
Displayed are the temperature of the laminate surface (solid) and the tape (dashed). Two different parameter sets with 25 mm/s and 1000 W laser power (black and grey lines) and 125 mm/s and 2600 W laser power (red and orange) are depicted. The reference 3D results are shown in black and red respectively with an additional point marker. Whereas the 2D simulation results are depicted in orange and grey. All individual results can be found in appendix G.

For all layup velocity and power combinations between 125 mm/s and 250 mm/s the reduced 2D model shows good compliance regarding the maximal laminate and tape temperature. The combined nip point temperature shows a sufficient fit with a maximum deviation of $\pm 10°C$. Whereas the laminate temperature gradient follows the reference closely, the tape starts to heat later and cools of faster. This can be explained with the simplified irradiation area applied in the 2D model. Especially the complex reflection behavior in the curvature is modeled in greater detail in the full model, by means of ray tracing.
For parameter sets with slower layup velocities, the laminate heating and nip point temperature are still modeled accurately. However, starting at a velocity of 75 mm/s the cooling under the compaction roller is diverging. This can be accounted to the missing compaction roller that gains influence at slower layup speeds.

Whereas the maximum tape temperature is modeled correctly for 75 mm/s, a considerable difference of 100°C is depicted for a layup speed of 25 mm/s. In general it can be concluded that the 2D FEM model shows good accordance to a majority of the tested parameters, reduced accuracy can be found for very low layup rates though.

5.3.3. Lumped Element Model

Since the reduction of the FE model is only possible to the degree shown in the last section, a more radical reduction approach is investigated: As shown in chapter 2.2 the simplest model for AFP is a one dimensional heat transfer calculation, that ignores in-plane heat conduction and solely focuses on temperature dissipation in laminate depth.
The resulting temperatures are calculated at specific, process relevant points, that will be used for the control of the process. These are namely: the highest temperature after laser heating of the tape and laminate, the temperature at the nip point as well as after the consolidation roller. Layup velocity is implemented as time span for laser heating and cooling only.
In order to reduce the individual model elements, the Lumped Element Method (LEM) is used, an electrical analogy to the heat transfer processes. A brief introduction to the method is given first, before the individual model elements are defined. Similar to the reduced finite element model, the results are compared to the temperature gradients of the three-dimensional multi-physics simulation.

Analogy Heat Transfer to Electric Circuits

Thermal systems show a high similarity to electric circuits, if defined accordingly. Based on Ohm's law this representation allows for significant simplifications of thermal processes by combining resistances, connected in serial or parallel, and individual capacities. If the temperature in a body is assumed homogenous one capacitor is sufficient to describe its behavior, hence the method is called lumped heat capacity method.
The thermal system is described by resistors and capacitors (RC elements), where heat fluxes triggered by a temperature difference can be attributed to a electrical resistance. The capacitors on the other hand, add a time dependent charge and discharge behavior and thus describe the dynamic system. A combination of several RC elements are used to describe complex systems. The correlations between thermal and electric parameters are shown in table 5.2.[76, 110]

Table 5.2.: **Overview thermal-electric analogy**

Thermal			Electric		
Temperature difference	ΔT	[K]	Voltage difference	ΔU	[V]
Heat transfer	$\dot{Q}$	[W]	Current	I	[A]
Thermal resistance	R_{th}	[K/W]	Electric resistance	R	[Ω]
Thermal conductivity	λ	[W/m^{2}K]	Electric conductivity	σ	[1/ΩK]
Heat capacity	C_{th}	[J/K]	Electric capacity	C	[F]

Two different thermal resistances for heat conduction $R_{th,\lambda}$ and convection $R_{th,\alpha}$ can be described. They are defined as:

$$R_{th,\lambda} = \frac{L}{\lambda A} \tag{5.4}$$

$$R_{th,\alpha} = \frac{L}{\alpha A} \tag{5.5}$$

Where L is the thickness of the material, A the area of the boundary, λ the heat conductivity and alpha the heat transfer coefficient. In order to determined thermal contact resistance, the same formula is used equivalently, with a specific contact conductivity. The heat capacity is defined with the known interrelationship: multiplying the specific heat capacity by the mass of the body.
The mesh and junctions laws of Kirchhoff do apply in this regime, which means the sum of the heat fluxes in a junction adds up to zero and the total temperature difference in a mesh is zero as well:

$$q_c - q_r = 0 \tag{5.6}$$

$$T_c - T_r = 0 \tag{5.7}$$

Using these formulas, the heat distribution for one specific process point can be described. Therefore a system of RC elements is designed first. Subsequently all mesh and junction equations can be determined, which deliver a state description for all elements in the system.

One important assumption for the lumped capacity model is that the thermal resistance for convection is high, compared to the conduction in incorporated material, meaning the problem is driven by heat conduction. This is confirmed using the so called Biot number, which need to be smaller than 0.1. It is defined as:

$$Bi = \frac{R_{th,\lambda}}{R_{th,\alpha}} \tag{5.8}$$

In order to evaluate the methods applicability the cooling behavior under the compaction roller is examined, due to the fact that the highest convection takes place here since the roller is modeled as convection. For the calculation a mean heat transfer coefficient for the CF/LMPEAK of 0.77 W/mK was assumed. The area of the boundary is determined using the width of the tape (38.1 mm) and the length of the consolidation area at 6 bar pressue (15.4 mm). For the convective heat flux the roller heat transfer coefficient used in the two dimensional FEM simulation was used (325 W/m^2K).
With these inputs a Biot number of 0.065 is derived and the model is therefore applicable.

Design Lumped Element Model

In order to model the relevant heat transfer processes using the lumped element model, a system of four sub-elements is designed: the tape heating, the laminate heating, the cooling behavior under the roller and open cooling. Each model calculates the relevant temperatures for the laminate and tape respectively. An overview is given in drawing 5.7, the red dots indicate the location of the individual temperatures simulated.

The outputs of the tape - and laminate heating models are joined as one nip point temperature. It is used as the input value for the roller cooling model. Subsequently its output provides the input temperature for the open cooling model. However, this is primarily needed to determine the incoming laminate and tooling temperature for rapid repasses or comparatively small CFRP layers, respectively.
It is important to mention that this one dimensional model calculates the through thickness heat dissipation for the given configuration in each sub-model. Depending on the layup velocity each sub-model is simulated for a given time, before the output temperature is transferred as initial state to the downstream model. Thus the mass flow is modeled indirectly using output temperatures.

One of the inherent inaccuracies of the lumped capacity method, is the assumption of a homogenous temperature per element. For simulation of the process in general, this could

Figure 5.7.: **Principal sketch lumped element model**

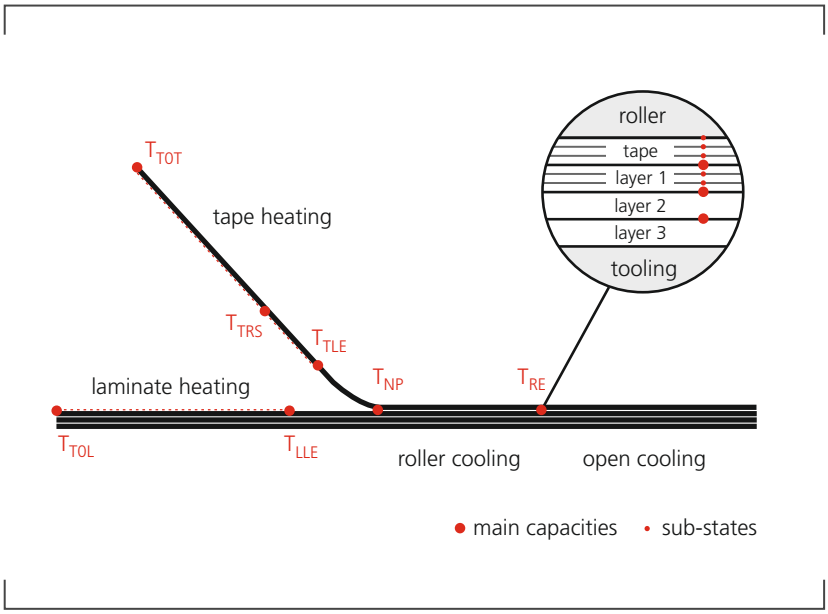

be tolerated. However, given the fact that the temperature is measured on the surface of the laminate and tape, this effect has to be compensated.
The approach chosen is shown schematically in the detailed view in figure 5.7. Instead of using one element per layer, several elements per layer are used. In the picture three elements for the tape and roller are indicated, and only one for layer two and three.
An increasing number of elements per layer increase the accuracy of the surface temperature, due to the smaller linearization effects. Simultaneously the computational effort rises. In order to quantify the accumulated error, an analysis with increasing numbers of elements was conducted for the laminate heating model. The error showed an asymptotic progression and the linearization error drops below 2.2 °C for 7 elements which is deemed sufficient for the application.
For all four sub-models the seven elements for the first layer and tape are set, the second laminate layer is modeled with five elements as ramp down and all remaining layers with one element. This ensures the highest resolution and lowest error at important process points. For a five layer laminate this results in 59 individual states, which is a massive reduction compared to the 2,967 elements used in the two dimensional FEM.

The formulation of the sub-models is described below. As the tape heating model is the first sub-model of the simulation, it is described in detail. For all subsequent models the applied boundary conditions and changes are laid out. The detailed state space matrices and vectors can be found in the appendix.

Figure 5.8.: **Circuit layout tape heating**

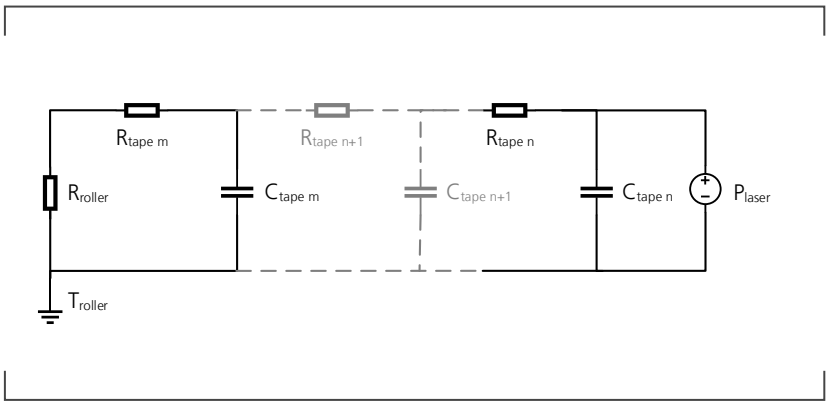

The tape heating model describes the laser impingement of the incoming tape. Two different configurations have to be covered: first the tape is in the air with no contact to the compaction roller. In this area the laser is constantly warming the tape. In figure 5.7 it is marked with T_{T0T} to T_{TRS}. The second configuration covers the laser tape heating while the tape touches the roller (T_{TRS} to T_{NP}). In order to model the shadow area in front of the nip point the laser power is defined as zero for the time the tape travels through this area.
The laser is defined as time varying power source and every layer consists of at least one RC element. If no rapid repass occurs, the tooling is defined with a standard temperature of 22 °C and is defined as the ground. For the second configuration an additional resistor implements the compaction roller. Its resistance is calculated using the heat conduction defined in the two dimensional FEM (325 W/m^2K). The resulting circuit layout can be found in figure 5.8.

The diagram shows the input laser power as source on the right. For every element a heat resistance $R_{tape\,n}$ and heat capacity $C_{tape\,n}$ is defined. It has to be considered that one tape has more than one element, e.g. for a laminate of 5 layers a total of 21 elements are used.
On the left side the resistance of the compaction roller and the last tape are shown, both are only active for the second configuration. For both simulation phases the temperatures are related to the roller temperature, indicated as ground in the diagram.

Using the circuit layout the according mesh and junction rules can be formulated and the model can be described as state space representation (refer to section 2.3.2). Where the system matrix is defined as:

$$A_{nxn} = \begin{pmatrix} -\frac{1}{C_1 R_1} & \frac{1}{C_1 R_1} & 0 & \cdots & 0 \\ \frac{1}{C_2 R_1} & -\frac{R_1 + R_2}{C_2 R_1 R_2} & \ddots & \ddots & \vdots \\ 0 & \ddots & \ddots & \ddots & 0 \\ \vdots & \ddots & \ddots & \ddots & \frac{1}{C_{n-1} R_{n-1}} \\ 0 & \cdots & 0 & \frac{1}{C_n R_{n-1}} & -\frac{1}{C_n R_{n-1}} \end{pmatrix} \tag{5.9}$$

Where n is the total number of RC elements. For the second configuration, the last element of the system matrix A_{nxn} is replaced to add the roller resistance as follows:

$$-\frac{R_n + R_{roller} + R_{n-1}}{C_n \cdot (R_n + R_{roller}) \cdot R_{n-1}} \tag{5.10}$$

The inputs of the tape heating model are described as:

$$B = \begin{pmatrix} \frac{1}{C_1} \\ 0 \\ \vdots \\ 0 \end{pmatrix} \tag{5.11}$$

Since all states should be observed individually the output matrix C is an identity matrix. The laminate model is built up identically to the second configuration of the tape heating. It is a rotated representation with tooling on the left side and the laser heat source on the right side of the circuit layout. Instead of the roller, a thermal resistance for the tooling is introduced and all RC elements of the laminate are added. For the tooling the known heat conduction of 250 W/m^2K is used and a standard temperature of 22°C is assumed.
The power of the laser heat source is split into 53 % that impinges on the tape and 47% on the laminate. These values were obtained by parameter variation and comparison to the full three-dimensional model.

For the compaction roller cooling model input, the outputs of the two heating models have to be merged. The total number of input states is one less of the sum of the output

states, due to the merge of the two states at the nip point. For the nip point the average temperature of the two heating model output elements is used.
The laminate bottom and the tape surface adopt the individual temperatures of the preceding models, because a considerable change is not anticipated. Between the outer temperatures and the averaged nip point temperature values are interpolated linear.

In order to model the cooling under the compaction roller, the system description of the laminate heating model can be adapted and adjusted to describe the thermal fluxes. For this purpose the resistance of the roller is switched to the right side of the circuit and on the left side the tooling a heat resistor is placed. In this case the system matrix changes significantly and is thus shown here:

$$A_{(n+1)x(n+1)} = \begin{pmatrix} -\frac{R_1+R_{roller}}{C_1R_1R_{roller}} & \frac{1}{C_1R_1} & 0 & \cdots & 0 & \frac{1}{C_1R_1R_{roller}} \\ \frac{1}{C_2R_1} & -\frac{R-1+R_2}{C_2R_1R_2} & \ddots & \ddots & \vdots & 0 \\ 0 & \ddots & \ddots & \ddots & 0 & \vdots \\ \vdots & \ddots & \ddots & \ddots & \frac{1}{C_{n-1}R_{n-1}} & \vdots \\ 0 & \cdots & 0 & \frac{1}{C_nR_{n-1}} & -\frac{R_n+R_{tool}+R_{n-1}}{C_n(R_n+R_{tool})\cdot R_{n-1}} & \vdots \\ 0 & \cdots & \cdots & \cdots & \cdots & 0 \end{pmatrix} \quad (5.12)$$

It can be seen that an additional row and column is added and the roller resistance is added to the first and last entry of the top row. Additionally, the roller is switched with the tooling resistance. This model has no inputs and the same output matrix described for the other sub-models.

As mentioned above a standard temperature of 22°C is assumed for process points that were not passed for a longer time period. This does not hold true for smaller reinforcement patches or parts. In these cases the cooling behavior needs to be modeled and added as input laminate temperature. For the finite element simulations this can be done easily by stretching the geometry or using the infinite areas in the models.
For the lumped element model an additional sub-model is introduced, the open cooling to determine the residual temperatures. Definition of the model is readily, due to the fact that it is an exact clone of the laminate heating model without any laser input.

Figure 5.9.: **Comparison lumped element model with full simulation for 5 layers**

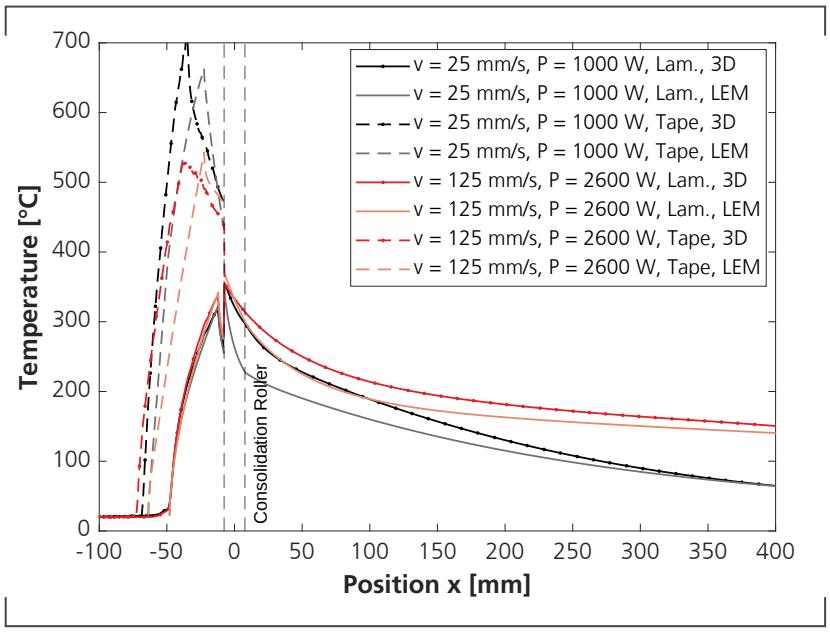

Results Lumped Element Model

For evaluation of the lumped element simulation results the same 24 parameter sets are used, already introduced for the two dimension FEM model validation (refer to section 5.3.2). In order to enable a readily comparison, the simulation results for the same parameter sets are depicted in figure 5.9. As a reminder, the two parameter sets are: firstly a layup velocity of 25 mm/s and a laser power of 1000 W (black and grey lines) and secondly 125 mm/s and 2600 W (red and orange). Both parameter sets were simulated on a five layer laminate.

The second parameter set in orange shows that the LEM simulation agrees comparatively well to full 3D simulation. Most important values like the tape, laminate and nip point temperature are predicted accurately. The cooling under roller is overestimated and results in a faster cool down, a systematic error throughout all parameter sets. However, the temperature converges for longer dwell times. The first parameter set is depicted in the grey plots and show an edge case, with the slowest layup speed, even though the cool down diverges significantly, the heating models provide reasonable predictions for the tape, laminate and nip-point temperatures.
In general, it can be stated that the laminate temperature is predicted with a very high accuracy for all layers. Although the simulation results conform best for ply 5, where the

highest deviation of the laminate temperature is only around 6 °C.
The tape temperature prediction quality is varying: For layer 5 it is overshooting for layup speeds lower than 175 mm/s with a maximum deviation of 19 °C, at 175 mm/s it is matching the 3D simulation and for higher speeds the tape temperature is colder by approximately 10 °C. An exception is the tape temperature at 25 mm/s that diverges by plus 60 °C However, the nip point temperature is predicted accurately, with a maximum deviation of approximately 10 °C, for all parameter sets with a laminate of two layers or thicker. For one layer the nip point temperatures diverge and are predicted consistently higher, compared to the 3D simulation.

As it was seen in the 2D model the cooling under the compaction roller is higher than anticipated in the 3D FEM simulation, this effect is even higher for the LEM model. For larger layup speeds the cooling gradients converge. This can be accounted to the missing thermal mass of the roller.

The open cooling exhibits a faster cool-down between the roller and x = 100 mm/s. For parameter sets above 175 mm/s the cooling plot is parallel to the benchmark, in contrast to lower speeds where the plots converge. If the layup speed of 75 mm/s is excluded, an error between 0 and 27 °C can be measured at a total distance of 400 mm. At this speed the 3D simulation shows a very different cooling behavior, whereas the 2D and LEM model both show consistent results.

In conclusion it can be stated that the model predicts the tape, laminate and nip point temperature in sufficient quality. The values diverge for edge cases especially for laminates with only one layer and velocities under 75 mm/s. The temperature behind the roller is predicted systematically lower than in the 3D FEM model. If this is accounted for in the model predictive controller design, the LEM model is able to provide fast and sufficiently accurate results.

5.3.4. Prediction Accuracy Reduced Models

In order to give a quantitative comparison between the two reduced models, key figures for the two models were calculated and can be found in table 5.3. For the mean values in the table, all 24 parameter sets were used and the simulations were benchmarked against the 3D simulation. All temperatures were derived from the laminate surface. The mean integral of squared errors (ISE) is defined in section 5.2.2 and was calculated here accordingly.
The ISE between the two-dimensional FE model and the lumped element model differ by roughly one order of magnitude. This describes well the inaccuracies of the LEM model

for edge cases such as low temperatures and thin laminates, which push the value up. However, while it performs rather unsatisfactorily in this regard, the correct prediction of crucial process temperature points is far more relevant.

Therefore the temperatures before and after the consolidation roller were compared to the full simulation and the mean difference was calculated. The 2D FE model reaches a mean nip point temperature accuracy of 6 °C, whereas the LEM model more than doubles the value with 13.5 °C. However, this value is deemed sufficient.
For the temperature directly after the roller the same trend can be seen even though the difference of approximately 8 °C is smaller. As expected a strong advantage is exploitable regarding the computational effort, when using the LEM model. The computation time was measured for the calculation of one parameter set. Whereas the LEM model is agnostic to large parameter changes, the FE model has to remesh for laminate changes. Therefore a mean time was calculated.

Qualitatively a few differences can be seen in the accuracy of the two models for the 24 parameter sets (all diagrams can be found in appendix G). Best results can be seen for the thicker laminates (3 and 5 plys), where the 2D model shows a good mapping of the full simulation with minor deviations in the cooling behavior for the two slowest layup velocities (25 and 75 mm/s). The lumped element model has a lower accuracy, especially for the roller and open cooling but shows sufficient accuracy for the heating and cooling under the compaction roller.
For thin laminates (1 ply) only the FEM model shows a good accordance to the full simulation.

In general it can be stated that the LEM model shows weaknesses in the prediction of the complete temperature gradient. This was anticipated as the model is indeed a one dimensional model that was extended in layup direction for discrete process points. However, the most important temperatures such as the maximum tape- and laminate temperature as well as the nip point and roller end temperatures are predicted within a reasonable bandwidth.
Additionally the the computational effort is two orders of magnitude smaller, which is beneficial for the optimization algorithm integrated in the MPC. The developed optimizer is tested with both models and a benchmark is performed via deposition trials of test specimen to evaluate the applicability of reduced models.

Table 5.3.: **Prediction accuracy reduced models**

	Unit	3D FEM	2D FEM	LEM
Mean ISE	[K^2]		$5.64 \cdot 10^4$	$5.85 \cdot 10^5$
Mean ΔT_{NP}	[°C]		6.0	13.5
Mean ΔT_{RE}	[°C]		16.1	24.3
Computation time	[s]	3.600	5.0	0.05

5.4. Implementation

In section 5.3.4 a tremendously reduced computational effort for both models could be shown. However, in order to implement the MPC in an online controller, it must be possible to optimize the control horizon within the control cycle time. For the used layup machine this is 60 Hz (approx. 0.017 s). Independent from the number of optimization iterations, it is clear that the MPC would be too slow independently of the applied model, as one cycle of the faster LEM model still needs 0.05 s. Together with the fact that both the models and the constraints for the MPC are non-linear, offline, non-linear MPC concept is pursued where the MPC acts as feed-forward control.
In this section the following aspects of the controller are detailed: the MPC design, the optimization of the shifting horizon, the cost and constrains formulation, the LEM and FEM integration, the dimensioning of the optimizer. Finally the integration into the lay-up machine controller is presented.

5.4.1. MPC Layout

The overall design of the model predictive controller is depicted in figure 5.10. Determination of the planned disturbances is conducted by a computer aided manufacturing (CAM) software. It details the composite design, that is previously defined by computer aided design (CAD) defining the surface, the ply numbers, boundaries and orientation. The CAM software details these plies by dividing them into tracks, using specific algorithms to optimize tape steering, gaps and overlaps. The current thickness is calculated for every layer and the link movements are build. In this work the CAM software VERICUT by CGTech was utilized. The software provides machine code (in this case KUKA KRL), that can be used directly by the layup machine.

Figure 5.10.: **MPC layout T-AFP control**

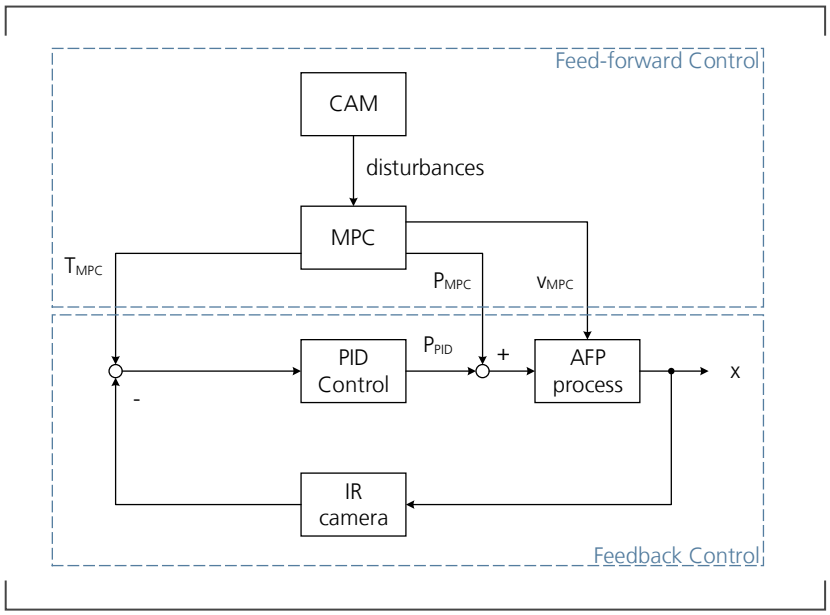

From this follows that the laminate fiber orientation, thickness and last pass can be obtained from the CAM software. Limitations regarding the robot movement could be derived from the surface curvature or a dedicated offline programming (OLP) tool, but where defined manually in this case. However, the automatic derivation of these planned disturbances is implementable with access to the interfaces.

The machine code is passed to the MPC. It parses the laminate thickness, ply orientation and maximal velocity for every track, using an array with a spacing of 10 mm. The MPC is built using MATLAB provided by Mathworks. For the laminate temperature the time since the layup machine passed is calculated. This is done once and only tracks with the same trajectory are considered. Calculation of the residual temperature results from the last temperature at roller end and the simulation of the open cooling during the machines retraction movement.

With these four different disturbances (thickness variation, ply orientation, maximal velocity and residual temperature), the MPC calculates optimized power and velocity values for each section of a track while simulating the occurring process temperatures.
Three outputs are given by the MPC: the predefined laser power is directly forwarded to the laser control and the velocity is fed into the robot program (compare figure 5.10). The set nip point temperature for the PID controller is derived by the expected nip point temperature. This approach has the advantage that the PID controller will only need to

compensate for unexpected disturbances and model inaccuracies.
The PID controller is building the fast feedback control element in the MPC. Its design is adapted unchanged from section 5.2.3.

5.4.2. Control Horizon and Window

Due to the fact that the process temperatures are influenced by the chosen preceding laser powers and layup velocities, the optimization has to be executed iteratively. This is realized by subdividing a given track in time sections. The sample time should be chosen small enough to obtain a sufficient resolution even for higher layup speeds, to react to abrupt disturbance steps. In this case a sample time T_S of 0.05 s is set, which corresponds to a distance of 6.25 mm for the standard velocity of 125 mm/s.
A subset of samples is grouped into one control horizon that is optimized as set and a track is optimized from the start to its end, by optimizing all control horizons after each other.

In order to increase stability of the optimization, the control horizons are designed to overlap each other, a method called overlapping horizons [98]. The overlap is determined by the tape heating and shadow length l, the mean velocity v_m during a track and the sample time T_S. The equation is given as:

$$n_{ol} = \frac{l \cdot 0.6}{v_m \cdot T_S} \tag{5.13}$$

A factor of 0.6 was introduced to ensure that the controller is able to correct previous inputs, even if a proportion of irradiation is already predefined. An overlap n_{ol} = 6 samples was determined.
To account for the preceding power and velocity levels, a window is defined that comprises all values which have an impact on the current process temperatures. It is defined similar to the overlap by determining the time of travel for the longest distance between laser irradiation and the roller end (in this case the tape) for the lowest layup velocity (25 mm/s).

In order to determine the optimal control horizon the LEM model was used to optimize a track with 800 mm length. The control horizon was varied between 5 and 50 using a step size of 5. Diagramm 5.11 shows the number of iterations needed for these different control horizon sizes, with an fixed overlap of 6 sample times (blue bars on the bottom).
As expected the number of iterations decrease with larger control horizons. However, the time needed to optimize one horizon increases almost linear. The overall time spend for

Figure 5.11.: **MPC control horizon for overlap 6 and 160 variables**

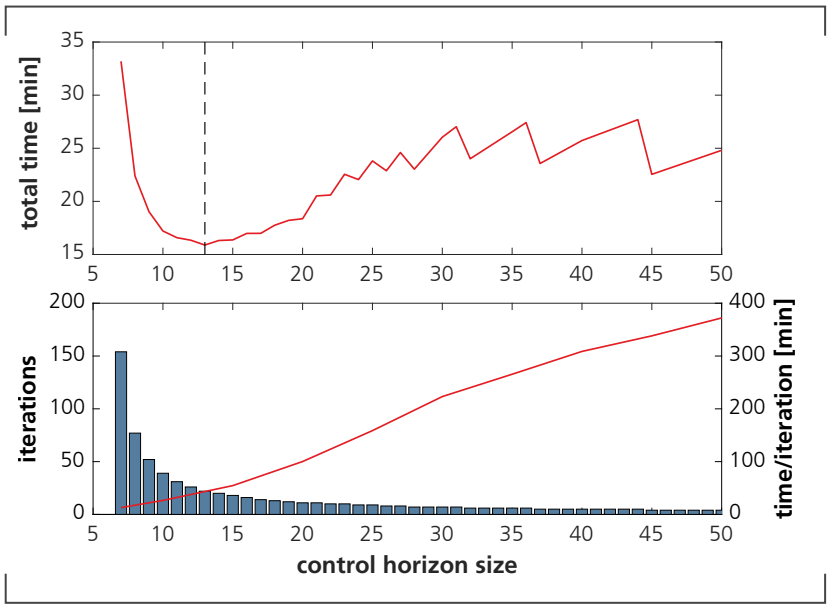

each optimization is plotted on the top. An optimum is achieved for a control horizon size of 13 samples.

5.4.3. Cost Function and Non-linear Constraints

One advantage of the application of a MPC is that, instead of iterating to an optimized parameter set for a specific material by trials, basic principles can be formulated directly and translated into a cost function. For this work the following cost function was developed:

$$f = \left(T_{NPset} - T_{NP}\right) \cdot \frac{100}{T_m} + (v_{max} - v) \cdot \frac{10}{v_m} \left[+\sqrt{0.05 \cdot (z_n - z_{n-1})^2}\right] \tag{5.14}$$

Where T_{NPset} is the desired nip point temperature, T_{NP} the simulated nip point temperature and T_m the mean error expected. On the right side of the equation v_{max} is the maximum velocity that can be realized at a given sample time and v the currently used velocity for the simulation, v_m is the mean expected velocity.
This cost function will minimize the distance between the simulated actual temperature and set nip point temperature, while maximizing the layup velocity. The fractions are added for normalization, whereas the constants weight the process temperature over

productivity, respectively layup speed, to ensure process feasibility. For the FEM based MPC the additional term in brackets is added to prevent the solution to oscillate, by devalue large differences between an already optimized horizon z_{n-1} and the current optimization vector z. Both vectors contain values for the laser power in watts.

Without constraints this cost formula could easily be solved, by increasing the laser power to its maximum, which would lead to over-heating and thus non applicable parameters. The constraints have to be chosen to cover all main process limits. The following constraints were defined:

$$C_1 = T_{TLE} - T_{TapeLimit} \leq 0 \tag{5.15}$$
$$C_2 = T_{LLE} - T_{LamLimit} \leq 0 \tag{5.16}$$
$$C_3 = T_{melt} - T_{TLE} \leq 0 \tag{5.17}$$
$$C_4 = T_{melt} - T_{LLE} \leq 0 \tag{5.18}$$
$$C_5 = T_{melt} - T_{NPset} \leq 0 \tag{5.19}$$
$$C_6 = T_{RE} - T_{melt} \leq 0 \tag{5.20}$$

Where the first couple of constraints ensure that the tape and laminate are not over-heated. Two different limits are defined due to the fact that all simulations show very high temperatures, often above degradation, for the tape. This is supported by infrared camera images and it is assumed that the temperature is only exhibited on the surface and for a short time frame. This might be the reason why degradation is prevented.
The third to fifth constraint ensure that the tape and laminate are above melting temperature and the held above this level until the nip point. Individual constraints for tape and laminate were introduced, to ensure that both are heated over the melting temperature which will result in a faster intimate contact and thus enhanced consolidation compared to a cold and hot surface.
The last constraint ensures that the material is cooled down under pressure, until the material is below the melt.

Naturally the temperatures are material dependent, for the used CF/LMPAEK the following values were applied:

$$T_{melt} = 305\,^{\circ}C \tag{5.21}$$
$$T_{NPset} = 350\,^{\circ}C \tag{5.22}$$
$$T_{TapeLimit} = 650\,^{\circ}C \tag{5.23}$$
$$T_{LamLimit} = 405\,^{\circ}C \tag{5.24}$$

5.4.4. Non-linear Optimization

Three different optimization algorithms were tested to identify the one with the highest performance: a simplex-, pattern and a gradient search algorithm. Subsequently the selected optimizer is tuned for the problem at hand. For the simplex search the MATLAB function fminsearch was implemented. Due to the fact that no constraints can be used, they are implemented into the cost function, applying a weight one order of magnitude higher than the nip point temperature cost.
Using the standard options with maximum iterations and evaluation values of 2.6E3 and a termination tolerance of 1E-4, the computation of a 800 mm track needed 49 min. The algorithm solved oscillating and non feasible results and was thus excluded.
The pattern search allows for additional constraints and upper and lower bounds. Due to its search method, a differentiable gradient in the cost and constraint functions is not necessary. Using the standard properties and algorithm, the pattern search was not able to compute feasible solutions and was thus not investigated further.

Fmincon is a gradient based non-linear optimizer, with the same features offered by pattern search. In this case the search algorithm Sequential Quadratic Programming (SQP) was utilized. It is applicable to differentiable cost and constraint equations, which applies in this case. The algorithm divides an given optimization problem into subproblems. Each subproblem is then optimizing a quadratic model, using linearized constraints. For a detailed description the reader may refer to Fletcher.[45]
With standard values the optimizer reduced the computing effort to roughly a fifth compared to the simplex search and was therefore implemented further. Tuning of the optimizer reduced the computational effort further to approximately 5 min for the 800 mm track. The optimization parameters can be found in table 5.4.

In order to improve the results upper and lower bounds for the laser power were introduced to the optimization. For the first control horizon optimization the bounds are maximized to 500 and 5000 W, respectively. Afterwards flexible bounds of 1500 W below or over the last mean are established. The layup speed has a given maximum value, by the

Table 5.4.: **Parameters Optimizer**

Parameter	LEM	FEM
Algorithm	SQP	SQP
P_0	2850 W	2850 W
Optimality Tolerance	2E-2	1E-6
Max. Iterations	30	30
Max. Evaluations	2000	2000
Step Tolerance	1E-5	1E-6
Function Tolerance	1E-6	1E-6

disturbance trajectory.
For the first control horizon a constant initial power guess is given. Afterwards the optimized values of the last half of the control horizon is used as initial guess for the next horizon. The missing second half of initial values are filled with the last value of the first half. The initial guess for the layup velocity is always set constant, with the mean value of 125 mm/s.

5.5. Experimental Validation

5.5.1. Experimental Setup

In order to get a comprehensive overview of the prediction and reaction capabilities of the two MPC variants, layup trials were conducted that comprise all four examined disturbances. Two different layup tests were designed and carried out for the enhanced PID controller, the lumped element MPC and the 2D FEM based MPC.
The ply laminate thickness, kinematic constraint and fiber orientation change are comprised in one test component. It is a two ply thick 800 x 600 mm base laminate, where the larger part of the plate is deposited in zero degree fiber direction. For the last 250 mm the fiber direction is changed to 90 degrees. On top of the laminate three additional layers are placed with a length of 150 mm. The resulting component is illustrated as a side view in figure 5.12, all dimensions are given in millimeters.

Figure 5.12.: **MPC validation part layout (dimensions in mm)**

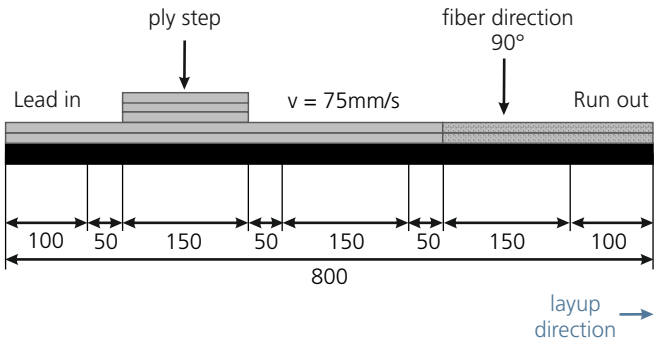

The base laminate is produced using CF/LMPAEK with a layup velocity of 125 mm/s and a temperature set point of 500 °C. All measurements for this part are taken for a layup on top of this base plate, starting at the right side of the illustration with the lead in. Afterwards the layup encounters the ply step, before the maximum allowed layup velocity is reduced to 75 mm/s. All individual disturbances are positioned with a distance of 50 mm to each other, in order to distinguish their individual effect on the process temperature and controller behavior. A total of eight tracks per controller version are measured.
The overall maximum velocity was limited to 125 mm/s for the MPC. This results in feasible solutions for both maximum allowed velocities and is therefore not suitable to test the velocity optimization. However, preliminary work on the process showed that consolidation of the material is insufficient for higher velocities and thus would interfere with the temperature and disturbance measurement and thus rendering comparability impossible.

The compensation of residual temperatures, for smaller parts or reinforcement patches, is tested on a second, single-track, test part of 400 mm length. Five layers are placed consecutively on top of each other to model the effect. Due to the single disturbance one test run per controller is deemed sufficient and pretrials showed no visible variations.
As described in the beginning of the MPC chapter, the IR camera readings are not calibrated. For the layup trials a preliminary, constant calibration was conducted using layup trials at constant power levels. Firstly they were measured with thermocouples and afterwards repeated with the IR camera. The trials showed that an offset of 150 °C can be

Figure 5.13.: **Results PID controller tape laying over stepped validation part**

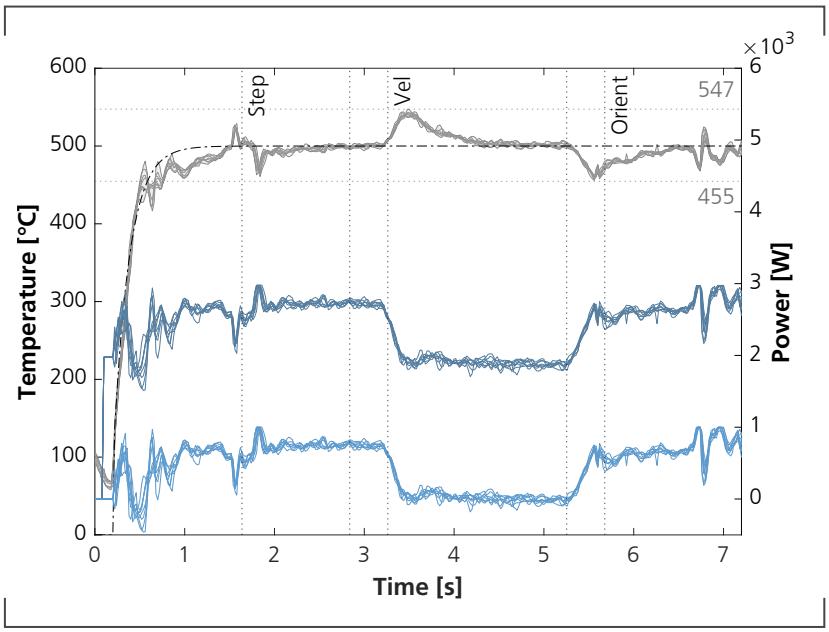

added to the MPC set temperatures for the expected laser power range between 2000 and 3000 W.

5.5.2. Results Enhanced PID Control

For comparison between the state of the art control and the new developed MPCs, the two validation parts are manufactured with PID controller first. It is described in detail in section 5.2.3. The results for the first experiment with the stepped laminate can be found in diagram 5.13, where the temperature is measured in the nip point via the infrared camera.
All eight measured temperatures are depicted in grey, the over all controlled laser power is shown in dark blue and the PID share in light blue on the bottom. The black non solid line is the given set temperature. Measurements were done with a constant preset of 1750 W.

The disturbances are marked as dotted lines for orientation. At the ply step it is clearly visible that at first a higher temperature is measured at the ply border before the temperature drops. This is accounted to the infrared camera sensor, which shows an elevated temperature for the edge of the border, an interpretation of this effect is given in the discussion.

After the step up the controller incrementally increases the power until it reaches the set power again at the end of the step, where no major deviation is observable. A maximum error of -10 °C is measured at the step edge and the given set point temperature is reached at the end of the step, only.
The layup speed reduction leads to a significant over-heating with a maximum deviation of 47 °C. In the middle of the slow speed area, the temperature reaches the set point again. As the robot speeds up a minimal under-heating of -55 °C is measured. Both effects are slightly time delayed, which can be explained by the limited robot acceleration, which reduces the jerk in the system.
The fiber orientation change is superimposed with the effects of the acceleration of the robot. In addition the tape cut introduces a measurement error at the end of track. Both effects complicate the interpretation of this measurement section. Nevertheless a systematic, minor under-heating is still traceable.

The results for the reoccurring laminate are depicted in diagram 5.14, using the same color scheme as before. Displayed are the four tapes that are deposited on the first layer of CFRP. Two main disturbances are displayed at the lead in and tape cut, where the main divergences from the set temperature occur. The temperature is measured in the nip point via the infrared camera.
For the second tape a considerable lower laser power is required, before the power jumps to a higher level. This results in an increased control effort of about 60 %, from approximately 480 to 780 W.

5.5.3. Results Lumped Element Model based MPC

The optimization results for the stepped validation part are depicted in figure 5.15. The graph is divided into three subplots, from top to bottom: the simulated process temperatures, the optimized laser power together with the layup velocity and the planned disturbances on the bottom. The ply orientation change is not depicted here, as it is ignored by the LEM model.
It can be observed that the cost function for the nip point temperature T_{NP} is closely optimized to 350 °C (red line), with negligible deviations. For the complete track the temperature behind the roller T_{RE} is beneath the melting temperature. The optimization shows that there is little buffer for a two ply laminate to this threshold. However, it increases significantly for the five ply zone, resulting in a smoother power optimization. T_{TLE} and T_{LLE} are the tape and laminate temperature after the laser heating respectively.
The same is apparent for the slow speed area, even though the distance to the melting temperature is smaller (approx. 290 versus 280 °C). Slight overrides in the area of the

Figure 5.14.: **Results PID controller reoccurring laminate**

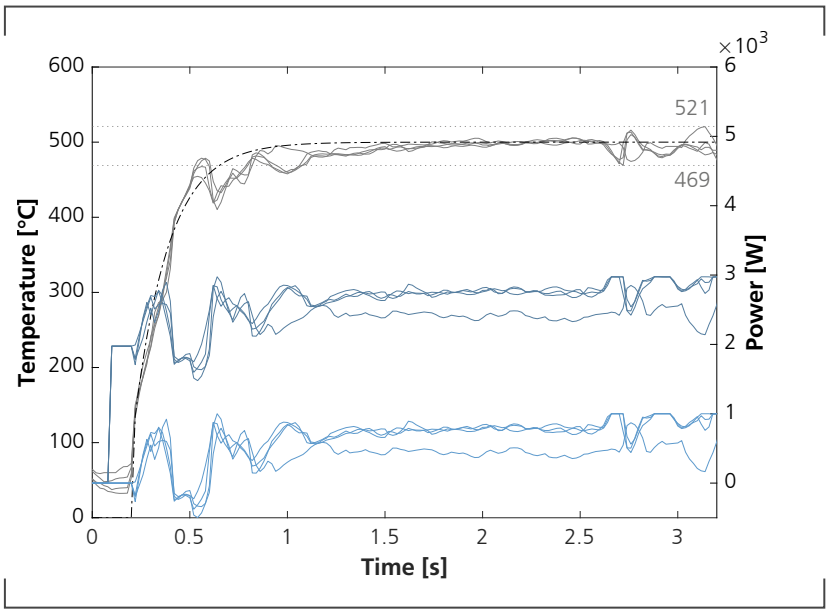

deceleration and acceleration of the layup machine are visible, before the optimized power smoothens towards the track end.

The layup trial results for the lumped element model based controller are depicted in diagram 5.16. It is similarly structured as the graphs before, with grey colored temperatures readings, dark blue overall laser power curves and the light blue PID, feedback controller share. Additionally the simulated required power for the track is plotted as red line. It is the feed-forward signal used for the experiment.

The ply step and velocity change areas show good accordance to the set temperature, that is held relatively constant throughout all disturbances. The highest deviation can be seen at the beginning of the ply step, at this point the control power is roughly 100 W above the PID benchmark and the sensor measurement shows an approximately 20 K higher temperature error.
Minimum under-heating triggered by the velocity step improved by 23 K and overheating by 10 K. For the fiber orientation change, a significant better conformance to the set point temperature can be seen. However, with elevated temperatures the gaps between the individual tracks show higher temperature readings by the infrared camera. This results in clearly visible peaks at the end of the temperature curves.

Figure 5.15.: **Results LEM MPC optimization stepped validation part**

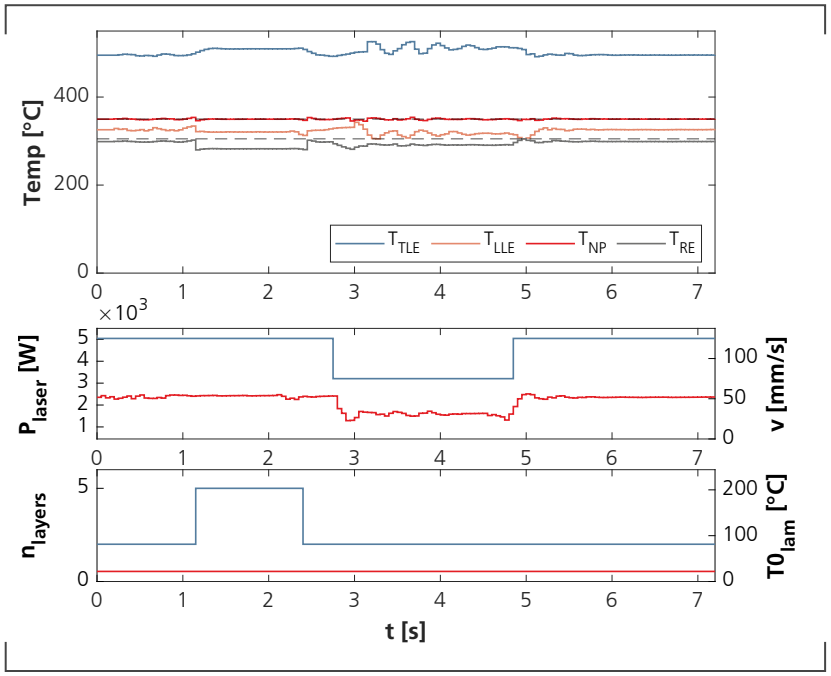

Figure 5.16.: **Results LEM MPC tape laying over stepped validation part**

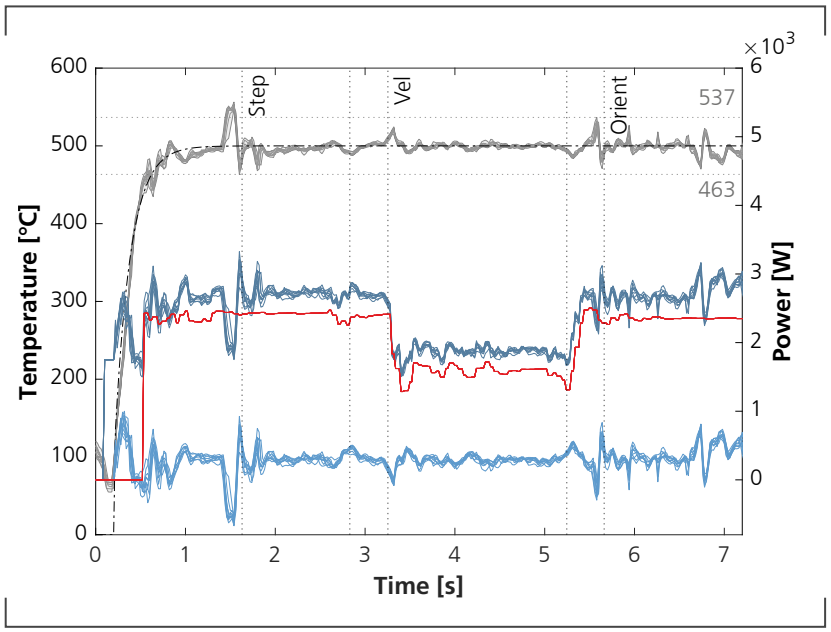

Figure 5.17.: **Results LEM MPC reoccurring laminate**

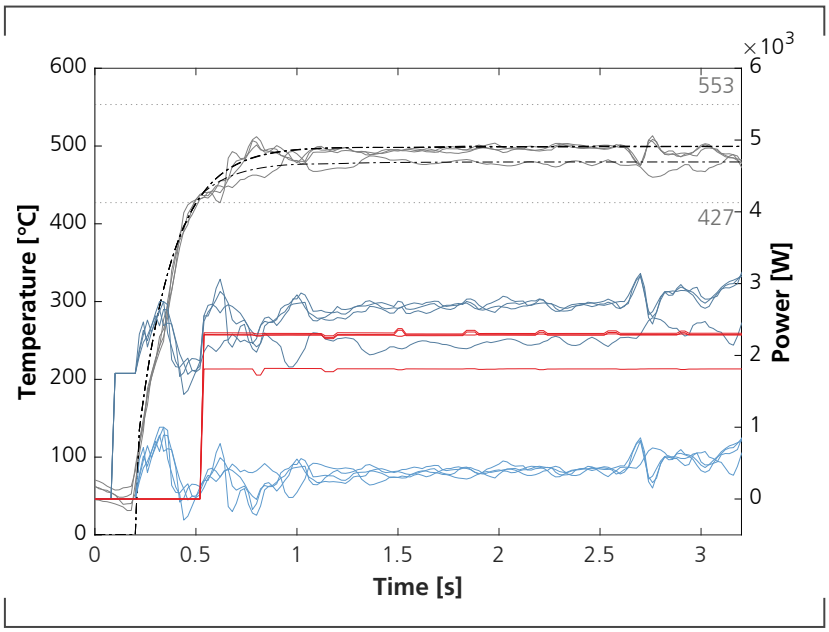

A look at the overall used laser power in comparison to the anticipated power shows that an almost constant offset of approximately 325 W has to be compensated by the live controller. Apart from this the power curve aligns well with the actual used power and the active control effort is reduced by around 100 W, compared to the benchmark.

Figure 5.17 shows the result of the five layer test track that incorporates the residual temperature. As the model needs to incorporate at least a one ply track, the optimization started with track 2. It is the only track for which the set temperature was reduced to 480 °C by the MPC. All subsequent tracks reach the 500 °C (respectively 350 °C) temperature set point. The temperature is measured in the nip point again using the IR sensor. Regarding the over all compliance to the set temperature is can be seen that the temperatures are reached earlier and the slight under-heating of the PID benchmark is eliminated. The PID control effort is homogenized to approximately 400 W for the MPC for all layers and is reduced from a mean of 680 W for the pure PID controller. Despite the residual temperatures of the laminate, the added CFRP dissipates the heat significantly better resulting in higher power levels needed for the subsequent layers.

Figure 5.18.: **Results FEM MPC optimization stepped validation part**

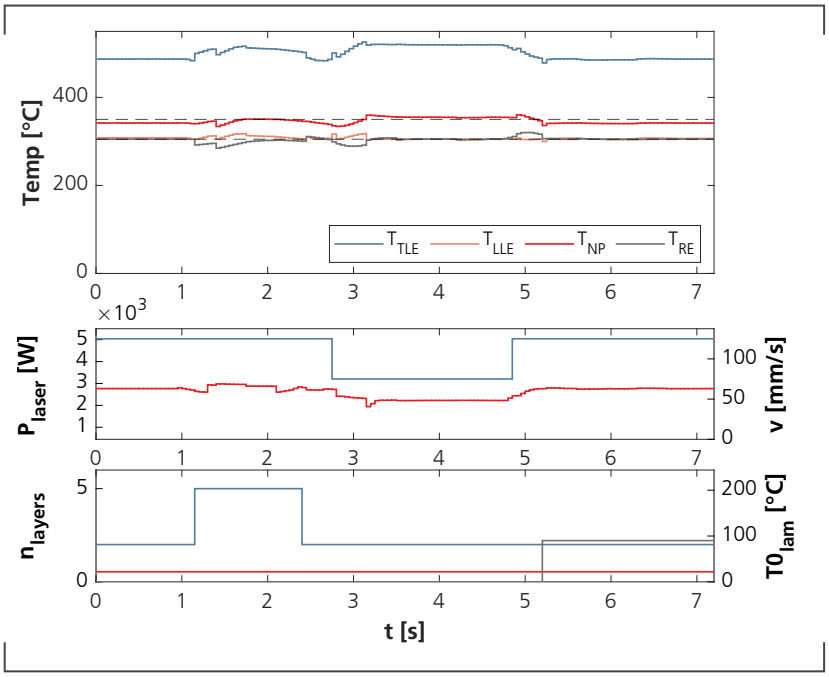

5.5.4. Results Finite Element Model based MPC

The optimization results for the FEM based MPC can be found in diagram 5.18, with the identical structure and coloring for the three plots. In the bottom subplot an additional grey line indicates the fiber orientation, where zero degrees are defined as the fiber being orientated in tape laying direction.
Whereas the LEM MPC model showed little deviation from the optimal 350 °C set temperature in the nip point, the FEM model shows deviations in the transition zones between ply and velocity changes. The lowest nip point temperature amount to 334 °C and the highest to 359 °C and are located at the velocity deceleration and acceleration respectively.

The aimed target of a nip point temperature of 350 °C and a compaction roller end temperature below the melt is narrowly missed by -9 °C, for the two ply configuration. Similarities to the LEM MPC model are evident for the thicker laminate and slower process speed, where the distance between the two process points (T_{NP} and T_{RE}) increases.
All constraints are adhered to, with the exception of an over-shoot of T_{RE} at the end of the slow speed area. At this critical point both temperatures around the compaction roller over-shoot. Together with the slightly lower nip point temperature these optimization errors were accepted due to the set margins for the cost and constraint results.

Figure 5.19.: **Results FEM MPC tape laying over stepped validation part**

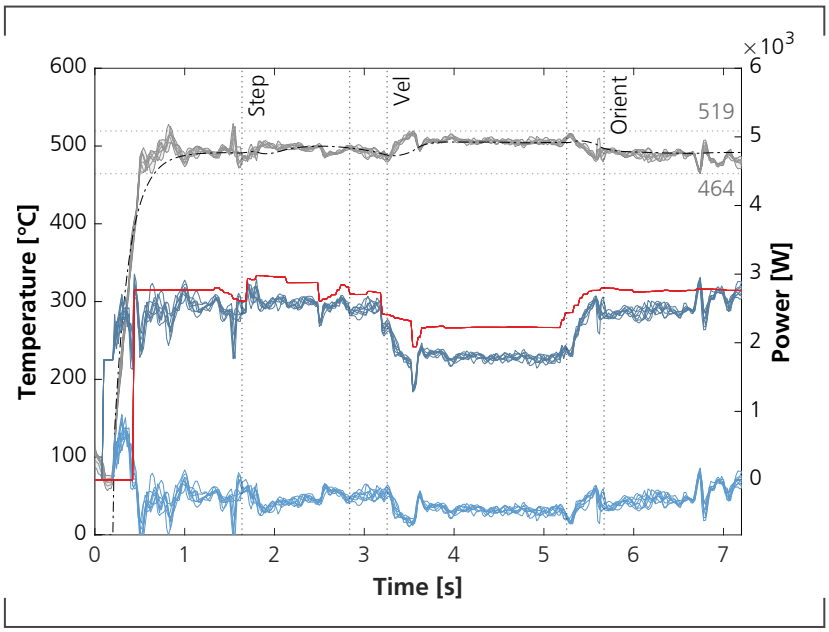

A comparatively smooth power optimization can be seen for this model which is partly accounted to the modified cost function, which penalizes large discontinuities between power levels of one optimization horizon. Tuning of its weight is crucial to gain feasible results but deteriorates the adaption of the optimizer at disturbances steps.

Utilizing this optimization, the layup trials yielded the results as depicted in diagram 5.19. Whereas the set temperature was relatively constant at 500 °C for the LEM MPC model, it is adjusted for the speed and ply changes here. A detailed evaluation of the ply step shows that the process temperature complies good to the set temperature. However, one drop is visible where an optimization flaw is clearly identifiable, visible as sudden power step. After a settling phase the FEM MPC shows the closest conformity to the set temperature so far. The same is true for the fiber orientation change, where the FEM MPC satisfies the set temperature well.

The comparison between total laser power and predicted laser power, shows that the required power is consistently over estimated. Although, the curve shows a good correlation to the actual used power. It is apparent that the simulation of the required power for the slow speed area deviates significantly more. Accordingly the active controller reduces the laser power over the course of the track, to reach the desired process temperatures. With an absolute mean control effort of 297 W the FEM MPC needs the lowest manipulation by the PID controller.

Figure 5.20.: **Results FEM MPC reoccurring laminate**

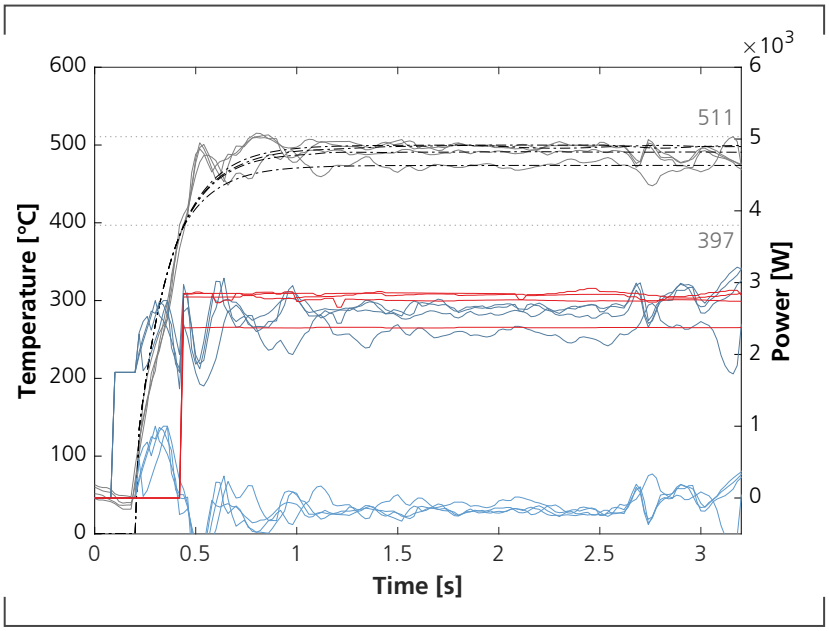

Figure 5.20 gives the results of the fast reoccurring track. Three different set temperatures are introduced by the model and thereby one level more than the LEM based MPC. With increasing thickness the desired 500 °C are reached. The FEM driven MPC estimates the required power significantly higher than the LEM model with approximately 2830 W. Due to the higher input power the temperature over-shoots the PT1 element at the track start, which actually means the process temperature is reached earlier. Whereas the last three tracks are at the same power level, the second track needs considerably less power. An estimation that was done by the LEM model as well. A look at the PID control shows that this estimate was correct.
The accuracy of the model is prooven by the low PID control effort required. With an absolute mean value of 223 W it is 173 W below the LEM driven MPC.

5.5.5. Discussion

Layup trials for the stepped structure with the enhanced PID proofed the need for a new control concept. All planned disturbances (the ply step, the low speed area and the laminate fiber orientation change) require different power levels.
Slow adaption to these changes result in turning points over and under 50 °C of the set temperature and thus considerably out of the processing temperature of LMPAEK. Despite

the enhancement of the temperature controller, adaption to all three disturbances took up to 1 s. This is explainable by the inertia shown by the process. However, for high layup speeds these large areas of a laminate might suffer from insufficient consolidation.
For the fast reoccurring sample track, the controller showed an increased control effort for tracks laid on a thicker laminate. Despite the increasing residual temperature the growing thermal mass and heat dissipation by the CFRP had a larger effect on the process. Even though the return time for this part was 10.2 s only.

At the rise of the ply step a large peak is visible in all three measurements. Investigation of the root cause was conducted, using the measurement stream of the infrared camera and visual inspection of the stepped base laminate. Given the design of the used layup machine, the incoming tape is traveling a considerable free length into the heating zone. In order to reach the consolidation roller with certainty, it needs to remain its structural integrity, resulting in a small poorly consolidated edge. This edge emerges as a line of significant higher temperature in the IR sensor. Since the measurement does not show an areal overheating, this effect should be regarded as measurement error.
Additional artifacts can be seen for the fiber orientation change, where the tape edges appear as higher temperatures. An attempt was made to compensate the error by using a minor, 1 mm staggering. However, the tape edges still remain visible in the results. Both effects should not be compensated by the controllers but rather by a more sophisticated IR camera evaluation.

The LEM MPC proofs that the impact of the planned disturbances can be minimized considerably. However, peaks are still visible for the slow speed part of the validation. For the fiber orientation change, a unsteady curve is visible that is accounted to the IR camera measurements. In general the control effort was reduced successfully. Nevertheless the eradication of the constant power prediction error would be of interest.
Optimization of the model was straight forward as it overestimates the cooling under the roller, which increases the solution space. However, preceding trials showed that a layup velocity of 125 mm/s is an absolute maximum for this material and machine combination, and that mechanical properties plunge for larger speeds. Therefore, it can be assumed that the model inaccuracy could lead to unsatisfactory process parameters.
Experiments for the reoccurring track showed that the MPC can reduce the control error by almost an order of magnitude, while homogenizing the needed PID adjustments for all tracks.

The FEM MPC model simulates the process in greater accuracy. This is reflected in optimization results that show solutions with minor constraint violations, which are only accepted because they are within the margins defined. Tighter margins would lead to an optimization with slower velocities, which was prevented in order to sustain comparability. However, the evaluation of the possible solutions show that only a slim parameter space

Table 5.5.: **Quantitative Comparison Controllers**

	Unit	Trial	PID	LEM MPC	FEM MPC
Mean ISE	[K^2]	VP1	$2.39{\cdot}10^6$	$8.32{\cdot}10^5$	$5.35{\cdot}10^5$
Min. Temp	[°C]	VP1	455	463	464
Max. Temp	[°C]	VP1	548	537	519
Control Effort	[W]	VP1	467	311	297
Mean ISE	[K^2]	VP2	$1.20{\cdot}10^6$	$3.10{\cdot}10^5$	$6.39{\cdot}10^5$
Control Effort	[W]	VP2	676	396	223

lead to feasible solutions. As a result the optimization is relatively unstable. Together with the inertia shown by FEM simulation a modification of the cost function was necessary to suppress power level oscillations.
Results of the layup trials showed that the FEM MPC adapts the power and set temperature well and reaches the consolidation temperature the quickest. It exhibits the lowest error, but it must be stated that it adapts the set temperature, which leads to a slightly inhomogeneous temperature curve compared to the LEM MPC model. Its good adaption to the fiber orientation has to be viewed with skepticism, since the power is adjusted by 10 W only and could also be caused by the lower power level that limits the effect of IR camera artifacts.
Due to the higher estimation of required power, the controller over-shoots for the second trial, which explains the almost twice as large ISE compared to the LEM based MPC. However, the effect of the more precise modeling of the process is shown by the reduced PID effort, which only needs to adjust the temperature with a mean control variable size of 223 W.

Table 5.5 gives an overview of the quantitative comparison of the three controllers. A substantial drop of the mean integral squared error can be seen between the PID and LEM MPC controller. The FEM based MPC exhibits the smallest error for the stepped demonstrator. Moreover, the minimum and maximum temperatures could be improved notably, with the introduction of the MPCs. The FEM MPC exhibits a slightly better performance against over-heating. The overall control effort dropped by 33-46 % for both MPC versions.
Regarding the second trail (VP2), both MPCs improve the error and the LEM MPC shows the smallest over all error, whereas the FEM MPC shows the lowest deviation from the actual needed power in this experiment.

6. Conclusion

The novel, three-dimensional, multi-physics T-AFP process simulation demonstrates and evaluates the complex interaction between its components. For instance, the mechanical model allows the direct assessment of the impact of the compaction force on both the laser irradiation and the heat transfer under the compaction roller. It thereby proofed high accuracy for the utilized silicone rubber roller and for all relevant compaction force points. In addition, the established simulation offers the possibility to evaluate new roller designs, materials or cooling principles by analyzing their effect on the process temperature profile. It should be noted, however, that the hyperelastic material model used, is highly dependent on the material properties, which must be adjusted in the case of material changes. Another factor is that the model outputs complex geometry that must be reintegrated as meshable geometry for the downstream simulations.

Modeling of the laser gives a precise distribution of the irradiation distribution and resulting shadows. This provides a solid basis for the heat transfer simulation. Areas that contribute the most to the laminate and tape heating are identified, which is non-trivial due to the wide range incident angles exhibited.
Adjustment of the laser angle or distance to the nip point can be easily performed with a direct evaluation of the effect on the CFRP heating. Since the laser source is simplified as a combination of the ray beam shape and a lens, adaptation to any laser system is possible. In general, any radiation-based heat source can be simulated using this approach e.g. infrared heaters as additional preheaters.
The challenge with the optical model is that the accuracy increases with the number of rays simulated. This means that about four million rays have to be simulated, if a detailed irradiance distribution is required. This results in to a substantial computational effort. Apart from this it became clear that specular reflection does not adequately model the complex reflection behavior of CFRP. As a compensatory measure isotropic scattering was introduced, which partially improved the result. Sophisticated distribution functions would most likely reduce the need for the implemented efficiency constant.

It has been demonstrated that the heat transfer of this highly transient process can be modeled with considerable higher precision than previous models. The simulation allows a detailed analysis of the heat fluxes. It provides the grounds for a sensible model reduction.

Besides the more obvious correlations e.g. between laser power and layup speed, the dominant effects of interlaminar thermal resistance and cross-track heating decrease were identified and subsequently quantified.
The simulation is a useful tool for virtual process point identification. It requires only a few material parameters, such as thickness and heat transfer coefficients, to sweep through the process parameter combinations. It can be readily adapted to different tool- or first ply setups, drastically reducing the process setup efforts.
More work needs to be invested on the through laminate thickness simulation, as it is consistently lower than the measurements taken. A possible reason could be the elevation caused by the thermocouples, although their foot print was reduced by developing of a custom design.
The introduction of the tooling and compaction roller into the FEM simulation increased the computational effort and complicated the meshing, due to the geometric dimension shifts. However, it also helps in the investigation of longer layups, as the residual heat e.g. in the roller can be simulated, which becomes essential over time.
In general, to the best of the authors knowledge, this simulations is the first three-dimensional T-AFP process simulation that integrates all of its physical aspects. The holistic approach solves the problem of highly interrelated process and environmental parameters and assists in making design decisions for further process improvements.

The state space model reduction promised great potential for an automated software chain that would feed an FEM simulation directly into the machine. However, for the highly non-linear T-AFP process this approach was likely to fail. The lack off access in the commercial COMSOL software made it impossible to develop a dedicated export. Nevertheless new export functionality for non-linear models or better linearization methods may enable this approach in the future.
Dimensional reduction of the FEM simulation showed that a two-dimensional simulation is adequate for modeling a nip-point temperature control system. Although it is important to note that both reduced models were tuned with the full simulation, a vital function of the model. The reduced FEM model achieves a great performance leap, with a computation time of about five seconds. An advantage that can be exploited not only in a MPC, but also for rough process point estimation.
On the downside, manual work with a detailed insight knowledge of the simulation was required to build the stripped model. This hinders the transfer to other thermal processes and limits the simulation to the current hardware layout. Besides this it has to be considered that the model showed improvable results at very slow layup speeds.
In order to improve the performance and evaluate the efficiency of the optimization, a simplified model using the lumped element method was developed. As expected it exhibited better performance, which was advantageous for the optimization. Disadvantages, however, are the complex definition of the model and the inaccuracy for thin laminates and slower layup speeds, despite the extensive tuning performed.

In conclusion, the white box model reductions proved that performance gains are possible while maintaining the physical meaning of the models. Both reductions showed high potential to be used in the future with greater accuracy in AFP and in other heat transfer processes. The approach of starting with a complex simulation showed the advantage of being able to simulate otherwise estimated parameters, such as the roller temperature.

Analysis and improvement of the temperature control system, using conventional control concepts already reduced the tolerance by approximately 40 % and the maximum temperature by 30 K. Implementation of the MPC additionally cut the integral squared error by one order of magnitude, while simultaneously reducing the control effort by half.
The use of a MPC for the T-AFP process proved to be a viable approach to the problem of planned disturbances, inherent in any complex lightweight component. It was demonstrated that four of the major interfering factors could be diminished, paving the way for defect-free in-situ consolidation without post-treatment.
Expanding on this approach, other disturbances such as material inaccuracies, integrated inlays or planned gaps could be easily implemented to further improve the control.
The definition of high-level costs and constraints shows great potential for investigating process interrelations rather than individual process parameters, which could lead to faster quality improvements.
Additional effort should be put into stabilizing and accelerating of the optimization results. In the current state, offline optimization is time consuming, which renders the online MPC concept impossible.
Since the validation trials showed that both FEM models can accurately simulate the process, a combination of a FEM that trains a black box model e.g. a neural network would most likely provide accurate prediction results in a fraction of the time and would therefore be a preferred way to proceed.

In conclusion a successful approach has been presented that solves some of the key issues of in-situ T-AFP, such as thermal inertia and complex temperature measurement, which introduced unacceptable temperature variations. It was shown that the set point temperatures are reached and maintained even for demanding layup tasks using the novel MPC approach for the Process. Equally, the reliability of the process was improved, enabling industrial implementation.
On a broader perspective the invented method to model and control highly non-linear, not observable processes can be adopted to a multitude of technologies within CFRP manufacturing and beyond, for example to control the ultrasonic or resistance welding of thermoplastics.

7. Outlook

As shown in the previous chapters a consistent simulation of all aspects of T-AFP and its direct integration into the layup machine control, paves the way for complex yet defect-free, in-situ consolidated components. However, further work is needed to close the gap between the current mechanical performance of the process and other consolidation techniques.
One promising approach is to consider holistically the entire process chain, including prepreg production, slitting, layup and post-processing. Throughout this thesis, it has become clear that improving the input quality of the material is one of the greatest potentials to influence the resulting part quality. Although this is true for all CFRP manufacturing processes, it is particular important for T-AFP where a short consolidation phase meets high viscosity resins that render defect compensation difficult.
This leads to the demand of quality enhancing post-processing such as annealing and re-passing. Due to the lower melting point of CF/LMPAEK vacuum bagging can by applied more easily, making oven annealing economically viable. However comprehensive studies on post curing are lacking, especially for complex parts. Practical trials show that insufficiently consolidated layers tend to slip and deform in oven post-treatment, in-situ consolidation could be advantageous here as temperatures below the melt would be sufficient. Simulation based re-passing could reduce thermally induced stresses and thus improve laminate performance.

Because of the persisting higher material prices for thermoplastic CFRPs, secondary advantages must be exploited in order to be economically viable. These could be, for example, the combination with fused deposition modeling for functional integration, the substitution of interfaces by over-taping, or the use of welding technologies. Another possibility is to increase the lightweight potential through the use of variable stiffness components manufactured with guide-curves.
In order to facilitate the adoption of T-AFP, more effort needs to be put into defining design rules for laminates, taking into account the consolidated tape width and incorporating a detailed understanding of the mechanical impact of gaps and overlaps. Investment costs could be pushed by more reliable, flexible hardware that includes full software integration with popular CAD tools.
An innovative concept is to substitute the expensive and inflexible deposition molds with

a second robot. Besides cost savings this would allow for instant prototyping and agile design changes for CFRP components.

The three-dimensional, multi-physics process simulation presented here has been used primarily to derive accurate, high-performance models. However, it offers a vast potential for future improvements of process setup as well as machine and part design.
Inclusion of more process points, materials and machine layout could lead to a generalized simulation that is adaptable to various layup machines. Furthermore the current cumbersome setup and adaption of the T-AFP process to new materials could be improved by incorporating simulation-based parameter presets that provide a starting point for additional fine tuning.
Based on the current simulation, it would be feasible to predict the resulting crystallinity and overall quality. This data, along with the temperature history of the material, could be fed back to the component design for residual stress analysis, allowing smaller safety margins and thus safe additional weight.

On basis of the mechanical and thermal simulations, the cooling phase of the tape could be controlled more precisely by developing compaction roller concepts, that directly control the temperature in the consolidation area. The optical model allows easy adaptation of the laser optics, to improve the heating, simulate the effect of preheaters or evaluate the development of complex laser heating systems, that control the laminate and tape temperature individually. In addition the effect of the size of irradiation areas or heat sinks, such as tape guides, on the consolidation quality can be directly determined.

With the implementation of a MPC control in a T-AFP layup machine its fundamental advantages have been demonstrated. Seamless software integration of the CAM and robot simulation is the next logical step to reduce manual intervention in the process. The development of a dedicated CAM software that provides detailed information on the time since the last pass of the layup machine occurred and the material thickness at any point would be beneficial. Further improvements to the MPC could be achieved if the simulation included the transition between to two states, such as the ply step.
Future work should investigate the improvement of the optimizer and its presets. Although extensive testing has been done in this thesis, additional cost and constraint variants need to be investigated in order to enhance the quality and computational complexity of the algorithm. It is conceivable that an optimizer tailored to the small solution space of the T-AFP process could improve the optimization results.
If quality is added to the simulation, the abstraction of the costs and constraints could be raised to another level, allowing to decide what quality or productivity should be achieved by the process. This could be easily integrated into the developed code base.

A multitude of benefits could be achieved by investigating and improving the model reduction: first, semi-automatic reduction would provide the ability to iteratively improve the full simulation and integrate updates directly into layup machine. Second, if the performance of the reduced model is enhanced the MPC could be used as a near to or even online optimization, with the opportunity for a more robust and flexible control. One approach could be to train a neural network fed with data from the 3D FEM simulation.

Another angle to improve AFP control systems might be the development of sensors with higher accuracy or direct access to the consolidation area. First concepts are currently developed to integrate pressure sensitive foils and temperature sensors into the consolidation roller. The continuation of these concepts might be promising.[157, 193]

List of Figures

List of Tables

A. Coefficients Gaussian Models and fit

Table A.1.: **Coefficients Gaussian models intensity profiles**

Parameter	x-direction	y-direction
a1	0.3576	2.2190
b1	9.8230	14.4600
c1	11.6700	6.6750
a2	0.1959	–0.0233
b2	–1.9270	–0.6264
c2	6.4920	2.6090
a3	0.1664	0.3784
b3	20.9200	–0.8655
c3	6.4380	9.8910
a4	0.1502	–1.9130
b4	–7.3950	14.3600
c4	4.2080	6.2000
a5	0.1598	0.1514
b5	26.1300	23.7000
c5	4.0550	3.1680
a6	0.1713	0.2002
b6	–10.7700	–11.8000
c6	2.8450	5.0700
a7	0.1596	0.1509
b7	29.5700	–16.3900
c7	2.6560	2.8270

Figure A.1.: **Measurement data and fitted gaussian functions for intensity**

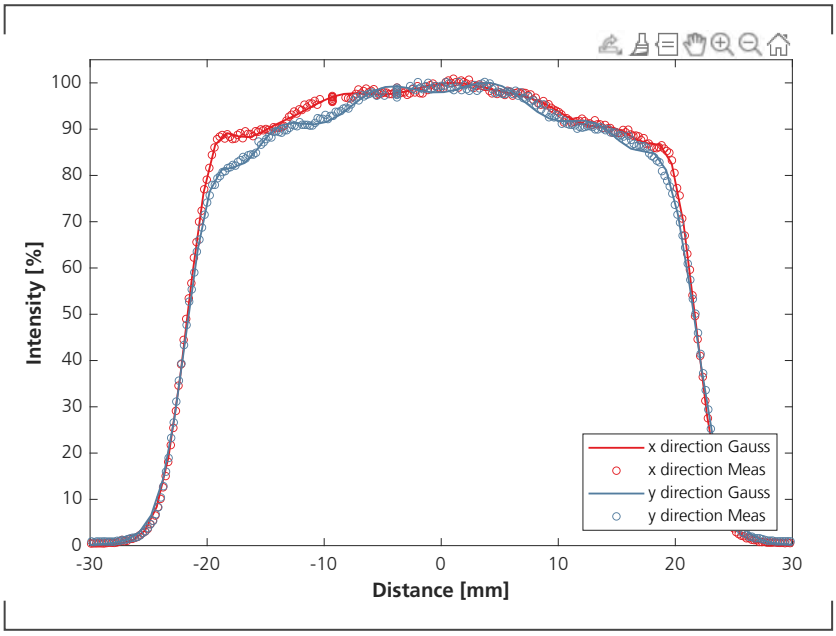

B. Geometric Layout Optic Mount

Table B.2.: **Geometric layout optic mount**

Parameter	Unit	Value
x_{RP}	mm	149.00
z_{RP}	mm	149.00
r_{roller}	mm	40.00
h_{laser}	mm	60.00
l_{laser}	mm	8.73
α	°	15.00

C. Boundary Conditions 3D FEM model

Table C.3.: **Mechanical boundary parameters**

Parameter	Unit	Value
C10	MPa	-0.0338
C01	MPa	0.3605
C20	MPa	0.8316
C02	MPa	0.7987
C11	MPa	-1.6722
μ_{Rubber}	kg/m^3	1120

Table C.4.: **Optical boundary parameters**

Parameter	Unit	Value
Nummer rays	1	4E6
Laser Power	W	1000-5000
$I_{initial}$	W/m^2	1000
η_{laser}	1	0.8
n_{CFRP}	1	1.96

Table C.5.: **Thermal boundary parameters**

Parameter	Unit	Value
v_{layup}	mm/s	25-275
T_{env}	C	20
$R_{tape/roller}$	Km^2/W	8E-4
$R_{lam/roller}$	Km^2/W	8E-4
$R_{lam/lam}$	Km^2/W	2E-4
λ_{rubber}	W/mK	0.18
$h_{roller/tool}$	W/m^2K	500
h_{roller}	W/m^2K	3.58
$h_{lam/tool}$	W/m^2K	250
L_{Tape}	m	0.1
L_{Tape}	m	0.5

D. Boundary Conditions 2D FEM model

Table D.6.: **Geometry 2D FEM model**

Parameter	Unit	Value
α_{laser}	deg	60
tape thickness	mm	0.18
consolidation length	mm	15.40
shadow laminate	mm	4.25
irradiation laminate	mm	36.00
length infinity	mm	5.00
shadow tape	mm	14.74
radius roller	mm	40.00
irradiation tape	mm	14.00
input length laminate	mm	5.00
length cool-down	mm	5.00
tape width	mm	38.10
input length tape	mm	5.00

Table D.7.: **Boundary Conditions 2D FEM model**

Parameter	Unit	Value
η_{laser}	1	0.8
$\eta_{laser/lam}$	1	0.45
$\eta_{laser/tape}$	1	0.55
$\eta_{laser/bound}$	1	$0.087 \cdot P_{laser} \cdot \eta_{laser}$
T_{env}	C	22
T_{tool}	C	22
T_{lam}	C	22
T_{roller}	C	120
h_{conv}	W/m^2K	15
$h_{lam/tool}$	W/m^2K	250
h_{roller}	W/m^2K	325
$R_{lam/lam}$	Km^2/W	2E-4

E. State Space Systems LEM model

Tape Heating without roller:

$$x_0 = \begin{pmatrix} T_{tape} - T_{roller} \\ \vdots \\ T_{tape} - T_{roller} \end{pmatrix} \tag{.1}$$

$$u(t) = \begin{pmatrix} P(t)_1 \\ \vdots \\ P(t)_n \end{pmatrix} \tag{.2}$$

$$A_{nxn} = \begin{pmatrix} -\frac{1}{C_1 R_1} & \frac{1}{C_1 R_1} & 0 & \cdots & 0 \\ \frac{1}{C_2 R_1} & -\frac{R_1 + R_2}{C_2 R_1 R_2} & \ddots & \ddots & \vdots \\ 0 & \ddots & \ddots & \ddots & 0 \\ \vdots & \ddots & \ddots & \ddots & \frac{1}{C_{n-1} R_{n-1}} \\ 0 & \cdots & 0 & \frac{1}{C_n R_{n-1}} & -\frac{1}{C_n R_{n-1}} \end{pmatrix} \tag{.3}$$

$$B = \begin{pmatrix} \frac{1}{C_1} \\ 0 \\ \vdots \\ 0 \end{pmatrix} \tag{.4}$$

$$C = \begin{pmatrix} 1 & 0 & 0 & \cdots & 0 \\ 0 & 1 & 0 & \cdots & 0 \\ 0 & 0 & 1 & \cdots & 0 \\ \vdots & \vdots & \vdots & \ddots & \\ 0 & 0 & 0 & \cdots & 1 \end{pmatrix} \tag{.5}$$

Tape Heating with roller:

$$x_0 = \begin{pmatrix} T_{tape} - T_{roller} \\ \vdots \\ T_{tape} - T_{roller} \end{pmatrix} \tag{.6}$$

$$u(t) = \begin{pmatrix} P(t)_1 \\ \vdots \\ P(t)_n \end{pmatrix} \tag{.7}$$

$$A_{nxn} = \begin{pmatrix} -\frac{1}{C_1 R_1} & \frac{1}{C_1 R_1} & 0 & \cdots & 0 \\ \frac{1}{C_2 R_1} & -\frac{R_1 + R_2}{C_2 R_1 R_2} & \ddots & \ddots & \vdots \\ 0 & \ddots & \ddots & \ddots & 0 \\ \vdots & \ddots & \ddots & \ddots & \frac{1}{C_{n-1} R_{n-1}} \\ 0 & \cdots & 0 & \frac{1}{C_n R_{n-1}} & -\frac{R_n + R_{roller} + R_{n-1}}{C_n \cdot (R_n + R_{roller}) \cdot R_{n-1}} \end{pmatrix} \tag{.8}$$

$$B = \begin{pmatrix} \frac{1}{C_1} \\ 0 \\ \vdots \\ 0 \end{pmatrix} \tag{.9}$$

$$C = \begin{pmatrix} 1 & 0 & 0 & \cdots & 0 \\ 0 & 1 & 0 & \cdots & 0 \\ 0 & 0 & 1 & \cdots & 0 \\ \vdots & \vdots & \vdots & \ddots & \\ 0 & 0 & 0 & \cdots & 1 \end{pmatrix} \tag{.10}$$

Laminate Heating:

$$x_0 = \begin{pmatrix} T_{lam} - T_{tool} \\ \vdots \\ T_{lam} - T_{tool} \end{pmatrix} \tag{.11}$$

$$u(t) = \begin{pmatrix} P(t)_1 \\ \vdots \\ P(t)_n \end{pmatrix} \tag{.12}$$

$$A_{nxn} = \begin{pmatrix} -\frac{1}{C_1 R_1} & \frac{1}{C_1 R_1} & 0 & \cdots & 0 \\ \frac{1}{C_2 R_1} & -\frac{R_1 + R_2}{C_2 R_1 R_2} & \ddots & \ddots & \vdots \\ 0 & \ddots & \ddots & \ddots & 0 \\ \vdots & \ddots & \ddots & \ddots & \frac{1}{C_{n-1} R_{n-1}} \\ 0 & \cdots & 0 & \frac{1}{C_n R_{n-1}} & -\frac{R_n + R_{tool} + R_{n-1}}{C_n \cdot (R_n + R_{tool}) \cdot R_{n-1}} \end{pmatrix} \tag{.13}$$

$$B = \begin{pmatrix} \frac{1}{C_1} \\ 0 \\ \vdots \\ 0 \end{pmatrix} \tag{.14}$$

$$C = \begin{pmatrix} 1 & 0 & 0 & \cdots & 0 \\ 0 & 1 & 0 & \cdots & 0 \\ 0 & 0 & 1 & \cdots & 0 \\ \vdots & \vdots & \vdots & \ddots & \\ 0 & 0 & 0 & \cdots & 1 \end{pmatrix} \tag{.15}$$

Roller Cooling:

$$x_0 = \begin{pmatrix} T_{re\prime am} - T_{tool} \\ \vdots \\ T_{re\prime am} - T_{tool} \end{pmatrix} \tag{.16}$$

$$u(t) = \begin{pmatrix} 0 \\ \vdots \\ 0 \end{pmatrix} \tag{.17}$$

$$A_{(n+1)x(n+1)} = \begin{pmatrix} -\frac{R_1+R_{roller}}{C_1R_1R_{roller}} & \frac{1}{C_1R_1} & 0 & \cdots & 0 & \frac{1}{C_1R_1R_{roller}} \\ \frac{1}{C_2R_1} & -\frac{R-1+R_2}{C_2R_1R_2} & \ddots & \ddots & \vdots & 0 \\ 0 & \ddots & \ddots & \ddots & 0 & \vdots \\ \vdots & \ddots & \ddots & \ddots & \frac{1}{C_{n-1}R_{n-1}} & \vdots \\ 0 & \cdots & 0 & \frac{1}{C_nR_{n-1}} & -\frac{R_n+R_{tool}+R_{n-1}}{C_n(R_n+R_{tool})\cdot R_{n-1}} & \vdots \\ 0 & \cdots & \cdots & \cdots & \cdots & 0 \end{pmatrix} \tag{.18}$$

$$B = \begin{pmatrix} 0 \\ \vdots \\ 0 \end{pmatrix} \tag{.19}$$

$$C = \begin{pmatrix} 1 & 0 & 0 & \cdots & 0 \\ 0 & 1 & 0 & \cdots & 0 \\ 0 & 0 & 1 & \cdots & 0 \\ \vdots & \vdots & \vdots & \ddots & \\ 0 & 0 & 0 & \cdots & 1 \end{pmatrix} \tag{.20}$$

Open Cooling:

$$x_0 = \begin{pmatrix} T_{lam} - T_{tool} \\ \vdots \\ T_{lam} - T_{tool} \end{pmatrix} \tag{.21}$$

$$u(t) = \begin{pmatrix} 0 \\ \vdots \\ 0 \end{pmatrix} \tag{.22}$$

$$A_{nxn} = \begin{pmatrix} -\frac{1}{C_1 R_1} & \frac{1}{C_1 R_1} & 0 & \cdots & 0 \\ \frac{1}{C_2 R_1} & -\frac{R_1 + R_2}{C_2 R_1 R_2} & \ddots & \ddots & \vdots \\ 0 & \ddots & \ddots & \ddots & 0 \\ \vdots & \ddots & \ddots & \ddots & \frac{1}{C_{n-1} R_{n-1}} \\ 0 & \cdots & 0 & \frac{1}{C_n R_{n-1}} & -\frac{R_n + R_{tool} + R_{n-1}}{C_n \cdot (R_n + R_{tool}) \cdot R_{n-1}} \end{pmatrix} \tag{.23}$$

$$B = \begin{pmatrix} \frac{1}{C_1} \\ 0 \\ \vdots \\ 0 \end{pmatrix} \tag{.24}$$

$$C = \begin{pmatrix} 1 & 0 & 0 & \cdots & 0 \\ 0 & 1 & 0 & \cdots & 0 \\ 0 & 0 & 1 & \cdots & 0 \\ \vdots & \vdots & \vdots & \ddots & \\ 0 & 0 & 0 & \cdots & 1 \end{pmatrix} \tag{.25}$$

F. Boundary Conditions LEM model

Table F.8.: **Boundary Conditions LEM model**

Parameter	Unit	Value
η_{laser}	1	0.8
$\eta_{laser/lam}$	1	0.47
$\eta_{laser/tape}$	1	0.53
$\eta_{laser/bound}$	1	0.16
$\lambda_{CFLMPAEK}$	W/mK	0.77
c_p	Ws/kgK	1250
$\rho_{CFLMPAEK}$	kg/m^3	1570
T_{env}	C	22
T_{tool}	C	22
T_{tape}	C	22
T_{lam}	C	22
T_{roller}	C	120
$h_{lam/tool}$	W/m^2K	250
h_{roller}	W/m^2K	325
$R_{lam/lam}$	Km^2/W	2E-4

G. Results Comparison LEM and FEM

Figure G.2.: **Comparison 2D FEM with 3D FEM for 1 ply laminate**

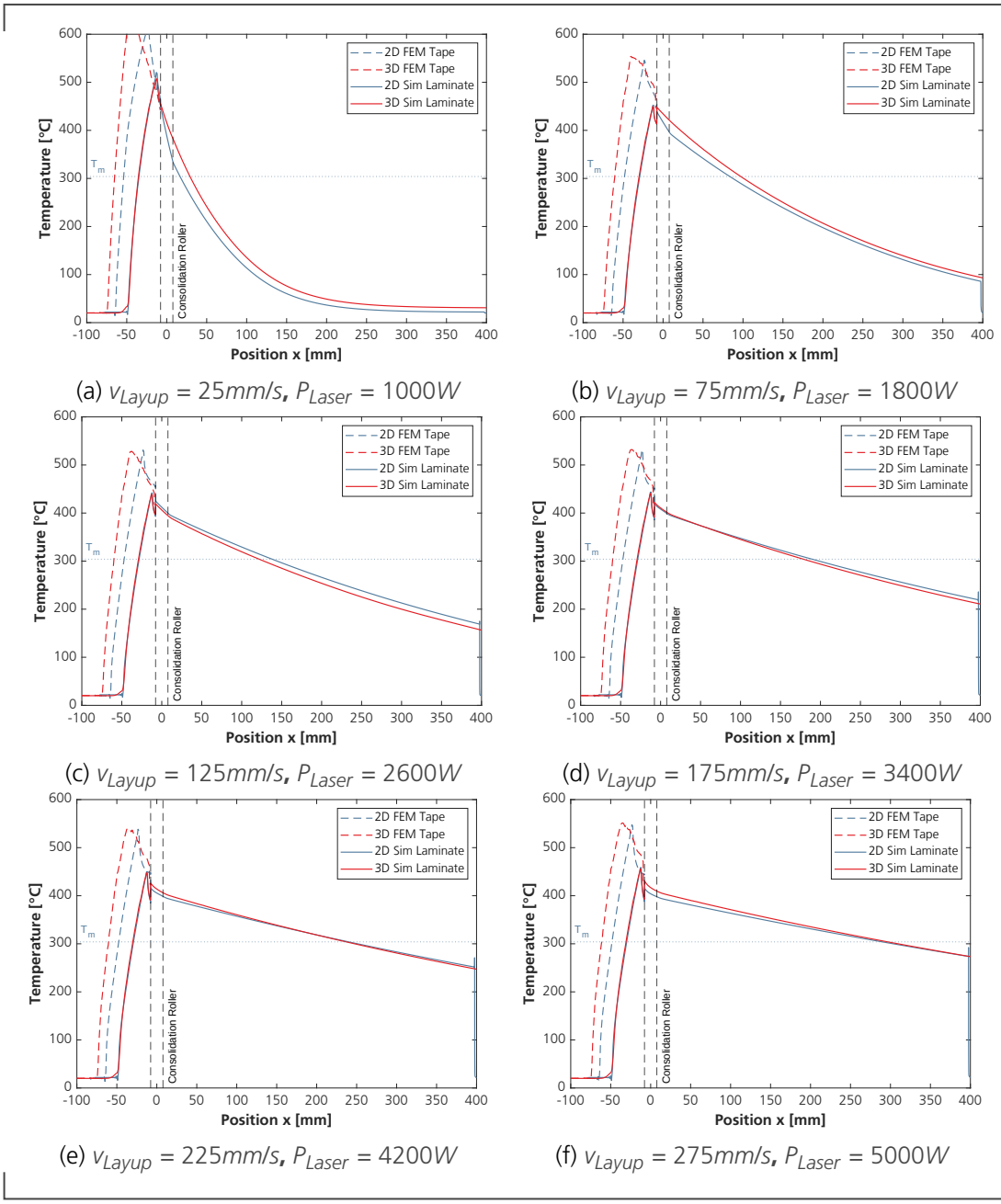

(a) $v_{Layup} = 25mm/s$, $P_{Laser} = 1000W$

(b) $v_{Layup} = 75mm/s$, $P_{Laser} = 1800W$

(c) $v_{Layup} = 125mm/s$, $P_{Laser} = 2600W$

(d) $v_{Layup} = 175mm/s$, $P_{Laser} = 3400W$

(e) $v_{Layup} = 225mm/s$, $P_{Laser} = 4200W$

(f) $v_{Layup} = 275mm/s$, $P_{Laser} = 5000W$

Figure G.3.: **Comparison 2D FEM with 3D FEM for 2 plies laminate**

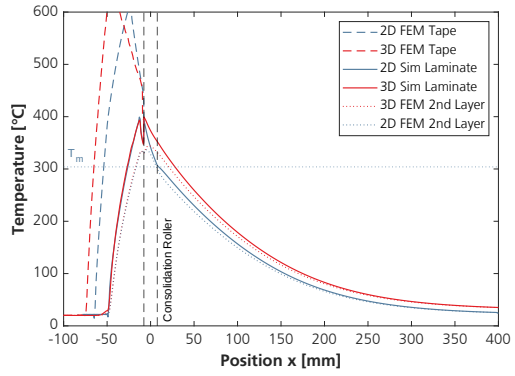

(a) $v_{Layup} = 25mm/s$, $P_{Laser} = 1000W$

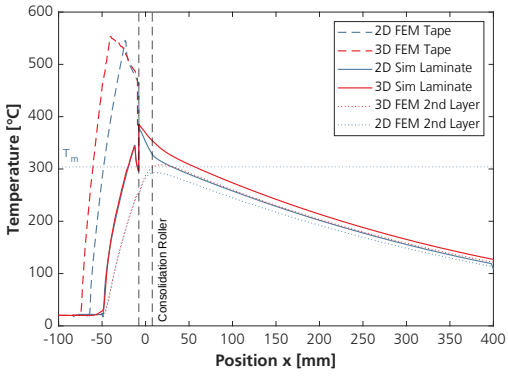

(b) $v_{Layup} = 75mm/s$, $P_{Laser} = 1800W$

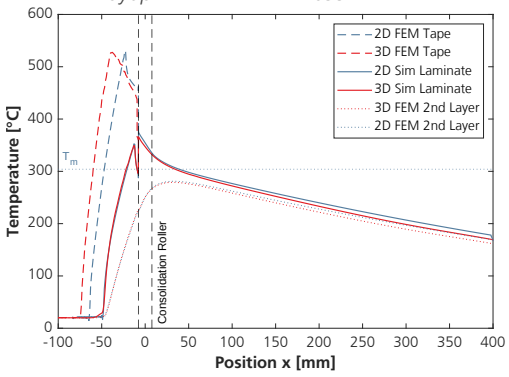

(c) $v_{Layup} = 125mm/s$, $P_{Laser} = 2600W$

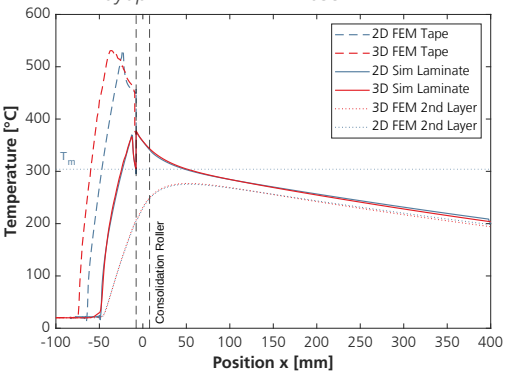

(d) $v_{Layup} = 175mm/s$, $P_{Laser} = 3400W$

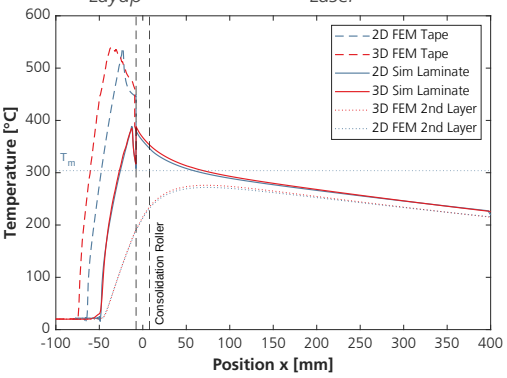

(e) $v_{Layup} = 225mm/s$, $P_{Laser} = 4200W$

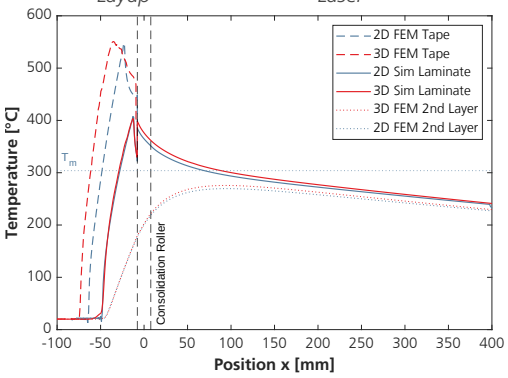

(f) $v_{Layup} = 275mm/s$, $P_{Laser} = 5000W$

Figure G.4.: **Comparison 2D FEM with 3D FEM for 3 plies laminate**

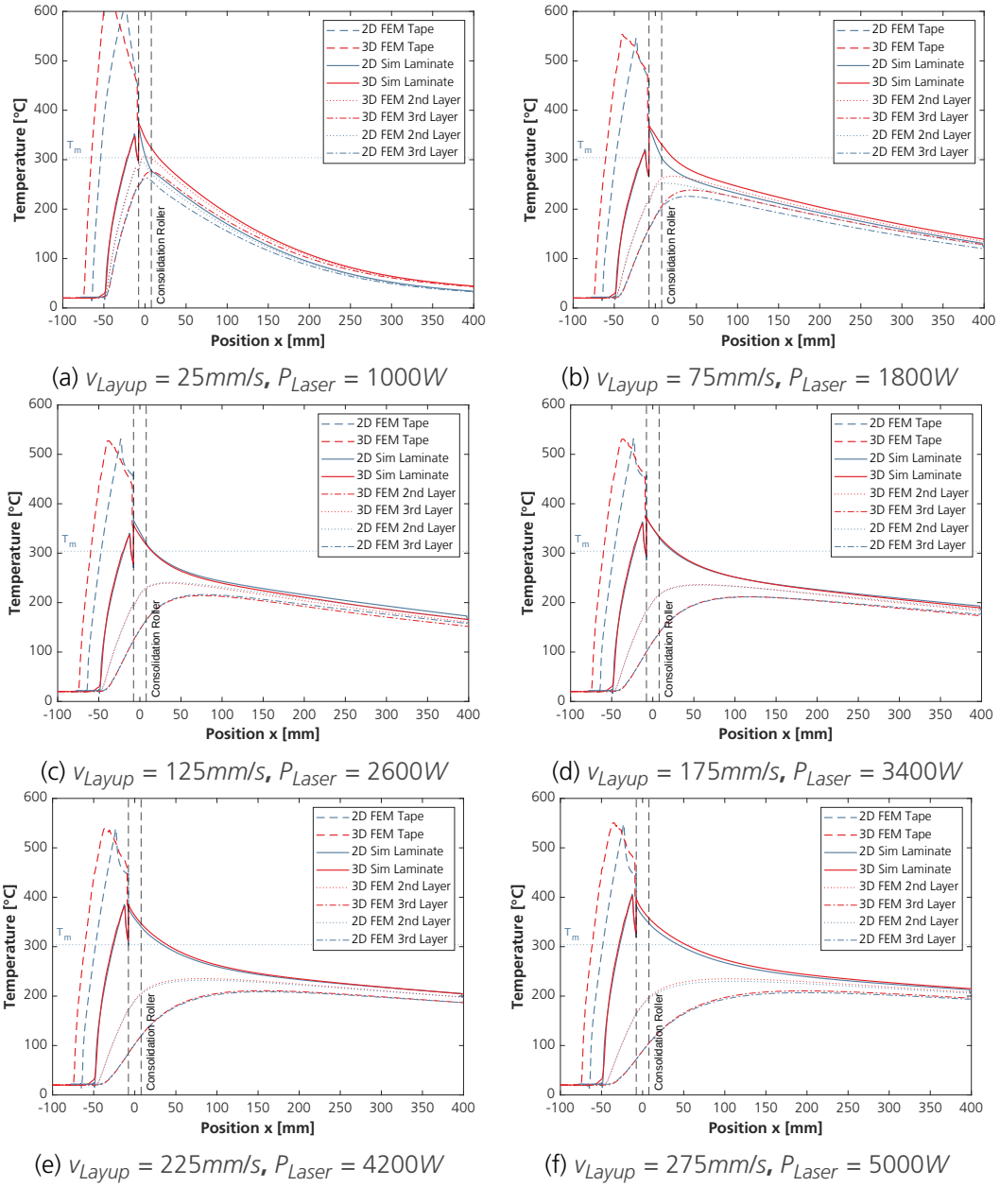

(a) $v_{Layup} = 25mm/s$, $P_{Laser} = 1000W$

(b) $v_{Layup} = 75mm/s$, $P_{Laser} = 1800W$

(c) $v_{Layup} = 125mm/s$, $P_{Laser} = 2600W$

(d) $v_{Layup} = 175mm/s$, $P_{Laser} = 3400W$

(e) $v_{Layup} = 225mm/s$, $P_{Laser} = 4200W$

(f) $v_{Layup} = 275mm/s$, $P_{Laser} = 5000W$

Figure G.5.: **Comparison 2D FEM with 3D FEM for 5 plies laminate**

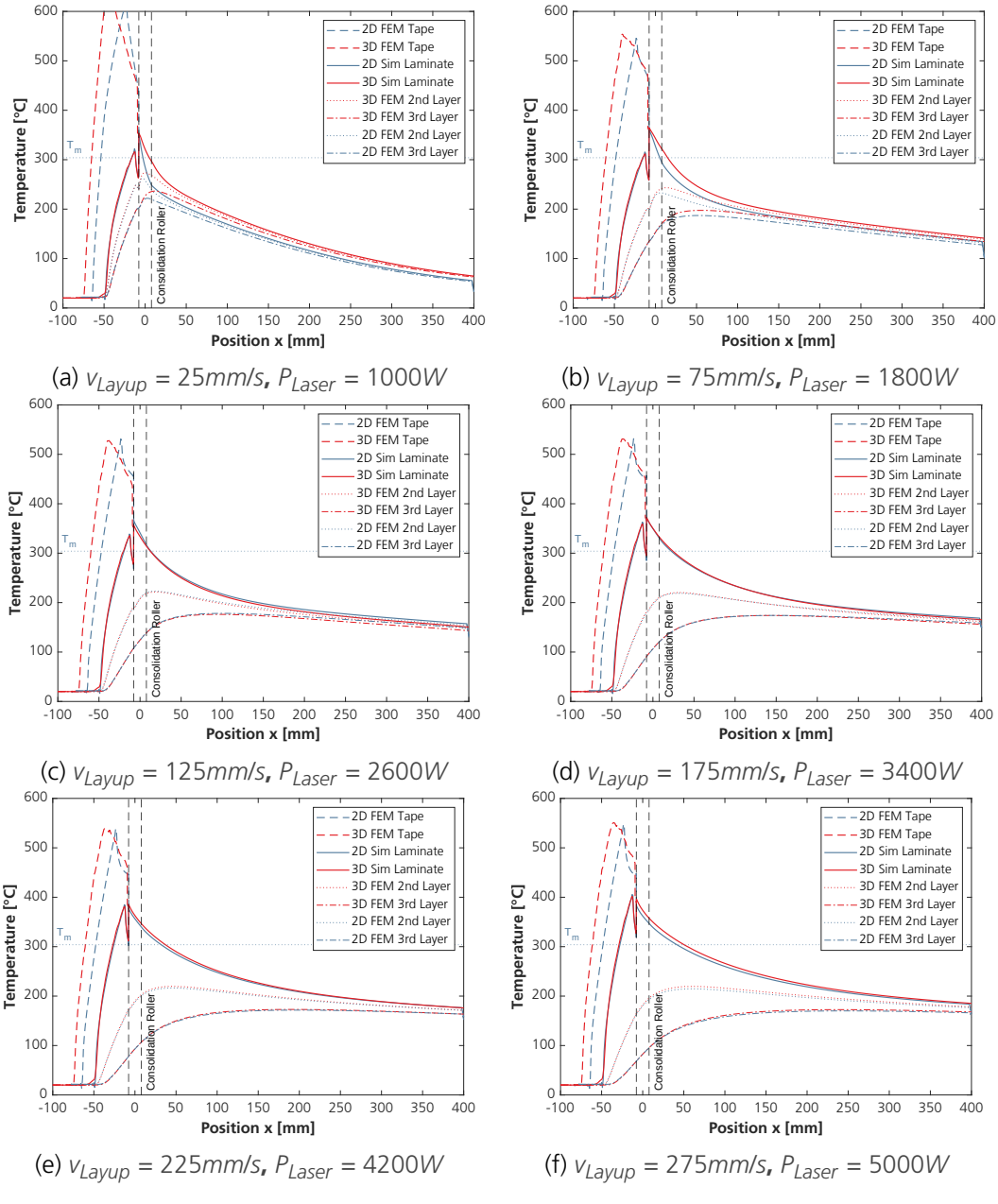

(a) $v_{Layup} = 25mm/s$, $P_{Laser} = 1000W$

(b) $v_{Layup} = 75mm/s$, $P_{Laser} = 1800W$

(c) $v_{Layup} = 125mm/s$, $P_{Laser} = 2600W$

(d) $v_{Layup} = 175mm/s$, $P_{Laser} = 3400W$

(e) $v_{Layup} = 225mm/s$, $P_{Laser} = 4200W$

(f) $v_{Layup} = 275mm/s$, $P_{Laser} = 5000W$

Figure G.6.: **Comparison LEM with 3D FEM for 1 ply laminate**

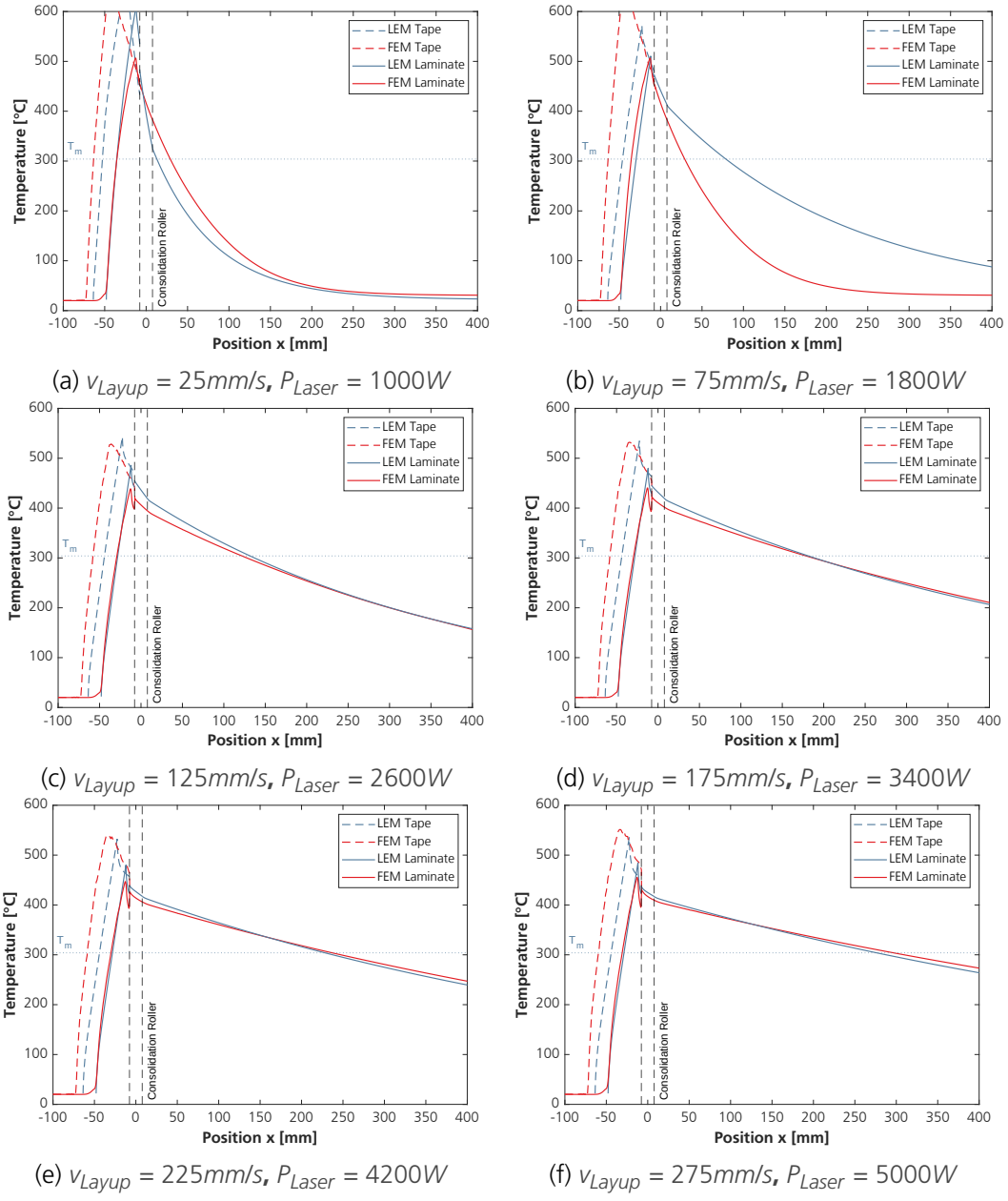

(a) v_{Layup} = 25mm/s, P_{Laser} = 1000W

(b) v_{Layup} = 75mm/s, P_{Laser} = 1800W

(c) v_{Layup} = 125mm/s, P_{Laser} = 2600W

(d) v_{Layup} = 175mm/s, P_{Laser} = 3400W

(e) v_{Layup} = 225mm/s, P_{Laser} = 4200W

(f) v_{Layup} = 275mm/s, P_{Laser} = 5000W

Figure G.7.: **Comparison LEM with 3D FEM for 2 plies laminate**

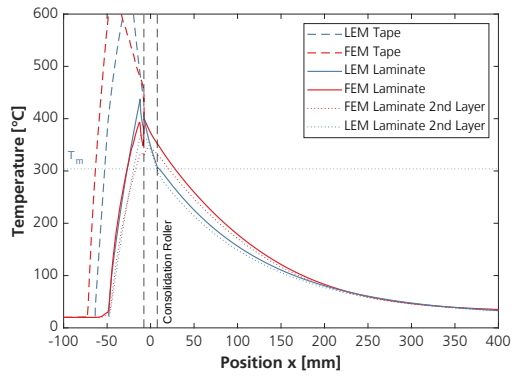

(a) $v_{Layup} = 25mm/s$, $P_{Laser} = 1000W$

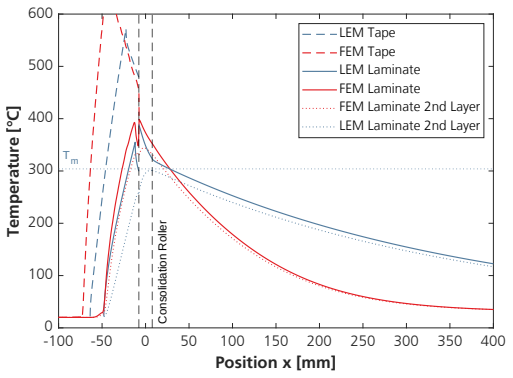

(b) $v_{Layup} = 75mm/s$, $P_{Laser} = 1800W$

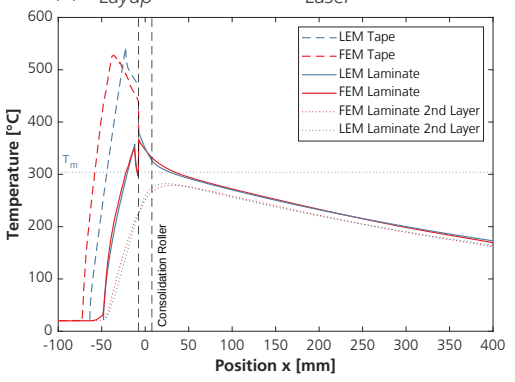

(c) $v_{Layup} = 125mm/s$, $P_{Laser} = 2600W$

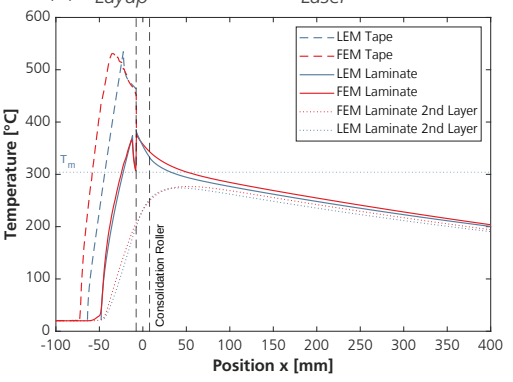

(d) $v_{Layup} = 175mm/s$, $P_{Laser} = 3400W$

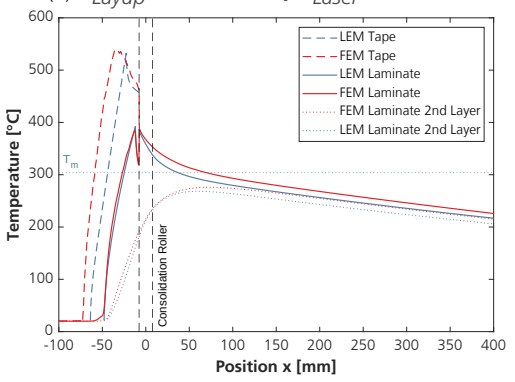

(e) $v_{Layup} = 225mm/s$, $P_{Laser} = 4200W$

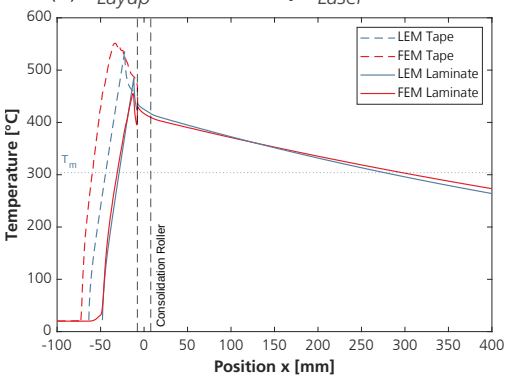

(f) $v_{Layup} = 275mm/s$, $P_{Laser} = 5000W$

Figure G.8.: **Comparison LEM with 3D FEM for 3 plies laminate**

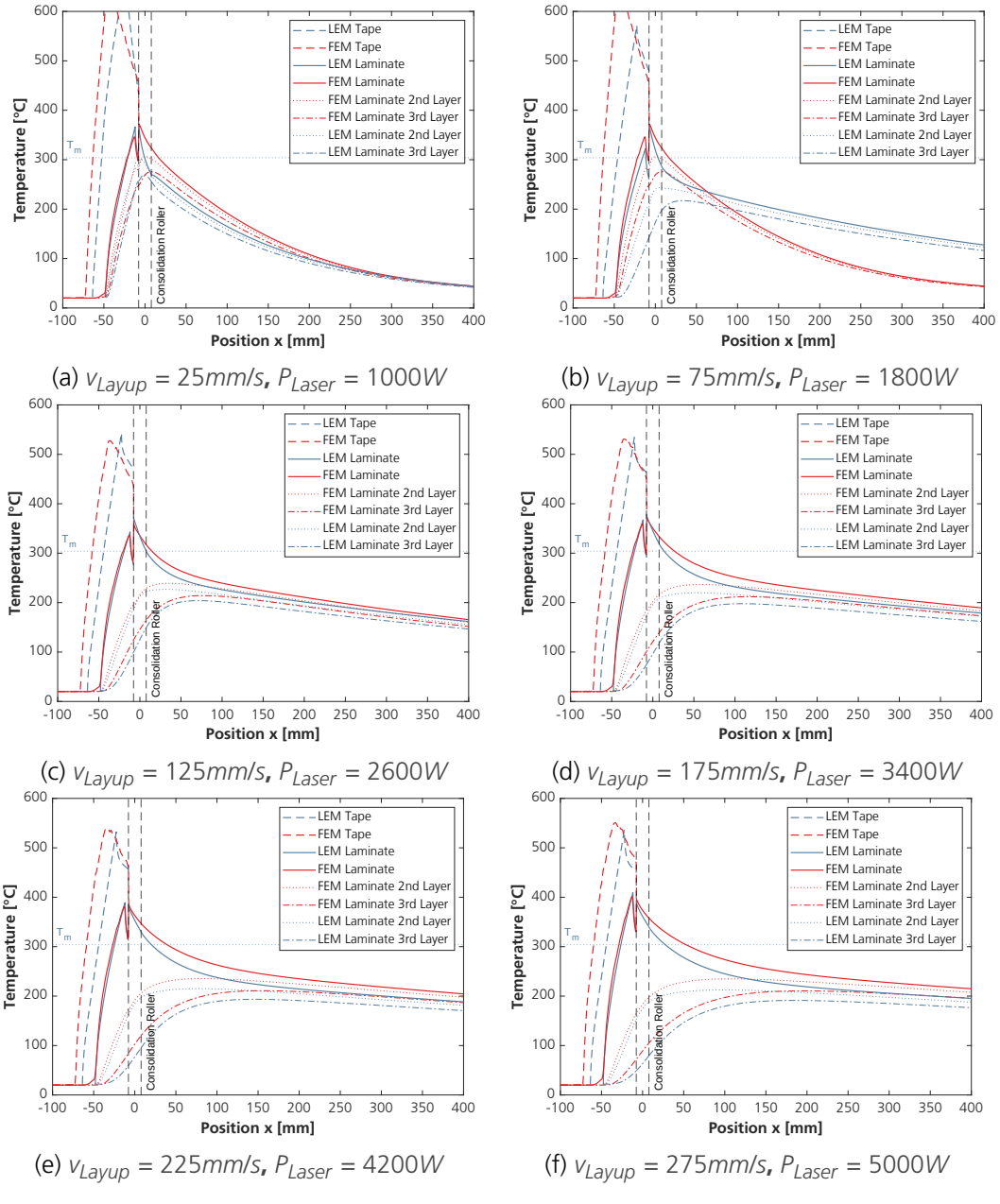

(a) $v_{Layup} = 25mm/s$, $P_{Laser} = 1000W$

(b) $v_{Layup} = 75mm/s$, $P_{Laser} = 1800W$

(c) $v_{Layup} = 125mm/s$, $P_{Laser} = 2600W$

(d) $v_{Layup} = 175mm/s$, $P_{Laser} = 3400W$

(e) $v_{Layup} = 225mm/s$, $P_{Laser} = 4200W$

(f) $v_{Layup} = 275mm/s$, $P_{Laser} = 5000W$

Figure G.9.: **Comparison LEM with 3D FEM for 5 plies laminate**

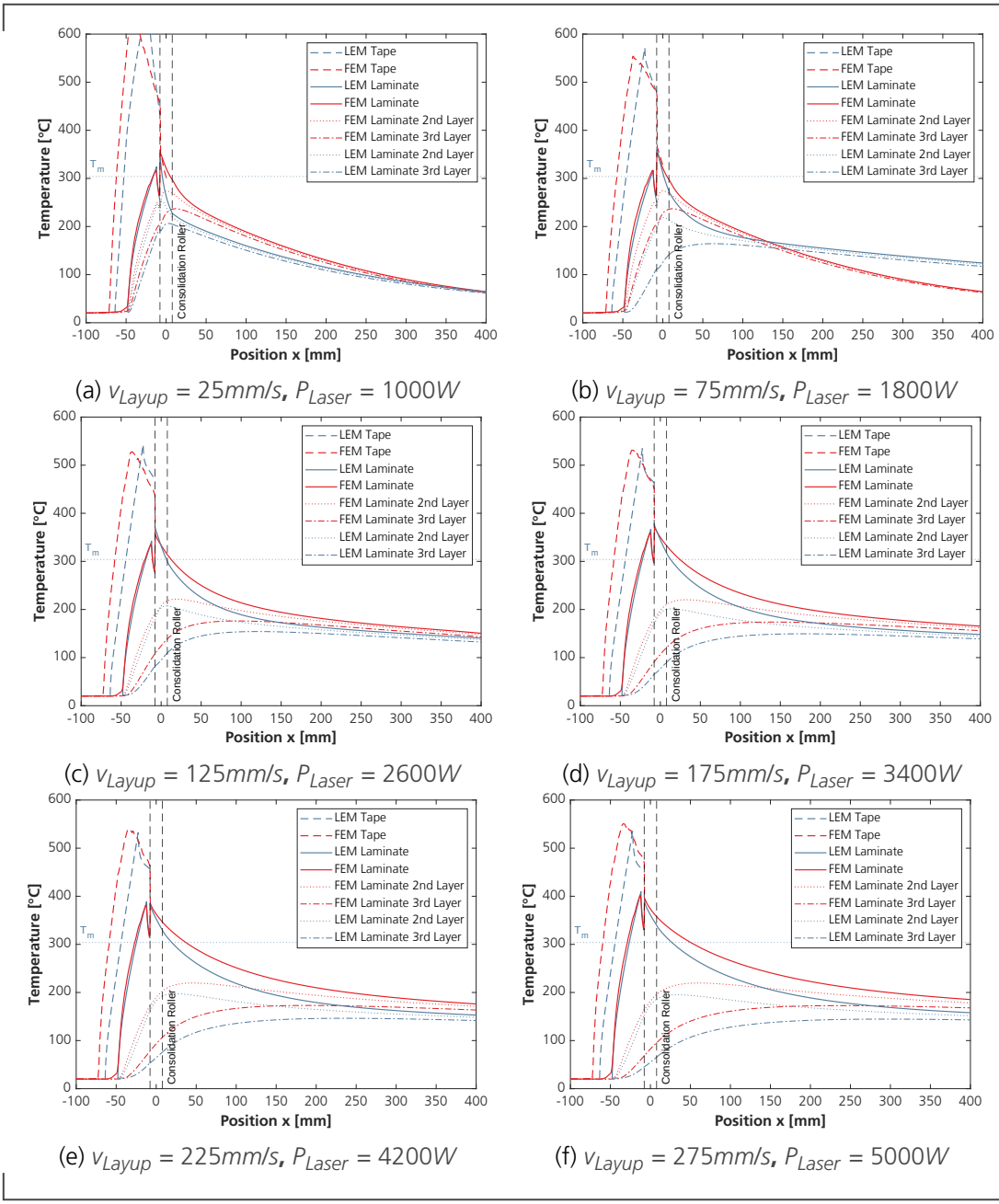

(a) $v_{Layup} = 25mm/s$, $P_{Laser} = 1000W$

(b) $v_{Layup} = 75mm/s$, $P_{Laser} = 1800W$

(c) $v_{Layup} = 125mm/s$, $P_{Laser} = 2600W$

(d) $v_{Layup} = 175mm/s$, $P_{Laser} = 3400W$

(e) $v_{Layup} = 225mm/s$, $P_{Laser} = 4200W$

(f) $v_{Layup} = 275mm/s$, $P_{Laser} = 5000W$

Bibliography

All publications produced by the author during the period of this thesis can be easily accessed via ORCID: https://orcid.org/0009-0007-8608-0759.

[1] International Air Transport Association (IATA). *Our Commitment to Fly Net Zero by 2050*. https://www.iata.org/en/programs/environment/flynetzero/ last visited on: 2023-08-02. July 2023.

[2] COMSOL AB. *COMSOL Contact Analysis Theory*. https://doc.comsol.com/5.6/doc/com.comsol.help.sme/sme_ug_theory.06.68.html last visited on: 2023-04-23.

[3] Vivek Agarwal et al. "Thermal Characterization of the Laser-Assisted Consolidation Process". In: *Journal of Thermoplastic Composite Materials* 5.2 (Apr. 1992), pp. 115–135. DOI: 10.1177/089270579200500203.

[4] Christoph Ament and Marcus Hamann. *Regelungstechnik 2*. Vorlesungsskript. 2020.

[5] Brian Anderson. *Optimal control : linear quadratic methods*. Englewood Cliffs, N.J: Prentice-Hall, 1989. ISBN: 978-0-13-638651-3.

[6] Jérémie Audoit et al. "Thermal, mechanical and dielectric behaviour of poly(aryl ether ketone) with low melting temperature". In: *Journal of Thermal Analysis and Calorimetry* 135.4 (Apr. 2018), pp. 2147–2157. DOI: 10.1007/s10973-018-7292-x.

[7] Zachary August et al. "Recent developments in automated fiber placement of thermoplastic composites". In: *SAMPE J* 50.2 (2014), pp. 30–37.

[8] Omar Baho et al. "Simulation of laser heating distribution for a thermoplastic composite: effects of AFP head parameters". In: *The International Journal of Advanced Manufacturing Technology* 110.7-8 (Sept. 2020), pp. 2105–2117. DOI: 10.1007/s00170-020-05876-9.

[9] Anaïs Barasinski et al. "An Improvement in Thermal Modelling of Automated Tape Placement Process". In: AIP, 2011. DOI: 10.1063/1.3552438.

[10] Marco Barile et al. "Thermoplastic Composites for Aerospace Applications". In: *Revolutionizing Aircraft Materials and Processes*. Springer International Publishing, 2020, pp. 87–114. DOI: 10.1007/978-3-030-35346-9_4.

[11] Jörgen Bergström. "Elasticity/Hyperelasticity". In: *Mechanics of Solid Polymers*. Elsevier, 2015, pp. 209–307. DOI: 10.1016/b978-0-323-31150-2.00005-4.

[12] T. Bernard and E. Ebrahimi Moghaddam. "Nonlinear model predictive control of a glass forming process based on a Finite Element model". In: *2006 IEEE Conference on Computer Aided Control System Design, 2006 IEEE International Conference on Control Applications, 2006 IEEE International Symposium on Intelligent Control*. IEEE, Oct. 2006. DOI: 10.1109/cacsd-cca-isic.2006.4776774.

[13] E. P. Beyeler and S. I. Guçeri. "Thermal Analysis of Laser-Assisted Thermoplastic-Matrix Composite Tape Consolidation". In: *Journal of Heat Transfer* 110.2 (May 1988), pp. 424–430. ISSN: 0022-1481. DOI: 10.1115/1.3250502. URL: https://doi.org/10.1115/1.3250502.

[14] Eric Beyeler, Walter Phillips and Selçuk I. Güçeri. "Experimental Investigation of Laser-Assisted Thermoplastic Tape Consolidation". In: *Journal of Thermoplastic Composite Materials* 1.1 (Jan. 1988), pp. 107–121. DOI: 10.1177/089270578800100109.

[15] Nicolas Boyard. *Heat Transfers in Polymer Composite Materials*. John Wiley & Sons, Ltd., Feb. 2016. 454 pp. ISBN: 978-1-84821-761-4. URL: https://www.ebook.de/de/product/23851041/nicolas_boyard_heat_transfers_in_polymer_composite_materials.html.

[16] Lars Brandt et al. "Thermocouple based process optimization for laser assisted automated fiber placement of CF/LM-PAEK". In: *Journal of Composite Materials* 57.24 (Sept. 2023), pp. 3897–3906. ISSN: 1530-793X. DOI: 10.1177/00219983231199833.

[17] Alex Brasington et al. "Automated fiber placement: A review of history, current technologies, and future paths forward". In: *Composites Part C: Open Access* 6 (Oct. 2021), p. 100182. DOI: 10.1016/j.jcomc.2021.100182.

[18] C. Brecher et al. "Adaptive tape placement process control at geometrically changing substrates". In: *Procedia CIRP* 85 (2019), pp. 207–211. DOI: 10.1016/j.procir.2019.09.018.

[19] Christine A. Butler et al. "An Analysis of Mechanisms Governing Fusion Bonding of Thermoplastic Composites". In: *Journal of Thermoplastic Composite Materials* 11.4 (July 1998), pp. 338–363. DOI: 10.1177/089270579801100404.

[20] F. C. Campbell. *Manufacturing processes for advanced composites*. New York: Elsevier, 2004. ISBN: 978-1-85617-415-2.

[21] Ozan Çelik et al. "Deconsolidation of thermoplastic prepreg tapes during rapid laser heating". In: *Composites Part A: Applied Science and Manufacturing* 149 (Oct. 2021), p. 106575. DOI: 10.1016/j.compositesa.2021.106575.

[22] Ozan Çelik et al. "Intimate contact development during laser assisted fiber placement: Microstructure and effect of process parameters". In: *Composites Part A: Applied Science and Manufacturing* 134 (July 2020), p. 105888. DOI: 10.1016/j.compositesa.2020.105888.

[23] A.R. Chadwick, K. Kotzur and S. Nowotny. "Moderation of thermoplastic composite crystallinity and mechanical properties through in situ manufacturing and post-manufacturing tempering: Part 1 – Mechanical characterisation". In: *Composites Part A: Applied Science and Manufacturing* 143 (Apr. 2021), p. 106286. DOI: 10.1016/j.compositesa.2021.106286.

[24] S. Chand. "Review Carbon fibers for composites". In: *Journal of Materials Science* 35.6 (2000), pp. 1303–1313. DOI: 10.1023/a:1004780301489.

[25] I.Y. Chang and J.K. Lees. "Recent Development in Thermoplastic Composites: A Review of Matrix Systems and Processing Methods". In: *Journal of Thermoplastic Composite Materials* 1.3 (July 1988), pp. 277–296. DOI: 10.1177/089270578800100305.

[26] Jiping Chen, Kunkun Fu and Yan Li. "Understanding processing parameter effects for carbon fibre reinforced thermoplastic composites manufactured by laser-assisted automated fibre placement (AFP)". In: *Composites Part A: Applied Science and Manufacturing* 140 (Jan. 2021), p. 106160. DOI: 10.1016/j.compositesa.2020.106160.

[27] F. Chinesta et al. "First steps towards an advanced simulation of composites manufacturing by automated tape placement". In: *International Journal of Material Forming* 7.1 (Sept. 2014), pp. 81–92. DOI: 10.1007/s12289-012-1112-9.

[28] F. N. Cogswell. *Thermoplastic aromatic polymer composites : a study of the structure, processing, and properties of carbon fibre reinforced polyetheretherketone and related materials*. Oxford England Boston: Butterworth-Heinemann, 1992. ISBN: 978-0-7506-1086-5.

[29] J. Colton and D. Leach. "Processing parameters for filament winding thick-section PEEK/carbon fiber composites". In: *Polymer Composites* 13.6 (Dec. 1992), pp. 427–434. DOI: 10.1002/pc.750130605.

[30] A.J. Comer et al. "Mechanical characterisation of carbon fibre–PEEK manufactured by laser-assisted automated-tape-placement and autoclave". In: *Composites Part A: Applied Science and Manufacturing* 69 (Feb. 2015), pp. 10–20. DOI: 10.1016/j.compositesa.2014.10.003.

[31] *D2344/D2344M-16, Standard Test Method for Short-Beam Strength of Polymer Matrix Composite Materials and Their Laminates*. ASTM International, 2016.

[32] Shao-Cong Dai and Lin Ye. "GF/PP Tape Winding with On-Line Consolidation". In: *Journal of Reinforced Plastics and Composites* 21.1 (Jan. 2002), pp. 71–90. DOI: 10.1106/073168402024283.

[33] P. H. Dara and Alfred C. Loos. "Thermoplastic matrix composite processing model". In: Virginia Polytechnic Inst. and State Univ. Blacksburg, VA, United States. 1985.

[34] Berend Denkena, Carsten Schmidt and Patricc Weber. "Automated Fiber Placement Head for Manufacturing of Innovative Aerospace Stiffening Structures". In: *Procedia Manufacturing* 6 (2016), pp. 96–104. DOI: 10.1016/j.promfg.2016.11.013.

[35] Mattia Di Francesco et al. "Influence of laser power density on the mesostructure of thermoplastic composite preforms manufactured by Automated Fibre Placement". English. In: *International SAMPE Technical Conference*. Vol. 2016-January. SAMPE Long Beach 2016 Conference and Exhibition ; Conference date: 23-05-2016 Through 26-05-2016. United States: Society for the Advancement of Material and Process Engineering, May 2016. ISBN: 978-1-934551-23-3.

[36] Mattia Di Francesco et al. "Influence of layup speed on the quality of thermoplastic preforms manufactured by laser-assisted automated fibre placement". In: *ECCM17-17th European Conference on Composite Materials, Munich, Germany*. 2016.

[37] *DIN 51007:2019-04, Thermische Analyse_(TA)_- Differenz-Thermoanalyse_(DTA) und Dynamische Differenzkalorimetrie_(DSC)_- Allgemeine Grundlagen*. DIN Deutsches Institut für Normung e.V. DOI: 10.31030/3025544.

[38] *DIN EN 2563, Unidirektionale Laminate Bestimmung der scheinbaren interlaminaren Scherfestigkeit*. DIN Deutsches Institut für Normung e.V, 1997.

[39] *DIN EN 2597, Kohlenstoffaserverstärkte Kunststoffe Unidirektionale Laminate Zugversuch senkrecht zur Faserrichtung*. DIN Deutsches Institut für Normung e.V, 1998.

[40] Georg Doll. "Thermoplastic composites technologies for future aircraft structures". In: *Proceedings*. Springer Fachmedien Wiesbaden, 2021, pp. 129–138. DOI: 10.1007/978-3-658-29701-5_11.

[41] Rickey Dubay et al. "Finite element based model predictive control for active vibration suppression of a one-link flexible manipulator". In: *ISA Transactions* 53.5 (Sept. 2014), pp. 1609–1619. DOI: 10.1016/j.isatra.2014.05.023.

[42] AVK - Industrievereinigung Verstärkte Kunststoffe e.V., ed. *Handbuch Faserverbundkunststoffe/Composites*. Gabler, Betriebswirt.-Vlg, 2014. 601 pp. ISBN: 978-3-658-02755-1. URL: https://www.ebook.de/de/product/22508807/handbuch_faserverbundkunststoffe_composites.html.

[43] Ralf Engelhardt et al. "In Situ Joining of Unidirectional Tapes on Long Fiber Reinforced Thermoplastic Structures by Thermoplastic Automated Fiber Placement for Scientific Sounding Rocket Applications". In: *Procedia CIRP* 85 (2019), pp. 189–194. DOI: 10.1016/j.procir.2019.09.015.

[44] Erich Fitzer. *Carbon fibres and their composites*. Berlin New York New York: Springer-Verlag UNFSSTD, 1985. ISBN: 978-3-540-15804-2.

[45] R. Fletcher. *Practical Methods of Optimization*. Wiley & Sons, Limited, John, 2013, p. 248. ISBN: 978-1-118-72320-3.

[46] Rob Flynn, Justin Nielson and Todd Rudberg. "Production Implementation of Multiple Machine, High Speed Fiber Placement for Large Structures". In: *SAE International Journal of Aerospace* 3.2010-01-1877 (2010), pp. 216–223.

[47] Mattia Di Francesco et al. "Heater power control for multi-material, variable speed Automated Fibre Placement". In: *Composites Part A: Applied Science and Manufacturing* 101 (Oct. 2017), pp. 408–421. DOI: 10.1016/j.compositesa.2017.06.015.

[48] Fujifilm. *Pressure measurement film Prescale*. https://www.fujifilm.com/de/en/business/inspection/measurement-film/prescale/feature last visited on: 2022-09-22.

[49] R. Funck and M. Neitzel. "Improved thermoplastic tape winding using laser or direct-flame heating". In: *Composites Manufacturing* 6.3-4 (Jan. 1995), pp. 189–192. DOI: 10.1016/0956-7143(95)95010-v.

[50] Shang-Lin Gao and Jang-Kyo Kim. "Cooling rate influences in carbon fibre/PEEK composites. Part 1. Crystallinity and interface adhesion". In: *Composites Part A: Applied Science and Manufacturing* 31.6 (June 2000), pp. 517–530. DOI: 10.1016/s1359-835x(00)00009-9.

[51] Carlos E. García, David M. Prett and Manfred Morari. "Model predictive control: Theory and practice—A survey". In: *Automatica* 25.3 (May 1989), pp. 335–348. DOI: 10.1016/0005-1098(89)90002-2.

[52] Ginger Gardiner. *Consolidating thermoplastic composite aerostructures in place, Part 1*. https://www.compositesworld.com/articles/consolidating-thermoplastic-composite-aerostructures-in-place-part-1 visited on 2022-01-26. 2018.

[53] Ginger Gardiner. *Thermoplastic composite demonstrators - EU roadmap for future airframes*. https://www.compositesworld.com/articles/thermoplastic-composite-demonstrators-eu-roadmap-for-future-airframes- last visted on: 2022-01-26. 2018.

[54] P. G. de Gennes. "Reptation of a Polymer Chain in the Presence of Fixed Obstacles". In: *The Journal of Chemical Physics* 55.2 (July 1971), pp. 572–579. DOI: 10.1063/1.1675789.

[55] Stuart Green. *Victrex AE250 - A novel polyaryletherketone polymer suited to automated tape placement and out of autoclave processing*. Tech. rep. https://www.victrex.com/-/media/downloads/whitepapers/victrex-ae-250---technical-paper-camx-2018_2.pdf last visited on: 2023-04-03. Victrex, 2019.

[56] W.J.B. Grouve. "Weld strength of laser-assisted tape-placed thermoplastic composites". PhD thesis. Universiteit Twente, 2012. DOI: 10.3990/1.9789036533928.

[57] W.J.B. Grouve et al. "Optimization of the tape placement process parameters for carbon–PPS composites". In: *Composites Part A: Applied Science and Manufacturing* 50 (July 2013), pp. 44–53. DOI: 10.1016/j.compositesa.2013.03.003.

[58] S.M. Grove. "Thermal modelling of tape laying with continuous carbon fibre-reinforced thermoplastic". In: *Composites* 19.5 (Sept. 1988), pp. 367–375. DOI: 10.1016/0010-4361(88)90124-3.

[59] Mark B Gruber, Mark A Lamontia and Brian J Waibel. "Automated fabrication processes for large composite aerospace structures: A trade study". In: *International SAMPE symposium and exhibition*. SAMPE; 1999. 2001, pp. 1986–1997.

[60] Mark B Gruber et al. "Thermoplastic in situ placement requires better impregnated tapes and tows". In: *Proceedings of the 2012 SAMPE conference and exhibition, Baltimore, MD*. 2012.

[61] X Guan and R Pitchumani. "Modeling of spherulitic crystallization in thermoplastic tow-placement process: heat transfer analysis". In: *Composites Science and Technology* 64.9 (July 2004), pp. 1123–1134. DOI: 10.1016/j.compscitech.2003.08.011.

[62] Thomas Guglhör. "Experimentelle und modellhafte Betrachtung des Konsolidierungsprozesses von carbonfaserverstärktem Polyamid-6". Doctoral Thesis. Universität Augsburg, 2017.

[63] Minh Binh Ha, Minh Binh Chu and Victor Sreeram. "Comparison between balanced truncation and modal truncation techniques for linear state-space symmetric systems". In: *IET Control Theory and Applications* 9.6 (Apr. 2015), pp. 900–904. DOI: 10.1049/iet-cta.2014.0919.

[64] Amir Hajiloo et al. "Thermal control design for an automated fiber placement machine". In: *Science and Engineering of Composite Materials* 21.3 (Jan. 2014). DOI: 10.1515/secm-2013-0009.

[65] Zhenyu Han et al. "Parametric Study on Heat Transfer for Tow Placement Process of Thermoplastic Composite". In: *Polymers and Polymer Composites* 22.8 (Oct. 2014), pp. 713–722. DOI: 10.1177/096739111402200810.

[66] Karl Stephan Hans Dieter Baehr. *Wärme- und Stoffübertragung*. Springer-Verlag GmbH, Aug. 2008. 789 pp. ISBN: 978-3-540-87689-2. URL: https://www.ebook.de/de/product/25408267/hans_dieter_baehr_karl_stephan_waerme_und_stoffuebertragung.html.

[67] D Heider and John W. Gillespie Jr. "Adaptive temperature control for the thermoplastic tow-placement". In: *Proceedings of the 43rd International SAMPE Symposium/Exhibition, Materials and Process Affordability—Keys to the Future, Part*. Vol. 1. 1998.

[68] Dirk Heider, Michael J. Piovoso and John W. Gillespie. "A neural network model-based open-loop optimization for the automated thermoplastic composite tow-placement system". In: *Composites Part A: Applied Science and Manufacturing* 34.8 (Aug. 2003), pp. 791–799. DOI: 10.1016/s1359-835x(03)00120-9.

[69] Dirk Heider, Michael J. Piovoso and John W. Gillespie Jr. "Application of a neural network to improve an automated thermoplastic tow-placement process". In: *Journal of Process Control* 12.1 (Jan. 2002), pp. 101–111. DOI: 10.1016/s0959-1524(00)00064-0.

[70] Berthold Heinrich. *Grundlagen Regelungstechnik*. Springer Fachmedien Wiesbaden, Oct. 2021. 275 pp. URL: https://www.ebook.de/de/product/41446934/berthold_heinrich_grundlagen_regelungstechnik.html.

[71] Florian Henne et al. "Thermoplastic in situ fiber placement for future solid rocket motor casings manufacturing". In: *SAMPE Europe SETEC* (2014).

[72] Hexcel. *HexTow AS4 Product Data Sheet*. https://www.hexcel.com/user_area/content_media/raw/AS4_HexTow_DataSheet.pdf last visited on: 2021-12-23.

[73] Suong Van Hoa, Minh Duc Hoang and Jeff Simpson. "Manufacturing procedure to make flat thermoplastic composite laminates by automated fibre placement and their mechanical properties". In: *Journal of Thermoplastic Composite Materials* 30.12 (Sept. 2016), pp. 1693–1712. DOI: 10.1177/0892705716662516.

[74] Ch. Hopmann et al. "Simulation of shrinkage and warpage of semi-crystalline thermoplastics". In: *AIP Conference Proceedings*. AIP, 2015. DOI: 10.1063/1.4918413.

[75] J van Ingen et al. "Double curved thermoplastic orthogrid rear fuselage shell". In: *SAMPE Europe Conference. Nantes, France*. 2019, pp. 1–10.

[76] John H. Lienhard IV and John H. Lienhard V. *A Heat Transfer Textbook*. Phlogiston Press, 2020.

[77] Shridhar R. Iyer and Lawrence T. Drzal. "Manufacture of Powder-Impregnated Thermoplastic Composites". In: *Journal of Thermoplastic Composite Materials* 3.4 (Oct. 1990), pp. 325–355. DOI: 10.1177/089270579000300404.

[78] Darryl L. James and W. Z. Black. "Thermal Analysis of Continuous Filament-Wound Composites". In: *Journal of Thermoplastic Composite Materials* 9.1 (Jan. 1996), pp. 54–75. DOI: 10.1177/089270579600900105.

[79] Kyle A. Jeffries. "Enhanced Robotic Automated Fiber Placement with Accurate Robot Technology and Modular Fiber Placement Head". In: *SAE International Journal of Aerospace* 6.2 (Sept. 2013), pp. 774–779. DOI: 10.4271/2013-01-2290.

[80] Brian J Jensen et al. "Materials for heated head automated thermoplastic tape placement". In: *Proceedings of the 2012 SAMPE Conference and Exhibition, Baltimore, MD*. 2012.

[81] Gautam Jeyakodi and Sonell Shroff. "Finite element simulation of in-situ consolidation of fibre placed thermoplastic laminate for prediction of residual stresses and laminate quality". In: *Third Symposium on Automated Composites Manufacturing (ACM3)*. 2017.

[82] Muhammad Amir Khan, Peter Mitschang and Ralf Schledjewski. "Tracing the Void Content Development and Identification of its Effecting Parameters during in Situ Consolidation of Thermoplastic Tape Material". In: *Polymers and Polymer Composites* 18.1 (Jan. 2010), pp. 1–15. DOI: 10.1177/096739111001800101.

[83] Salman Khan. "Thermal control system design for automated fiber placement process". MA thesis. Concordia University, 2011.

[84] Hee June Kim, Sun Kyung Kim and Woo Il Lee. "A study on heat transfer during thermoplastic composite tape lay-up process". In: *Experimental Thermal and Fluid Science* 13.4 (Nov. 1996), pp. 408–418. DOI: 10.1016/s0894-1777(96)00095-7.

[85] Young Hwa Kim and Richard P. Wool. "A theory of healing at a polymer-polymer interface". In: *Macromolecules* 16.7 (July 1983), pp. 1115–1120. DOI: 10.1021/ma00241a013.

[86] Thijs Kok. "On the consolidation quality in laser assisted fiber placement: the role of the heating phase". PhD thesis. 2018. DOI: 10.3990/1.9789036546065.

[87] Andreas Kollmannsberger. "Heating characteristics of fixed focus laser assisted Thermoplastic - Automated Fiber Placement of 2D and 3D parts". Dissertation. München: Technische Universität München, 2019.

[88] Andreas Kollmannsberger et al. "Numerical analysis of the temperature profile during the laser-assisted automated fiber placement of CFRP tapes with thermoplastic matrix". In: *Journal of Thermoplastic Composite Materials* 31.12 (2018), pp. 1563–1586. DOI: 10.1177/0892705717738304. eprint: https://doi.org/10.1177/0892705717738304. URL: https://doi.org/10.1177/0892705717738304.

[89] Patrick Kölzer. "Temperaturerfassungssystem und Prozessregelung des laserunterstützten Wickelns und Tapelegens von endlos faserverstärkten thermoplastischen Verbundkunststoffen". Zugl.: Aachen, Techn. Hochsch., Diss., 2008. PhD thesis. Aachen, 2008, IX, 145 S. : Ill., graph. Darst. URL: https://publications.rwth-aachen.de/record/50377.

[90] Laserline. *Handbuch Lichtleitfaser*. 1_01_01. Laserline GmbH. 2018.

[91] Laserline. *Hochleistungsdiodenlaser für die Industrie*. https://www.laserline.com/de-int/hochleistungsdiodenlaser/ last visited on: 2023-04-05.

[92] Laserline. *Inbetriebnahmehandbuch Diodenlaser*. 1st ed. Laserline GmbH. 2020.

[93] Laserline. *OTS Optics Power on the Spot*. https://www.laserline.com/fileadmin/Katalog/Produkte/Laserline-OTS-optics-OTSOptics-power-on-the-spot/Laserline-OTS-optics-OTSOptics-power-on-the-spot.html last visited on: 2023-04-17.

[94] Munki Lee. "Heat transfer and consolidation modeling of composite fiber tow in fiber placement". PhD thesis. Virginia Polytechnic Institute and State University, 2004.

[95] Woo Il Lee and George S. Springer. "A Model of the Manufacturing Process of Thermoplastic Matrix Composites". In: *Journal of Composite Materials* 21.11 (Nov. 1987), pp. 1017–1055. DOI: 10.1177/002199838702101103.

[96] Michael LeGault. *Building a better tail boom*. http://short.compositesworld.com/158cG3pz last visited on: 2022-01-26. 2013.

[97] François Lemarchand et al. "A Multi-scale Method to Predict Residual Stress Appearance in the Process of on-line Consolidation of Thermoplastic Composites". In: *International Journal of Forming Processes* 10.4 (Dec. 2007), pp. 471–498. DOI: 10.3166/ijfp.10.471-498.

[98] Alberto Leva, Simone Formentin and Silvano Seva. "Overlapping-Horizon MPC: A Novel Approach to Computational Constraints in Real-Time Predictive Control". en. In: Schloss Dagstuhl – Leibniz-Zentrum für Informatik, 2022. DOI: 10.4230/OASICS.NG-RES.2022.3.

[99] Arthur Levy et al. "Inter-layer thermal contact resistance evolution with the degree of intimate contact in the processing of thermoplastic composite laminates". In: *Journal of Composite Materials* 48.4 (Feb. 2013), pp. 491–503. DOI: 10.1177/0021998313476318.

[100] Arthur Levy et al. "Modeling of inter-layer thermal contact resistance during thermoplastic tape placement". In: *International SAMPE Technical Conference, Baltimore, MA, USA*. 2012.

[101] Arthur Levy et al. "Simulation And Optimization Of The Thermoplastic Automated Tape Placement (ATP) Process". In: Jan. 2012.

[102] Zhimeng Li, Tao Yang and Yu Du. "Dynamic finite element simulation and transient temperature field analysis in thermoplastic composite tape lay-up process". In: *Journal of Thermoplastic Composite Materials* 28.4 (May 2015), pp. 558–573. DOI: 10.1177/0892705713486135.

[103] P. F. Lichtenwalner. "Neural network-based control for the fiber placement composite manufacturing process". In: *Journal of Materials Engineering and Performance* 2.5 (Oct. 1993), pp. 687–691. DOI: 10.1007/bf02650058.

[104] Boris Lohmann and Behnam Salimbahrami. "Ordnungsreduktion mittels Krylov-Unterraummethoden (Order Reduction using Krylov Subspace Methods)". In: *at - Automatisierungstechnik* 52.1 (Jan. 2004), pp. 30–38. DOI: 10.1524/auto.52.1.30.25436.

[105] Xin Long. "Finite element analysis of residual stress generation during spot welding and its affect on fatigue behavior of spot welded joints". PhD thesis. University of Missouri Libraries, 1971. DOI: 10.32469/10355/4171.

[106] Dirk H.-J.A. Lukaszewicz, Carwyn Ward and Kevin D. Potter. "The engineering aspects of automated prepreg layup: History, present and future". In: *Composites Part B: Engineering* 43.3 (Apr. 2012), pp. 997–1009. DOI: 10.1016/j.compositesb.2011.12.003.

[107] Jan Lunze. *Regelungstechnik 1*. Springer-Verlag GmbH, Aug. 2014. 728 pp. ISBN: 978-3-642-53909-1. URL: https://www.ebook.de/de/product/23218029/jan_lunze_regelungstechnik_1.html.

[108] Jan Lunze. *Regelungstechnik 2*. Springer-Verlag GmbH, Aug. 2014. 682 pp. ISBN: 978-3-642-53944-2. URL: https://www.ebook.de/de/product/25412814/jan_lunze_regelungstechnik_2.html.

[109] Susan C. Mantell and George S. Springer. "Manufacturing Process Models for Thermoplastic Composites". In: *Journal of Composite Materials* 26.16 (Jan. 1992), pp. 2348–2377. DOI: 10.1177/002199839202601602.

[110] Rudi Marek and Klaus Nitsche. *Praxis der Wärmeübertragung: Grundlagen-Anwendungen-Übungsaufgaben*. Carl Hanser Verlag GmbH Co KG, 2019.

[111] Dennis Maurer and Peter Mitschang. "Laser-powered tape placement process – simulation and optimization". In: *Advanced Manufacturing: Polymer & Composites Science* 1.3 (July 2015), pp. 129–137. DOI: 10.1080/20550340.2015.1114798.

[112] Justin Merotte et al. "Automated Fiber Placement of Thermoplastic Materials: Pursuit of Low Porosity Without the Autoclave". In: *SAMPE 2019 - Charlotte, NC*. SAMPE, Apr. 2019. DOI: 10.33599/nasampe/s.19.1564.

[113] L. Meyer, S. Jayaram and E. Cherney. "Thermal characteristics of filled silicone rubber under laser heating". In: *2003 Annual Report Conference on Electrical Insulation and Dielectric Phenomena*. IEEE, 2003. DOI: 10.1109/ceidp.2003.1254873.

[114] D. Modi et al. "Thermoplastic composites: in-situ consolidation or in-situ welding?" en. In: (2013). DOI: 10.13140/RG.2.1.3454.5682.

[115] P Monnot, D Williams and MD Francesco. "Power control of a flashlamp-based heating solution for Automated Dry Fibre Placement". In: *ECCM18-18th European Conference on Composite Materials*. 2018.

[116] M. Mooney. "A Theory of Large Elastic Deformation". In: *Journal of Applied Physics* 11.9 (Sept. 1940), pp. 582–592. DOI: 10.1063/1.1712836.

[117] Jae-Do Nam and James C. Seferis. "Generalized composite degradation kinetics for polymeric systems under isothermal and nonisothermal conditions". In: *Journal of Polymer Science Part B: Polymer Physics* 30.5 (Apr. 1992), pp. 455–463. DOI: 10.1002/polb.1992.090300505.

[118] Manfred Neitzel, Peter Mitschang and Ulf Breuer, eds. *Handbuch Verbundwerkstoffe*. Hanser, Carl GmbH + Co., July 3, 2014. 576 pp. ISBN: 978-3-446-43697-8. URL: https://www.ebook.de/de/product/22572119/handbuch_verbundwerkstoffe.html.

[119] M. N. Ghasemi Nejhad, J. W. Gillespie and R. D. Cope. "Prediction of Process-Induced Stresses for In-Situ Thermoplastic Filament Winding of Cylinders". In: *Computer Aided Design in Composite Material Technology III*. Springer Netherlands, 1992, pp. 225–253. DOI: 10.1007/978-94-011-2874-2_15.

[120] M.N. Ghasemi Nejhad, R.D. Cope and S.I. Güceri. "Thermal Analysis of in-situ Thermoplastic Composite Tape Laying". In: *Journal of Thermoplastic Composite Materials* 4.1 (Jan. 1991), pp. 20–45. DOI: 10.1177/089270579100400102.

[121] Mehrdad N. Ghasemi Nejhad. "Thermal Analysis for Thermoplastic Composite Tow/Tape Preheating and Pultrusion". In: *Journal of Thermoplastic Composite Materials* 10.6 (Nov. 1997), pp. 504–523. DOI: 10.1177/089270579701000601.

[122] C. Nicodeau et al. "In-situ consolidation process optimization for thermoplastic matrix composites". In: *International SAMPE Symposium and Exhibition (Proceedings)* 51 (Jan. 2006).

[123] Aidan O'Dwyer. "A Summary of PI and PID Controller Tuning Rules for Processes with Time Delay. Part 1: PI Controller Tuning Rules". In: *IFAC Proceedings Volumes* 33.4 (Apr. 2000), pp. 159–164. DOI: 10.1016/s1474-6670(17)38237-x.

[124] Katsuhiko Ogata. *Discrete-time control systems*. Prentice-Hall, Inc., 1995.

[125] Vincenzo Oliveri et al. "Design, Manufacture and Test of an In-Situ Consolidated Thermoplastic Variable-Stiffness Wingbox". In: *AIAA Journal* 57.4 (Apr. 2019), pp. 1671–1683. DOI: 10.2514/1.j057758.

[126] Sadik L. Omairey et al. "Development of innovative automated solutions for the assembly of multifunctional thermoplastic composite fuselage". In: *The International Journal of Advanced Manufacturing Technology* 117.5-6 (Aug. 2021), pp. 1721–1738. DOI: 10.1007/s00170-021-07829-2.

[127] Ebrahim Oromiehie et al. "Automated fibre placement based composite structures: Review on the defects, impacts and inspections techniques". In: *Composite Structures* 224 (Sept. 2019), p. 110987. DOI: 10.1016/j.compstruct.2019.110987.

[128] Spiros Pantelakis and Konstantinos Tserpes, eds. *Revolutionizing Aircraft Materials and Processes*. Springer-Verlag GmbH, Mar. 2020. 403 pp. URL: https://www.ebook.de/de/product/38746008/revolutionizing_aircraft_materials_and_processes.html.

[129] Patricia P. Parlevliet, Harald E.N. Bersee and Adriaan Beukers. "Residual stresses in thermoplastic composites—A study of the literature—Part I: Formation of residual stresses". In: *Composites Part A: Applied Science and Manufacturing* 37.11 (Nov. 2006), pp. 1847–1857. DOI: 10.1016/j.compositesa.2005.12.025.

[130] Bisma Parveez et al. "Scientific Advancements in Composite Materials for Aircraft Applications: A Review". In: *Polymers* 14.22 (Nov. 2022), p. 5007. DOI: 10.3390/polym14225007.

[131] L. Pedrotti, Hartmut Schmidt and W. Bausch. *Optik für Ingenieure*. Springer Berlin Heidelberg, Oct. 2007. 872 pp. ISBN: 978-3-540-73471-0. URL: https://www.ebook.de/de/product/6697944/l_pedrotti_hartmut_schmidt_w_bausch_optik_fuer_ingenieure.html.

[132] Mario Pianta and Matteo Lucchese. "Rethinking the European Green Deal". In: *Review of Radical Political Economics* 52.4 (Sept. 2020), pp. 633–641. DOI: 10.1177/0486613420938207.

[133] C.M. Pistor, M.A. Yardimci and S.I. Güçeri. "On-line consolidation of thermoplastic composites using laser scanning". In: *Composites Part A: Applied Science and Manufacturing* 30.10 (Oct. 1999), pp. 1149–1157. DOI: 10.1016/s1359-835x(99)00030-5.

[134] R. Pitchumani, J. W. Gillespie and M. A. Lamontia. "Design and Optimization of a Thermoplastic Tow-Placement Process with In-Situ Consolidation". In: *Journal of Composite Materials* 31.3 (Feb. 1997), pp. 244–275. DOI: 10.1177/002199839703100302.

[135] R. Pitchumani et al. "Analysis of transport phenomena governing interfacial bonding and void dynamics during thermoplastic tow-placement". In: *International Journal of Heat and Mass Transfer* 39.9 (June 1996), pp. 1883–1897. DOI: 10.1016/0017-9310(95)00271-5.

[136] S.Joe Qin and Thomas A. Badgwell. "A survey of industrial model predictive control technology". In: *Control Engineering Practice* 11.7 (July 2003), pp. 733–764. DOI: 10.1016/s0967-0661(02)00186-7.

[137] Z. Qureshi et al. "In situ consolidation of thermoplastic prepreg tape using automated tape placement technology: Potential and possibilities". In: *Composites Part B: Engineering* 66 (Nov. 2014), pp. 255–267. DOI: 10.1016/j.compositesb.2014.05.025.

[138] Sridhar Ranganathan, Suresh G. Advani and Mark A. Lamontia. "A Non-Isothermal Process Model for Consolidation and Void Reduction during In-Situ Tow Placement of Thermoplastic Composites". In: *Journal of Composite Materials 1995.29:1040-1062* (1995).

[139] L. Raps et al. "CF/LM-PAEK: Characterisation and sensitivity to critical process parameters for automated fibre placement". In: *Composite Structures* 284 (Mar. 2022), p. 115087. DOI: 10.1016/j.compstruct.2021.115087.

[140] Dipa Ray et al. "Fracture toughness of carbon fiber/polyether ether ketone composites manufactured by autoclave and laser-assisted automated tape placement". In: *Journal of Applied Polymer Science* (Nov. 2014), n/a–n/a. DOI: 10.1002/app.41643.

[141] Jasper Reichardt, Ismet Baran and Remko Akkerman. "New analytical and numerical optical model for the laser assisted tape winding process". In: *Composites Part A: Applied Science and Manufacturing* 107 (Apr. 2018), pp. 647–656. DOI: 10.1016/j.compositesa.2018.01.029.

[142] R. S. Rivlin and D. W. Saunders. "Large elastic deformations of isotropic materials VII. Experiments on the deformation of rubber". In: *Philosophical Transactions of the Royal Society of London. Series A, Mathematical and Physical Sciences* 243.865 (Apr. 1951), pp. 251–288. DOI: 10.1098/rsta.1951.0004.

[143] Robert H Rizzolo and Daniel F Walczyk. "Ultrasonic consolidation of thermoplastic composite prepreg for automated fiber placement". In: *Journal of Thermoplastic Composite Materials* 29.11 (Aug. 2016), pp. 1480–1497. DOI: 10.1177/0892705714565705.

[144] F Rodriguez-Lence, MI Martin and K Fernandez Horcajo. "In-situ consolidation of integrated thermoplastic fuselage panels: The future in structural comercial aerocomposites". In: *ECCM18–18th European conference on composite materials*. 2018.

[145] Warren Max Rohsenow, James P. Hartnett and Young I. Cho, eds. *Handbook of Heat Transfer*. Mcgraw-Hill Education, 1998.

[146] Todd Rudberg et al. "Improving AFP Cell Performance". In: *SAE International Journal of Aerospace* 7.2 (Sept. 2014), pp. 317–321. DOI: 10.4271/2014-01-2272.

[147] D. Saenz-Castillo et al. "Effect of processing parameters and void content on mechanical properties and NDI of thermoplastic composites". In: *Composites Part A: Applied Science and Manufacturing* 121 (June 2019), pp. 308–320. DOI: 10.1016/j.compositesa.2019.03.035.

[148] Diego Saenz-Castillo et al. "A comparison of mechanical properties and X-ray tomography analysis of different out-of-autoclave manufactured thermoplastic composites". In: *Journal of Reinforced Plastics and Composites* 39.19-20 (May 2020), pp. 703–720. DOI: 10.1177/0731684420924081.

[149] Tony E. Saliba, David P. Anderson and Ronald A. Servais. "Process Modeling of Heat Transfer and Crystallization in Complex Shapes Thermoplastic Composites". In: *Journal of Thermoplastic Composite Materials* 2.2 (Apr. 1989), pp. 91–104. DOI: 10.1177/089270578900200202.

[150] Samoil Samak et al. "Some experimental investigation of products from thermoplastic composite materials manufactured with robot and LAFP". In: *International Journal of Engineering Research & Technology (IJERT)* 9.Issue (2020).

[151] Hugo Sarrazin and George S. Springer. "Thermochemical and Mechanical Aspects of Composite Tape Laying". In: *Journal of Composite Materials* 29.14 (Sept. 1995), pp. 1908–1943. DOI: 10.1177/002199839502901407.

[152] P.M. Schaefer et al. "Analysis and improved process response prediction of laser-assisted automated tape placement with PA-6/carbon tapes using Design of Experiments and numerical simulations". In: *Composites Part A: Applied Science and Manufacturing* 96 (May 2017), pp. 137–146. DOI: 10.1016/j.compositesa.2017.02.008.

[153] Ines Schiel et al. "An investigation of in-situ AFP process parameters using CF/LM-PAEK". In: *Advanced Manufacturing: Polymer & Composites Science* 6.4 (Oct. 2020), pp. 191–197. DOI: 10.1080/20550340.2020.1826772.

[154] Jos Schijndel. "Getting State-Space Models from FEM Simulations". In: Nov. 2017.

[155] R. Schledjewski. "Thermoplastic tape placement process –in situconsolidation is reachable". In: *Plastics, Rubber and Composites* 38.9-10 (Dec. 2009), pp. 379–386. DOI: 10.1179/146580109x12540995045804.

[156] R. Schledjewski and M. Latrille. "Processing of unidirectional fiber reinforced tapes - fundamentals on the way to a process simulation tool (ProSimFRT)". In: *Composites Science and Technology* 63.14 (Nov. 2003), pp. 2111–2118. DOI: 10.1016/s0266-3538(03)00108-8.

[157] Carsten Schmidt. *Innovative method of temperature measurement for Automated Fiber Placement*. Tech. rep. https://www.ifw.uni-hannover.de/en/institute/news-und-veranstaltungen/news/news-details/news/innovative-method-of-temperature-measurement-for-automated-fiber-placement last visited on: 2024-01-11. Leibnitz Universität Hannover, 2023.

[158] Helmut Schürmann. *Konstruieren mit Faser-Kunststoff-Verbunden mit 39 Tabellen*. BerlinHeidelbergNew York, NY: Springer, 2007. ISBN: 978-3-540-72189-5.

[159] Richard Sharp, Scott Holmes and Cindy Woodall. "Material Selection/Fabrication Issues for Thermoplastic Fiber Placement". In: *Journal of Thermoplastic Composite Materials* 8.1 (Jan. 1995), pp. 2–14. DOI: 10.1177/089270579500800102.

[160] Pavel Simacek et al. "A non-local void filling model to describe its dynamics during processing thermoplastic composites". In: *Composites Part A: Applied Science and Manufacturing* 46 (Mar. 2013), pp. 154–165. DOI: 10.1016/j.compositesa.2012.10.015.

[161] *Sintermetalle, ausgenommen Hartmetalle - Ungekerbte Probe für den Schlagzähigkeitsversuch*. DIN Deutsches Institut für Normung e.V. DOI: 10.31030/2806571.

[162] Fazil O. Sonmez and H. Thomas Hahn. "Analysis of the On-Line Consolidation Process in Thermoplastic Composite Tape Placement". In: *Journal of Thermoplastic Composite Materials* 10.6 (Nov. 1997), pp. 543–572. DOI: 10.1177/089270579701000604.

[163] Fazil O. Sonmez and H. Thomas Hahn. "Modeling of Heat Transfer and Crystallization in Thermoplastic Composite Tape Placement Process". In: *Journal of Thermoplastic Composite Materials* 10.3 (May 1997), pp. 198–240. DOI: 10.1177/089270579701000301.

[164] Fazil O. Sonmez, H. Thomas Hahn and Mustafa Akbulut. "Analysis of Process-Induced Residual Stresses in Tape Placement". In: *Journal of Thermoplastic Composite Materials* 15.6 (Nov. 2002), pp. 525–544. DOI: 10.1177/0892705702015006207.

[165] G. H. Spencer and M. V. R. K. Murty. "General Ray-Tracing Procedure†". In: *Journal of the Optical Society of America* 52.6 (June 1962), p. 672. DOI: 10.1364/josa.52.000672.

[166] J.E Spruiell and Chris J. Janke. *A review of the measurement and development of crystallinity and its relation to properties in neat poly(phenylene sulfide) and its fiber reinforced composites*. Tech. rep. U.S. Department of Energy, 2004.

[167] C.M. Stokes-Griffin and P. Compston. "A combined optical-thermal model for near-infrared laser heating of thermoplastic composites in an automated tape placement process". In: *Composites Part A: Applied Science and Manufacturing* 75 (Aug. 2015), pp. 104–115. DOI: 10.1016/j.compositesa.2014.08.006.

[168] C.M. Stokes-Griffin and P. Compston. "Optical characterisation and modelling for oblique near-infrared laser heating of carbon fibre reinforced thermoplastic composites". In: *Optics and Lasers in Engineering* 72 (Sept. 2015), pp. 1–11. DOI: 10.1016/j.optlaseng.2015.03.016.

[169] C.M. Stokes-Griffin and P. Compston. "The effect of processing temperature and placement rate on the short beam strength of carbon fibre–PEEK manufactured using a laser tape placement process". In: *Composites Part A: Applied Science and Manufacturing* 78 (Nov. 2015), pp. 274–283. DOI: 10.1016/j.compositesa.2015.08.008.

[170] C.M. Stokes-Griffin et al. "Modelling the automated tape placement of thermoplastic composites with in-situ consolidation". In: *Sustainable Automotive Technologies 2012*. Springer, 2012, pp. 61–68.

[171] C.M. Stokes-Griffin et al. "The effect of processing temperature on wedge peel strength of CF/PA 6 laminates manufactured in a laser tape placement process". In: *Composites Part A: Applied Science and Manufacturing* 121 (June 2019), pp. 84–91. DOI: 10.1016/j.compositesa.2019.02.011.

[172] Christopher Stokes-Griffin. "A combined optical-thermal model for laser-assisted fibre placement of thermoplastic composite materials". en. PhD thesis. 2015. DOI: 10.25911/5D5E716081EEC.

[173] Christopher Mark Stokes-Griffin et al. "Thermal modelling of the laser-assisted thermoplastic tape placement process". In: *Journal of Thermoplastic Composite Materials* 28.10 (Nov. 2015), pp. 1445–1462. DOI: 10.1177/0892705713513285.

[174] Wei-Ching Sun, Susan C Mantell and Kim A Stelson. "Modeling and control of the in-situ thermoplastic composite tape-laying process". In: (1998).

[175] Omid Aghababaei Tafreshi et al. "Heat transfer analysis of automated fiber placement of thermoplastic composites using a hot gas torch". In: *Advanced Manufacturing: Polymer & Composites Science* 5.4 (Oct. 2019), pp. 206–223. DOI: 10.1080/20550340.2019.1686820.

[176] Teijin. *Tenax Filament Yarn*. https://www.teijincarbon.com/fileadmin/PDF/Datenblätter_en/Product_Data_Sheet_TSG01en__EU_Filament_.pdf last visited on: 2021-12-23.

[177] John Tierney and J. W. Gillespie. "Modeling of In Situ Strength Development for the Thermoplastic Composite Tow Placement Process". In: *Journal of Composite Materials* 40.16 (Jan. 2006), pp. 1487–1506. DOI: 10.1177/0021998306060162.

[178] John Tierney and John W. Gillespie. "Modeling of Heat Transfer and Void Dynamics for the Thermoplastic Composite Tow-Placement Process". In: *Journal of Composite Materials* 37.19 (Oct. 2003), pp. 1745–1768. DOI: 10.1177/002199803035188.

[179] Briana N. Tomboulian and Robert W. Hyers. "Predicting the Effective Emissivity of an Array of Aligned Carbon Fibers Using the Reverse Monte Carlo Ray-Tracing Method". In: *Journal of Heat Transfer* 139.1 (Aug. 2016). DOI: 10.1115/1.4034310.

[180] Toray. *T700G Standard Modulus Carbon Fiber*. https://www.toraycma.com/wp-content/uploads/T700G-Technical-Data-Sheet-1.pdf last visited on: 2021-12-23.

[181] Toray. *Toray Cetex 1225*. https://www.toraytac.com/product-explorer/products/gXuK/Toray-Cetex-TC1225 last visited on: 2023-04-03.

[182] Yves M.P. Toso, Paolo Ermanni and Dimos Poulikakos. "Thermal phenomena in fiber-reinforced thermoplastic tape winding process: computational simulations and experimental validations". In: *Journal of Composite Materials* 38.2 (Jan. 2004), pp. 107–135. DOI: 10.1177/0021998304038651.

[183] S. Tumkor et al. "Modeling of heat transfer in thermoplastic composite tape lay-up manufacturing". In: *International Communications in Heat and Mass Transfer* 28.1 (Jan. 2001), pp. 49–58. DOI: 10.1016/s0735-1933(01)00212-3.

[184] U. K. Vaidya and K. K. Chawla. "Processing of fibre reinforced thermoplastic composites". In: *International Materials Reviews* 53.4 (July 2008), pp. 185–218. DOI: 10.1179/174328008x325223.

[185] Chris N. Velisaris and James C. Seferis. "Crystallization kinetics of polyetheretherketone (peek) matrices". In: *Polymer Engineering and Science* 26.22 (Dec. 1986), pp. 1574–1581. DOI: 10.1002/pen.760262208.

[186] Thomas Weiler et al. "Tailored irradiation by VCSEL for controlled thermal states in thermoplastic tape placement". In: *Laser 3D Manufacturing V*. Ed. by Henry Helvajian, Alberto Piqué and Bo Gu. SPIE, Feb. 2018. DOI: 10.1117/12.2291015.

[187] Thomas Weiler et al. "Transient thermal analysis of laser-assisted thermoplastic tape placement at high process speeds by use of analytical solutions". In: *Journal of Thermoplastic Composite Materials* 31.3 (Mar. 2017), pp. 311–338. DOI: 10.1177/0892705717697780.

[188] Nils Widmaier and Lukas Raps. "Analysis of New Concepts for the Consolidation Roller in Laser-Assisted Automated Tape Placement Processes". In: *Stuttgart Conference on Automotive Production 2022*. Nov. 2022, pp. 282–295. URL: https://elib.dlr.de/189463/.

[189] David Williams and Martin Brown. "Xenon Flashlamp Heating for Automated Fibre Placement". In: *Automated Composites Manufacturing-Third International Symposium*. acm. 2017.

[190] F. Yang and R. Pitchumani. "A fractal Cantor set based description of interlaminar contact evolution during thermoplastic composites processing". In: *Journal of Materials Science* 36.19 (2001), pp. 4661–4671. DOI: 10.1023/a:1017950215945.

[191] F. Yang and R. Pitchumani. "Nonisothermal healing and interlaminar bond strength evolution during thermoplastic matrix composites processing". In: *Polymer Composites* 24.2 (Apr. 2003), pp. 263–278. DOI: 10.1002/pc.10027.

[192] Khaled Yassin and Mehdi Hojjati. "Processing of thermoplastic matrix composites through automated fiber placement and tape laying methods". In: *Journal of Thermoplastic Composite Materials* 31.12 (Nov. 2017), pp. 1676–1725. DOI: 10.1177/0892705717738305.

[193] Xiulun Yin et al. "Smart Roller: Soft Sensor Array for Automated Fiber Placement". In: *Advanced Sensor Research* 2.9 (May 2023). ISSN: 2751-1219. DOI: 10.1002/adsr.202200074.

[194] Ali Yousefpour, Mehdi Hojjati and Jean-Pierre Immarigeon. "Fusion Bonding/Welding of Thermoplastic Composites". In: *Journal of Thermoplastic Composite Materials* 17.4 (July 2004), pp. 303–341. DOI: 10.1177/0892705704045187.

[195] Ali Yousefpour and Mehrdad N. Ghasemi Nejhad. "Experimental and Computational Study of APC-2/AS4 Thermoplastic Composite C-Rings". In: *Journal of Thermoplastic Composite Materials* 14.2 (Mar. 2001), pp. 129–145. DOI: 10.1106/1rqv-317q-36k0-1e6p.

[196] Amin Zaami, Ismet Baran and Remko Akkerman. "Experimental and numerical analysis of laser reflection for optical-thermal process modeling of tape winding". In: *21st International Conference on Composite Materials*. 2017.

[197] Amin Zaami et al. "Optical characterization of fiber-reinforced thermoplastic tapes for laser-based composite manufacturing". In: *Composites Part A: Applied Science and Manufacturing* 146 (July 2021), p. 106402. DOI: 10.1016/j.compositesa.2021.106402.

[198] Danning Zhang, Dirk Heider and John W Gillespie. "Determination of void statistics and statistical representative volume elements in carbon fiber-reinforced thermoplastic prepregs". In: *Journal of Thermoplastic Composite Materials* 30.8 (Dec. 2015), pp. 1103–1119. DOI: 10.1177/0892705715618002.

[199] Ridong Zhang, Anke Xue and Furong Gao. *Model Predictive Control*. Springer-Verlag GmbH, Aug. 2018. 137 pp. ISBN: 978-981-13-0083-7. URL: https://www.ebook.de/de/product/33793509/ridong_zhang_anke_xue_furong_gao_model_predictive_control.html.

[200] Wuxiang Zhang et al. "Overview of current design and analysis of potential theories for automated fibre placement mechanisms". In: *Chinese Journal of Aeronautics* 35.4 (Apr. 2022), pp. 1–13. DOI: 10.1016/j.cja.2021.04.018.

[201] Dacheng Zhao et al. "Effects of processing parameters on the performance of carbon fiber reinforced polyphenylene sulfide laminates manufactured by laser-assisted automated fiber placement". In: *Journal of Composite Materials* (Nov. 2021), p. 002199832110558. DOI: 10.1177/00219983211055827.